Development and production of Lab-on-Chip systems for DNA mapping

Østergaard, Peter Friis

Publication date:
2014

Document Version
Publisher's PDF, also known as Version of record

Development and production of Lab-on-Chip systems for DNA mapping

Peter Friis Østergaard
Ph.D. Thesis

DTU Nanotech
Department of Micro- and Nanotechnology

Development and production of Lab-on-Chip systems for DNA mapping

Peter Friis Østergaard
DTU Nanotech, Department of Micro- and Nanotechnology
Technical University of Denmark

A thesis submitted for the degree of
Philosophiæ Doctor (Ph.D.)

Lyngby, March 2014

Supervisors: Rafael Taboryski, Rodolphe Marie, and
Kenneth Harlow

til Frode B. Friis
1914-2008

Abstract

During the last two decades, there has been a significant increase in the academic work in Lab on a Chip systems, while the number of commercial products has only increased a little. Many universities have research groups working within the field of Lab on a Chip and Micro Total Analysis Systems, and much funding has gone into the development of systems capable of performing a variety of different tasks. Meanwhile the industry has not seen the same potential in Lab on a Chip systems as the academic societies, resulting in knowledge being kept in the universities and not helping the population at large.

To try and overcome this situation, this thesis demonstrates a fabrication platform with the potential of producing thousands of identical polymer Lab on a Chip systems, containing structures in the length scale from 100 nm to 50 µm on the same device and with a price that drops significantly as more devices are fabricated.

Such systems can be created, at the department, with a throughput of 25 devices per hour, and with a potential price as low as DKK 17.-

During the process, efforts were taken in developing a bonding scheme capable of giving a high yield on structures having aspect ratios as low as 1:200.

The developed polymer systems are tested by conducting two different experiments on DNA. Since such experiments are highly sensitive, efforts have been taken in order to lower the autofluorescence of the devices, resulting in a decrease of the background signal to roughly half the initial value.

The first experiment concerns mapping of short strands of λ-DNA and T4GT7-DNA against a theoretically obtained signal while stretched out in nanochannel confinements. The DNA is initially counterstained with a molecule that binds specifically to certain parts of the DNA. This counterstaining affects the staining with a fluorescent dye which, as a result of the first molecule, will distribute itself in a predictable, sequence specific, configuration along the DNA, thereby creating a fluorescent profile.

The nanochannels stretches the DNA to around 25% of their contour length and since several nanochannels can be placed parallel to each other, a large number of DNA molecules can be investigated.

In the second experiment, mapping is performed on human DNA in nanoslit devices. A fluorescent profile is created by heating the sample up to a temperature, where the DNA is partially denatured. The fluorescent dye will diffuse away from the denatured regions, and by analysing these black areas, the DNA molecule can be identified and potential mutations can be found.

In the nanoslits, the DNA is stretched out via a shear flow, resulting in a stretching of more than 95% of the contour length meaning a higher resolution compared to what was found when using the nanochannels.

Resumé

Gennem de sidste to årtier har der været en massiv forøgning i det akademiske arbejde i Lab on a Chip systemer, mens antallet af kommercielle produkter kun er steget svagt. Mange universiteter har forskningsgrupper, der arbejder inden for området og mange forskningsmidler er blevet brugt på udvikling af systemer, der kan udføre et utal af forskellige opgaver. Industrien har imidlertid ikke set det samme potentiale i Lab on a Chip systemer, som de akademiske kredse har. Resultatet af dette er, at viden bliver holdt på universiteterne, hvor den ikke kan gøre nytte for den almene befolkning.

I et forsøg på at overkomme denne situation, demonstreres her en fabrikationsplatform, der har potentiale til at producere tusinder af identiske Lab on a Chip polymeremner indeholdende strukturer i længdeskalaen fra 100 nm til 50 µm på samme emne og med en pris der falder markant, jo flere emner der produceres.

Sådanne systemer kan fabrikeres, på instituttet med en produktionshastighed på 25 emner i timen og en pris der potentielt kan nå DKK 17,-.

I løbet af processen er der brugt kræfter på at udvikle en bondingprotokol, der giver et højt udbytte på strukturer, der har et forhold mellem højde og bredde så lavt som 1:200.

De udviklede polymeremner er testet ved at udføre to forskellige forsøg på DNA. Da sådanne forsøg er meget følsomme, er der brugt kræfter på at sænke autofluorescensen på emnerne, hvilket har resulteret i, at baggrundssignalet er blevet næsten halveret fra den oprindelige værdi.

Det første forsøg omhandler identificering af korte strenge af λ-DNA og T4GT7-DNA ved sammenligning med et teoretisk signal, når molekylet er udstrukket i en kanal med bredde og højde i nanometerskalaen. DNAet er indledningsvist behandlet med et molekyle, der binder specifikt til visse områder af DNAet. Denne behandling påvirker indfarvningen med det fluorescerende molekyle, der nu vil fordele sig på deterministisk, sekvensspecifik, konfiguration langs molekylet og dermed skabe en fluorescerende profil.

Kanalerne giver i dette tilfælde en udstrækning på ca. 25% af konturlængden og da flere nanokanaler kan placeres parallelt, kan antallet af målinger være højt.

I det andet forsøg udføres identificering af human DNA i nanoslit emner. I disse forsøg skabes den fluorescerende profil ved at opvarme prøven til en temperatur, hvor DNAet er delvist denatureret. Det fluorescerende stof vil diffundere væk fra disse områder og en analyse af de sorte områder identificeres DNAet samt eventuelle mutationer deri.

I disse forsøg bliver DNAet udstrukket via en væskestrøm. Dette giver en udstrækning på mere end 95% af konturlængden og derved en højere opløsning end hvad der blev fundet ved brug af nanokanaler.

List of Abbreviations

3D	3-Dimensional
A	Adenine
AFM	Atomic Force Microscope
BME	β-MercaptoEthanol
bp	basepair
BSA	Bovine Serum Albumin
C	Cytosine
CAD	Computer Aided Design
CNC	Computer Numerical Control
COC	Cyclin Olefin Co-polymer
COP	Cyclin Olefin Polymer
ddNTP	di-deoxyriboNucleic TriPhosphate
DEEMO	Dry Etching, Electroplating, MOulding
DNA	DeoxyriboNucleic Acid
dNTP	deoxyriboNucleic TriPhosphate
DTU	Danmarks Tekniske Universitet/ Technical University of Denmark
e-beam	electron-beam
EMCCD	Electron Multiplying Charge-Coupled Device
FDM	Focused Deposition Modelling
FGS	First Generation Sequencing
FIB	Focused Ion Beam
FoV	Field of View
G	Guanine
HMDS	HexaMethylDiSilazane
LIGA	LIthographie, Galvanoformung, Abformung
LoC	Lab-on-a-Chip
NGS	Next Generation Sequencing
NIL	NanoImprint Lithography
P	Persistence length
PC	PolyCarbonate
PCR	Polymerase Chain Reaction
PDMS	Poly(DiMethylSiloxane)
PE	PolyEthylene
PoC	Point-of-Care

PMMA	Poly(MethylMethAcrylate)
RF	Radio Frequency
R_g	radius of gyration
RIE	Reactive Ion Etch
RNA	RiboNucleic Acid
sccm	standard cube centimetre per minute
SEM	Scanning Electron Microscope
slm	standard litre per minute
T	Thymine
TBE	Tris/Borate/EDTA
T_g	glass transition temperature
UV	Ultra Violet

Preface

The Ph.D. thesis presented here is the result of a 3 year Ph.D. project carried out at the Technical University of Denmark, Department of Micro- and Nanotechnology, in the research group of Rafael Taboryski from 2011 to 2014. A three months stay at McGill University, Department of Physics in Canada took place during the spring of 2012.

The project was supported by the Danish Council of Strategic Research through the Strategic Research Center PolyNano (grant no. 10-092322/DSF) and the Danish Agency for Science, Technology and Innovation through DELTA's performance contract, CiPOC (grant no. 10-076609)

The Ph.D. project has been supervised by Rafael J. Taboryski, associate professor and leader of the POLYMIC group at DTU Nanotech, as main supervisor with Rodolphe Marie, associate professor of the Optofluidics group at DTU Nanotech and Kenneth W. Harlow, Point-of-Care specialist at DELTA as co-supervisors.

Currently, almost all Lab on a Chip devices used in academia are fabricated in expensive silicon and silica material or by the use of low yield PDMS casting techniques. Such fabrication techniques are good when a few devices are required, of if the design is changed between each experiment. The downside of this approach is that it becomes difficult to expand Lab on a Chip devices to a broader audience, since many scientists, not directly involved in the Lab on a Chip community, do not have the time or experience to fabricate their own systems, and companies do not want to invest heavily in order to reinvent the production platform to make large throughput fabrication possible.

The goal of this the project has been to fabricate mass producible, low cost Lab on a Chip polymer systems for use in DNA mapping experiments. Such experiments are very sensitive, both towards topological defects in the device, and towards background signals in the material. By using delicate cleanroom procedures, combined with optimised injection moulding as a fabrication platform, structures can be replicated in large quantities, while an investigation of the material used for the injection moulding allows for a significant decrease in background signal.

In chapter 1, an introduction to conventional DNA sequencing is given. This includes the original Sanger sequencing along with the Next Generation Sequencing methods that have been developed during the last decade. The background for why optical mapping can help reduce the price of sequencing and at the same time increase the credibility of the results is explained.

Chapter 2 describes the production of the polymer devices, from the cleanroom fabrication of a silicon master to injection moulding of a high number of replicas and the bonding of them, leading to the final device. In this chapter,

the economical advantages of mass production is also investigated in calculations showing the economics of scale with the devices fabricated in the thesis.

In chapter 3, the work and results from the 3 month stay at McGill University is discussed. The work comprises a number of experiments performed on λ-DNA and T4GT7-DNA, where the molecules were treated with a counterstaining agent prior to being stained with the fluorescent dye. These experiments also show that the polymer devices that contains nanochannels can be used for obtaining barcodes when the DNA is stretched out by means of entropy.

Devices containing nanoslits 100 nm in height and 20 µm in width are demonstrated in chapter 4. The nanoslit devices are used for performing melting mapping on DNA from the human genome. For these experiments to work, a low background signal and surface roughness is required.

Finally, chapter 5 concludes the thesis and gives future perspective.

Lyngby, March 31, 2014

Peter Friis Østergaard

Acknowledgements

I would like to thank my supervisors, Rafael Taboryski, Rodolphe Marie, and Kenneth Harlow for motivation, help, and encouragement during the period of my thesis. I would also like to thank Walter Reisner for letting me stay in his lab in Montreal and for inspiration and guidance during my stay.

I also thank Joanna Lopacinska-Jørgensen for help with my experiments performed in the last part of my project, and Jonas Nyvold Pedersen for analysing my data.

I would like to thank the employees at DTU Danchip, especially Claus Højgaard Nielsen and Tage Larsen for helping me out when the machines did not want to collaborate.

Furthermore I would like to thank my fellow group members for keeping the spirit high, being able to talk about non-work related subjects and for some good times during conferences around the world.

Finally, and most importantly, I would like to thank my girlfriend, my friends and my family for continuously reminding me that there is a world outside of the laboratory.

Contents

Chapter 1

Introduction

In this project, the aim has been to develop a fabrication scheme for production of high quality Lab on a Chip (LoC) devices for biomedical purposes in large volumes.

Lab on a chip technology offers has qualities, that can not be obtained with conventional laboratory procedures, but has historically had a production scheme that makes them undesirable for the industry at large, due to slow production cycles and high device cost.

If a development and production scheme that improves the production time and decreases the cost per device can be established, it will increase the likelihood for LoC technology to contribute to the industry.

1.1 Lab-on-a-Chip

A LoC is a small device intended to perform one or several procedures from a standard laboratory, but scaled down to fit into a device, typically the size of a credit card or smaller, as seen in Figure 1.1.

There are several advantages when scaling down laboratory procedures to fit into a small device. The small dimensions of a LoC means that only small volumes of reactants are used when performing experiments. The small dimensions typically also causes small diffusion distances within the device, giving

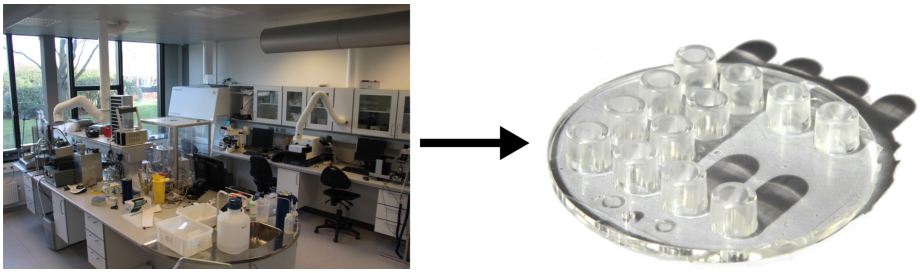

Figure 1.1: In a Lab on a Chip system, one or several laboratory procedures is incorporated into a small device.

faster reaction times and producing results at a faster rate.

Small reaction volumes in a LoC means that only small amounts of expensive reagents are used, thereby reducing the cost of the experiment. When the sample being investigated is only available in small amounts, a LoC device can also be of interest.

In conventional laboratory processes, large volumes are often needed to conduct an analysis and a small sample can end up being so diluted that any signal from it becomes too low to detect. If the system is scaled down, the small sample volume will still result in a high concentration and thereby a good signal.

There are many advantages when the sample size needed for analysis is reduced, especially within biology and chemistry.

The price for developing new pharmaceuticals is increasingly high. In 2003 the cost of developing a new drug was around $800 million US dollars, rising to around $1.3-1.7 billion dollars in 2009[Col09] and still growing. One of the biggest challenges faced by pharmaceutical companies is that potential drug candidates are only rejected late in the process after heavy investments in clinical trials. If a better screening of candidates prior to clinical testing could be performed, the price per developed drug making it to the market would decrease[LZZ+14, TMC+13].

For environmental purposes, a fast analysis can be critical for making a decision in time. If a water source is polluted, the risk of humans and animals getting ill because they drink the water will increase drastically as a function of time. The small dimension of LoC along with the possibility for fast analysis of a sample makes it possible to get fast results from many places, giving an increased consumer security[ACT+02, JSL+11, BTS+11].

In the field of biology, small samples are often of interest. When investigating individual cells, the sample size will always be small, even after amplification. The consequence of this is that conventional methods of analysis can have problems with loosing information since the single cell of interest is either diluted to a degree where no signal is acquired, or it is mixed with many other cells that are not of interest. By isolating the cells in individual droplets, interaction between cells will not occur, and analysis of the single cells can be performed, thereby gaining knowledge about the diversity of cells in e.g. a cancer tumour[KAD+08, CTLB+08, SDK+10].

Putting an analytical task down on a LoC can also lead to automation in a so called Point of Care (PoC) system. This can minimize the amount of human interaction with the analysis, a reduction in the need for highly trained technicians, and ultimately in a smaller degree of human error. PoC systems also allow for easier distribution at low costs, promising better medical diagnostics in developing countries that do not have access to conventional laboratories[YEF+06, MPC+08, MPW10].

As such, LoC technology offers many advantages in smaller sample sizes, increased automation, and faster results.

1.2 Fabrication of Lab on a Chip Devices

There are several techniques used for fabricating LoC devices. All the techniques available can be classified into two categories; direct fabrication or replication,

depending on whether the fabrication scheme ends up with a single device or in a master, intended for the replication of several devices.

Direct fabrication is when a device is being processed from one end of the production chain to the other and only ends out with a single device. Typical techniques used for this type of fabrication is micro milling[RSSH03], laser ablation[Mal06a, Mal06b], 3D printing[KRS+12, TWL03], and cleanroom processing[HFS+93, AvdB03]. Common for these fabrication schemes is, that the material used in the beginning of the processing is incorporated into the final device.

Since the starting material is an integrated part of the final device, the entire fabrication process will only end up in a single LoC. If more devices are needed, the entire process has to start all over again.

There are many advantages of using direct fabrication techniques, especially in the developing phase of a project, where new iterations of a design have to be tested, changed and optimized. Since no complicated replication techniques are used, a single device can be fabricated and tested within a short time frame. Using results from the testing, the structure can be optimized fast, and a new version can be made.

If many devices are required, direct fabrication does have significant flaws. Since the manufacturing of a single device can take several hours or even days, the manufacturing of multiple devices can take weeks. As such, these devices cannot be considered disposable, since the quantity that can be fabricated is limited.

When multiple instances of the same system has to be produced, replication of a master structure is often advantageous.

By fabricating a master structure and then replicating this, all the steps leading up to the master structure do not need to be performed for all proceeding devices.

Often the master device is fabricated through the same processes as used for direct fabrication. If a mould having the inverse shape of the desired structure is milled using a micro milling tool, replicas can be made by casting Polydimethylsiloxane (PDMS) onto it. After removal of the PDMS, the mould can be used again and will produce an exact replica of the first device.

Several techniques exist for replicating a master device, such as elastomer casting[DMSW98], microfluidic stickers[BDNS08], hot embossing/nanoimprint lithography (NIL)[CKR96], and micro injection moulding[NEW98, WE98].

Even though these fabrication processes all fall within the same category, there is still a large difference in production time for a given device, along with differences in the physical properties of the material. While injection moulding can produce several devices in one minute, PDMS casting typically uses hours or days for replicating a system[BG08].

1.2.1 Micro Milling

As with regular computer numerical control (CNC) milling of materials, micro milling, Figure 1.2a), works by having a milling machine following the trails defined by an external, computer generated file. As the name implies, micro milling uses cutters which are smaller than conventional cutters, making it possible to fabricate much smaller structures. There are still limits to how small cutters can be fabricated. This causes the technique to have a cutter defined

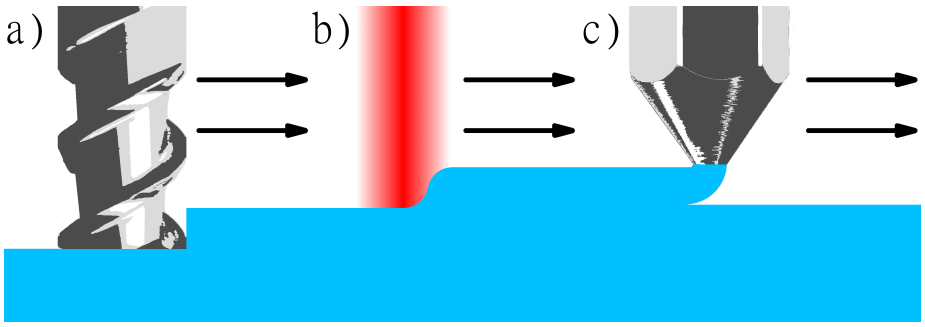

Figure 1.2: Methods for direct fabrication of LoC devices. a) Micromililng works by removing material by the use of a milling machine cutting away the substrate. b) Laser ablation removes the substrate by high intensity laser power. c) 3D printing adds on material, gradually building up the device.

minimum resolution in the horizontal plane in the length scale of $\sim 100\,\mu m$, while the vertical resolution, which is defined by the machine, can go lower.

Micro milling has several advantages. Since it can be used for fabricating a device directly from a computer generated file, it is easy to change the design for a new iteration. This makes it a good option for prototyping, since several designs can be tested within a short time frame.

Furthermore, micro milling can be performed on a variety of materials, making it applicable for many different applications. As such, it is used for milling of Lab on a Chip systems in various polymer materials such as Cyclic Olefin Copolymers (COC)[KLC+13] and Poly(Methyl MethaAcrylate) (PMMA)[XLT+06]. It can also be used for fabricating masters having the a negative polarity of the desired part. Replication of this master can then be performed in order to get the final part[WKK+11, XXQ+12].

While micro milling contains its own qualities, the minimum feature size defined by the cutter sets limitations on which features can be created using this technique. The technique also has a relatively low throughput caused by the direct fabrication. Although minimum feature sizes are limited when using this technique, surface roughness can be found down in the nanometre scale, making the technique usable for the production of optical surfaces[LJY10].

1.2.2 Laser Ablation

By using a powerful laser system, enough energy can be deposited in a substrate material to vaporise it, as sketched in Figure 1.2b). This technique can be used in order to define geometries for a LoC system in a fast manner, since, as with micro milling, the structures are read directly from a computer generated file into the machine, which then writes the structure into the substrate.

Because of the non linearity interaction of certain laser systems, such as femtosecond lasers, this technique is capable of structuring the material inside a transparent substrate[EMMV+12]. However, more common laser systems, such as CO_2 lasers, which are linearly absorbed in polymers, will only create trenches in the surface of the substrate[KKG02]. Since the laser ablates the

material by adding a large amount of energy to it[BL02], stress can be accumulated in the substrate, leading to buckling and loss of positional control during fabrication[SvWY13].

While this technique can be used for fast prototyping, the trenches created by laser ablation have the same profile as the intensity of the laser beam. This makes it difficult to obtain vertical side walls, Microfluidic systems based on capillary forces however, can still be fabricated directly in a substrate using this production scheme[MD13].

1.2.3 3D Printing

Where as the micro milling and laser ablation techniques works by removing material from a substrate, 3D printing is performed by continuously adding material to the device being fabricated. Furthermore, 3D printing consists of a variety of techniques, ranging from 2 photon lithography[Nan], to laser sintering[KLKC07, GTH12], to Fused Deposition Modelling (FDM), where material is added in the form of molten polymer[sHM96]as sketched in Figure 1.2c).

As FDM works by adding material to the device through a nozzle in the 3D printer, the integration of several different materials is possible in devices fabricated using this technique[CEC+13]. This includes rubber like materials for tight connections to external equipment, or the fabrication of support structures during manufacturing, that can be chemically removed after the part has been printed.

Despite the advantages found in 3D printing, it has severe limitations in resolution, making it difficult to fabricate true micro fluidic systems, since channels smaller than 100 µm in width are hard to obtain[SSC+14].

1.2.4 Cleanroom Fabrication

Cleanroom fabrication consists of a variety of different fabrication schemes, from growing of oxides, dry etching and wet etching, deposition of materials such as metals and nitrides, to doping of the substrate in order to change the electrical properties of it.

When fabricating LoC devices, only part of these processes are of interest. Since most LoC devices only use the geometry of the fabricated device, changing the electrical properties of the substrate is not of much interest. Instead, the small dimensions which can be created using cleanroom manufacturing are of much larger interest in the LoC society. Electron-beam (E-beam) lithography and Focused Ion Beam (FIB) makes it possible to define structures as small as 10 nm[Danb, LJmC+10, cDWX13], wile standard ultra-violet (UV) lithography and reactive ion etches (RIE) makes it possible to fabricate well defines structures in the micro meter range[TOM+12].

Such techniques have been used to make miniaturized gas chromatographs in the first published LoC paper in 1979[TJA79], and has since been used for the fabrication of systems such as microreactors[TvMB+05], polymerase chain-reaction (PCR) chips[EHL07], and cell growth chambers[NY07], but also for smaller structures such as nanochannels[RLS+10, WSDR12, LKB+13].

Fabricating low tolerance structures in cleanroom environments does have a cost. At DTU Danchip, national centre for micro- and nanofabrication, located at DTU, Denmark, accessing the cleanroom without using any equipment, costs

DKK 750.-/hour[Dana]. Since much of the equipment requires highly trained personal, and is in itself expensive, resulting in a high down-payment, devices fabricated using this technology are generally expensive. That being said, commercial products, fabricated in silicon and silica wafers, such as the disposable parts to the automated patch clamping devices fabricated in silicon from Sophion Biosciences[Biob], and 45 nm wide and deep nanochannels fabricated in silica from BioNano Genomics[Gen, LHL+12] do exist.

1.2.5 Elastomer Casting

Elastomer casting is a production technique, where a polymer, such as PDMS is cured after the addition of a hardener. Before curing, the elastomer is poured over a mould having the reverse polarity of the final part as seen in Figure 1.3a). This mould can be created, either by the use of micromilling, UV lithography of SU-8, or any other technique that ends up with the desired structure. After curing of the polymer, the device is peeled off, and bonded to a glass slide by van der Waals forces[MDA+00]. This bonding can be made irreversible by exposing the PDMS and the glass to an oxygen plasma prior to the bonding[DMSW98].

As the master structure used for defining the elastomer device is left behind intact, several identical devices can be fabricated without much added work. The throughput of devices fabricated is quite limited, since the curing of the elastomer takes a few hours when cured at 80 °C[RDK+09], and up to a day if cured at 65 °C[FY10].

Because production of elastomer devices does not require much equipment, PDMS casting has become a widely used material in microfluidic device fabrication[FY10]. The material has certain characteristics, not seen in many other materials used for LoC. The flexibility of PDMS makes it possible to create fluidic valves[UCT+00]. Its permeability towards gasses can be advantageous in cell experiments, due to the transfer of oxygen and CO_2[TB06], but can also cause problems due to evaporation of water[CAS+03].

Although elastomers can take a long time to process, commercial products containing PDMS microvalves, like NanoFlex^{TM}valves from fluidigm[flu], are available.

1.2.6 Hot Embossing/NIL

Hot embossing and NIL has, as elastomer casting, a negative master which is used for replication of structures into a polymer.

Unlike elastomer casting, standard hot embossing and nanoimprint lithography uses a thermoplastic, not an elastomer, as the final substrate. The master stamp is heated up to a temperature above the glass transition temperature (T_g) of the thermoplastic and pressed into the polymer as seen in Figure 1.3b). Slowly cooling down the master hardens the polymer and allows for the master to be removed, leaving the desired structure in the polymer.[TZS+03]

These structures can either be used on its own, or as a etch mask when working on silicon. Structures fabricated using this technique were as small as 25 nm back in 1996[CKR96] and 10 nm in 1997[CKZ+97].

Re-flow of the polymer during imprint caused by capillary effects and bending of the stamp can cause artefacts in the final device[Guo04]. Despite this, LoC systems have been fabricated by the use of hot embossing with the first

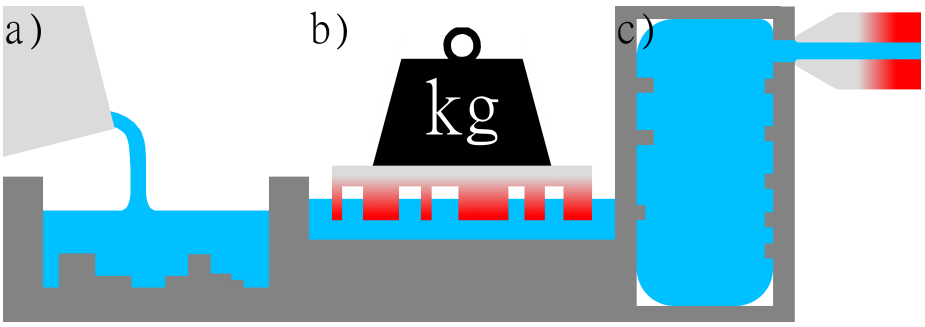

Figure 1.3: Simplified sketches of replication techniques: a) In elastomer casting, an uncured elastomer is cast over a mould containing a negative version of the structures to be replicated. After casting, the elastomer is cured at an elevated temperature. b) In hot embossing/NIL, the master stamp, containing the structures to be replicated, is heated to a temperature exceeding T_g of the thermoplastic. The heated stamp is pressed into the polymer and cooled down. This leaves the structures in the solidified substrate. c) Injection moulding works by melting the thermoplastic and injecting it into a cavity containing the desired structures. The polymer is cooled down and solidified inside the mould cavity.

system published in 2002[SPC02], while more recently nanoslits[CHP+10] and nanochannels have been manufactured[LJS+13].

1.2.7 Injection Moulding

Injection moulding is a widely used fabrication process in the industry, to produce a variety of different polymer devices, ranging from toothbrushes to car bumpers. It has also been shown to work well for the replication of structures for LoC devices[MNM+97, AHM+10]

Injection moulding is as a technique quite similar to hot embossing. A thermoplastic is being structured by the use of heat and pressure, the polymer is cooled down, and the final device is ejected from the machine.

Unlike hot embossing, injection moulding typically works by having a tool at constant temperature, and heating up the polymer. The polymer is heated up to above the melting temperature and injected into a cavity as seen in Figure 1.3c). A pressure is applied to the polymer, making it fill out the cavity, thereby reproducing the structures of the cavity surface. With the mould at a temperature below T_g, the polymer solidifies, and the device can be rejected from the mould.

Although most injection moulding processes run as isothermal processes with the mould having a constant temperature, variotherm processes, where the mould is heated up to above T_g of the substrate, can be beneficial for the production of nanostructures[UPKL11]. The downside of using isothermal processes is that the cycle time increases significantly.

1.2.8 Polymer Materials

For the production of cheap consumable LoC devices, polymers are the materials of choice. Polymers consists of a wide variety of materials such as Polycarbonate (PC), Polyethylene (PE), and Cyclic Olefin Polymers/Copolymers (COP/COC).

When choosing the material for a LoC, several factors have to be considered. If optical measurements are being performed on the chip, autofluorescence of the material used has to be low; if strong chemicals are used in the chip, the material get degraded by these; if high temperatures are required, the material has to have a high glass transition temperature. For devices investigated in this project, the price of the polymer is so low compared to other expenses, that this factor is not of significant importance.

Many materials have been used for injection moulding of LoC devices, such as COC, PC, and High Density PE[YYC13].

The COC from TOPAS Advanced Polymers havs previously been used for the production of microfluidic chips since it contains many of the properties mentioned above[MGP+06, HS03, NNB+03]. Because of these properties it is the standard polymer available for the injection moulder at DTU Danchip. The TOPAS COC grade 5013L-10, which has been used during this project, has a T_g of 134 °C[Gmba], meaning it can withstand being heated up during experiments. At 23 °C it has a low water absorption of 0.1%, meaning that buffers will not go into the material and modify these. Furthermore, it shows good optical properties for wavelengths above 300 nm[Gmbc], and is chemically inert to most chemicals, except for non-polar organic solvents[Gmbb].

These properties allow good optical results when acquiring data from single molecules, and ensure that systems are not compromised by the chemicals used during experiments.

1.3 DNA

The devices fabricated in this project are aimed at being used for analysis of large strand DNA. Since the aim is to perform optical imaging of individual DNA molecules, a LoC device is the obvious choice for manipulating the sample. The DNA molecules have a diameter of around 2 nm, meaning that the devices used for manipulating the molecules also need to have small dimensions.

The structure of DNA has been known since 1953, where Watson and Crick proposed the double helical structure based on the measurements performed by Rosalind Franklin[WC53]. The general outline of this structure is seen in Figure 1.4a).

The double helical structure of DNA consists of a backbone containing deoxyribose along with the four nucleotides, adenine (A), thymine (T), guanine (G), and cytosine (C). In the structure, adenine from one of the strands making up the helical structure always binds to thymine from the other strand, while the same is the case between guanine and cytosine as seen in Figure 1.4b) and c).

Throughout this thesis, a simplified schematic representation of DNA will be used as seen in Figure 1.4d).

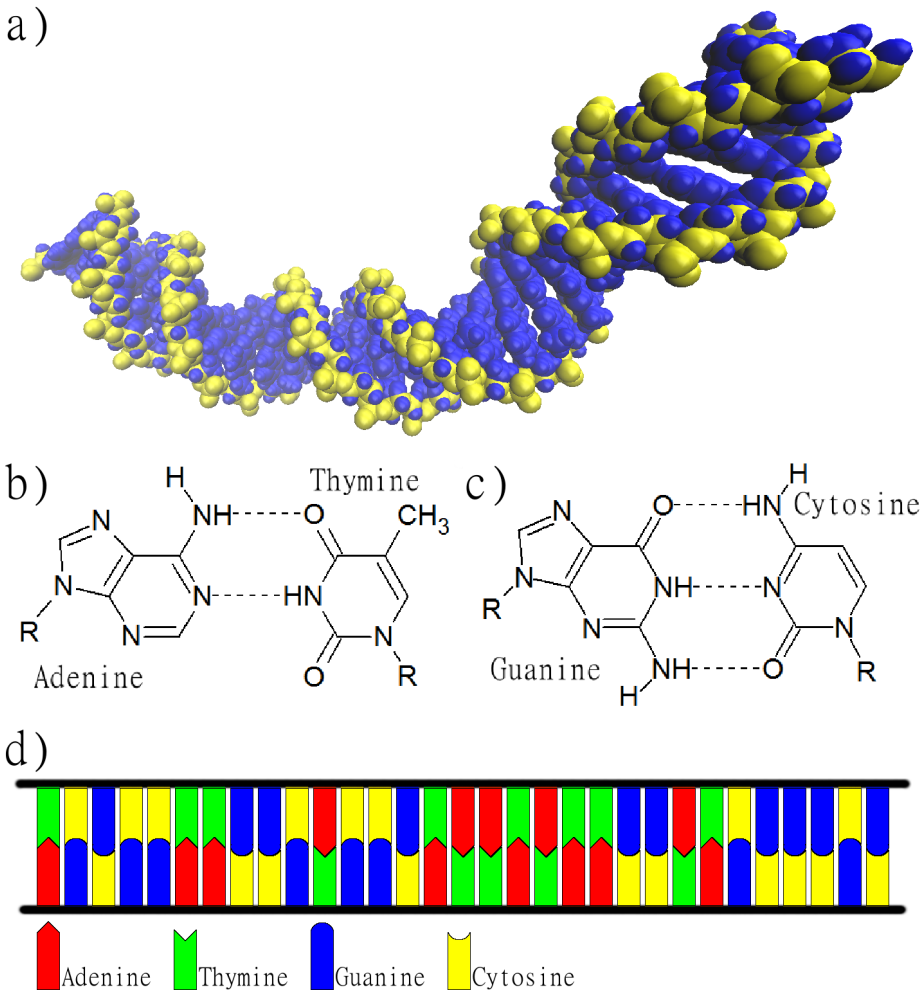

Figure 1.4: a) The double-helical structure of DNA, rendered in VMD. b)+c) Schematic representation of the AT and GC base pairs. Because AT base pairs are held together with two hydrogen bonds, and GC base pairs with three, it takes more energy/a higher temperature to break a GC base pair apart than it does to break an AT base pair apart. d) The schematic representation of DNA as it is used throughout the thesis.

Figure 1.5: The central dogma states, that information flows in one direction. DNA codes for RNA, which codes for proteins. DNA copies itself during cell division, and certain viruses, retro viruses, can translate RNA into DNA.

DNA is the blueprint of biology, and contains all the information needed in order to make a cell function in the way it is intended[HC52].

With the exception of DNA duplicating itself during cell division and retroviruses transcribing ribonucleic acid (RNA) into DNA[Gal05], the information encoded in DNA flows in one direction; DNA is translated into RNA which is then transcribed into proteins as seen in Figure 1.5. The flow of information going from DNA to RNA to proteins is also known as the central dogma[PSOH04].

The central dogma has as a consequence that if there is a mutation in a single protein, the result is not so bad, since there are many other good proteins that can do the job.

If there is a mutation in a strand of RNA, the proteins made from this strand of RNA will be defect, but all other proteins will still function as intended. However, if there is a mutation in the DNA, all the RNA coming from this part of the DNA will have the same defect, and so will all the proteins.

As much as 98% of the human genome does not code for proteins[EV08], meaning that not all mutations are equally significant and many will not cause any changes in the functionality of the cell. This is furthermore seen by the fact, that an amino acid is defined from the sequence of three consecutive base pairs in the DNA. There are $4^3 = 64$ possible combinations of three consecutive base pairs, but only 20 different amino acids, that are the building blocks of proteins. This means that almost all amino acids can be created from several different base pair sequences[PSOH04], and a mutation affecting a single nucleotide might not change the amino acid that the sequence transcribes into.

Since certain mutations in the DNA carries the responsibility for malfunctioning cells, and not all mutations are equally bad, a fast analysis of the type of mutation that has occurred in e.g. cancer patients can be of high importance if the best treatment should be given.

Diagnosing people that are not ill can also be of interest, since certain hereditary diseases can be discovered before they break out. In certain cases it is possible to take pre-emptive measures and avoid the disease altogether, or at least extend the time before it erupts[GBK+03, PDF10]. (Any ethical and moral discussions regarding this subject are not to be treated in this thesis.)

Along with DNA microarrays for the analysis of point mutations[AP03, ALP+08], one of the main sources of analysing mutations is by means of sequencing, where the genetic code of the DNA of a cell is found by different means. After the Human Genome Project[Con01] ended, any newly sequenced DNA strand can be matched up against the standard sequence, and differences can be discovered, showing potential mutations in the test sample.

During the last decade, the prize for sequencing a genome has fallen dras-

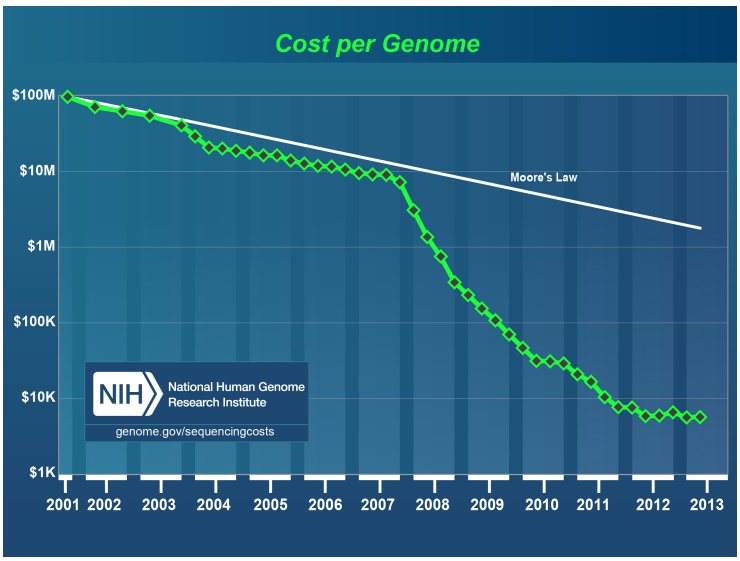

Figure 1.6: The price per genome of sequencing as a function of time. The rapid decrease seen in 2008 is caused by the introduction of NGS techniques. Figure has been adapted from `http://www.genome.gov/sequencingcosts/`[Wet].

tically due to Next Generation Sequencing (NGS) techniques[SJ08] as seen in Figure 1.6. These techniques are capable of analysing vast amounts of DNA in short times, however not without certain problems regarding sequencing of repetitive regions[TS12].

In order to help out with this problem, optical mapping of DNA can be performed. Optical mapping has a limited resolution caused by the optical setup and the wavelength used. As such, it can not give base pair resolution of a DNA molecule, but it can handle DNA strands with sizes in the mega-base pair regime, making it easy to identify large scale deletions, insertions, and repetitions[LNG+07, ZBP+07].

1.4 DNA Sequencing and Mapping

Prior to the Human Genome Project, Sanger sequencing, also known as First Generation Sequencing (FGS), was the main tool in DNA sequencing. Despite several developments and improvements of this technique, it has not changed much. It was not until 2007-2008, that sequencing improved drastically with the introduction of NGS[Mar11].

Despite the introduction of NGS, there are still challenges in the sequencing protocols used today. In order to obtain any further reduction in price and improvement in sequencing quality, new methods have to be developed.

Methods such as optical mapping of DNA has the potential of becoming one of the methods that can help improve NGS. Although optical mapping does not have base pair resolution, it has an overview that modern day NGS does not.

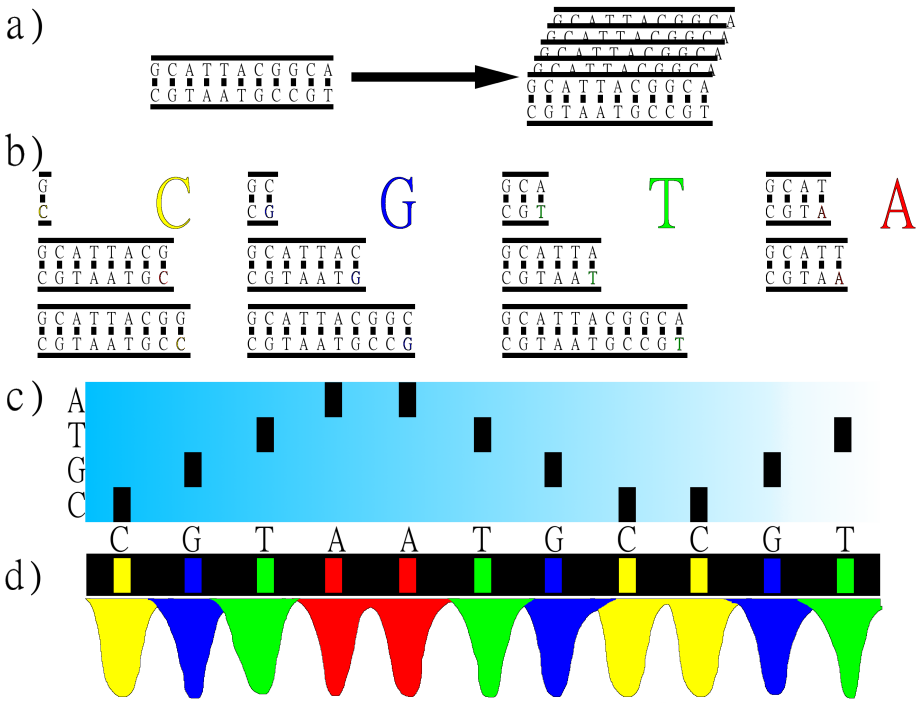
a)
b)
c)
d)
A
T
G
C
C G T A A T G C C G T
C G T A A T G C C G T
C G T A A T G C C G T

in Figure 1.7c.

Instead of using four different wells, each ddNTP can also be labelled with individual fluorophores and the end sample can be imaged using the colour code as seen in Figure 1.7d).

This method of sequencing was first proven by Sanger et al. in 1975[SC75] and was used almost exclusively with only minor modifications and improvements up until 2008[Wet].

As such, it was also the technique used for the Human Genome Project [Con01], and is still used widely when sequencing few genes at the time [Reh13].

Since each molecule under investigation requires its own well, there is a natural limitation the the level of parallelism possible when using this technique, setting a limit on the throughput.

1.4.2 Next Generation Sequencing

Since Sanger sequencing is referred to as First Generation Sequencing, everything after Sanger sequencing is referred to as Next Generation Sequencing (NGS)[Met10].

NGS consists of a multitude of different techniques, all aiming at performing parallel sequencing of short DNA fragments in order to increase sequencing speed and reduce the price.

The one thing that all NGS techniques have in common is that they perform heavy fragmentation of the sample in order to obtain shorter strands of DNA. These short fragments are then sequenced and afterwards combined[Met10]. All NGS technologies identify DNA fragments with a length between 25 and 1000 base pairs. These fragments are then stitched together to form the overall sequence of the genome.

The short read length of NGS makes it necessary to read the same position on the genome several times to get the correct stitching of the different fragments. The read length also causes a high risk for large-scale repetitions in the genome to be overlooked during the combination of the small reads[DHlH10]. Even though such repetitions only comprise a small fraction of all the repetitions, the number of reads from a single run with a NGS device will be as large as 6 billion. Considering that around 50% of the human genome consisting of repetitions, these still constitute a large problem in the assembly of the genome[TS12].

One way of avoiding the problem with repetitions is by only looking at specific cites of the genome, known to encode for certain diseases when sequencing a sample[Reh13]. However, this option is not always preferential in a research environment, where the main objective is to investigate which genes are at play, and not to verify the existence of a specific genetic mutation.

Despite the above mentioned problems regarding NGS, there has been a rapid development in the systems. The price for sequencing a genome has dropped significantly since 2008, where the NGS technology started replacing the automated sanger method. Using NGS, the price for sequencing a human genome has dropped below $10.000 USD, as seen in Figure 1.6[Wet].

1.4.3 Optical mapping

As a potential answer to the shortcomings of NGS, optical mapping can give an overview of the DNA molecule being investigated.

In order to perform optical mapping, the DNA molecule has to be visible under a microscope. A series of fluorophores that binds to DNA have been developed. One of these is YOYO-1 which has become the de facto standard fluorescent dye when performing single molecule experiments with DNA[RD10]. The advantage of YOYO-1 is that it stains the DNA homogeneously and does not alter the mechanical properties of the molecule significantly[GMS10]. Furthermore, YOYO-1 increases in fluorescence by 19.000 times when bound to double stranded DNA compared to when in solution[GR92]. This makes it easy to distinguish DNA molecules in the buffer solution.

Optical imaging cannot be used as a substitute for NGS. Optical limitations in the setup and the wavelength used during experiments sets a maximum resolution which, in the best case, is still much larger than a base-pair resolution. As such, optical imaging can never be used as a standalone sequencing technique[NDH11].

Instead, optical imaging is capable of mapping long strands of DNA without having to fragment the DNA first. Because of this, it has the potential of proving itself a perfect partner for NGS, since NGS has the resolution, while optical mapping has the big picture[MPB+13].

A combination of these two techniques can potentially solve the problem regarding loss of large scale repetitions as described by Treangen and Salzberg[TS12]. If such repetitions can be seen by the optical mapping, it can be taken into account when performing the assembly of the reads obtained by the NGS, thereby improve analysis and conclusions found on behalf of modern sequencing.

In order to perform optical mapping it is necessary to first be able to fabricate a deterministic optical pattern along the molecule that can be seen using appropriate equipment, and then to be able to stretch out the DNA in order to position the pattern and identify it on a reference genome.

In the last few years, several techniques have been suggested for optically indexing stretched out DNA molecules. Some of these aim at finding one or more specific sites, while more recent techniques try to characterize the entire sequence of the DNA in one go.

1.4.4 Discrete Location Mapping

Amongst the first techniques performed for such analysis was the use of restriction enzymes. By stretching out the DNA either on a charged microscope slide or in a dedicated device, after which the buffer is removed by evaporation, the DNA strand will stick to the surface of the glass. A restriction enzyme, which cuts the DNA at certain well known sequences, is then introduced. Due to the restricted entropy of the molecule when it is stretched out, the ends where the enzyme cut the molecule in two will coil up by a small amount, which can be seen in the microscope as a hole in the molecule[TWG+10].

This procedure tells the investigator, how far there is between two of these specific sites on that particular strand of DNA. By comparing the distance measured with the expected distance calculated from a reference genome, a conclusion on whether an insertion or deletion has occurred between two restriction sites can be inferred.

There are certain drawbacks of this technique. The molecule under investigation is destroyed in the process, making it impossible to use it for further analysis. Furthermore, only discrete sites of the molecule, corresponding to

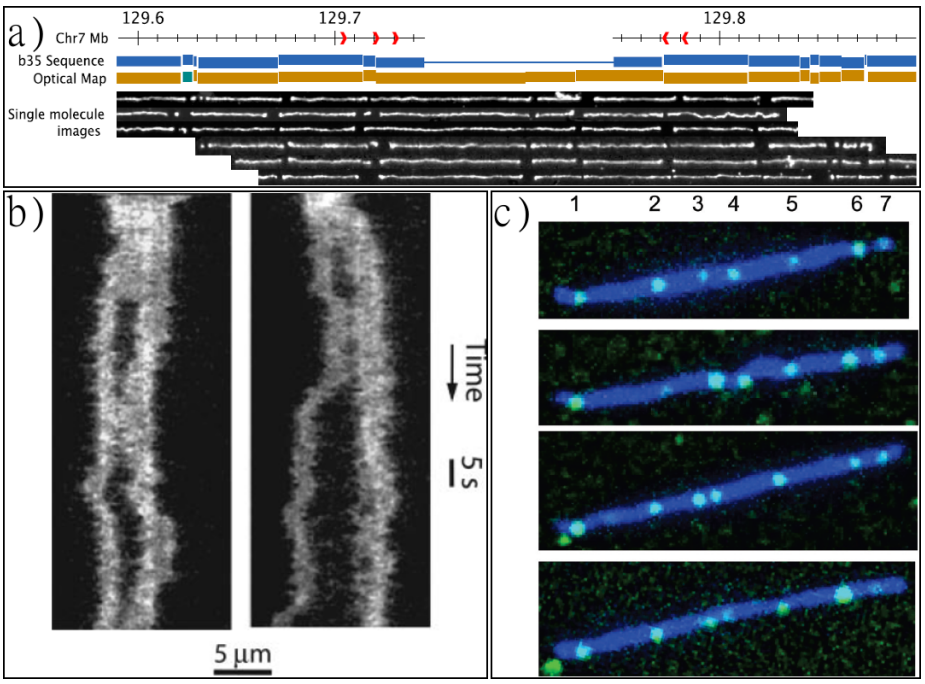

Figure 1.8: Examples of mapping of DNA using specific, discrete sites for identifying the molecule. Figure a) shows DNA stretched out on a positively charged glass slide. After stretching, a restriction enzyme cuts the DNA at specific locations, and the DNA close to the cuts will curl up due to larger entropy (Figure adapted from Teague et al.[TWG+10]). In Figure b), the DNA is stretched out in nanochannels before the restriction enzyme cuts the molecules. This technique allows the experimentalist to flush the system and perform many experiments in the same channels (Figure adapted from Riehn et al.[RLW+05]). In Figure c), a fluorescently labelled binding enzyme is used for detecting specific locations on the molecule. This way, the molecule is kept intact during the experiment (Figure adapted from Xiao et al.[XPH+07]).

the restriction enzyme, contribute to the information gained from the molecule. This means, that it is possible to detect the size of a deletion or insertion, while the resolution of its location is limited by the distribution density of the restriction sites. The stretching of the molecule on a microscope slide might also end up in different levels of stretching along the molecule.

Similar to this technique is one, where a fluorescently labelled binding enzyme is added to the molecule before stretching. By illuminating the sample with a precisely defined wavelength, the site occupied by the enzyme will light up, thereby revealing the position of these sites relative to each other[XPH+07, DAA+10].

Contrary to the restriction enzyme, the DNA is still intact after this procedure. Several different fluorophores can then be used to reveal more detail about the different locations on the DNA[CGH+04]. However, it is still only possible

to gain knowledge of discrete positions of a certain sequence of the DNA in one experiment. Any knowledge concerning the exact location of a large scale mutation is still unknown when using this technique.

Examples of restriction mapping and mapping using the binding enzyme is seen in Figure 1.8.

1.4.5 Fluorescent Barcoding

Another way of obtaining information about the structure of the DNA backbone is to stain the molecule homogeneously, and then perform a process in order to break the homogeneity of the staining.

If done right, the intensity of the staining will then reveal the structure of the backbone, without breaking it before analysis.

As explained in Figure 1.4b) and c), DNA consists of four molecules, adenine (A), thymine (T), guanine (G), and cytosine (C). These bind together in pairs of A to T, having two hydrogen bonds, and G to C, having three hydrogen bonds. This difference in the number of hydrogen bonds makes the AT basepairs break at a lower energy than the GC basepairs.

One way of adding the energy needed to break the hydrogen bonds of the base pairs in the sample is to heat them up above the denaturation temperature of the double stranded DNA.

When a temperature slightly lower than this denaturation temperature is used, the AT base pairs will denature while the GC base pairs, having more hydrogen bonds and hence a higher denaturation temperature, will stay double stranded. Since the YOYO-1 molecule does not bind to single stranded DNA, it will diffuse away from the AT rich regions, leaving these darker when observed in fluorescent microscopy.

Such a discrepancy between AT and GC-rich areas of the DNA can also be obtained, by assuring that the fluorescent molecule never gets to bind to AT-rich or GC-rich regions of the DNA in the first place.

By using a molecule that binds specifically to AT- or GC-rich regions but which is not fluorescent itself, the equilibrium distribution of the YOYO-1 molecule will not be homogeneous along the DNA molecule due to the counter-staining.

Since these two methods for creating an intensity profile along the molecule depends solely on the sequence of the DNA, it is possible to map the observed profile with a theoretically obtained profile from the genome in question, and thereby identify the molecule that is being observed.

1.5 Stretching out DNA in nanofluidics

To take advantage of an optical identifier on the DNA, the molecule has to be stretched out to a known fraction of its full contour length in order to find the distance between the identifiers.

One way of stretching out DNA is by the use of molecular combing[BSC+94, MEF+97]. This method works by anchoring one end of the molecule to a surface and then stretching it out by the use of viscous drag. Stretching out and immobilising the DNA on a surface has the drawback, that the DNA cannot

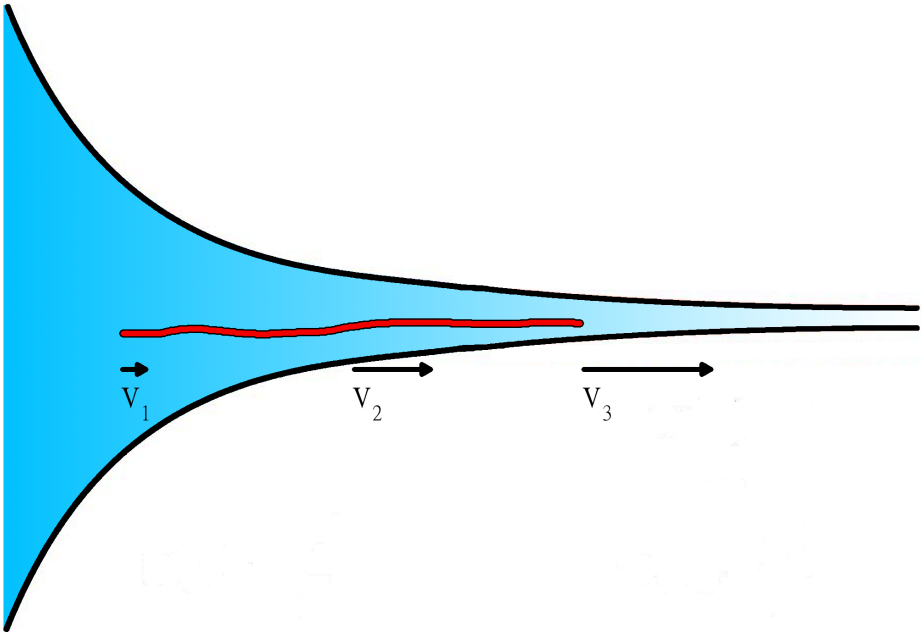

Figure 1.9: Stretching of DNA through microconfinements. The ever decreasing channel width accelerates the buffer which in return forces the DNA to stretch out.

be used for post processing, and the surface can only be used for a single run, because the DNA cannot be flushed away.

As an alternative, stretching of DNA can be done using nanofluidics. This can be accomplished either by using microcontractions[RSD06, HWL09], entropic confinements[TPC+04, RLS+10] or shear flow stretching[DSTJJ+10, MPB+13]. All of these techniques have their advantages and disadvantages.

Microcontractions allows for a system, where the flow can be kept constant during the entire experiment; entropic confinements has the advantage of being capable of massive parallelism with hundreds to thousands of nanofluidic channels next to each other; nanoslits allows for unprecedented levels of stretching and thermal stability of the molecule.

Other means for stretching out DNA is also available, such as optical tweezers and thermophoresis. Although optical tweezers offer a high freedom of manipulation of the sample[MCSB08], the setup needed to perform optical tweezing is often unnecessarily complex for the objectives under investigation in this thesis, and so this technique will not be explained here. Thermophoresis[TLK10] which uses a heat gradient for stretching out the DNA is still a technique that requires more development, and for this reason it has not been considered for any application in this thesis.

1.5.1 Microcontractions

Microcontractions function by having an ever decreasing nanoslit in the design. If a flow is applied through this contraction, it will accelerate throughout the

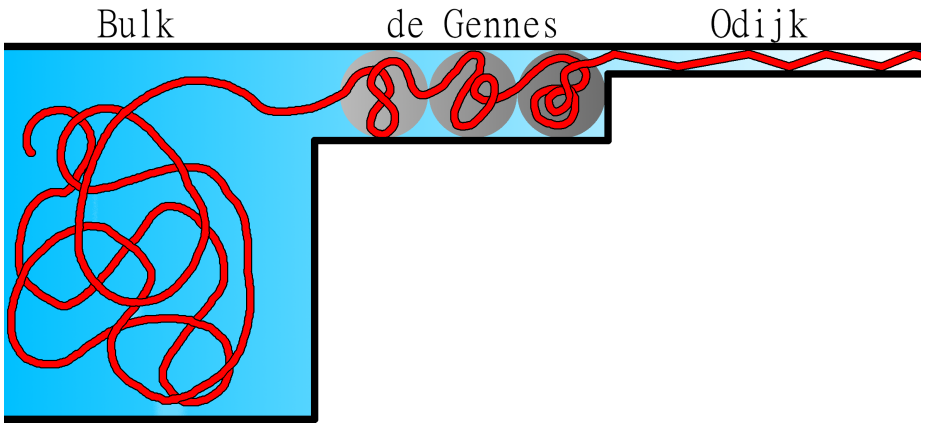

Figure 1.10: The three main regimes of entropically stretched polymers. When in a bulk solution, the molecule curls up with a specific radius of gyration, R_g. If the channel is smaller than R_g, but still larger than the persistence length, P of the molecule, it will enter the de Gennes regime, where it will arrange itself in small isometric blobs. If the cross section of the nanochannel is decreased below P, the DNA molecule will enter the Odijk regime, where it can be characterised as being small segments, deflected by the walls of the channel.

entire active area. A DNA molecule positioned in this fluid will experience a shear force caused by the accelerated flow along the backbone, making the molecule stretch as sketched in Figure 1.9[RSD06, HWL09].

Larson *et al*[LYZ+06] found that stretching of DNA using this type of system, is most efficient when the strain rate, $\dot{\epsilon}(x) = \frac{\mathrm{d}v(x)}{\mathrm{d}x}$ is linear, while the DNA is kept at a constant stretching, when the strain rate is constant.

To obtain the best results, Griffis *et al*[GPC+13] have made a system that combines the above results, causing the layout to have a stretching section with a width following the function $w(x) = F_1/x^2$ and a data acquisition section with a width following the function $w(x) = F_2/x$, where F_1 and F_2 are defined from the boundary conditions.

Stretching DNA this way allows for a high throughput of molecules, reported to be as high as 1000 fully extended 185 kbp long molecules per minute[LYZ+06]. Stretching out DNA using this technique has been reported to obtain diffraction limited resolution during data acquisition[GPC+13].

1.5.2 Entropic confinement

Nanochannels work as an entropic confinements for a molecule. In order to function properly, the nanochannel has to have a cross sectional area much smaller than the radius of gyration R_g of the molecule that is being looked at[BD77, RPA12].

By forcing DNA into a channel with dimensions smaller than the radius of gyration, R_g of the molecule, the molecule has to stretch out to a fraction of its

contour length. Several regimes of stretching exists; which of these the molecule will fall into depends on the dimensions of the nanochannel and the stiffness of the molecule. Two of these regimes are particular distinctive, namely the de Gennes regime and the Odijk regime[BD77, Odi77]. While other regimes do exist, these are often seen as being transition regimes between these two.

In the de Gennes regime, the dimensions of the nanochannels are smaller than radius of gyration R_g but still much larger than persistence length P of the molecule. This confinement causes the DNA molecule to stretch out from the curled up state in which the DNA exists in a bulk solution, but inside the channel, where it will still be in a state of multiple blobs attached to each other[BD77].

In the Odijk regime, the dimensions of the nanochannels are even smaller than the persistence length of the molecule. This makes it impossible for the molecule to curl up inside the channel. It will instead position itself as a series of stretched out segments, deflected off of the wall of the nanochannels[Odi77].

A sketch showing the dynamics of the two regimes is seen in Figure 1.10.

The cross sectional area needed to go from one regime to another depends strongly on the salinity of the buffer used. When a low salt concentration buffer is used, the charge of the DNA molecule will not be screened by free salt ions, and so, it will appear stiffer[BSBB97]. With a stiffer molecule, the Odijk regime will be reached at a larger cross sectional area than if the molecule is highly flexible.

For a given stiffness of a polymer chain, the length of the stretched out molecule in the de Gennes regime is found to be

$$R \cong Na\left(\frac{a}{D}\right)^{2/3} \tag{1.1}$$

where N is the number of monomers, a is the diameter of one monomer, and D is the characteristic length scale of the nanochannel.

In theory, a DNA molecule can be stretched out close to 100% of its contour length using small nanochannels, but this requires that these channels have a characteristic length scale smaller than 10 nm[WRTD12]. Such small length scales are both difficult to fabricate, and the force needed to introduce the molecule into such channels will furthermore be so high, that using a pressure difference to introduce the molecule into the channel, could compromise the rest of the device. Alternatively, the persistence length of DNA can be increased by lowering the salinity of the buffer[Hag88, BSBB97]. DNA can also be stretched out to a large fraction of its contour length by having a low salinity of the buffer[KKK$^+$11], but low salt concentrations generally makes it difficult to work with molecular biology.

Since it is possible to position hundreds of nanochannels next to each other, it is possible to make simultaneous acquisitions of several parallel nanochannels, giving a high rate of data acquisition.

Nanochannel confinements have been used for DNA mapping experiments. Such experiments include restriction mapping[RLW$^+$05], sequence specific fluorescent probes [DAA$^+$10, LHL$^+$12], and melting mapping[RLS$^+$10, WSDR12].

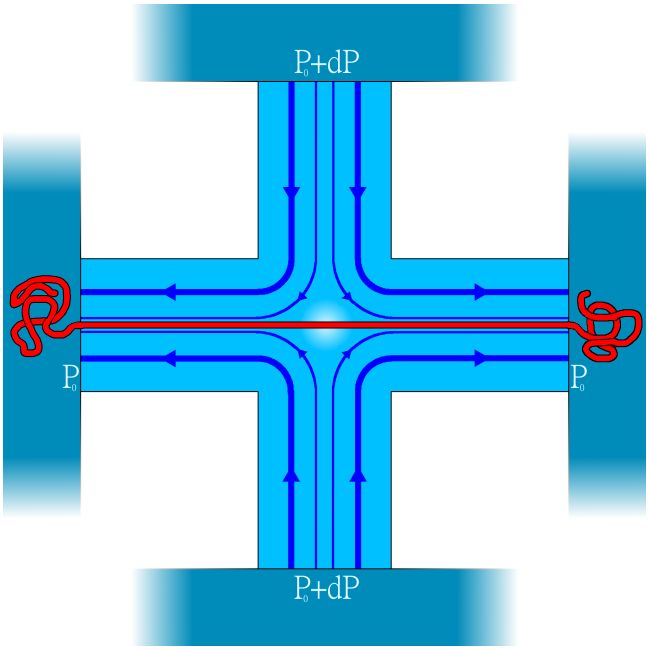

Figure 1.11: When applying an overpressure on two inlets in the slit-structure, a flow will be present in the cross. The viscosity of the fluid creates a drags on the DNA molecule away from the centre of the cross, and equally strong in opposite directions in the two arms. This stretches out the molecule, while keeping it from flowing to either side. Because of this design, no flow appears in the centre of the cross.

1.5.3 Shear Flow Stretching

A method of stretching out DNA, somehow similar to the microcontractions, is by use of shear flow stretching on a fixated molecule. Instead of letting the DNA molecule flow along with the accelerating buffer, a system which contains a mirror symmetry as seen in Figure 1.11 can be designed.

If pressure is applied to the top and bottom inlet, a flow will go from these two inlets, towards the centre and equally towards the two outlets, in the meantime creating a stagnation point in the middle of the cross. Any molecule that is placed symmetrically in the middle of this device will feel an equally large force in both directions[DSTJJ+10], and so, it will stay still in the nanoslit, and only be extended as an effect of the drag from the flow, as if it was anchored in the centre of the cross.

If the flow rate is large enough, the drag on the molecule will become so large, that any Brownian motion of the molecule can be neglected[MPB+13], and the DNA will not change position relative to its surroundings.

Sketches of DNA being stretched out in nanochannels and nanoslits are seen in Figure 1.12. It is evident that the nanoslit design is inappropriate for smaller molecules, since the device only works as intended for molecules stretching from one end of the cross to the other.

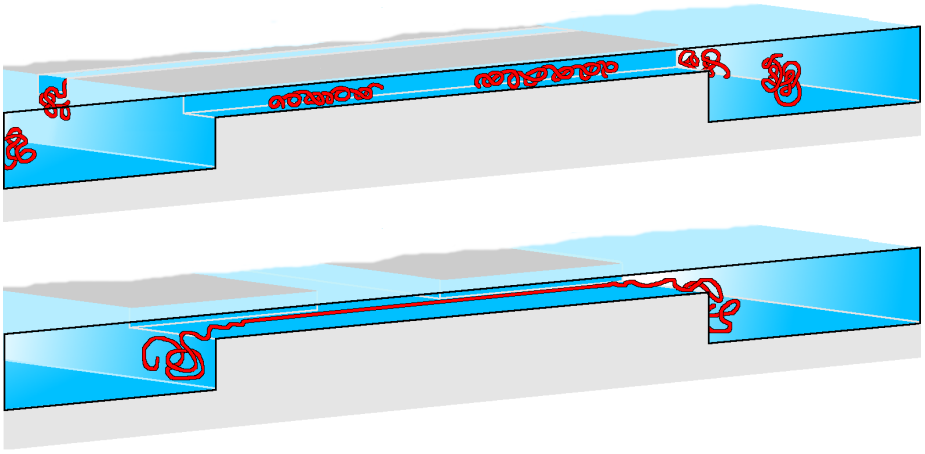

Figure 1.12: The nanochannels, seen in the top of the figure, allows for parallel acquisition of data from several molecules at the same time, but with only a limited level of stretching. The nanoslit, seen in the bottom of the figure allows for almost 100% stretching, but only works with long DNA molecules, and can only acquire data from one molecule at the time.

1.6 The PolyNano and CiPoC Projects

This PhD project is funded by two projects; PolyNano and CiPoC.

The aim of the PolyNano project is to "remove the technology barrier between lab-scale proof-of-principle and high-volume low-cost production of LoCs"[Kri], while the CiPoC "focuses on establishing component and platform technologies for use in Point of Care diagnosis"[Bec].

Currently a catch 22 situation is present in the field of LoC. Despite large amounts of academic research within the area during the last two decades, not many devices have been introduced into commercial products.

This is mainly due to two reasons. Many scientist, who do not work directly with LoC, although might be interested in the prospects of the technique, are not willing to spend weeks, or even months, on fabricating devices suited for their needs. This has the consequence that academic results from groups working within biology and chemistry do not include results obtained using these devices, and so the demand for them remains low. Simultaneously, scientists who are working with LoC systems, prefer working with techniques that are well suited for prototype fabrication over large scale fabrication. This creates a large barrier of entry, since companies that are willing to start producing LoC will have to reinvent the fabrication process.

Since it has previously been shown, that injection moulded devices can be used successfully as LoC[UPKL11, AHM+10], this project will aim at trying to solve the current catch 22 situation.

LoC systems, produced by methods normally used for mass production of items, can be supplied to academic groups who do not normally use such devices. It is the goal of this project to convince academic groups that there are several advantages in LoC devices, while simultaneously showing the industry that there

is a market, and that the barrier of entry does not have to be high.

Chapter 2

Fabrication of Polymer Devices

The devices in this project have all been fabricated using injection moulding. This fabrication technique facilitates cheap and fast production of a high quantity of devices.

Injection moulding consists of three steps: a mould cavity is filled with molten polymer, the polymer is cooled down, the device is released. After the release, the process can start over again, producing hundreds or thousands of identical parts without human intervention.

Since the aim of this project is to produce structures with micro and nanostructures, part of the mould has to have these structures integrated into it in order to transfer them to the final part. Devices fabricated this way has been shown to function from previous work performed by Andresen *et al*[AHM+10] and Utko *et al*[UPKL11].

The process used for producing devices this way consists of four steps:

Step 1: Mask Design; a mask design is drawn in a computer aided design (CAD) program and chromium masks are ordered.

Step 2: Cleanroom Fabrication; a master silicon wafer is processed and electroplated in the cleanroom resulting in a nickel shim.

Step 3: Injection Moulding and Bonding; The nickel shim is used for injection moulding of several polymer chips outside of the cleanroom, and these chips are bonded to finish the device.

Step 4: Validating and Iterating; Flaws in the design and production process are identified. Optimization of the chip layout and fabrication based on this.

Compared to previous work in this field, this project manages to optimise the design of the different devices fabricated in order to obtain better injection moulding, decrease the production time for injection moulded chips, increase the throughput of the bonding process, bond low aspect ratio structures with an aspect ratio of 1:200, and decrease the autofluorescence of the polymer devices by almost 50%.

Three different designs were investigated in this project: two consisting of structures in two levels, one consisting of structures in three levels.

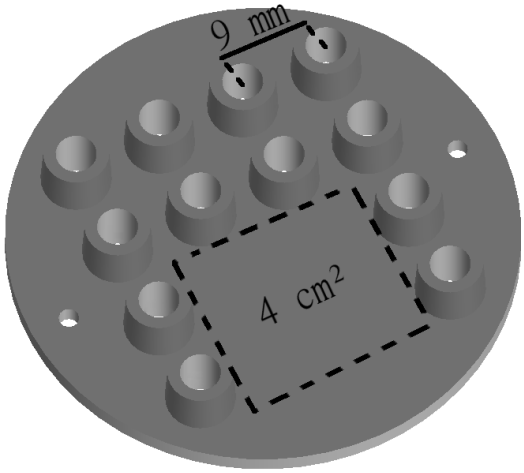

Figure 2.1: The standard chip layout defined by the injection moulder. The chip is 2 mm thick, has a diameter of 5 cm and has 12 integrated Luer connectors. A $\sim 4\,\mathrm{cm}^2$ area without Luer ports is present which is well suited for delicate structures.

By the use of the production scheme investigated in this project, the price per device can get as low as DKK 17 corresponding to approximately \$3 USD[1]

The fabrication method used in this project, namely injection moulding, sets a certain amount of limits to the design of the chip.

Injection moulding does not allow for overhanging features in the design, since these can not be de-moulded during the process. Limitations to the designs fabricated in this thesis are also generated by the injection moulding tool used in this project. This tool has a general design leading to polymer devices as seen in Figure 2.1. These chips are 2 mm thick, 5 cm in diameter and have 12 integrated Luer connectors for easy access of instruments, such as pressure regulators. The chips contain an area of $4\,\mathrm{cm}^2$ without Luer ports which is well suited for delicate structure

The positioning of the Luer ports restricts where channels can be placed. The large area without Luer ports is found to be better suited for placing critical structures, since the polymer flow here is not affected by the Luer ports, which can have negative effects on structures placed elsewhere.

These aspects of the chips were taken into consideration when designing the masks, fabricating the silicon master, and performing the injection moulding.

During the project, several iterations of the designs were performed, aimed at increasing yield and performance of the devices.

2.1 Step 1: Mask Design

The project mainly focused on two chip designs that were fabricated and optimized during this project: one with three clusters of nanochannels having depths

[1] Based on exchange rates as of May 29, 2014

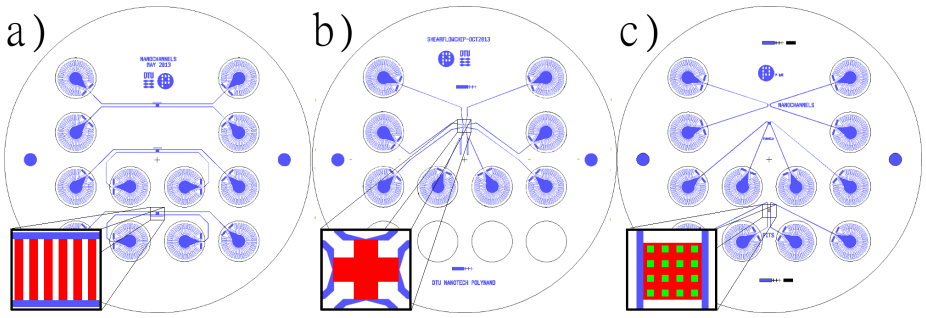

Figure 2.2: Overview of the three designs fabricated in this project. The design shown in a) contains three sites with nanochannels having depths of 100 nm and lengths of 450 µm. One set of channels has a width of 240 nm, one set of channels has a width of 440 nm, and one set of channels has a width going from $140 - 1\,040$ nm. The middle design, b), contains a nanoslit in a cross-design. The nanoslit has a width of 20 µm, a length of 450 µm, and a depth of 110 nm. The design to the right, c), contains nanopits as small as 150 nmin sidelength and 125 nm in depth at the bottom of 10 µm wide, 110 nm deep, and 450 µm long nanoslits. This device also contains nanochannels with a width of 120 nm and a depth of 110 nm.

of 110 nm, lengths of 450 µm, and widths ranging from 140 nm to 1040 nm, another with a nanoslit design having a height of 110 nm, a length of 450 µm, and a width of 20 µm, giving it an aspect ratio of almost 1/200. These two designs are seen in Figure 2.2a) and b).

A third chip design was also fabricated containing 3 level structures along with nanochannels. This device contains nano-sized pits with side lengths ranging from 150 nm×150 nm to 1000 nm×1000 nm and depths of 125 nm on the bottom of a low aspect ratio nanoslits, having widths of 10 µm, depths of 110 nm, and lengths of 450 µm. The nanochannels on these devices have a width of 120 nm and a depth of 110 nm. This design is seen in Figure 2.2c).

All designs use carrier channels with a width of 50 µm and a depth of $4.5 - 5$ µm

One mask for each layer in the device is designed in the CAD program L-Edit[2] and exported as a CIF-file. This file is transferred to Delta Mask[3] in order to obtain a chromium mask.

2.2 Step 2: Cleanroom Fabrication

With the design at hand, cleanroom fabrication of the master silicon wafer is started.

The cleanroom processing is performed in order to fabricate a nickel insert, known as a shim, which is used during the injection moulding.

[2] L-Edit v. 15, Tanner EDA, CA, USA
[3] Delta Mask B.V., Enschede, Netherlands

Process	Nanoslits	Nanochannels	Nanopits
SiO_2 Growth	1050 °C dry oxidation; t=100 min + 20 min annealing		
Spin coating	HMDS vapor deposition 1 µm AZ5214 soft-bake: 90 °C for 90 sec	100 nm ZEP502A soft-bake: 180 °C for 120 sec	
SiO2 Etch	CF_4/CHF_3=14 /26 sccm, t=240 sec P_{RF}=60 W,p =100 mTorr		
Spin Coating			HMDS vapor deposition 1 µm AZ5214 90 °C for 90 sec
$Si + Si_2$ Etch			$SF_6/O_2/CHF_3$=30 /29 /15 sccm, t=100 sec P_{RF}=20 W, p=31 mTorr CF_4/CHF_3=14 /26 sccm, t=240 sec P_{RF}=60 W, p=100 mTorr
Spin Coating	HMDS vapor deposition 1.5 µm AZ5214E soft-bake: 90 °C for 90 sec		
Si Etch	CF_4/CHF_3=14 /26 sccm, t=4.5 min P_{RF}=60 W, p=100 mTorr SF_6/O_2=32/8 sccm, t=13.5 min P_{RF}=30 W, p=80 mTorr		
Sputtering	Ni/V (7% V) t=1000 sec, P=157 W, U=310 V, p=5 mTorr		
Electroplating	330 µm Ni 18 Ah		

Table 2.1: Process flow in the fabrication of the master silicon wafer. A silicon layer is grown which defines the height of the nanoslit or nanochannels. Photolithography and an oxide etch creates the slit, channels, or pits. A second photolithographic step defines the carrier channels, and finally a seed layer of nickel vanadium is sputtered on the wafer, which is then electroplated. For the nanopits, an extra lithographic step is added after the definition of the pits. This lithographic step defines the slit in which the pits are positioned.

As far back as in 1982, a process similar to the one used in this project was developed in Germany for creating high aspect ratio structures used for uranium purification[BEM82]. This process uses lithography, electroplating and moulding, or in German, Lithographie, Galvanoformung, Abformung, and is generally known as a LIGA process. The LIGA process defines its structures using x-ray lithography. This type of lithography requires expensive synchrotron sources, unavailable anywhere in Denmark, thus not a technique that is realistic to use in this project. Furthermore, the substrate used for performing the process has to be conductive in order to perform the electroplating.

A cheaper way of performing LIGA processes is by using UV-LIGA, where the x-ray beam is replaced with an UV light source. This makes the process available to a broader audience. However, the electroplating step using a conductive material as a substrate, still only allows for single layer structures.

In order to overcome this problem, a technique using dry etching, electroplating and moulding, also known as DEEMO was developed in 1995 at the university of Twente in the Netherlands[EJE95]. This technique takes advantage of the ongoing development in cleanroom fabrication that has happened during the last decades.

The desired topography is fabricated in a silicon wafer which is then electroplated in a nickel bath and released from the wafer. The electroplated part is then used as an insert in an injection moulder.

Since it is easy to produce hierarchical structures in a silicon substrate by use of multiple lithographic steps, the shim, and hence the injection moulded polymer chips, can also contain several levels of structures. Multiple layers of structures will not increase the production time of injection moulded devices.

To perform the DEEMO process, a silicon wafer has to be processed so it ends up with the same topography as the desired polymer chip. To obtain this, several cleanroom techniques are used.

Since only the topography survives in the silicon master, and only dry etching is used during the process, the direction of the crystal planes in the wafer is not of importance to the fabrication. Because of this, standard 4 inch <1 0 0> single side polished wafers with a thickness of 525 µm are used.

The entire process is described below, and an overview is seen in Table 2.1 and Figure 2.3.

2.2.1 Oxide Growth

The first step of the silicon fabrication process is the growth of an oxide layer, that defines the height of the nanoslit or nanochannels. Since the layer is going to define either the height of a nanoslit or of nanochannels, it has to be $100 - 110$ nm high and homogeneous over the wafer, so that a small misalignment of the first lithographic step does not effect the height of the nanoslit or nanochannels.

The oxide layer is produced by performing a dry oxidation at 1050 °C for 90 min with an oxygen flow of 5 slm followed by 20 min of annealing with an oxygen flow of 3 slm in a Tempress horizontal furnace. While the furnace is heating and cooling, a nitrogen flow of 3 slm is used[TOM+12]. The thickness of the oxide layer is controlled in a Filmtek 4000 using reflectivity measurements.

This step corresponds to Figure 2.3a).

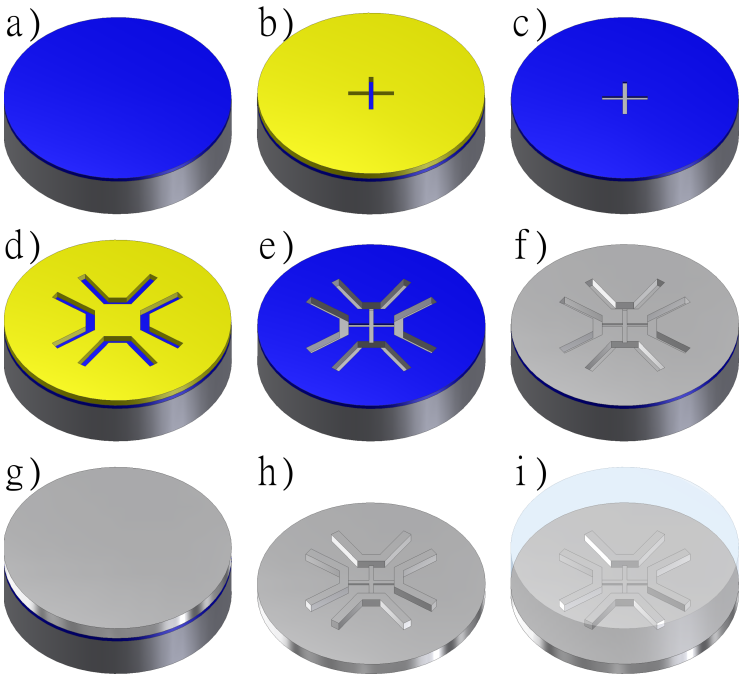

Figure 2.3: Overview of cleanroom procedures. a) A 10 nm oxide layer is thermally grown on the silicon wafer. b) Spin on of photoresist and lithography (UV or e-beam) is performed to define the nanostructures. c) The nanostructures are etched using an oxide specific reactive ion etch that has the silicon substrate as an etch-stop. d) An UV lithography step is conducted to define the carrier channels. e) The carrier channels are etched using a reactive ion etch. f) A seed layer of 100 nm Ni/V is sputtered onto the wafer. g) The wafer is electroplated in a nickel bath. h) The wafer is removed, leaving the nickel shim behind. i) The nickel shim is used to define the structures in the injection moulding process.

2.2.2 First Lithography Step

The nanoslit and nanochannels are defined during the first lithography step. This step is the only step where there is a difference in the process flow between the nanochannel and nanoslit devices. This difference is caused by the different lateral dimensions between the slit and the channels. The nanoslit is so wide that it can be defined using UV lithography, while the nanochannels are so narrow that e-beam lithography is required.

The device containing the nanopits has three lithography steps, and is in many ways a combination of the two other devices.

UV lithography for nanoslit

For the nanoslit, conventional UV lithography is performed. Prior to the spin on of the UV sensitive photoresist, a hexamethyldisilazane (HMDS)-treatment of the silicon wafer is performed in order to increase adhesion between the photoresist and the oxide on top of the wafer.

A 1.5 µm layer of AZ5214E photoresist is spun on top of the wafer and the wafer is then soft-baked at 90 °C for 90 sec. The nanoslit design from the nickel mask is transferred to the photoresist using the 365 nm line from a mercury lamp at an intensity of 7.0 mW/cm^2 for 7 sec, and the resist is developed for 70 sec in AZ351 developer.

The result of this step is seen in Figure 2.3b).

e-beam lithography for nanochannels and nanopits

Because of the width of the nanochannels being as narrow as 140 nm, these structures cannot be defined using UV-lithography. Instead, e-beam lithography can be used.

A 200 nm layer of ZEP520A e-beam resist is spun on top of the wafer and the wafer is then soft baked at 180 °C for 60 sec. The nanochannels are defined using a JEOL JBX-9500 e-beam writer with an energy density of 220 µC/cm^2. The resist is developed in N50 developer for 2 min before being cleaned in IPA for 30 sec and blow dried with N_2

2.2.3 Oxide Etch

The 110 nm oxide layer, grown as the first step in the process of making the nanoslits and nanochannels, is made in order to define the height of the structures. By applying an oxide specific etch, the etching process will stop automatically once it reaches the silicon substrate. Since the silicon works as an etch stop for the RIE, the height of the nanoslit and nanochannels will only be as deep as the thickness of the oxide layer.

To perform the etch, the wafer is placed in a STS cluster system C004. A RIE is conducted by having a CF_4/CHF_3 flow of 14 /26 sccm, for 240 sec with an effect of the radio frequency (RF) antenna of 60 W and a chamber pressure of 100 mTorr.

After the oxide etch, the remaining photoresist is removed by plasma ashing, using a flow of O_2/N_2 with flow rate of 400 /70 sccm and a RF effect of 700 W for 15 min.

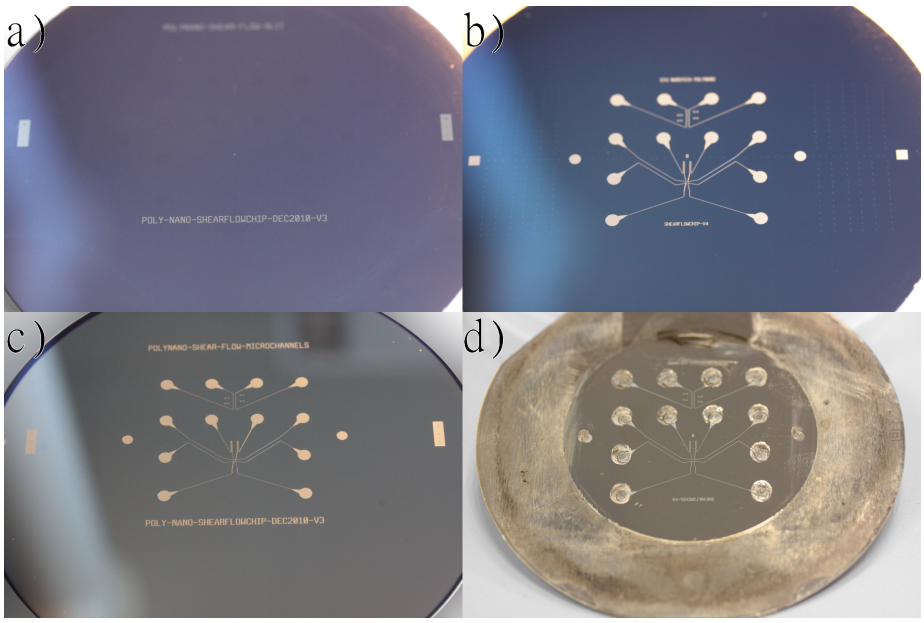

Figure 2.4: The process flow of the silicon wafer containing nanoslits. In Figure a), the shallow nanoslits are etched, followed by the etching of the carrier channels in Figure b). In figure c) the wafer has been sputtered with 100 nm Ni/V, making it possible to electroplate it in order to obtain the final nickel shim seen in Figure d).

An image showing a silicon wafer containing the nanoslit structure after the oxide etch is seen in Figure 2.4a). This step also corresponds to Figure 2.3c).

Three layer structures

For the nanopits, three layers are designed into the device.

In order to obtain the three layers, the pits are first defined using the same e-beam lithography step, as used for the nanochannels and, and then a RIE through the oxide layer is performed.

After the etching of the pits, a UV lithography step is performed, using the same procedure as when defining the nanoslit. This lithography step defines the nanoslits that the pits are positioned in.

The lithography step is followed by a silicon specific RIE, where the pits are etched down into the silicon layer using a gas flow of $SF_6/O_2/CHF_3$ with a flowrate of 30 /29 /15 sccm for 100 sec with an effect of the RF antenna of 20 W and a chamber pressure of 31 mTorr.

The silicon etch is followed by an oxide specific RIE, defining the nanoslits. This process has a CF_4/CHF_3 gas flow of 14 /26 sccm for 240 sec with an effect of the RF antenna of 60 W and a chamber pressure of 100 mTorr.

This results in pits with a depth of 125 nm in the bottom of slits with a depth of 110 nm.

By performing the etching this way, nanochannels, also defined by e-beam lithography and only having the depth of the silicon layer, can be fabricated on

the same wafer as the nanopits.

2.2.4 Second Lithographic Step

The second lithographic step is performed in order to define the microchannels used for transporting the sample from the inlet of the final polymer chip and to the nanochannel and nanoslit.

The procedure for defining these channels is identical to the UV lithography step performed in Section 2.2.2 when defining the nanoslit.

This step corresponds to Figure 2.3d).

2.2.5 Silicon etch

The microchannels have to be deeper than the nanoslit and nanochannels in order to be able to transfer the sample to the nanoslit and nanochannel within a short time, without the use of excessive pressure differences between the inlet and the outlet. This makes it necessary to etch down into the silicon wafer. First the oxide layer is etched away in a process identical to the etch performed when defining the nanoslit and nanochannels. After this, a flow of SF_6/O2 with a flow rate of 32/8 sccm is applied with an effect of the RF antenna of 60 W and a chamber pressure of 100 mTorr for 13.5 min. This gives a channel depth of $4.5 - 5\,\mu m$.

The remaining photoresist is removed by plasma ashing, in a process identical to the one used after the oxide etch. This step corresponds to Figure 2.3e), and an image showing the wafer after the silicon etch is seen in Figure 2.4b).

2.2.6 Seed Layer and Electroplating

The electroplating of the silicon wafer is only possible if the wafer is covered with a conductive material.

The wafer is placed in a Kurt J. Lesker sputter system, and a 100 nm Ni/V layer (93% nickel, 7% vanadium) is sputtered on top of the silicon wafer, using a chamber pressure of 4 mtorr an RF bias of 90 W and a voltage bias of 380 V.

Nickel/vanadium is used as a seed layer for two reasons. The nickel adheres to the nickel deposited during electroplating, meaning that the nanostructures will not fall off or get compromised during injection moulding, and the vanadium ensures that the seed layer does not oxidise prior to electroplating.

This step corresponds to Figure 2.3f), and a wafer with the seed layer sputtered onto it is seen in Figure 2.4c).

The sputtered wafer is placed in a Technotrans electroplater and electroplated with a total charge of 18 Ah, giving a thickness of the nickel shim of 330 µm over the entire 4 inch wafer, corresponding to Figure 2.3g).

Finishing the nickel shim

The structures fabricated during processing of the silicon wafer only fill a small part of the wafer. Because of this, adhesion between the silicon wafer and the electroplated nickel shim is low. This allows for easy removal of the nickel shim, which can be lifted off by hand.

Figure 2.5: Equipment for punching out the nickel shim to the dimensions that makes it mountable in the injection moulder.

A single nickel shim was removed from the wafer by dissolving the silicon wafer in KOH at a temperature of 80 °C overnight. This procedure was only performed once, since it was experienced that the KOH also attacked the vanadium, thereby compromising the surface roughness of the devices. This will be explained further in Section2.4.2.

The nickel shim has to be cut in to shape in order to fit correctly into the injection moulder. This is done using a dedicated punching tool as seen in Figure 2.5.

The final shim, corresponding to Figure 2.3h) is seen in Figure 2.4d). The photo of this shim is taken after it has been used in the injection moulder. It is seen, that the injection moulder causes several scratches on the shim in the areas, where the shim is in contact with the machine.

2.3 Step 3: Injection Moulding and Bonding

Injection moulding corresponds to Figure 2.3i), where the structures from the nickel shim are replicated into a polymer substrate.

This process is explained in detail in Figure 2.6. An empty cavity, Figure 2.6a), is filled with molten polymer, injected through a hole in the tool (Figure 2.6b)), until it is filled. At this step, it is only the macroscopic struc-

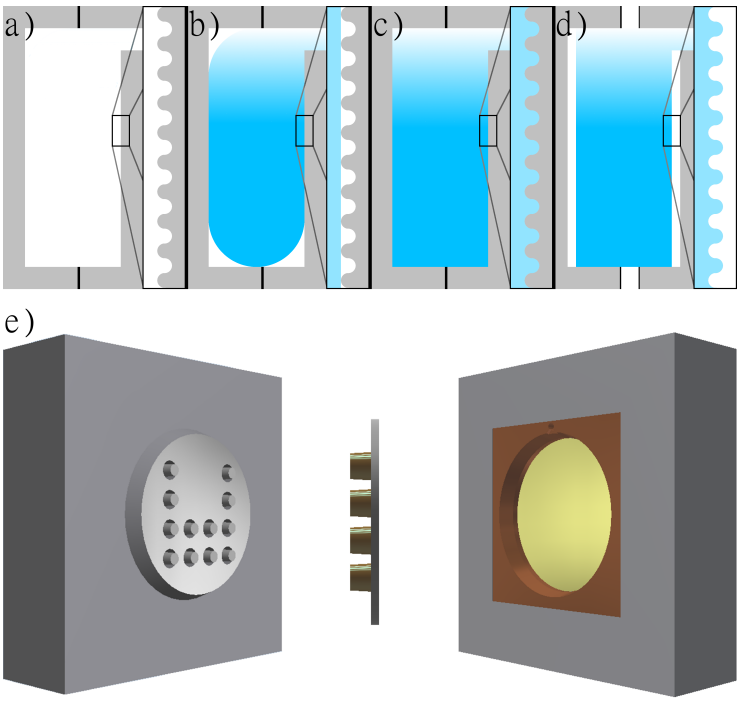

Figure 2.6: During an injection moulding cycle, the two parts of the mould closes, leaving a closed cavity in between them as seen in a). Molten polymer is injected into the cavity, as seen in b), and a high holding pressure is applied to make the polymer fill out the micro and nanostructures as seen in c). Finally, the part is cooled down and the mould is opened, leaving the final device to be removed from the injection moulder, as seen in d) and e).

tures that are replicated.

A holding pressure, typically around 1000-2000 bar is applied, and the polymer is forced into the small cavities of the structure, thereby replicating the nanoscale structures as seen in Figure 2.6c). After the polymer has cooled down and solidified, the mould is opened, and the device is removed as seen in Figure 2.6d) and e).

At DTU Danchip, an ENGEL Victory Tech 80/45 injection moulder capable of performing both isotherm and variotherm processes is available.

As suggested by the names, injection moulding using an isotherm process operates using a constant temperature of the mould, while a variotherm process changes the temperature of the mould during the moulding cycle.

The advantage of having a variotherm process is that the mould can be heated up to above the glass transition temperature of the polymer. By doing this, the polymer will keep on flowing when injected into the mould cavity, making it possible to fill out the entire mould cavity, thereby also filling out high aspect ratio structures.

Contrary to this, an isotherm process keeps the mould cavity at a constant temperature below the glass transition temperature of the polymer. This causes

the polymer to create a solid film at the interface to the mould cavity, as soon as these gets into contact with each other.

This makes it more difficult to fill out the entire mould, but it does decrease the cycle time of the injection moulding significantly, as the entire mould does not have to change temperature during the process.

The chips fabricated in this project are all used with biological sample, making it important that the polymer from which they are made is bio-compatible. To ensure this, the co-polymer TOPAS COC 5013L-10 (TOPAS Advanced Polymers GmbH) is used. Alongside being bio-compatible, this polymer also has excellent optical properties. Because of this, this polymer is the standard polymer of use in the injection moulder at DTU Danchip.

All chips in this project were moulded in an isotherm process with a nozzle temperature of 270 °C, mould temperature of $115 - 117$ °C, a holding pressure of $1200 - 1700$ bar and an injection speed of the polymer of 9 cm^3/s. This process can run successfully at cycle times as low as 30 sec, although the nanopit structures need cycle times as high as 90 sec due to a design that was not optimised for the moulding cavity.

Compared to the reported cycle times of $5 - 8$ min per device as found by Utko *et al*[UPKL11] using the same injection moulder, the obtained cycle times of around 1 min is a significant improvement, given that the nanochannel structures fabricated in this project are almost identical to the ones produced by Utko.

Because of changes to the tool and injection moulder over the duration of the project, the process had to be changed from time to time. This meant that recipes using variotherm processes, as well as changing the temperature of the tool and the injection speed of the polymer were explored.

While some of these processes did produce results that could be used, they either had cycle times as long as 5 min, the corners of the channels were rounded off so much, that the structures would not work as intended, or the polymer was too soft when de-moulding the part, causing the polymer to deform and create barriers along the intersection between the microchannel and nanoslit or nanochanels.

A polymer part with structures on the surface will in itself not be able to stretch out DNA. In order to do so, it has to be sealed of by bonding it to a polymer foil.

The polymer foil used for bonding the polymer chip consists of the same grade of polymer as the injection moulded chip, and has a thickness of 150 µm.

For the nanochannel devices, bonding was performed by UV assisted thermal bonding.

The polymer chip and the foil are placed underneath an UV lamp for 30 sec and the foil is placed on top of the chip. A 2 mm thick piece of PDMS is placed on top of the foil in order to compensate for potential mis-alignment between the top and the bottom of the bonding press.

The stack consisting of polymer chip, polymer foil, and PDMS piece is placed in a designated holder and positioned in a press, where it is bonded for 10 min at 125 °C and 1.5 bar pressure.

The press used for bonding the devices is seen in Figure 2.7a).

The chips containing nanoslits requires bonding scheme which is optimised further in order to avoid collapse of the structures during bonding.

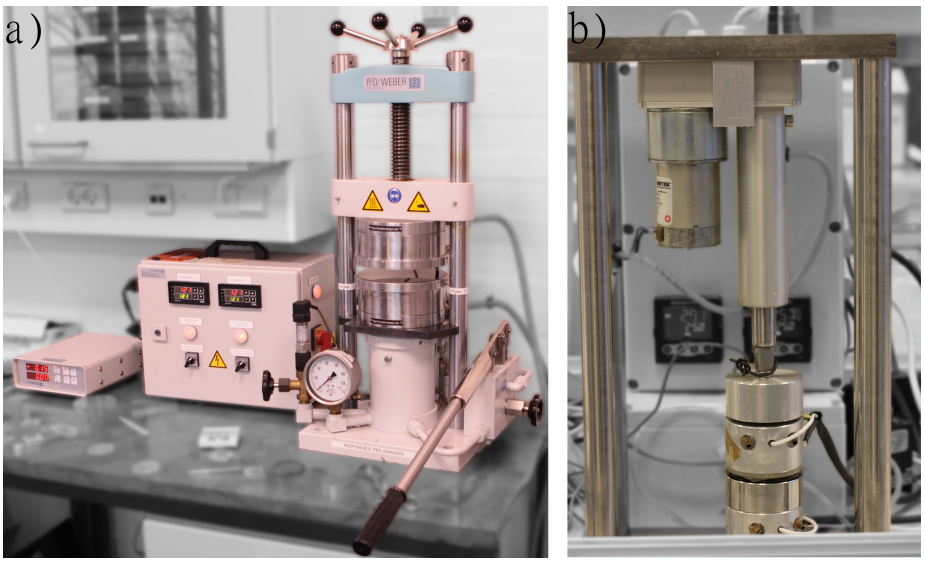

Figure 2.7: The large press seen in a) is used for the bonding of the polymer chips, where 5 chips can be bonded at the time. The small press, seen in figure b) is used for flattening out the polymer foil.

In order to avoid this from happening, two custom made PDMS pieces that distribute pressure during bonding are fabricated, so only a small amount of pressure is applied directly on top of the nanoslit, causing it not to collapse.

The PDMS pieces are fabricated by milling a casting mould in PMMA, see left of Figure 2.8. The mould is then filled with Sylgard PDMS (1 part hardener for 10 parts PDMS) and cured at 80 °C for 2 hours. The PDMS piece is removed from the mould and excessive material is removed. A model of the finished PDMS piece is seen in the right of Figure 2.8.

One of the two PDMS pieces contains a 3 mm in diameter hole at the position of the nanoslit, and the other PDMS piece contains a 1 cm in diameter hole at the same position.

Prior to the bonding, the polymer foil is flattened out by placing it in a

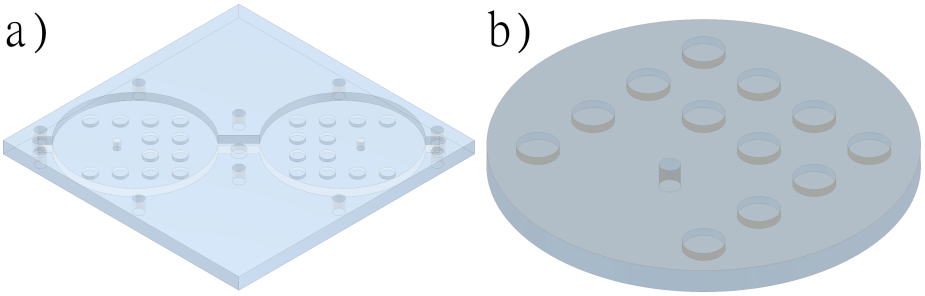

Figure 2.8: The PMMA mould is used for casting the PDMS piece. Cavities in the PDMS part is created to avoid collapse of the structures at low aspect-ratio parts of the chip.

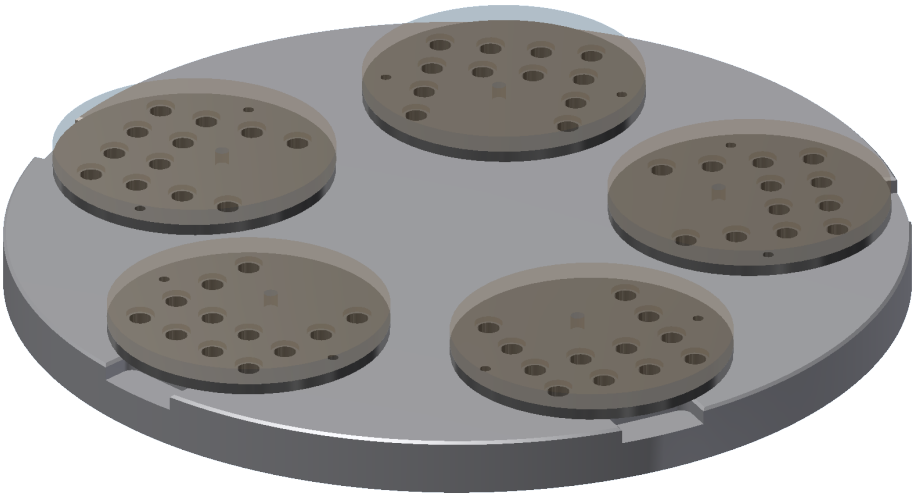

Figure 2.9: Chip holder designed for bonding 5 chips at the time. Bonding 5 chips at the time significantly speeds up the production time, and hence decreases production costs.

sandwich between two polished silicon wafers, heating it up to a temperature of 135 °C and applying a pressure of 1.5 bar for 10 min. This is done in order to partly remove extrusion marks from the foil. The equipment used for flattening out the polymer foils is seen in Figure 2.7b). This procedure will not remove all the extrusion marks from the polymer foil, but areas with a width of around 1 mm will occur, making it possible to bond the nanoslits.

The polymer chip and the flattened out foil is UV treated similar to described for the nanochannels. The foil is placed on top of the chip, and an area not containing extrusion marks is aligned on top of the nanoslit.

The PDMS piece containing the 3 mm hole is aligned on top of the foil, with the hole being right on top of the slit area.

The stack consisting of polymer chip, polymer foil, and PDMS piece is placed in the designated holder and positioned in a press, where it is bonded for 5 min at 125 °C and 0.75 bar pressure. The PDMS piece is replaced with the piece containing the 1.0 cm hole, and the stack is bonded for an additional 5 min at 125 °C and 1.5 bar pressure.

In order to speed up the process, a holder containing 5 chips at the time was developed. Using this, there is a theoretical upper production limit of 30 chips per hour, and in practice as many as 25 chips per hour could be bonded.

The chip-holder containing 5 chips is seen in Figure 2.9.

2.4 Step 4: Validating and Iterating

Errors need to be checked in the fabrication flow from design to final chip. The design itself can be flawed with channels having an aspect ratio that is too small for bonding or large for injection moulding, or structures might have been miss-aligned between different layers in the CAD-file.

In the cleanroom, etching processes might cause unintended under-etching

of the structures, leading to a nickel shim that cannot be used for injection moulding.

Injection moulding parameters, which are not optimal for the design, can be used, leading to thermal contraction during cooling of the polymer, which again can render the chip useless.

Finally, bonding of the devices can fail when pressures too high are applied, resulting in the structures collapsing.

2.4.1 Mask design

A change in the design of the layout can potentially have the largest implications on the functionality of the chip. Validation of the design might reveal that certain areas of the chip do not appear as intended due to design flaws that have to be changed in the CAD files. Changing the CAD file means that an entirely new batch of silicon masters has to be fabricated in the cleanroom, which takes time and cost money. In order to avoid to many costly and time consuming design iterations, all aspects of a given design iteration should be tested in order to adjust for as many flaws as possible in a new iteration.

For the nanochannels, three iterations were fabricated. The main difference between these three iterations is the location of one of the nanochannel clusters, see Figure 2.10 along with a widening of the nanochannels at the interface between nanochannels and the microchannels, see Figure 2.11. In addition, support structures at the inlet were integrated into the chip, as seen in Figure 2.12.

The change in the position of the nanochannels was caused by two problems experienced through the process flow. With sensitive structures placed far away from each other on the chip as seen in Figure 2.10a), contraction of the polymer when it cooled down in the mould cavity would create structural defects in the area where the nanochannels and the microchannels meet. Furthermore it was experienced that obtaining good results during bonding was difficult to achieve at the location of the lower structures in Figure 2.10a). Because of this, these structures were moved up to a position seen in Figure 2.10b), where problems regarding contraction of the polymer were minimised, and where bonding was efficient.

Changes were also made in the design in order to improve experimental conditions. The entrance to the nanochannels was broadened as seen in Figure 2.11. During experiments, the initial nanochannels (Figure 2.11a)) forced the DNA used, to have a sudden decrease in entropy since it became constricted in two dimensions at the same time. By having a gradual horizontal constriction of the nanochannels as seen in Figure 2.11b), it becomes easier to introduce the DNA into the channels.

The inlets were also redesigned during the project. In the first iteration, the inlets were consisting of plain pads at the positions of the Luer ports, as seen in Figure 2.12a). These pads turned out to contain areas with aspect ratios too low, making them collapse during bonding. This issue led to the introduction of support pillars on the pads as seen in Figure 2.12b), increasing the local aspect ratio significantly.

Another problem emerged when using the nickel shim for injection moulding several times. During the injection moulding process, pins are used for defining the holes of the Luer ports. These pins are pushed against the nickel shim. When

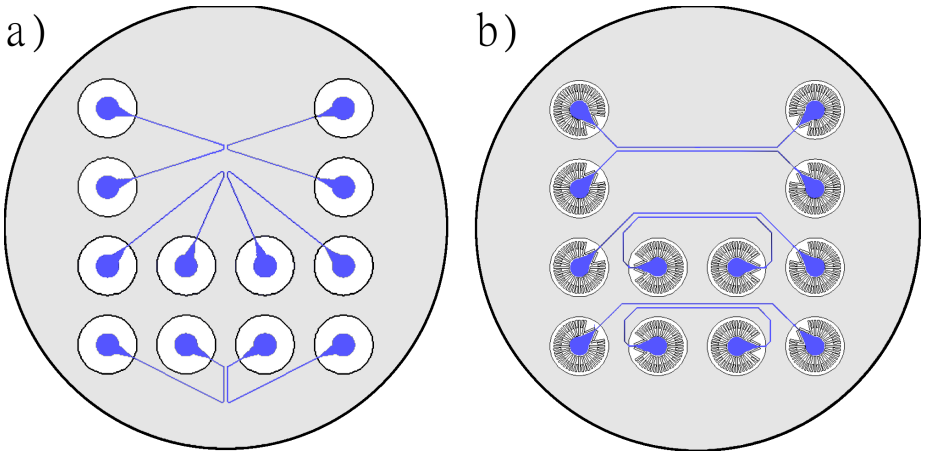

Figure 2.10: Layout of the microchannels in the two iterations. The lower cluster of nanochannels in Figure a) is moved up in Figure b) in order to improve bonding properties and facilitate injection moulding.

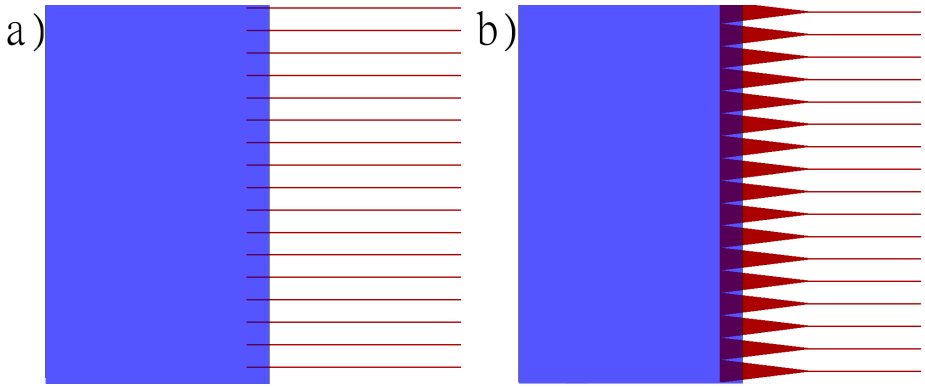

Figure 2.11: Layout of the interface between nanochannels and microchannel. In the later iteration (Figure b)), the nanochannels are widened towards the microchannel. This way, the elongation of the DNA is not sudden but gradual, making it easier to introduce the DNA into the channels.

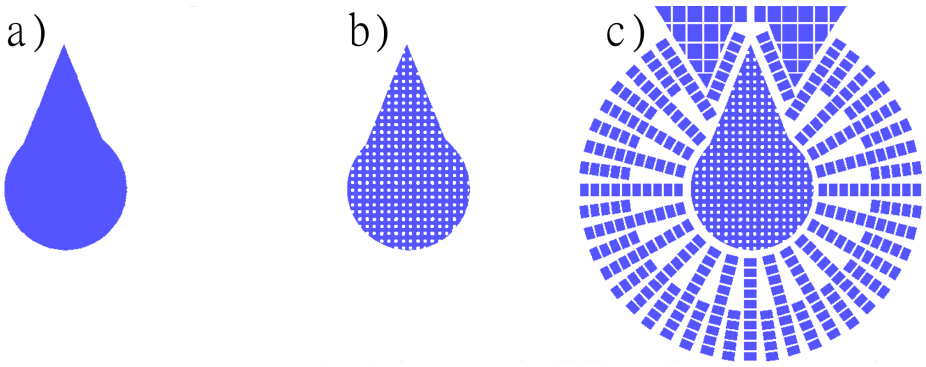

Figure 2.12: In the first iteration (Figure a)), the design of the structures under the Luer port only consists of a plain pad. For the first new iteration (Figure b)), structures were added in order to avoid collapse of the polymer foil at the inlet due to a too small aspect ratio. For the third iteration (Figure c)), structures were added in order to avoid damaging of the fluidic channels from the pins defining the Luer ports during injection moulding.

a nickel shim is used in the injection moulder several times, it is impossible to align it exactly the same way each time. This leads to the pins pushing against the shim at slightly different positions, where it sometimes happened to push hard against the structures defining the carrier channels. If this happened during one injection moulding process, and the shim was not positioned the exact same way during the next injection moulding process, channels would be blocked and the moulded devices would become useless. To avoid this, structures were integrated into the design that would take the force from the Luer-defining pins, leaving the carrier channels intact for several moulding processes. These structures are seen in Figure 2.12c).

The nanoslits devices, seen in Figure 2.13a), demanded a few more iterations in order to work as intended due to the low aspect ratio of the slit-area.

Apart from the structures at the Luer ports, that were modified identically to the modification for the nanochannels, this design was optimised both in the design of the nanoslit, and in the design of the microchannels leading up to the nanoslit.

The nanoslits were the target of several optimisation iterations. The first design proposal was a copy of the silica device previously used by Marie *et al*[MPB+13], which containes a nanoslit that is 100 nm deep and 50 µm wide (Figure 2.13b)). This low aspect ratio turned out to be impossible to bond, and collapsed in all attempts. Because of this, the width of the slit was reduced to 20 µm as seen in Figure 2.13c). Along with the bonding technique developed in this project, this resulted in a yield of 95%.

Despite the high yield obtained in the bonding of the 20 µm wide nanoslits, problems were experienced when performing experiments with these chips.

Since the slit design contains a cross, a single point of the lid of the slit has more than 40% as long to a support structure than the rest of the lid. This causes the height of the slit to be slightly different along the active area.

A first suggestion aimed at solving this was to place pillars at the cross

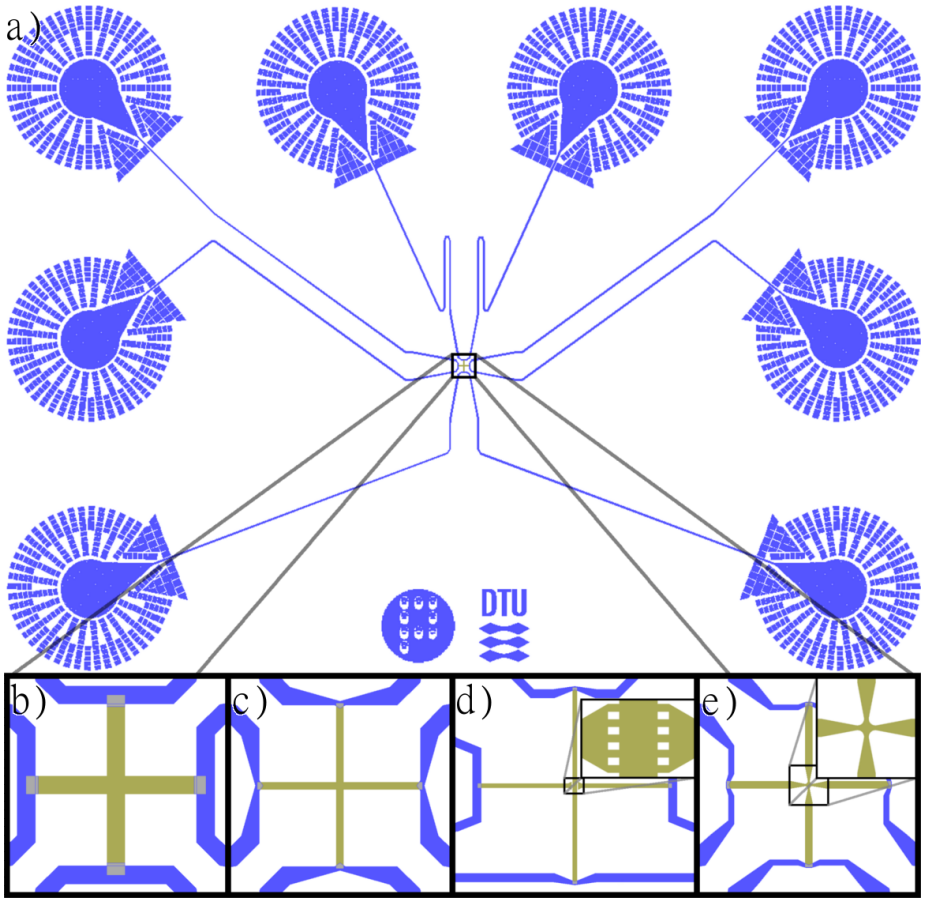

Figure 2.13: Nanoslit iterations. a) The general overview of the design used for the nanoslit devices. b) In the first iteration, nanoslits were 50 µmwide, causing the structures to collapse during thermal bonding. c) The second iteration contained 20 µm nanoslits that can be bonded with a yield of 95%. The carrier channels leading up to the nanoslits were changed to a design that narrows as it comes closer to the nanoslit, thereby pre-stretching the DNA. d) Support structures are introduced in the centre of the nanoslit in order to obtain a constant height of the nanoslit. This turned out not to work, since long strands of DNA would move in between the pillars. e) A final design has been developed that narrows the nanoslit close to the centre of the cross. This design has been optimised in order to have the best flow through the slit, while keeping a short distance from the centre of the cross to the nearest supporting wall.

along the part of the slit that was not used for stretching out the DNA as seen in Figure 2.13d). This proposal turned out to be problematic, since the DNA would go around the pillars and make turns on itself, h again making working with long DNA in the device difficult. Instead, a second design has been proposed. The slit narrows in at the cross, as seen in Figure 2.13e). By doing this, the centre of the cross is closer to the edge, and the height of the nanoslit will be more constant throughout the area.

The microchannels were also modified several times. Since the nanoslit chips are designed to work with long DNA strands, it is preferable if the strand is already partly stretched out before entering the nanoslit. This can be obtained in a fashion similar to the microcontractions described in Section 1.5.1. By narrowing the carrier channels near to the interface between the carrier channels and the nanoslit, the buffer fluid will accelerate locally, and the DNA will stretch out because of this. This helps, both when trying to find molecules that are long enough, and also when manipulating the molecule to go towards the entrance to the nanoslit.

2.4.2 Injection moulding

While functional injection moulding processes were obtained during the project, several problems were experienced. Three of these effects are seen in Figure 2.14a).

The first of these effects is an effect, locally known as scratch marks. Scratch marks occur when the polymer in the mould cavity shrinks during cooling. Since the shrinkage is uniform, there will always have a centre of the shrinkage. This implies that some of the polymer will be forced up against the structures of the nickel shim, creating a large pressure.

Once the chip is ejected, the increased pressure creates an increased frictional force at polymer/shim interface, dragging polymer along with it. If this occurs at the interface between a microchannel and the nanoslit or the nanochannels, the polymer wall that is created will completely block the nanostructures as seen in Figure 2.14b), where this effect has been highlighted.

This effect can generally be removed by either lowering the holding pressure or the temperature of the cavity during injection moulding, since this makes it more difficult for the polymer to fill out all the corners of the shim, thereby reducing the stress during ejection. If overhanging structures are present in the shim, this problem is increasingly difficult to avoid.

The second effect noticed during the project occurred when the silicon wafer was removed using KOH. If the KOH etching was not stopped in time, it would start attacking the Ni/V-seedlayer, creating artefacts resulting in the pits highlighted Figure 2.14c). These artefacts create a problem, since the pits create small entropic traps, thereby modifying the local elongation of the confined DNA in the nanochannels.

To avoid this problem, the nickel shim should either be removed from the silicon wafer by physical means, or the KOH etching should be timed so that it does not have time to attack the seedlayer.

The last problem experienced during injection moulding was seen, when the temperature of the polymer was too hot before being injected into the mould. As stated, the nozzle temperature used during the project is 270 °C however, if this temperature was increased by 10 °C to 280 °C, the surface of the polymer part

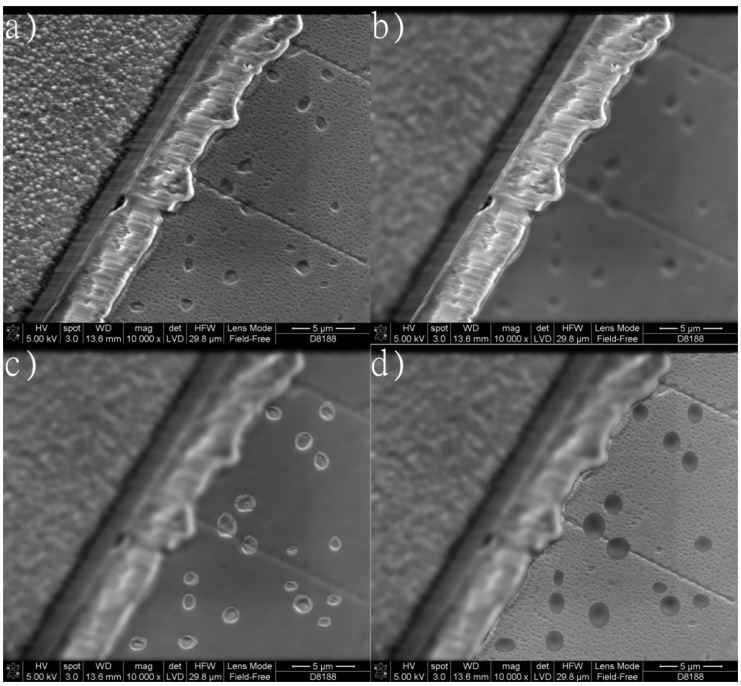

Figure 2.14: Production defects found in an injection moulded device. On the top right picture, all but the scratch-marks blocking the nanochannels have been blurred. In the bottom left, the marks created from over-etching with KOH during release of the nickel shim from the silicon wafer is highlighted, while the lower right shows the marks found after injection moulding with a temperature of the molten polymer being too warm.

would start getting small pits with a diameter smaller than 100 nm as highlighted in Figure 2.14d). This problem was solved by lowering the temperature of the nozzle of the injection moulder.

2.4.3 Bonding

The bonding step is the final step in the process flow, where mistakes can be made, rendering the device useless. Nanoslits, especially, caused problems during this step due to their low aspect ratio. These problems were also the reason for the development of the specific bonding process described in Section 2.3.

In order to know if a batch of chips would work during experiments, the chips had to be tested to see if collapse of the structures had occurred during the bonding scheme. As biological tests are quite cumbersome, easier means of testing the devices are required.

For the nanoslit, an inverted Zeiss Axioscope using a 20× air objective could be used. If the nanoslit is not collapsed, the difference in refractive index between the polymer and the air in the slit makes the slit stand out, whereas no change in intensity is seen if the slit is collapsed.

Examples of both are seen in Figure 2.15, where the structure in Fig-

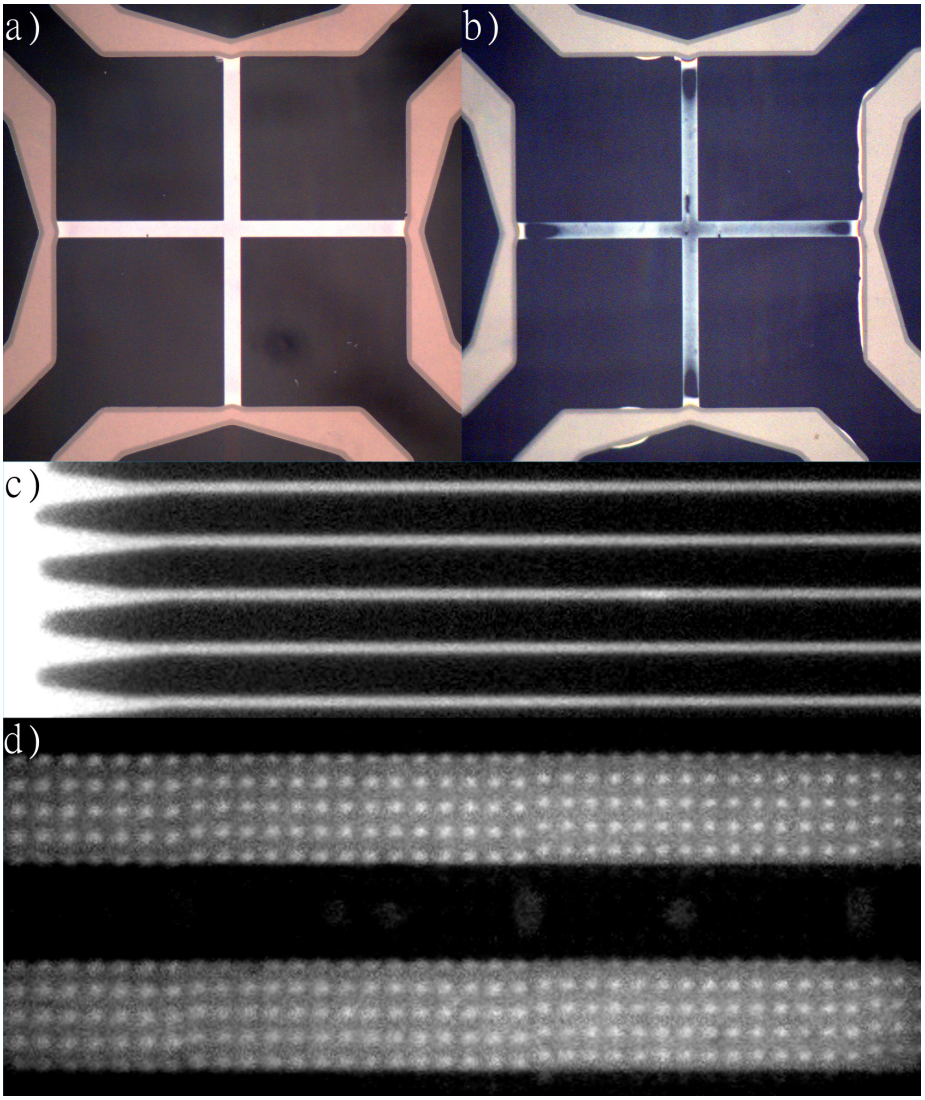

Figure 2.15: Using reflective microscopy reveals if the nanoslit is bonded without collapse of the structure as seen in a), or with a collapse of the structure as seen in b). Since the nanochannels have dimensions much smaller than the nanoslit, they are verified by filling them with fluorescein and acquiring images using an EMCCD, as seen in c). d) The three-layer nanopit structures can be verified identically to the nanoslit devices. The pits at the bottom of the nanoslits are easily observed.

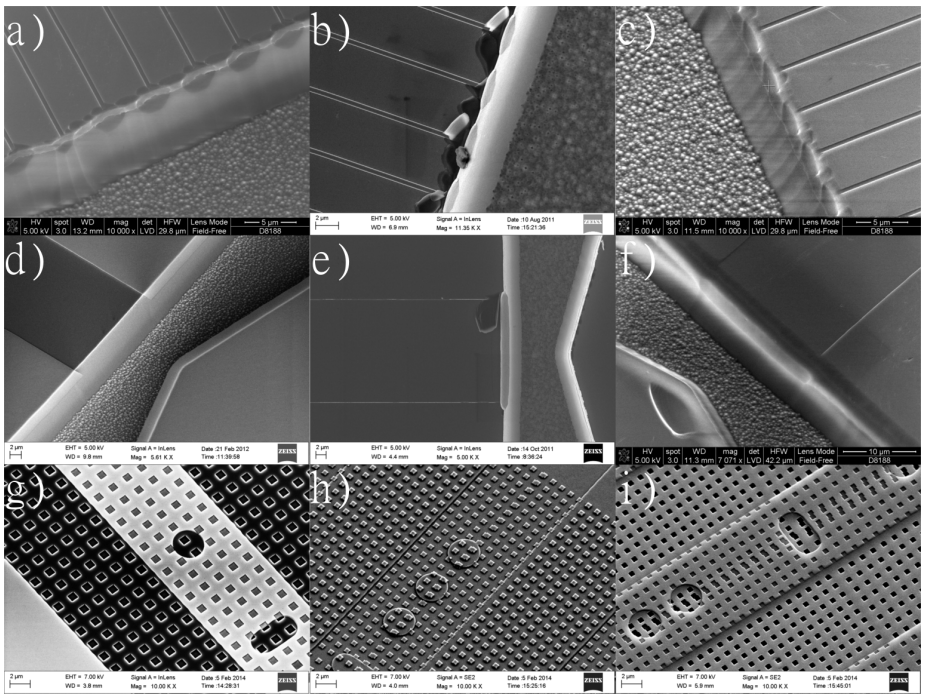

Figure 2.16: Replication of nanostructures from silicon master (left) to nickel shim (middle) to polymer part (right). The three rows correspond to nanochannels (top), nanoslit (middle), and nanopits (bottom).

ure 2.15a) is seen not to have collapsed, while the structure in Figure 2.15b) has.

The dimensions of the nanochannels makes the technique of looking at the contrast impossible. Instead, these are tested by filling them up with fluorescein and imaged using the same setup as is used for the experiments described in Chapter 4. Results from a testing of nanochannels is seen in Figure 2.15c).

Since the nanopits consist of pits at the bottom of a nanoslit, these are tested in a similar way as the nanoslits. An example of uncolapsed nanoslits containing nanopits is seen in Figure 2.15d).

2.5 Replication Fidelity

To ensure that the intended design is consistent when going from silicon master to nickel shim to polymer device, all parts were imaged at several occasions.

In Figure 2.16, the nanochannels, nanoslits, and nanopits can be seen both in the original silicon master, the nickel shim, and the final polymer device.

In the scanning electron microscope (SEM) image of the wafer containing the nanoslit (Figure 2.16 middle-left) it is seen that underetching is taking place during the RIE. The overhang of the oxide layer does not have any negative effect on the nickel shim, since it will only get integrated into it.

Furthermore it is seen that the polymer device does not have corners as

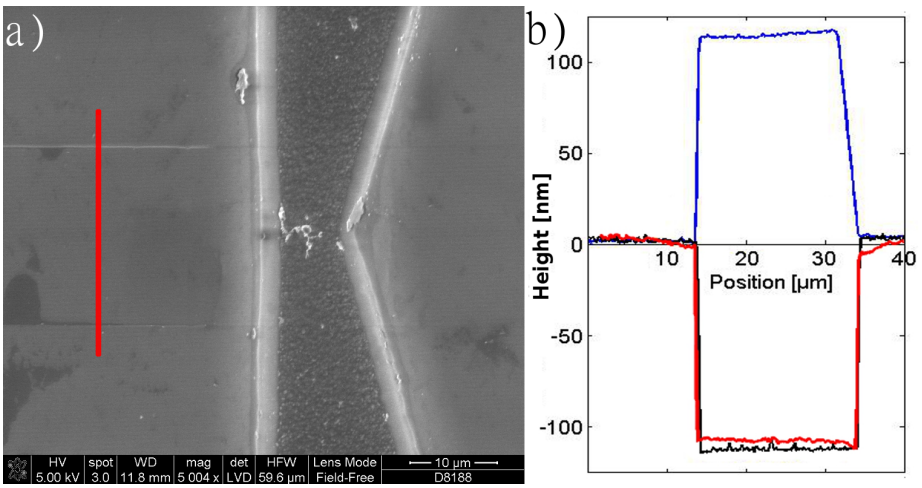

Figure 2.17: Profile of the nanoslit in the silicon wafer. a) Both silicon wafer, nickel shim, and polymer device have been measured at the red line. b) The black line corresponds to measurements on the silicon wafer, the blue line to the nickel shim, and the red line to the polymer chip

sharp as the silicon master in the slit. This is because of the settings of the injection moulder during fabrication. The temperature of the injected polymer along with the temperature of the cavity and the holding pressure define how well the cavity is filled, and how sharp the corners are.

For the experiments performed in this project, a smooth transition from the microchannels to the nanochannels and nanoslit can be an advantage, since the change in entropy for the molecule is slower. This makes it easier to introduce the molecule into the nanochannel and nanoslit, and is less damaging to the fragile DNA molecule[CTAC02].

Although it is not critical if the transition from microchannel to nanoslit is perfectly replicated, the nanoslit itself has to be replicated with great precision, since the dimensions of the slit decides if the device will work as intended.

To verify this, the width and height of the nanoslit is measured using an atomic force microscope (AFM). The result from this measurement is seen in Figure 2.17, where the nanoslit is replicated between the different materials, and the device fabricated through injection moulding has the same dimensions, both laterally and horizontally as the original silicon wafer.

2.6 Background Signal of Chips

An important factor when performing experiments is the signal to noise ratio. If the background noise is too high, it is difficult to extract the signal for a proper analysis.

TOPAS has previously been reported to have a low autofluorescence[HY03, PNL+05], but this characteristic of the material was further investigated here. Since the excitation light used during experiments will excite potential autofluorescent sources throughout the entire width of the substrate, chips that

Figure 2.18: Injection moulded chips in different colours. Adding 2% of a master batch to the polymer granulate will fully colour the injection moulded chip.

contained 2% (w/w) of a colourant as seen in Figure 2.18 were fabricated. The colouring of the chips is expected to lower the amount of light capable of exciting the polymer substrate, thereby lowering the level of autofluorescence.

In an initial test, the autofluorescence of the coloured chips was benchmarked against chips produced in pure TOPAS COC 5013L-10.

For the test, the chips were illuminated with a wavelength of 480 nm and data was recorded at 535 nm, corresponding to the wavelengths used when performing the DNA experiments described in Chapter 3 and Chapter 4. This method has previously been proposed by S. Stavis[Sta12]. 8 different colours from two different manufacturers were tested, and 3 chips from each sample were used during the measurements. The result from this test is seen in Figure 2.19a).

From this test it is evident, that most of the colourants increase the autofluorescence of the chip. One of the samples has even been excluded from the test, because the signal was so high that the camera got saturated. The black additive from Gabriel Chemie does, however, give good results, and the background signal from this sample appears to be significantly lower than the transparent polymer chip,–even as low as a standard silica chip.

To elaborate on these results, an experiment was set up, where the polymer chip is placed in focus on a microscope under full illumination. One image was taken every 30 sec for the duration of 30 min. This was done for 4 transparent chips, fabricated in 100% pure TOPAS COC 5013L-10, and for 4 chips fabricated in TOPAS COC 5013L-10 containing 2% (w/w) black additive from Gabriel Chemie.

The results from this experiment is seen in Figure 2.19b). From this it is seen, that the background signal from the chips containing the black additive is significantly lower than from the transparent chips.

For both of the chips, the signal can be described as following a curve of the

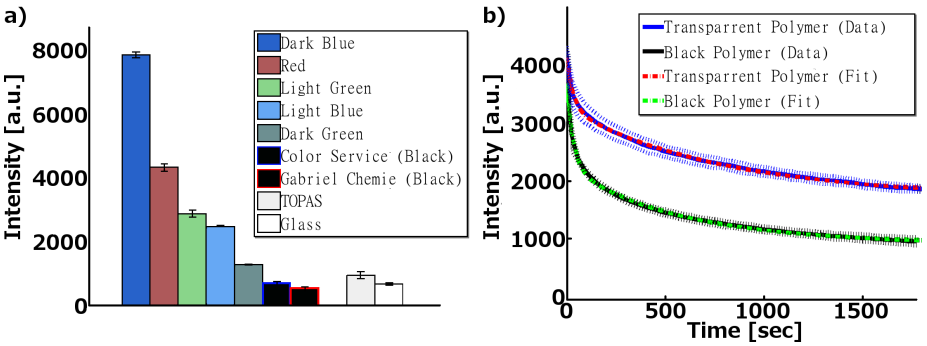

Figure 2.19: a) Initial results from tests of autofluorescence from coloured polymer chips. Most of the colourants are seen to increase the autofluoresence, but two colourants decrease the signal from the substrate. b)Fluorescent measurements of transparent and black polymer chips during illumination with fluorescent light. The autofluorescence of the black polymer chips is seen to end at a level almost half as small as that of the transparent polymer chips.

Parameter	Black Chip	Transparent Chips
c_0	939 $\pm$ 10	1744 $\pm$ 16
c_1	1323 $\pm$ 14	1530 $\pm$ 12
c_2	1438 $\pm$ 25	872 $\pm$ 22
t_1	572 sec $\pm$ 17 sec	782 sec $\pm$ 23 sec
t_2	34 sec $\pm$ 1 sec	34 sec $\pm$ 2 sec

Table 2.2: Parameters for best fitting of the model seen in Equation 2.1.

type

$$I(t) = c_0 + c_1 \times \exp(-t/t_1) + c_2 \times \exp(-t/t_2) \tag{2.1}$$

This sort of behaviour indicates that the background signal originates from several sources in the polymer substrate.

The parameters used for modelling the behaviour of the two chips, using the above mentioned equation are seen in Table 2.2 The results found here also clearly indicate that prior to performing sensitive fluorescent experiments on the chip, it should undergo a pre-quenching process for around 572 sec$\approx$10 min in order to avoid changes in background signal during the experiment.

2.7 Functional Test of Nanopits

The three layer structures fabricated during this project were supposed to be used similarly to devices described by Klotz *et al*[KaR12].

Even though thorough experiments were never conducted, Rodolphe Marie succeeded in performing a functional test of the devices, using T4GT7 DNA.

In the experiment, the T4GT7 DNA is stained with YOYO-1 and suspended in a buffer consisting of 0.5$\times$TBE containing 3% BME and 0.5% Triton X-100. The DNA is introduced into the nanopit array, where the nanopits work as

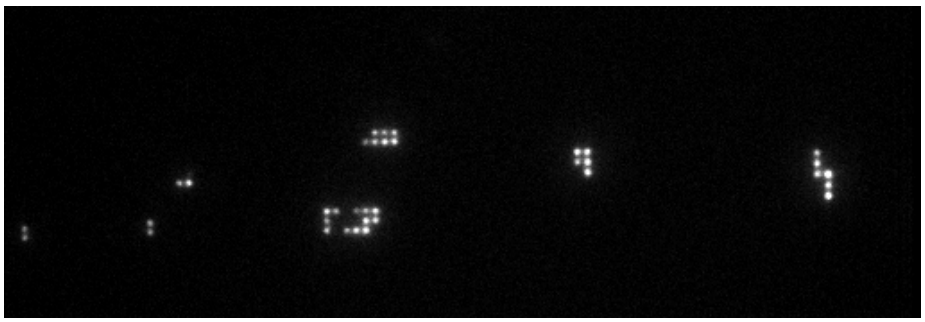

Figure 2.20: Functional test of the nanopit device. The pits work as entropic traps for the DNA, as explained by Klotz *et al*[KaR12].

entropic traps. These entropic traps partly confines the DNA. DNA molecules in the nanopit device are seen in Figure 2.20.

2.8 Economics of Scale of Injection Moulded Chips

If LoC systems are to have a future in the industrial world, it is important to keep the cost low. According to Becker[Bec09b, Bec09a] who was invited to write several focus papers, raising awareness concerning the industrialisation of microfluidic devices in "Lab-on-a-Chip" in 2009, there are several reasons why only a few microfluidic devices have some success in the consumer world.

One of the main reasons is the cost of production. When people in academia calculate the price of a device, they often forget factors such as the salary of the student or the cost of equipment, which is already present at the department[Bec09a]. This way, the calculated price is much lower than what it would be if a company would like to produce and commercialize the product.

In order to become successful on the market, there has to be some economics of scale, where the price per unit is lowered, as more units are produced. In his articles, Becker has an overview of the economics of scale for different production platforms. As seen in Figure 2.21, injection moulding has a high starting cost, since both the injection moulder and the tool used are expensive. Once the machine is up and running, the cost of producing an extra unit is low. Thus, the more devices that are moulded, the lower the price for the individual unit.

Elastomer-casted devices have a contrary pricing model to that of injection moulded devices. For elastomer devices, starting costs are low, since the machinery needed to start production is relatively cheap. However, the development time for each device is long, causing the added cost for an extra produced device to be high, meaning that the final price of the first device is almost equal to that of device number 100,000.

The production scheme used in this project has several costs integrated into it. Since the nickel shim is fabricated in a cleanroom, a large fraction of the cost comes from making this, rather than from producing the hundreds or thousands of devices in the injection moulder afterwards.

To get an idea of the costs of the different steps involved in the fabrication of the nickel shim, Table 2.3 gives an overview of the individual processes for

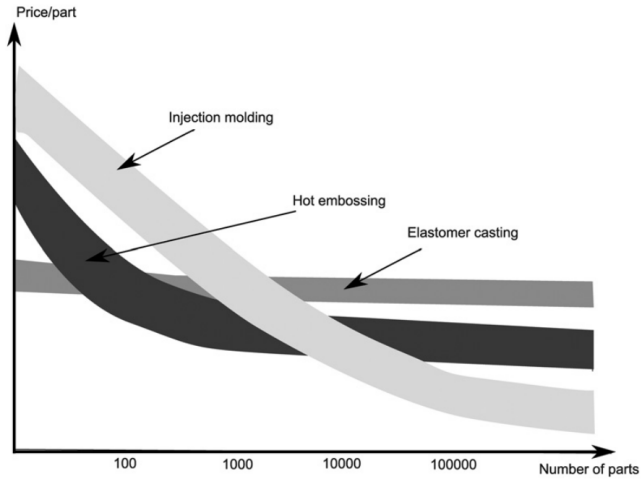

Figure 2.21: Development in the cost per unit, depending on the number of units produced using different replication technologies. Figure has been implemented from Becker[Bec09b].

the fabrication of the shim used for nanoslits. For the nanochannels, the use of e-beam lithography increases the cost.

In this calculation, the cost of the engineer working with the sample is seen to be significant, especially when the cleanroom time is included. The DANCHIP cleanroom facility does however have a rule, that no more than DKK 15,000 is charged for a person working in the cleanroom per month. This will have significant influence on the price per nickel shim, if a single engineer is working full time, 37 hours a week, 4 weeks per month, in the cleanroom, producing several nickel shims in that period.

Despite the potential savings in the pay for cleanroom time, many of the processes seen in Table 2.3 cannot be ran in parallel, and a person is needed at all time during the process. This means that the cost in production of several identical shims, produced simultaneously, is still almost linearly increasing.

Once a shim has been produced, the devices are injection moulded. The injection moulder at DANCHIP has a price of DKK 350.-/hour, including material and service. Since cycle time of the devices fabricated in this thesis is between 30 sec and 90 sec, 40 to 120 devices could be moulded every hour, giving an added cost per device of DKK 3.00 - 9.00 If a tool was fabricated in a way that was optimized for the each individual device made in this thesis, the cycle time can be lowered. The industry standard for injection moulding of CDs and DVDs uses a cycle time of around 5 sec per device. This corresponds to 1,800 devices per hour. If such a production time is obtained, the price per device would be as low as DKK 0.20.

Because of the low price of an injection moulded device, the price of the final device relies heavily on the number of chips fabricated. This is furthermore caused by the fact that the injection moulder needs to warm up prior to production, and a technician has to be present during this stage, adding costs to the process. Once the machine starts producing large quantities of devices, it can run autonomously.

Product	Price pr Unit/Hour (DKK)	Number of Units/Hours	Total Cost (DKK)
Wafers	120	4	480
Oxidation in Furnace	350	4	1,400
Spincoating of Photoresist	350	1	350
UV Aligner	350	1	350
RIE	600	2	1,200
Spincoating of Photoresist	350	1	350
UV Aligner	350	1	350
RIE	600	2	1,200
Sputtering of Seedlayer	600	2	1,200
Electroplating	350	4	1,400
SEM verification	350	4	1,400
Cleanroom Time	750	16	12,000
Engineer Pay	360	16	5,760
Total			27,440

Table 2.3: Worst case estimate of the costs involved in the fabrication of the nickel shim. The pay of the engineer has been taken as the average pay of an engineer with a 5 year education as found on the Danish engineering unions website[Ing]. In case of alignment problems in the lithography steps, particles in the photoresist etc. 4 wafers are processed, but only one is electroplated.

The price for bonding the chips is more difficult to calculate. Bonding the chips requires a bonding press, and such a press is available, free of charge at DTU Nanotech. For the bonding of chips, a student employee can be hired at a price of DKK 130,- per hour. Since 25 chips can be bonded per hour, this adds DKK 5.20 to each chip.

Table 2.4 shows an estimate of the price for producing different amounts of devices, and the cost savings involved in large scale production.

In this project, a typical number of devices made from each shim has been around 100-1000 and with a bonding yield of 95%, this causes each functional device to have a price of DKK 44.00 - 333.00, everything included.

For comparison, the price of a chip produced in silica can be calculated. Prior to this project, nanoslit chips were produced on silica wafers[MPB+13], with 9 chips on each wafer. Since the production scheme for these silica chips is almost identical to the production of the shim, the fabrication of 4 wafers containing a total of 36 chips costs DKK 24,840.00.

These chips have to be fusion bonded individually. Fusion bonding takes roughly 30 min per chip with a yield of around 60%, increasing the cost of each device by DKK 505.00. The fusion bonded chip also has to be annealed in a furnace overnight. This furnace has a price of DKK 350.00 per hour, so an overnight annealing of 10 hours costs 3,500.00.

In total, a batch containing 36 potential chips costs 24,840.00 for the processing of the wafers, corresponding to 690.00 per chip. 505.00 is used for each chip in cleanroom time and salary for the engineer for the initial bonding procedure, and 97,- is used per chip for the annealing, adding up to 1,292.00 per chip.

Product	Cost of			
	10 Devices	100 Devices	1,000 Devices	10,000 Devices
Nickel Shim	27,440	27,440	27,440	27,440
Startup of Injection Moulder	350	350	350	350
Salary for Technician during Startup	300	300	300	300
Injection Moulding (40 devices per hour)	87.50	875	8,750	87,500
Bonding (25 devices per hour)	52	520	5,200	52,000
Total Price	28,230	29,485	42,040	167,590
Price per Device	2,823	295	42	17

Table 2.4: Since the cost of the nickel shim is so high compared with the price of an extra produced device, there is a huge reduction in the price per device, as the number of produced devices is increased. If 10 devices are produced, only 0.3% of the cost of the injection moulded chip is an effect of the injection moulder moulding devices, and more than 97% of the price of the moulded chip is coming from the cost of the original nickel shim. If 10.000 devices are moulded, 75% of the cost of a moulded chip originates in the actual moulding process, while only 24% of the cost is from the nickel shim.

Since the yield is only around 60%, the price for each functional chip becomes DKK 2,150.00.

This means, that when 100 polymer chips are fabricated, the cost per chip is only 16% of the price for a silica chip. If 10,000 polymer chips are produced, the price for a polymer chip is as low as 0.2 percentage of the cost of a silica chip. Consequently, if experiments are done where a high chip consumption is expected, the cost savings of using injection moulded chips over silica chips should be given significant consideration.

Chips fabricated in an elastomer have different production bottle necks, making price comparisons to injection moulded chips more difficult.

In spite of records showing the fabrication of PDMS devices containing aspect ratios of 1:10[KKK+11], the fabrication of aspect ratios as low as 1:200 has not yet been shown in the literature.

To get an impression of the cost of a PDMS device, the following parameters have to be considered: Cost of mould, cost of labour, and cost of material.

Typically, a PDMS mould can be fabricated using SU-8 lithography or micro milling. At DTU Nanotech, CNC micro milling is the preferred method for mould manufacturing for many of the employees. The department has 3 micro millers at free disposal for the employees, along with free PMMA blocks for milling.

A typical casting mould will take roughly 3-5 hours to make, depending on the number of different diameter cutters that are needed for the device, the finish of the device and other parameters. With the salary of an engineer of DKK 360 per hour, this ends up at around DKK 1080 - 1800.

For each device that has to be fabricated, PDMS has to be degassed and

casted onto the mould. This takes another estimated 1 h, costing additionally DKK 360. The device is baked in an oven for 4 hours, where the engineer is disposable to other tasks, making it possible to neglect the labour cost here.

Finally the PDMS device has to be bonded onto a glass slide using an oxygen plasma. This can be done in around 15 min at a cost of DKK 90. Altogether this costs DKK 1,530 to 2,250 for the first chip and an additional DKK 450 for each extra chip.

While the price per chip here is comparable with the chip costs when fabricating 100 chips in the injection moulder, the production time per chip, once production is up and running, is much slower, resulting in a much more inefficient chip production.

As an example, if 100 chips should be used, this would take 2,5 hours to fabricate in the injection moulder plus 4 hours of bonding, equal to a total of 6.5 hours. By elastomer casting, one chip would take 4 hours for baking and an additional 15 min for bonding, resulting in a total of 425 hours or 2.5 weeks, non-stop for the production of the 100 chips.

2.9 Conclusion

In this chapter it is seen, that it is possible to fabricate highly complex LoC systems containing nanostructures and low aspect ratio structures using conventional, low cost injection moulding processes.

Conventional cleanroom fabrication techniques have been used for the fabrication of a master silicon wafer with tolerances of a few nanometres, difficult to obtain with any other means of production.

Several problems were encountered during the development of the injection moulding protocol that could potential all make the polymer chips useless, but these were all corrected, making the injection moulded chips of a quality good enough for the intended purposes.

Using injection moulding as the production platform gives control over the transition rate from microchannels to the nanostructures. This is an advantage in certain biological experiments, where DNA is introduced into a nanochannel or nanoslit, since the transition from the DNA being in bulk solution to being constrained in a nanochannel or nanoslit is slower, leading to an easier transfer of the molecule to the final confinement.

The background signal of the coloured chips is seen to be comparable to that found in chips fabricated in silica. The background signal is of high importance, since it is easier to obtain a good signal if the background signal is low. For the single molecule experiments that will be described in the next chapter, the signal is low, meaning that the background signal also has to be low in order not to drown the signal from the molecules.

By replicating the silicon wafer in cheap polymer using injection moulding, massive cost savings are obtained. Compared to fabricating more devices in silicon/silica, the price per device becomes significantly lower, once a sufficient amount of chips are fabricated, and cost savings as high as 99.8% can be obtained, making the polymer chips suitable as disposable devices.

Since both injection moulding and the bonding process have the potential of being automated to a high degree, the price for a produced LoC can get even lower in an industrial setting, where the injection moulder can run autonomously

for long periods of time, and the bonding can be performed with only little human interaction.

Chapter 3

Counterstaining Mapping

This chapter will deal with experiments performed on the nanochannel chips fabricated in Chapter 2. These chips are used in order to test the idea of performing optical mapping using a counterstaining agent for obtaining a fluorescent barcode as described in Section 1.4.5.

The different base pairs present in DNA allows for site specific binding of certain chemical compounds. This makes it possible to differentiate between AT-rich and GC rich regions by using a compound that will only bind to one of the two base pairs.

Staining the DNA with a fluorescent molecule that does not discriminate between base pairs while additionally adding a molecule that does, creates an inhomogeneous equilibrium distribution of the fluorescent dye along the DNA molecule. This inhomogeneity can be used for mapping the molecule against a theoretically obtained profile.

The chip design used for these experiments has certain interesting features due to the entropic stretching of the DNA. Once a strand of DNA has been introduced into a nanochannel, the chip is completely passive. This makes the chip robust, since no flows are present to make the molecule drift out of the field of view (FoV) of the camera observing it.

Entropic confinement generally does not give as large a degree of stretching of the DNA molecules as can be obtained using shear flow stretching. However, devices with such structures have been used for identifying genes of the yeast molecule[RLS+10, WSDR12]. This shows the capability of the design to produce results, good enough for the objective at hand.

Entropic confinement using nanochannels also has the advantage, that hundreds or thousands of parallel channels can be fabricated, leading to a high data yield during experiments.

3.1 DNA preparation

The technique for creating fluorescent profiles along a DNA molecule by the use of a counterstaining molecule is still in its early phase. Because of this, relatively short, well known DNA molecules, having a characteristic AT-GC distribution are used.

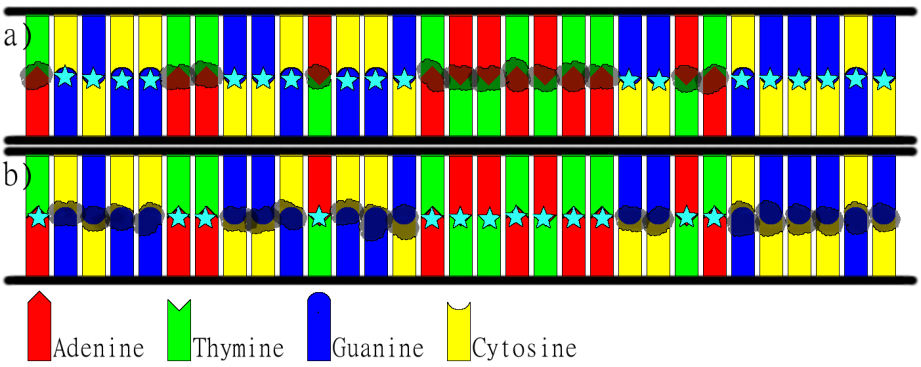

Figure 3.1: Principle of the counterstaining approach. Figure a) corresponds to counterstaining, using netropsin, that binds to AT rich regions of the DNA, lowering the binding of the YOYO-1 at AT rich regions. Figure b) corresponds to counterstaining using actinomycin D, that binds to GC rich regions of the DNA, lowering the degree of binding of YOYO-1 at GC rich regions.

Two molecules that have these qualities are the linear λ-DNA (48.5 kbp) and the linear but circularly permuted sequence T4GT7-DNA (168.5 kbp). These are used as test constructs to assess the counterstaining technique in injection-moulded devices on a proof of concept scale.

By using one molecule that binds specifically to AT and one that binds specifically to GC, it is expected that the fluorescent profiles originating from these two samples will be inverted. Because of this, the DNA used in the barcoding experiment is stained with YOYO-1 (Invitrogen), using either netropsin (Sigma-Aldrich) or actinomycin D (Invitrogen) as the counterstaining agent. Netropsin is known to bind to the AT-rich regions of the DNA molecule[WLW74], limiting the binding of YOYO-1 at this position as seen in Figure 3.1a). For limiting the binding of YOYO-1 to the GC-rich regions, actinomycin D is used[SJB$^+$88, WJZ$^+$88] as seen in Figure 3.1b). Counterstaining with netropsin will thus result in an inverted fluorescent intensity profile to the one obtained by counterstaining with actinomycin D.

For 100 µL of stained DNA, counterstained with actinomycin D, 1 µg of DNA is mixed with actinomycin D and YOYO-1. The ratio of base pairs to YOYO-1 molecules is 10:1 and the ratio of actinomycin D molecules to YOYO-1 molecules is 250:1.

The suspension is incubated for 2 h at 50 °C, and stored at −20 °C until use. The best results are obtained if experiments are performed shortly after staining of the DNA. Counterstaining with netropsin is performed exactly as described above, only exchanging the actinomycin D with netropsin in a concentration that is 4000 times higher than the concentration of YOYO-1.

3.2 Experimental setup

The polymer nanochannel chips, as described in Section 2.1, are initially pre-wetted with a 7% ethanol solution. This is exchanged with 0.5×Tris/Borate/EDTA

(TBE) prior to introduction of DNA. The counterstained and YOYO-1 labelled DNA solution is diluted 1:10 in de-gassed 0.5×TBE. Triton X-100 (Sigma-Aldrich) is added at 0.5% (v/v) to the loading buffer to prevent sticking of the DNA to the polymer surface. In addition, 0.5×TBE containing 3% (v/v) β-Mercaptoethanol (BME) (Sigma-Aldrich) is added to avoid photonicking. The DNA solution is introduced into one of the Luer ports on the device and the ports are connected to an air-pump for applying positive pressure.

DNA molecules are brought from the Luer reservoir to the nanochannel inlet by applying the pressure drop across the microchannel. The flow is redirected to drive DNA into the nanochannel array by applying pressure across the nanochannels. As the DNA enters the nanochannel, the channel confinement forces the DNA to stretch out to around 25% of its contour length, in good agreement with previously published simulated data[WTD11].

The dimensions of the channels corresponds to the DNA being in the de Gennes regime, as described in Section 1.5.2. While a more profound stretching would be beneficial for the resolution of the data[WRT12, KKK$^+$11], it was still possible to get a high confidence of the results obtained during the experiments.

The fluorescence profile along the DNA contained in the nanochannels contains sequence information with a resolution limited by optical diffraction and the degree of stretching to around 2 kbp. Raw images of λ-DNA inside the nanochannels are shown in Figure 3.2. Data acquisition is performed using an inverted Nikon microscope (Nikon Eclipse Ti) with a 100x oil immersion objective (NA=1.4) and an electron multiplying charge-coupled device (EMCCD) (Andor). Molecules are imaged for 50 consecutive images with a frame rate of 10 fps.

During the time used for an experiment, no significant photo nicking nor photo bleaching was experienced.

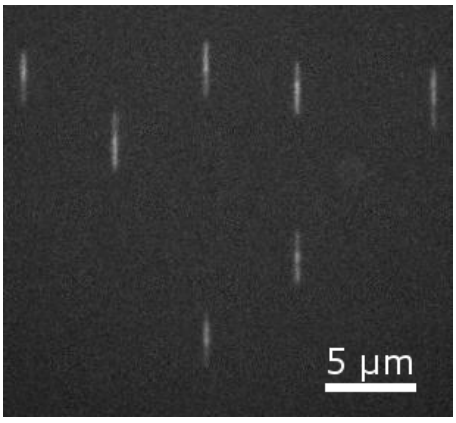

Figure 3.2: λ-DNA inside the nanochannels. The physical confinement of the nanochannels forces the DNA molecules to stretch out.

3.3 Data Analysis

The goal of the analysis procedure is to extract a high-signal to noise barcode from the raw single-molecule data. To obtain this goal, it is important, that the

autofluorescence of the polymer chip is as low as possible.

As it was shown in Section 2.6, the background signal of the TOPAS chips is low. For the setup used in these experiments, an average background signal measured over the entire field of view, was only 1.6 ± 0.3 times higher than that of a similar chip, fabricated in fused silica under curcumstances similar to what is used during experiments.

The intensity profile transverse to the axis of stretching contains information only about the optical resolution. Consequently, for a given molecule, the intensity transverse to the nanochannel axis is summed and plotted along the nanochannel, converting the image stack to a gray scale plot of intensity vs. the position along the channel on one axis and time on the other axis. In order to average intensity profiles captured at different times, thermal (Brownian) fluctuations of the molecule that induce distortions of the barcode between frames must be taken into account. Brownian dynamics create displacements of the center-of-mass position via diffusion and fluctuations in local molecule concentration (arising as a superposition of spatial Fourier modes along the extended molecule). Thermal fluctuations are taken into account via the approach described by Reisner et al.[RLS$^+$10]. Center-of-mass motion of DNA is removed via direct calculation of molecule spatial translation (obtained from correlation of intensity profiles between frames). Concentration fluctuations are removed by computing the series of local dilations that minimize the least squared difference between a reference frame (taken as the initial frame) and a given frame in the image series. If this procedure is applied to all frames acquired, the intensity profile between frames will be normalized and can be averaged together, yielding a single-molecule barcode with the highest signal-to-noise possible for the given data set. For each set of parameters used, at least 30 molecules are measured, so that it is possible to obtain average barcodes that represent the consensus of a number of single-molecule measurements.

It is expected that the intensity variation arising from counterstaining to be a function of the local AT/GC concentration. In particular, it is expected that the local intensity $I(s)$ as a function of sequence position s along the nanochannel extended molecule is proportional to the local GC concentration (for netropsin) and AT concentration (actinomycin D) with a proportionality factor that depends on the level of YOYO-1 staining. The local AT/GC concentration is obtained convolving a binary version of the genetic code, where ATs and GCs are converted into either ones or zeros, depending on whether netropsin or actinomycin is used. For the convolution, a Gaussian profile having a standard deviation of 1.5 pixel/200 nm is used to simulate broadening due to finite optical resolution.

The experimentally obtained barcode is normalized using the algorithm

$$P_{exp} = \frac{I_{exp} - \langle I_{exp} \rangle}{\sqrt{\left\langle \left(I_{exp} - \langle I_{exp} \rangle \right)^2 \right\rangle}}$$

where I_{exp} is the EMCCD camera pixel value reading.

Similarly, the theoretically obtained barcode is normalizeed using the algorithm

$$P_{theory} = \frac{I_{theory} - \langle I_{theory} \rangle}{\sqrt{\left\langle \left(I_{theory} - \langle I_{theory} \rangle \right)^2 \right\rangle}}$$

The inter-profile shift that yields a minimum of the squared intensity difference between the profiles (summed across all pixels), was then found, i.e. the least squares estimator for barcode no. i is found as

$$\delta_i = \min \sum_{n=s}^{m+s} \frac{(P_{exp,i}(n) - P_{theory}(n))^2}{m}$$

where s is the starting point along the theoretical barcode that is used as an optimizing parameter, and m is the pixel length of the barcode.

During this alignment process, dilation or contraction of the theoretical barcode by up to 15% was implemented in order to yield the best fit. This procedure takes into account the fact that the measured barcode may not exactly represent the true equilibrium profile. In addition, for the linear λ-DNA sequence, the reading direction of the molecule that yields the best alignment must be found. Alignment of the circularly permuted T4GT7-DNA sequence also requires determination of the sequence-starting point. The average of the fitted barcodes, $P_{consensus} = \langle \delta_i \rangle$, from the DNA used in the experiments is shown in Figure 3.3. The expected inversion of the barcodes, occurring as an effect of changing the counterstaining agent from actinomycin D to netropsin, is easily seen, when comparing the figures to the left of Figure 3.3 to the figure to the right.

It is shown that there is a clear correspondence between the measured intensity and the level of AT/GC content in the molecule, although the difference in exposure over the field of view of the microscope makes it impossible to directly translate a measured intensity profile to an AT/GC content of a molecule. However the intensity variation caused by non-uniform illumination can always be normalised by analysis of how the background levels vary. This normalization was not necessary for the relatively short molecules used in these experiments as the region of interest was small enough for the background to be constant within the region. Hence, if part of the molecule is known, the AT/GC level of the rest of the molecule can also be measured.

3.3.1 Validity of fit

To ensure that the fit to the theoretical barcode is not just a fit based on random noise in the system, but a fit to the underlying DNA sequence, the experimental profile is also aligned to 500 randomly generated barcodes, giving 500 consensus barcodes, using the same procedure as the alignments to the true theoretical barcode. In order to measure the goodness of fit, an estimator that is the standard deviation between the average experimental barcode and the theoretical barcode is defined.

$$\sigma_j = \sqrt{\left\langle \left(\Delta P_j - \langle \Delta P_j \rangle\right)^2 \right\rangle}$$

ΔP being the difference between the consensus barcode, and its corresponding, randomly generated, theoretical barcode.

In the case of T4GT7 DNA stained with actinomycin D, estimator values for all 500 random barcodes are histogramed and are seen to follow a near perfect Gaussian distribution with a mean of 0.742 and standard deviation of 0.086 as seen in Figure 3.4. It is observed that the estimator value found when

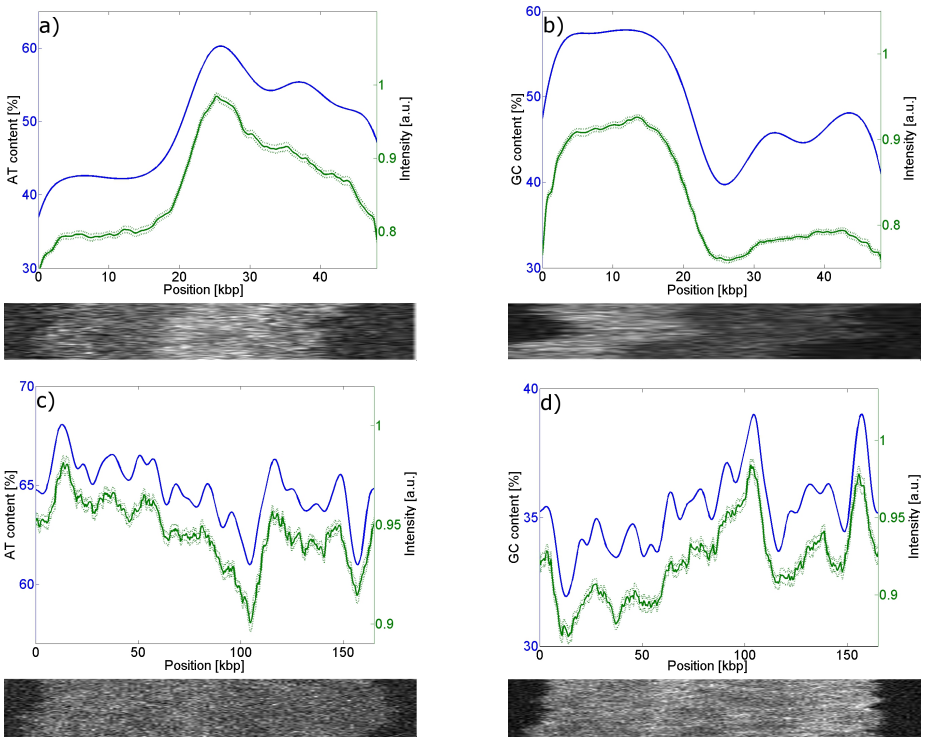

Figure 3.3: Theoretical and experimental barcodes for the DNA sequences used in the experiments. Sub-figure a) is λ-DNA counter stained with actinomycin D, b) is λ-DNA counter stained with netropsin, c) is T4GT7-DNA counter stained with actinomycin D, and d) is T4GT7-DNA counter stained with netropsin. In all cases, the blue line uses the y-axis on the left, and corresponds to the theoretical barcode, while the green line uses the y-axis on the right, and corresponds to the average experimental barcode. The dotted green lines indicate the standard deviation of the average barcode. Below each barcode is seen a recording of a single molecule, measured for that specific experiment. At least 30 molecules were used in order to get the average experimental barcode and the corresponding confidence limits.

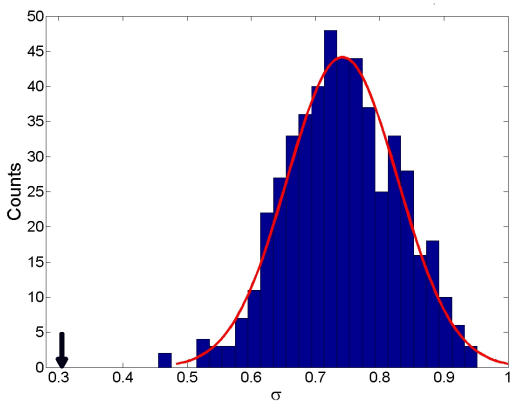

Figure 3.4: Distribution of estimator values σ obtained by comparing experimental barcode for T4GT7 counter stained with actinomycn D against random barcodes. The dark arrow indicates the estimator value obtained from the fit against a theoretical barcode determined from the known sequence. This estimator value is sufficiently low that we would not expect it to occur by chance.

aligning the experimental barcodes to the real theoretical barcode is far away from the centre of this distribution. Obtaining such a small value by chance has a probability of 1.9×10^{-7}. However, even though there is a clear correspondence between the data and the theory in Figure 3.3, some deviations are observed. Peaks between 30- and 50 kbp are not present in the data at in Figure 3.3b). These deviations can most probably be explained by shortcomings of the simple theoretical model applied here. As previously described by Nyberg et al.[NPB+12], the large peaks in the intensity map are easily seen when comparing the experimental data with the theoretical curve, but the small features are blurred out due to thermal fluctuation and diffusion.

3.4 Conclusion

In conclusion a demonstration of a proof of concept that direct barcoding using counterstaining against YOYO-1 with either GC or AT selective ligands can facilitate fast identification of specific DNA samples has been shown. Furthermore it has been demonstrated that this barcoding can be performed via disposable injection moulded devices, a feature which may facilitate future adoption of this technology. The possibility of mapping chemistries that can probe either GC or AT content is highly advantageous, as it allows selection of the mapping chemistry that gives the highest signal contrast possible for a given sequence region. For example, if a sequence loci under investigation is known to have a large GC concentration, it would be beneficial to use netropsin, since this will still leave the GC sites mostly free and YOYO-1 will bind to the residual regions of high AT concentration. The same is true for sequences having a large AT content, where it would be beneficial to use actinomycin D. Along with the use of cheap, disposable polymer chips, this counterstaining technique has potential of redu-

cing the cost of performing genetic barcoding, as–with the single exception of YOYO-1–it does not require any expensive fluorescent probes or reagents.

Chapter 4

Melting Mapping

Melting mapping refers to the process of obtaining a fluorescent profile along a DNA molecule by means of denaturation and renaturation. The areas that are denaturated during the process will loose their fluorescent molecule, which non-fluorescent areas along the molecule. This can be observed in an optical setup as a fluorescent profile. This fluorescent profile can finally be mapped to a theoretically obtained reference profile.

The nanoslits fabricated in Chapter 2 have been used for the experiments performed in this chapter. Here, human chromosomal DNA with a length of several mega base pairs is stained with the fluorophore YOYO-1.

As it was seen in Figure 1.4b) and c), AT and GC base pairs do not contain the same number of hydrogen bonds. Consequently, it takes less energy to break an AT basepair apart than a GT basepair. This results in regions containing a high degree of AT base pairs going from being double stranded to single stranded at a lower energy than regions containing a high degree of GC base pairs. YOYO-1 does not bind to single stranded DNA, and will diffuse away from denaturated regions. A fluorescent profile, known as a barcode, is created along the molecule this way.

A barcode can be revealed by stretching the DNA out in nanoslits, and the acquired data can be mapped against a reference genome. By using a flow for stretching out the molecules, they can be stretched out to almost 100% of their contour length. This gives optimal resolution with the microscopic setup available.

Since the nanoslit device presented in this thesis is intended as a replacement for the silica devices used by Marie *et al*[MPB$^+$13], it has to perform equally well as this device. This means that the chip has to support three main features during the experiments:

- Denaturation-Renaturation: The chip has to withstand the chemicals and temperatures required in order to digest the histones and perform the denaturation-renaturation process.

- Stretching of DNA: The chip should be of a quality so good, that DNA can be stretched uniformly from one end of the slit to the other for a period of time so long, that data can be acquired.

- Data Acquisition: The optical properties of the chip have to be good enough for acquiring high quality data during experiments.

These three features leads to a check list that has to be fulfilled for a device used for these experiments.

For the denaturation-renaturation, the chip has to go through the following processes without breaking:

- Digestion of histiones: The histones of the DNA are digested during an enzymatic reaction at an elevated temperature for a prolonged time.

- Denaturation and renaturation: To obtain the barcodes of the DNA, the sample is heated up to almost 90 °C and cooled down rapidly.

Both of these processes require that the nanoslit device is resistant to the chemicals used in the buffer at elevated temperatures, and that the structure of the chip can handle the required temperature ramps, both slow and fast.

For the stretching of the DNA, the chip has to fulfil the following requirements:

- DNA should be stretched in the nanoslit in a straight line so a direct correlation between horizontal location in the chip and position on the molecule is obtained.

- DNA has to be stable in the nanoslit and not drift during experiments.

- The fluorescent barcode created by the melting process should be stable throughout the experiment.

- The DNA should not break during data acquisition.

Finally there are certain requirements to the optical properties of the device; during data acquisition, the following has to be considered:

- The background signal has to be uniform over the FoV.

- Data has to be good enough for stitching together neighbouring field of views.

- Data has to be good enough for stitching together data from molecules that are longer than the length of the slit, that is molecules which require several data acquisitions before the entire profile is recorded.

4.1 DNA preparation

Before the start of the experiments, the DNA has to be prepared. The DNA used in these experiments was supplied from the University of Copenhagen[1] in 100 µl 0.6% agarose gels.

[1] Sample was provided from Joanna Lopacinska-Jørgensen, KU-Sund

4.1.1 Staining of DNA

When the DNA is delivered in the agarose gels, it is still unstained and inside the cell nuclei. Prior to experiments, the agarose gel has to be digested, the nuclei degraded, and the DNA stained.

The agarose gel is melted by heating the gel to a temperature of 67 °C for 10 min. The solution is cooled down to 42 °C over a period of 2 min and 2 µl of β-agarase (1000 U/ml) (New England Biolabs) is added. The sample is incubated at 42 °C for 3 h. These steps ensure that the agarose has been digested, thereby releasing the nuclei. Digestion of the agarose also prevents the gel from blocking the microchannels during experiments.

500 µl 0.5× TBE (Sigma-Aldrich, MO, USA) is added to the solution and the DNA stock incubates for an additional 16 h at 42 °C. Doing this disintegrates the nuclei, thereby releasing the DNA to the buffer.

DNA is stained in a 0.1 µM YOYO-1(Invitrogen, CA, USA) solution. The solution incubates for 1 h at room temperature, followed by 1 h at 50 °C. After staining, the sample is ready for use. It is kept at 5 °C until experiments are performed.

4.1.2 Denaturation temperature

In order to extract information from the DNA, it is important to denaturate the sample at the right temperature. If the temperature is to low, no DNA will denaturate and no fluorophore will leave the molecule; all that is seen in the microscope is a homogeneously stained DNA strand. If the DNA is denaturated at a temperature that is to high, all the DNA will denaturate and no fluorophore will remain in the molecule; no signal will be left to record.

The denaturation temperature of the DNA depends on a series of factors: an increase in the salinity of the buffer increases the denaturation temperature[FFB$^+$10, KP05], long strands of DNA have a higher denaturation temperature than short strands[KP05], high AT concentration in the DNA strand lowers the denaturation temperature[BFBM86], an increase in the concentration of the fluorophore used increases the denaturation temperature[BF02].

The concentration of DNA in the sample used has not been measured prior to the experiments. Because of this the YOYO-1 to DNA ratio obtained during the staining process is also unknown. Since the denaturation temperature depends strongly on this ratio, this temperature can not be calculated; it has to be found experimentally.

To find the optimal denaturation temperature for the experiments, stained DNA solution in buffer is melted in PCR tubes.

A simplified sketch of the denaturation-renaturation is seen in Figure 4.1.

In order to perform the denaturation-renaturation, a buffer consisting of 0.5% (v/v) triton X-100 (Sigma-Aldrich), 3% (v/v) BME (Sigma-Aldrich), 1% (v/v) 10 mg/ml bovine serum albumin(BSA) (New England Biolabs) , and 2% proteinase K 20 mg/ml (Invitrogen) in 0.5× TBE is mixed.

10 µl DNA solution is mixed in 90 µl of the buffer, and is placed in a regular PCR machine. This situation corresponds to a state of the DNA seen in Figure 4.1a). A temperature cycle is run, heating the sample up to 55 °C for 1 h, allowing the proteinase K to digest the histones, as seen in Figure 4.1b).

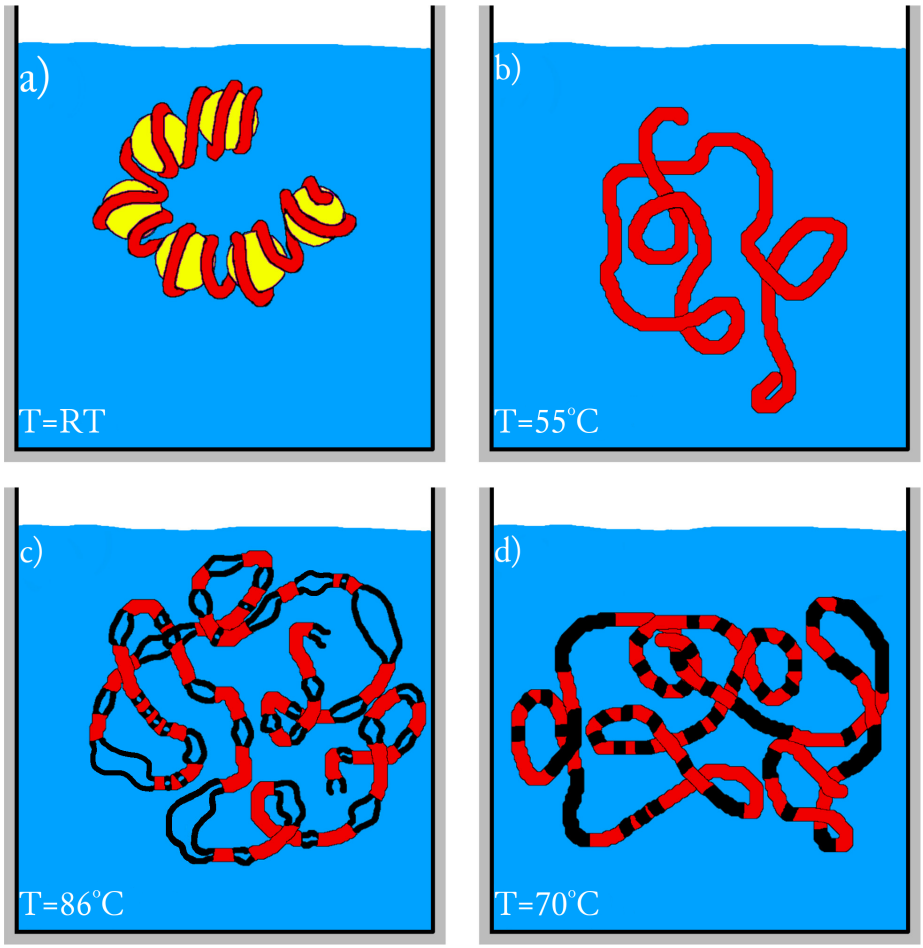

Figure 4.1: Steps involved in melting of the DNA molecules. a) Initially, the DNA is coiled up around histones in the buffer suspension at room temperature. b) The sample is heated up to T=55 °C where the proteinase K digest the histones, thereby releasing the DNA for stretching in the nanoslit. c) Heating the DNA up to a temperature of 86 °C for 10 min denaturates the AT rich parts of the DNA and the YOYO-1 flourophore is released, leaving these areas dark. d) Cooling the sample down to 70 °C for one minute, followed by putting the sample on ice, renaturates the DNA, ensuring homogeneous mechanical properties along the molecule.

This is followed by a temperature ramping of 0.1 °C/s up to the denaturation temperature, which is held for 10 min, corresponding to Figure 4.1c).

Denaturation temperatures of 81 °C, 83 °C, 86 °C, and 89 °C are tried. After the denaturation, the sample is renaturated by cooling it down to 70 °C for 1 min and then putting it on ice in order to avoid any thermal degradation of the sample. This corresponds to the state seen in Figure 4.1d).

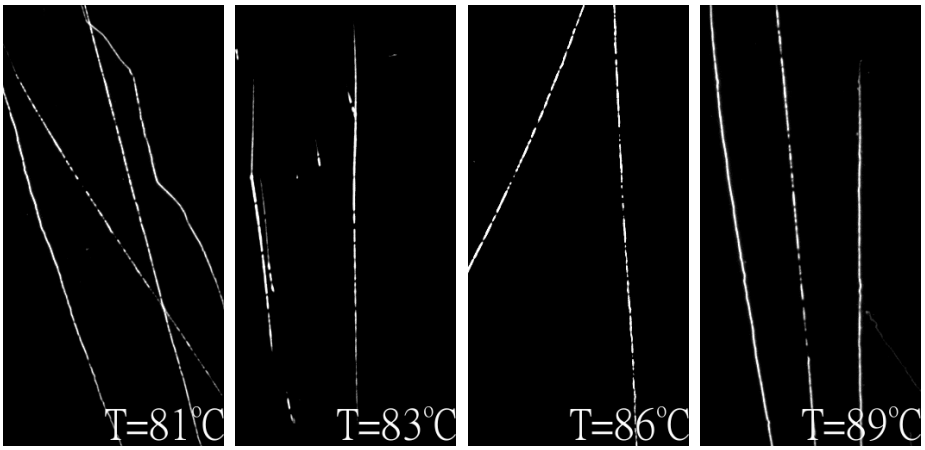

Figure 4.2: DNA stretched out on positively charged microscope slides. From top left to right, Denaturation was performed at 81 °C,83 °C,86 °C, and 89 °C Because of the difference in AT to GC content along the DNA molecule, the denaturation temperature differs amongst the human chromosome.

After every temperature, 5 µl DNA solution is stretched out on a positively charged glass slide, and images are acquired as seen in Figure 4.2.

From these experiments it is decided to use 86 °C as the denaturation temperature because of the contrast along the DNA.

4.2 Experimental preparations

Before conducting experiments on the polymer chip, the autofluorescence of the device is quenched as a consequence of the results obtained in Section 2.6. The polymer chip is fastened to a custom made chuck as seen in Figure 4.3 and positioned on the stage of the microscope used during the experiments. Here it is exposed to high intensity of light with a wavelength of $478 - 495$ nm, the same wavelength used for exciting the fluorescent dye.

Along with lowering the general background signal, this procedure also helps acquiring a constant background signal over the entire nanoslit throughout the experiments.

To ease the filling of the microchannels and reduce the degree of photonicking, 0.5× TBE is degassed in an ultrasonic bath for 1 h just prior to the experiments and three buffers are prepared.

Buffer 1: 0.5× (v/v) triton X-100, 3% (v/v) BME and 1% (v/v) 10 mg/ml BSA in 0.5× degassed TBE.

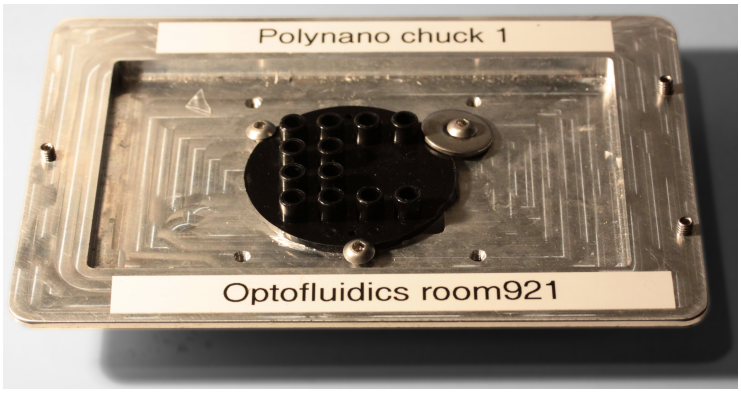

Figure 4.3: A microfluidic chip positioned on the custom made chuck. The chuck fits onto the microscope stage, making it possible to acquire data from the experiments.

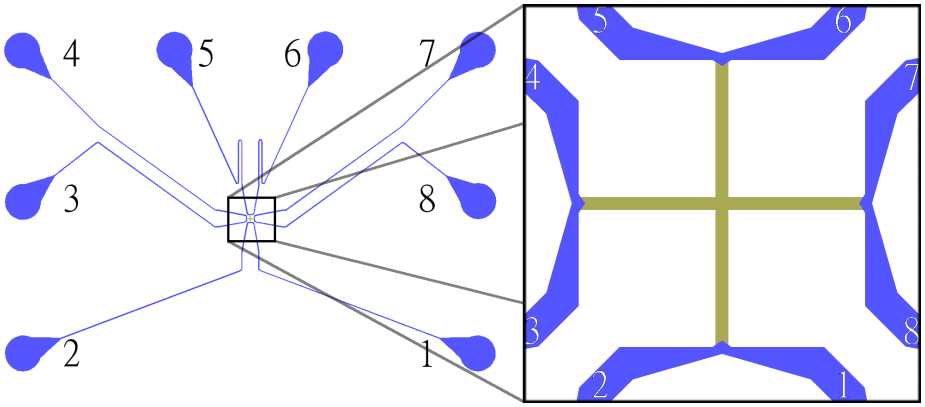

Figure 4.4: The chip layout used in the experiments descriped in this chapter. The numbers refer to the inlets, also referred to in the text.

Buffer 2: 2.5% (v/v) triton X-100 in Buffer 1.

Buffer 3: 2% (v/v) proteinase K (20 mg/ml) in Buffer 1

The chip is wetted in a solution consisting of 7% (v/v) ethanol in the degassed 0.5× TBE. This solution is exchanged with Buffer 2. The chip is left for incubation at room temperature for 10 min in order for the triton X-100 and the BSA to inhibit the surface of the microchannels. This avoids the sticking of the DNA to the walls of the channel by unspecific binding.

After incubation, Buffer 2 is flushed out using Buffer 1. 3 µl DNA solution is placed in inlet 3 and 8 (for inlet numbering, see Figure 4.4) along with 30 µl of Buffer 3. The remaining inlets are filled with 30 µl of Buffer 1, and the chip is unmounted from the chuck.

Inlet 3 and 8 are used for the DNA sample due to symmetry reasons in the design of the device.

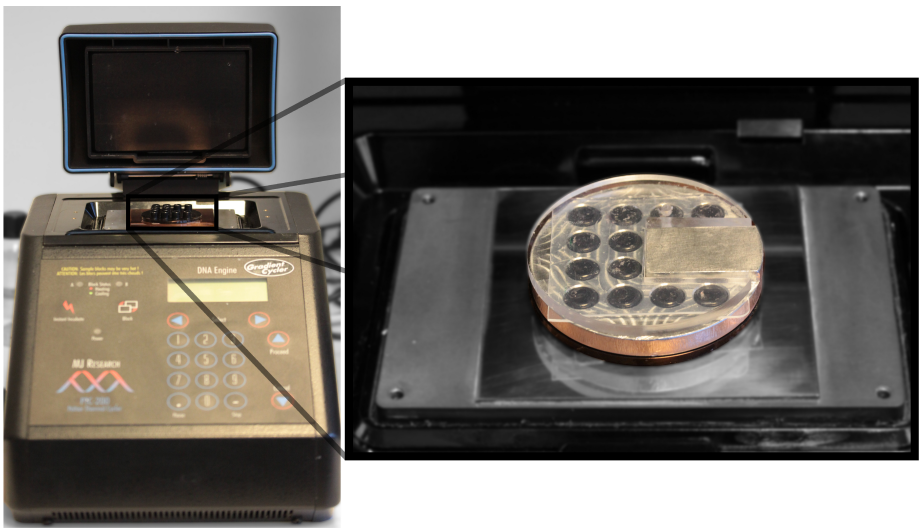

Figure 4.5: Left: The flatbed PCR machine used for the thermal cycling during digestion of the histones at 55 °C and the melting of the DNA at 83 °C. Right: The chip inside the PCR machine. An aluminium heat bridge is positioned on top of the chip. The Luer ports are sealed off using PCR take, and a PMMA device is used for holding it together.

4.3 Denaturation-Renaturation

In order for the chip to work as a replacement for the expensive silica chip, it has to be intact after a heat cycle, where the DNA is denaturated and renaturated. The elevated temperature will increase any chemical reactions taking place, and a thermal gradient in the chip can potentially produce enough stress in the substrate to break the chip or the polymer foil.

Prior to the denaturation-renaturation, a custom made heat conducting device, fabricated in aluminium, is positioned on top of the polymer chip. The inlets are sealed off using a PCR-foil (Microseal 'A' Film, Bio Rad), and a custom made PMMA device is fitted over the heat conductor. This gives a good sealing of the Luer ports, ensuring that buffer does not evaporate out of the system during denaturation.

The chip is positioned in a flatbed PCR-machine as seen in Figure 4.5. The lid is closed tightly, and a heat cycle, identical to the one described in Section 4.1.2 is performed with a denaturation temperature of 86 °C. During the heat cycle, the temperature of the lid is kept 5 °C warmer than the set point of the PCR-machine in order to avoid condensation of the sample on the PCR-foil.

During initial experiments, the chip was heated up through the aluminium heat conductor alone. A heating cartridge and a type K thermocouple can be fitted into this device, and a heat cycle can be controlled via a computer.

Heating the chip this way turned out not to work; the heat gradient throughout the polymer device caused an inhomogeneous thermal expansion of the device. This lead to a stress in the polymer foil that made it break.

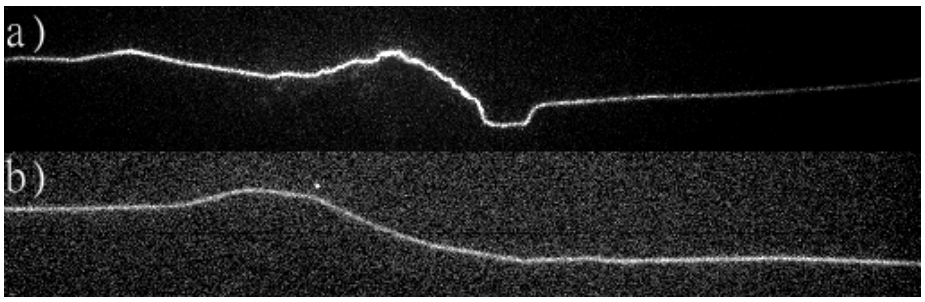

Figure 4.6: a) Because of the inhomogeneity in the height of the nanoslit and the flow behaviour at the centre of the nanoslit, the DNA can bend in unfavourable ways, making it impossible to map the region of the molecule with the reference genome. b) This problem can be solved by optimising the flow from the side channels.

By heating the device from both top and bottom at the same time ensured that the thermal expansion of the polymer foil happened at the same rate as the rest of the chip. This made avoided foil-breakage during denaturation-renaturation.

4.4 Stretching out DNA

Once fastened to the microscope stage, a fluigent pressure controller is attached to the Luer ports of the chip, with the channels corresponding to the ones shown in Figure 4.4. DNA is pushed down through the microchannel to the intersection with the nanoslit by applying a pressure of $10 - 20\,\text{mbar}$ to port 3.

The pressure is changed to gain a net flow into the nanoslit by applying a pressure of $300 - 500\,\text{mbar}$ from port 3 and 4. If for some reason, the DNA from port 3 is not functional, the sample from port 8 is used.

When a strand of DNA is inside the nanoslit, the pressure is changed to stretch out the DNA. This is done by applying 50 mbar of pressure from port 1-2 and 5-6. This creates a flow going from the centre of the cross towards each of the two ends of the DNA molecule.

In order to acquire good data from the nanoslit chips, the DNA has to be stretched out in the nanoslit from one end to the other. For this to happen, the DNA has to have a length exceeding the $450\,\mu\text{m}$ of the nanoslit. Good data also requires that the DNA is stretched out in a straight line in the nanoslit, and that it does not drift from one end to the other. Finally, data acquisition of the molecule can only take place, if the molecule does not break during the experiment.

4.4.1 Straight DNA in the nanoslit

When introducing the DNA into the nanoslit, it has to pass the centre of the cross seen in Figure 4.4. Because of the geometry in this point, the flow behaviour is not easily predicted. This is further complicated by the change in channel height caused by the increased distance to support structures from this location as explained in Section 2.4.1.

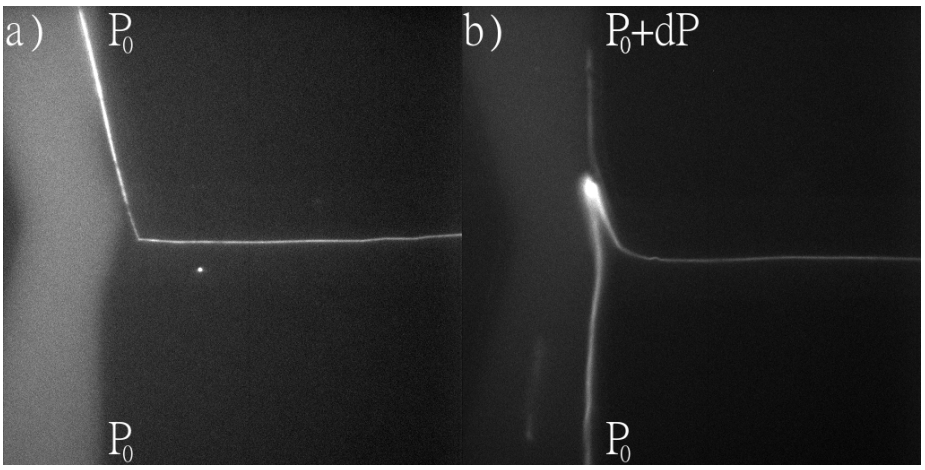

Figure 4.7: A parasitic flow in the carrier channels can pull the DNA in the nanoslit towards that specific carrier channel, as seen in Figure a). This is easilly accounted for by applying a small pressure on the Luer port towards which the DNA is drifting as seen in Figure b).

The effect of the change in flow dynamics at this point is seen in the stretching of the molecule, which is not always straight in the cross as seen in Figure 4.6a). When the DNA is not straight, it is not possible to correlate horizontal location in the nanoslit with a position on the molecule. The algorithm finding the barcode of the molecule only gives a single intensity value for each column of pixels in the acquired images; it does not take the extra length of the DNA that comes from the twisting of the molecule into account. Bending of the DNA will make the region of the molecule seem shorter on the barcode than it should be, and if this effect is strong enough, it is not possible to map the section of the molecule to the reference genome.

It is possible to minimize the bending of the molecule at the centre of the nanoslit by optimizing the flow from the side channels, as seen in Figure 4.6b).

4.4.2 Drifting of DNA

The functionality of the design of the nanoslit relies on the symmetry of the two arms of the nanoslit that the DNA occupies. If these two arms are not exactly equal in length and height, there will be a higher fluidic resistance towards one end than the other. This will create an instability in the location of the molecule, which will experience a drag that is higher towards one of the two arms.

Since optical alignment is necessary in the fabrication process of the master silicon wafer, small alignment errors will occur in the production cycle, which will often lead to the DNA drifting in one direction.

Drifting can also originate from a parasitic flow in the microchannels. If a large fraction of the DNA molecule is in the microchannel and a small flow is present here, this flow will pull on the end of the DNA. This pulling will drag the DNA in the nanoslit towards that particular microchannel.

This effect is seen in Figure 4.7a). Drifting due to a parasitic flow is easily accounted for when using a Fluigent pressure controller, where the pressure of

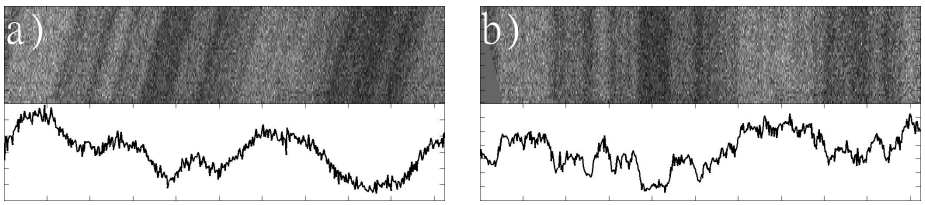

Figure 4.8: Timelapse from a single field of view, along with the corresponding intensity average. In Figure a), drifting of the molecule is unaccounted for. This smears out the average fluorescent intensity at a given location, lowering the quality of the data. In Figure b), least sum of squares has been used to compensate for the drifting. Here it is seen, that the contrast in the average fluorescent intensity is a lot higher, thereby containing more information.

the channel, towards which the DNA is floating, can be increased slightly, as seen in Figure 4.7b).

During post processing, a fluorescent barcode is used which is an average based on 30-50 frames. If any drifting is not accounted for in the experiment, such an average barcode will loose much of its contrast due to the drifting, as seen in Figure 4.8a).

To compensate for such drifting, a small script is implemented prior to finding the barcode of the molecule. By making a simple least sum of squares between the individual images in the time lapse, the drifting can be corrected for. The effect of this is seen in Figure 4.8b), where it is noticed that the contrast of the resulting barcode is much higher, thereby containing more information, than the barcode in Figure 4.8a).

The script correcting for drifting of the molecule was used as a standard script on all the molecules investigated during data analysis.

More generic alignment algorithms can be implemented, which can also take thermal fluctuations of the molecule into account[NNF$^+$13]. However, this was not necessary in these experiments.

Drifting was not reported in the silica devices used by Marie *et al*[MPB$^+$13], which can indicate that the drifting of the molecules occur as an effect of the transition from silica to polymer. However, drifting of the molecule can be compensated for by a change as small as 1 mbar in the pressure on one of the Luer ports. This indicates a good possibility that the drifting of the molecule is an effect originating from the Fluigent pressure controller, rather than from the device itself. The work performed by Marie *et al* used a system, where only one pressure source was available, and where the pressure on the different inlets could not be regulated individually; an identical pressure was guaranteed between matching inlets. With the Fluigent pressure controller, containing eight individually controlled pressure ports, the chance of having a small difference between the applied pressure from two different ports in the order of 1 mbar not unlikely.

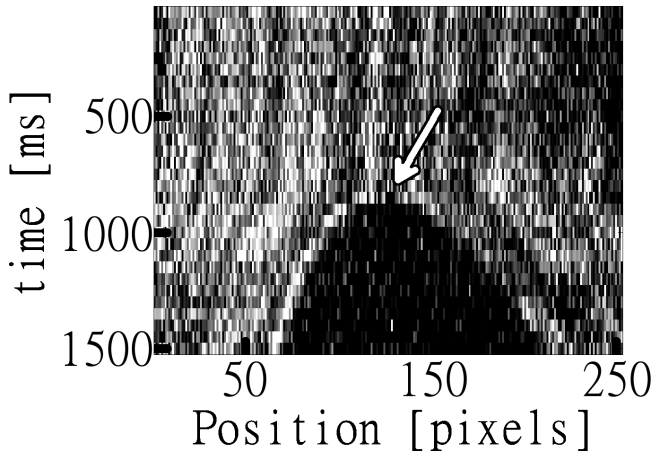

Figure 4.9: Time trace of a molecule experiencing photonicking. After around 800 ms, the molecule breaks, and the two ends move towards each their end of the nanoslit.

4.4.3 Photonicking

When performing autofluorescent measurements of single molecules, he molecule can break as an effect of the energy of the light used to excite the fluorophore, an effect known as photonicking[GFGL02]. The BME is added to the experimental buffer in order to minimise this effect, but it is not able to stop it completely.

An example of a molecule breaking due to photonicking is seen in Figure 4.9. Here, a time-trace of the molecule is shown. After the breaking of the molecule, the two opposing shear forces makes the two DNA fragments drift towards each their end of the nanoslit.

For the majority of molecules investigated in this project, photonicking did not occur during data acquisition. The effect was only seen when the total exposure time for a specific location exceeded 5 sec, and the intensity from the fluorescent lamp was at its maximum.

4.4.4 Diffusion of YOYO-1

During the experiments it was observed that signals were stronger and had a higher contrast in the barcode at the beginning of the experiment. After having measured on molecules for several hours, the contrast of the fluorescent profile would decline, and the intensity would become more homogeneous across the FoV.

Similar effects have been observed by other people in the lab, who have experienced that barcodes would disappear if melted DNA was stored overnight in the fridge.

The loss of contrast can be due to several factors. The YOYO-1 can diffuse along the DNA strand, which is also the reason why the entire chip is put on ice right after the renaturation procedure. The diffusion rate of YOYO-1 will increase at an elevated temperature, but it will still take place during experiments performed at room temperature.

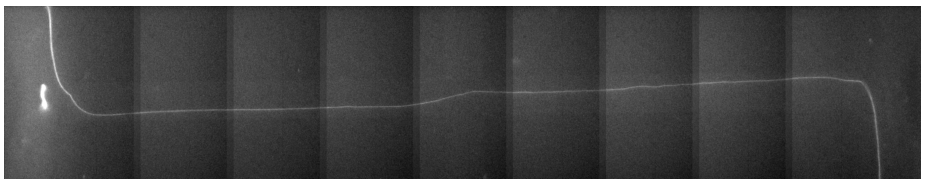

Figure 4.10: DNA from the Jurkat cell line. The DNA has been stained homogeneously and the histones have been digested by the Proteinase K, but no melting of the molecule has been performed.

The YOYO-1 released during the denaturation process has a strong binding affinity towards the double stranded DNA. Given enough time, the free YOYO-1 will re-integrate itself into the vacant positions of the DNA. The majority of the vacant positions are in the dark areas, and so, most of the YOYO-1 molecules will bind to the DNA here. This makes the dark areas brighter, decreasing the contrast of the barcode.

The other potential reason for the decrease in the signal is photobleaching of the fluorophore. This effect has been observed previously[RPA12, KAT01]. Although other sources have shown that this effect is minimal over a 30 min time period[TBBB94], especially when BME is added to the buffer[Ha01] this does not necessarily imply that the effect is not large enough to cause a significant drop in intensity when experiments are run over several hours.

Altogether, the lower contrast of the fluorescent profile along the DNA can indicate, that the experiments should not take too long. Once the experiment is initiated, the best results are obtained within the first few hours.

4.4.5 Fragmentation of Old DNA

DNA from the Jurkat cell line was initially supposed to be used for the experiments described in this chapter. This sample has been stored unstained in a fridge at the department since 2011.

Initial experiments using this DNA sample showed that the staining procedure worked well, and so did the digestion of the histones. This allowed for the release of releasing DNA and for the stretching of homogeneously stained DNA all across the nanoslit, as seen in Figure 4.10.

It was also possible to perform experiments in order to find the optimal denaturation temperature as described in Section 4.1.2, see Figure 4.11.

In spite of the initial tests working fine, no sufficiently long strands of DNA were found when these chromosomes were melted in the nanoslit chip. This had the consequence that it was not possible to stretch a piece of DNA over the entire length of the slit.

The lack of long strands of DNA is most likely an effect of a slight degradation of the sugar backbone of the DNA. In order for a DNA strand to fragment, a defect has to be present in both DNA strands, across from each other. If only a single defect is present, the complementary strand will hold the entire double stranded DNA together and in one piece as seen in Figure 4.12a).

During the denaturation process, large sections of the DNA starts being two single stranded molecules rather than one double stranded. If a defect is present on both of the two single stranded pieces of DNA, the molecule will no longer

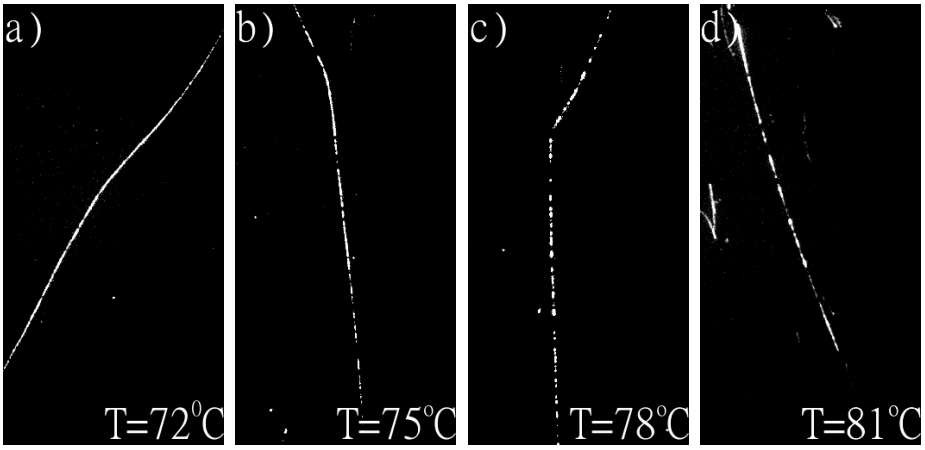

Figure 4.11: Optimization of the denaturation temperature for the Jurkat DNA. The DNA in Figure a) is denaturated at 72 °C, b) at 75 °C, c) at 78 °C, and d) at 81 °C

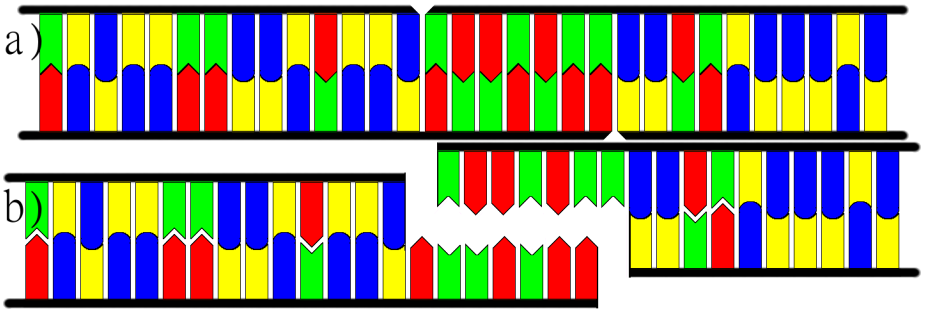

Figure 4.12: When DNA is stored for a long time, the backbone might break at descrete positions along the molecule. As long as the DNA is not denaturated, such defects in the backbone does not have any effect on the DNA, since it is held together by the other backbone through the basepairs, as seen in Figure a). If the sample is denaturated, several defects in the backbone can appear across from each other, fragmenting the molecule into smaller peices.

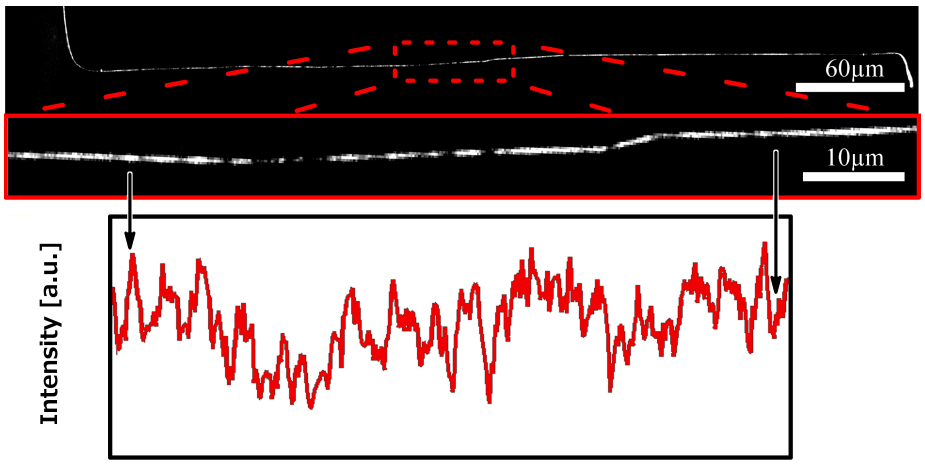

Figure 4.13: DNA containing a barcode and stretched from one end of the nanoslit to the other.

be bound together and will fragment into two smaller DNA strands. Cooling down and renaturating the single stranded DNA into double stranded will not reverse this effect, as sketched in Figure 4.12b).

Because of this, DNA that has a long shelf-time and as such is more likely to have defects in the sugar backbone, will have a higher tendency of breaking apart during the denaturation process.

4.5 Data Acquisition

Data acquired during the experiments has to be of a quality good enough for mapping against a reference genome. In order for this to be possible, the contrast of the fluorescent profile has to be as high as possible.

With the DNA stretched out in the nanoslit, a script is run in the camera acquisition software MetaMorph, acquiring 30-50 images with a shutter speed of 50 ms from 9 different FoVs. From the acquired images, the DNA is located and an the intensity along the molecule is found.

A strand of DNA stretched out from one end of the nanoslit to the other is seen in Figure 4.13, where the intensity profile for part of the molecule is also shown.

Data acquisition is performed using a Nikon Eclipse microscope as seen in Figure 4.14. This setup consists of a 60× NA=1.4 objective. Furthermore, the microscope has the ability for a further 1.5× magnification, resulting in 90× magnification.

Using this setup, the diffraction limit can be found by the Abbe equation:

$$d = \frac{\lambda}{2 \cdot \mathrm{NA}} \tag{4.1}$$

Since the emission wavelength of YOYO-1 is $\lambda = 509\,\mathrm{nm}$, the diffraction limit is $d = 182\,\mathrm{nm}$, slightly larger than the width of a recorded pixel (172 nm) of the EMCCD camera. With a single basepair having a length of 0.34 nm, the

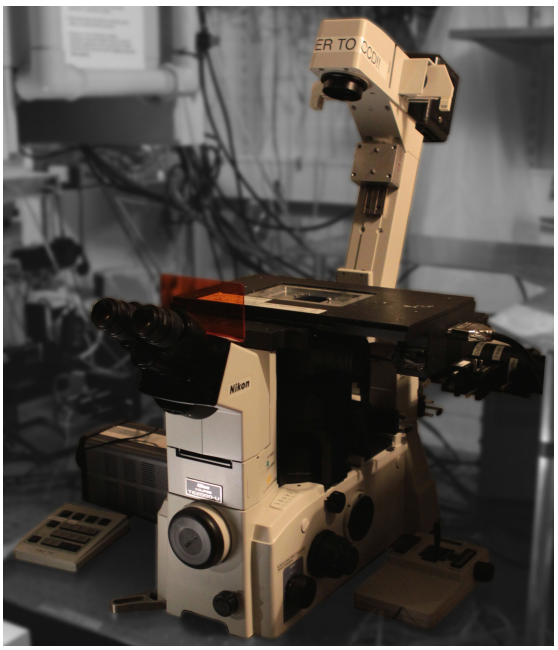

Figure 4.14: The setup used for the experiments. The setup comprises a Nikon Eclipse microscope mounted with a 60x n=1.4 oil objective, an EMCCD, along with an electronic stage and shutter controller.

maximum resolution using this setup is 535 bp when the DNA is stretched out 100%.

4.5.1 Background Signal

Similar to the case in Section 3.3, the light intensity is not perfectly uniform over the entire FoV. When part of the FoV is exposed to a higher light intensity than others, the signal from the DNA in this part will also appear higher than at other parts, in spite of a potentially lower concentration of the fluorophore in these regions.

Whereas this was not a problem with the relatively short molecules used when performing counterstaining mapping in Chapter3, it is a problem here, as the molecule goes from one end of the FoV to the other.

In order to compensate for the change in illumination across the FoV, the intensity of the DNA molecule is normalised by dividing the measured pixel intensity by the measured background intensity next to it, and multiplying all pixels containing the DNA molecule with an average background signal. This will lead to the following normalisation of the measured barcode intensity:

$$I_{corrected}(n) = \frac{I_{meassured}(n)}{BG_{meassured}(n)} \cdot \langle BG_{measured} \rangle \tag{4.2}$$

The normalisation ensures that the intensity used for analysis is independent on where in the FoV the molecule was recorded.

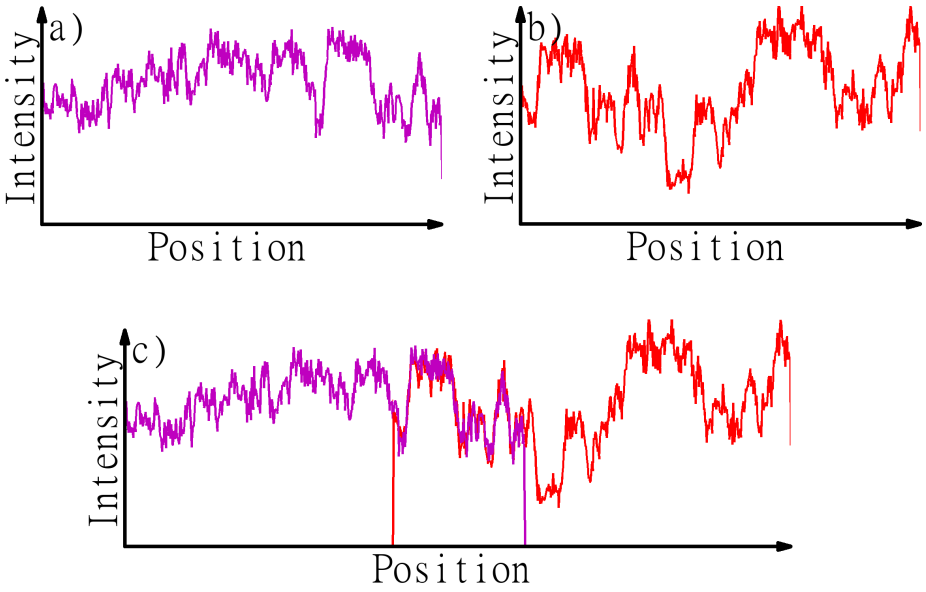

Figure 4.15: The barcode from FoV 1 (a)) and FoV 2 (b)) are combined into one long, barcode, c).

4.5.2 Stitching together Field of Views

A first impression on whether the acquired data is good enough for mapping against the reference genome is found, when data from the different FoVs are stitched together.

Since the nanoslit has a total length of 450 µm, and the width of each FoV is only 90 µm, the measured intensities from the individual FoVs are stitched together, where the overlap region is decided by means of a least sum of squares method as described by Marie *et al*[MPB+13].

An example of data from two neighbouring profiles being stitched together to one, combined profile is seen in Figure 4.15, where the obtained fluorescent profile from one FoV, Figure 4.15a) is matched with the profile from the neighbouring FoV, Figure 4.15b), resulting in one long profile, Figure 4.15c).

4.5.3 Identification of Molecules

By acquiring data and stitching together FoVs as described above, profiles from 49 different molecules were found during 2 days of experiments.

Out of these 49 molecules, 24 had a contrast in their barcode which was expected to be good enough for potential mapping against a reference genome.[2].

That efforts were not taken in order to try to map the remaining molecules was caused by a lack in the contrast in their barcode. This lack of contrast had several origins: some of the molecules were imaged after several hours of performing experiments, where the potential diffusion of the YOYO-1 molecule could have reduced the contrast significantly, some molecules experienced a level

[2]The mapping of data towards the reference genome was performed by researcher Jonas Nyvold Pedersen

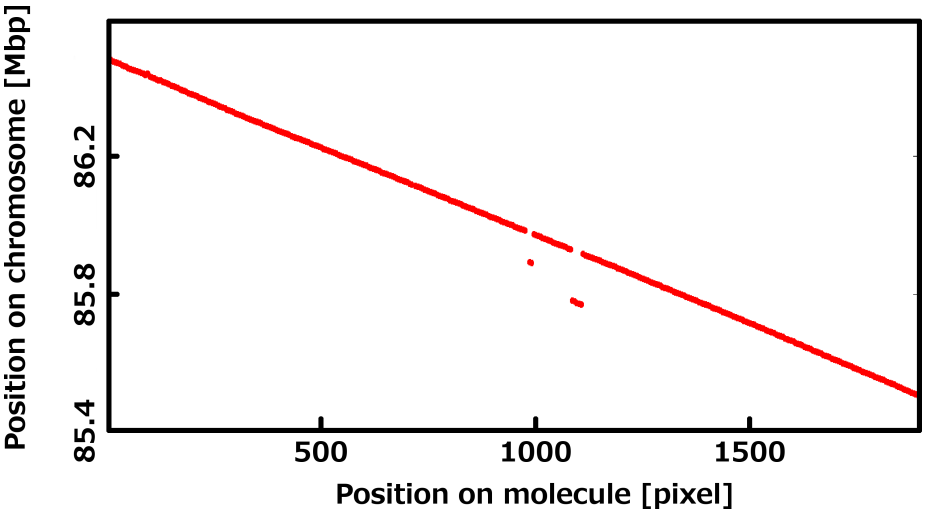

Figure 4.16: Mapping of an obtained fluorescent profile against chromosome 16. A clear correspondance is seen between location on the molecule and location in the genome.

of drifting that the simple script intended for correction of this was not sufficient, some were simply out of focus.

The ratio of AT to GC in the molecules can also change between different positions on different chromosomes, meaning that the optimal denaturation temperature for one chromosome is not the optimal denaturation temperature for others. For a given denaturation temperature, some molecules would appear too bright with a faint pattern, while others would appear too dark with only a few bright spots.

Out of the 24 molecules chosen for further analysis, 20 were successfully mapped, giving a mapping efficiency of 83%.

The reference barcode used during mapping of the obtained profiles was obtained using Bubblyhelix[TLJH03] and the reference genome hg18[Bioa]. 7% of this reference genome consists of black areas where the genetic code is unknown. The level of black regions in the reference genome gives a probability of 9% to this being the only reason why 4 of the molecules could not be identified. This probability is rather large, and it cannot be excluded that it is the only reason why these molecules could not be mapped.

Other reasons why 4 of the molecules could not be identified can be attributed to diffusion of YOYO-1 during the duration of the experiments as discussed in Section 4.4.4. -One of the molecules was recorded more than 4 hours after the first molecule.

Two other molecules that could not be identified were both shorter than the length of the nanoslit; even though drifting of the molecule is accounted for in the data analysis, it only applies to horizontal drifting along the direction of the nanoslit, not vertical drifting perpendicular to the length of the nanoslit.

Shorter molecules tend to be more unstable in the nanoslit, and their position perpendicular to the direction of the nanoslit will also vary during the acquisition of the data. The algorithm that extracts the data from the acquired microscope

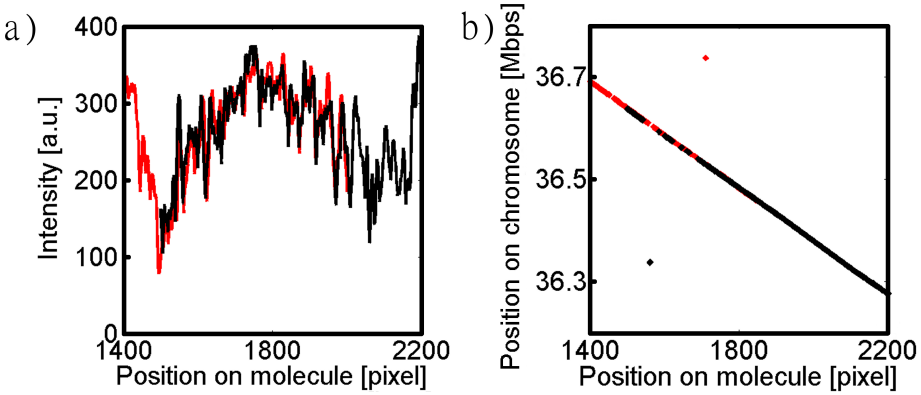

Figure 4.17: When the DNA molecule is much longer than the length of the nanoslit, data can be acquired several times by pushing the molecule through gradually. Figure a) shows an overlay between two acquisitions of the same molecule, and Figure b) shows the overlap in the mapping of the two acquisitions on the reference genome.

images, averages the intensity over 5 pixels. Instability perpendicular to the molecules was seen to make the average signal as wide as 10 pixels for some of the short molecules

For the identified molecules, data is seen to be of a high quality. Figure 4.16 shows the mapping of a molecule to chromosome 16, where a clear correlation between location on the molecule and location on the genome is seen.

4.5.4 Identifying long DNA molecules by stitching together several barcodes

For molecules longer than the nanoslit, it is possible to obtain data at several locations on the molecule. By first obtaining data from one end of the molecule, move the molecule partly through the slit and obtaining a new set of data, these two dataset can be combined into one large data set. As such, the length of the nanoslit is not limiting the amount of information that can be found from a single molecule, similar to what was shown by Marie *et al*[MPB$^+$13].

One of the advantages of analysing DNA this way is, that it is only necessary to localise the chromosome for the first set of data. If it is known that two datasets are from the same molecule, the location of the second dataset will be the same as for the first, and known prior to mapping.

An example of two datasets being combined is seen in Figure4.17. Figure 4.17a) shows the matching intensity profiles from the two reads of the molecule, and Figure4.17b) shows that the overlap is mapped to the same location on the genome both times.

4.5.5 Identification of mutations

As shown by Marie *et al*[MPB$^+$13], large scale mutations in the genome can be identified using melting mapping. Such mutations are seen as jumps in the

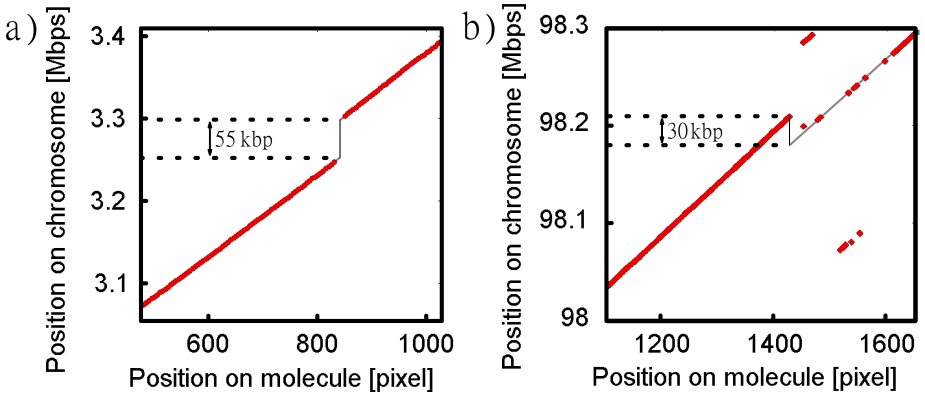

Figure 4.18: a) Identification of a deletion on the short arm of chromosome 11, in the cytogenetic band position 11p15.4. The deletion is identified as the vertical jump up in the mapping location of the molecule. b) Identification of an insertion on the long arm of chromosome 7, in the cytogenetic band position 7q22.1. The insertion is identified as the jump down in the mapping location of the molecule.

mapping data, where neighbouring areas from the molecule can not be mapped to neighbouring areas on the genome.

Two such cases were found within the 20 identified molecules. These two cases corresponds to a deletion on the short arm of chromosome 11 spanning approximately 50 kbp in the cytogenetic band position 11p15.4 (3,250,000-3,300,000), seen in Figure 4.18a) and an insertion on the long arm of chromosome 7, in the cytogenetic band position 7q22.1, seen in Figure 4.18b).

Although the data from these experiments suggest large scale mutations at these two positions, the mutations have to be confirmed by other means in order to verify this finding.

4.6 Conclussion

83% of the molecules were identified on the reference genome, and a statistically plausible level of explanation exists for the lack of mapping of the remaining molecules due to black regions in the reference genome. This shows that the polymer chips are able to produce data with a quality as good as the silica devices previously used by Marie *et al*[MPB+13].

The polymer chip is capable of withstanding the chemicals used during digenstion of the histones, and the denaturation-renaturation of the DNA at elevated temperatures, and the barcoded DNA can be introduced into the nanoslit.

Once the DNA is in the nanoslit, it can be stretched out with only minimal drifting of the molecule. Any remaining drift can either be adjusted for during the experiments, by a change in the pressure on one of the inlets, or after the experiment, by a simple algorithm.

The fluorescent barcode was seen to be stable for a sufficient amount of time, making it possible to obtain the data needed from the molecules. The molecules

were also seen to be mechanically stable, and did not break during experiments, unless they were exposed to a high light intensity for a prolonged period of time.

Finally, the data acquired from different FoVs could be stitched together in order to obtain a single intensity profile. This barcode can be positively matched to a reference genome.

Using this technique, two potential mutations in the DNA used during experiments were identified, although these mutations have to be confirmed by other methods.

When acquiring data from long strands of DNA, it was possible to acquire data from part of the molecule, move the molecule partly through the nanoslit and acquire data once again. These two sets of data could be stitched together, forming a fluorescent profile that was not restricted by the length of the nanoslit.

The data obtained in these experiments have all been found on all polymer devices with a price per device significantly lower than on conventional silica devices. The development of a suitable experimental protocol also used a number of chips that were all disposed after use. Something that was only possible due to the low cost and short production time of the devices.

From the number of molecules being detected using polymer chips, it can be concluded that the quality of the polymer chips is sufficiently high for the required purpose. As such, it has been shown that it is possible to perform high throughput, low noise optical measurements on single molecules with a quality good enough for unique mapping to the human genome. All of this has been done on a platform having a price a fraction of that seen on state of the art silica devices.

With a low cost, mass producible production platform, this technique has the potential for massively aiding next generation sequencing in identifying large scale repetitions, deletions and insertions, that are otherwise difficult to find with the techniques at hand today. This can increase the credibility of the results from NGS platforms, thereby helping to decrease the overall cost of the procedure. This can potentially pave the road towards even cheaper genome sequencing.

Chapter 5

Results, Conclusion, and Outlook

The main objective of this thesis has been to address the current catch 22 situation; academic research in LoC is intensive, but the results obtained through this research are unfortunately not actively being used by scientist outside of the LoC community, and the industry does not want to produce the systems due to a high barrier of entry.

This important issue has been addressed by investigating how devices developed in academia can be produced using an industrially well-known fabrication process: injection moulding.

By considering this production method from the beginning of the development of the systems, state-of-the-art Lab on a Chip devices can be fabricated in large numbers from the beginning. This has the effect, that if a system turns out to be of interest for a broad scientific society, industrial partners can easily adapt the process and commercialise the platform, without having to redesign the entire fabrication process.

During this project, it was shown, that injection moulding was capable of producing devices containing structures and tolerances in the nanometre scale, with a cycle time of $30 - 90$ sec per device. Three different devices were fabricated using this technique: one system containing nanochannels with a depth of 100 nm and width going from 140 nm to 1040 nm, one system containing nanoslits with a width of 20 µm and a depth of 110 nm, one system containing nanopits with a width ranging from 150 nm to 1000 nm and depths of 125 nm at the bottom of 10 µm wide, 110 nm deep nanoslits.

The autofluorescent background signal from these devices were investigated, and a reduction of almost 50% was obtained by the addition of a black masterbatch to the polymer granulate.

The devices containing the most delicate structures, the nanoslit with a width of 20 µm and a height of 100 nm could be bonded with a throughput of 25 devices per hour and a yield of 95%. With this cycle time, the price per device can go as low as DKK 17.00, if enough devices are fabricated.

With an academic setup capable of producing large quantities of high quality devices, these devices could be produced at a price of DKK 17.00, making them truly disposables. This ensures that cross contamination does not become a problem during experiments, as a new chip can be used for each new

experimental run. Several devices can also used for the optimisation of the experimental protocol.

The production techniques used during this project makes it easy for a commercial enterprise to adapt the technology and commercialise the product.

To show that the produced devices were of a high enough quality for fabricating data suitable for scientific explorations, the nanochannels and the nanoslits were used for experimental work.

Two different experiments were performed to test the usability of the devices.

Nanochannels were used in a set of experiments, where short, well known λ-DNA and T4GT7-DNA, were counterstained with a molecule binding specifically to either GC-rich regions or AT-rich regions of the DNA. Doing this created an equilibrium state during the staining of the molecule, where the fluorescent molecule was not distributed homogeneously along the DNA. This inhomogeneity could be identified during acquisition, and a consensus barcode of the DNA molecules could be mapped with statistical significance to a theoretical barcode created from the known DNA sequence.

The nanochannel chips used for these experiments have the advantage of being a passive system, meaning that once the DNA is introduced into the nanochannels, the molecule is stretched out, solely due to the dimensional confinements of the channels. This means that hundreds of nanochannels can be positioned next to each other, and thus, data from several molecules can be obtained during one acquisition.

Another set of experiments were performed using the nanoslit chips and human DNA with a length of several Mbp.

In these experiments, a fluorescent profile is created by staining the DNA homogeneously, followed by a partial denaturation of the molecule. The fluorescent molecule only binds to double stranded DNA. As an effect of the denaturation, the fluorescent molecule will diffuse away from these areas, creating a fluorescent profile along the DNA. Since AT rich regions of the DNA denature before GC rich regions, the denaturated regions can be predicted, and the experimentally obtained profile can be mapped to a theoretically obtained barcode.

Such experiments have been performed before, making it possible to benchmark the injection moulded polymer devices against previously obtained data from expensive silica devices. This benchmarking revealed, that the polymer chips could be used for the experiments and that data, that is equally good as what was found in silica could be acquired.

The two experiments clearly show that the polymer devices used were of a high quality, and that results obtained using the devices are adequate for scientific explorations.

It has been demonstrated that the current catch 22 situation can be solved, since experiments on devices fabricated using an industrially available production platform have successfully been performed.

If the scientists working in the field of LoC start thinking about the design of their devices in such a way that it is easy to produce in large quantities, it will become easier to convince scientists from other areas of expertise to use them. Furthermore it will be much easier for potential industrial partners to start large scale production of the devices, since they do not have to through the trouble of reventing the design.

Altogether this can help push the advantages of LoC to a bigger market, in the favour of both industry and science.

Bibliography

[ACT+02] Mar Alvarez, Ana Calle, Javier Tamayo, Laura M. Lechuga, Antonio Abad, and Angel Montoya. Development of nanomechanical biosensors for detection of the pesticide ddt. *Biosensors and Bioelectronics*, 18:649–653, 2002.

[AHM+10] Kristian Odegaard Andresen, Morten Hansen, Maria Matschuk, Soren Terpager Jepsen, Henrik Schiott Sorensen, Pawel Utko, David Selmeczi, Thomas S. Hansen, Niels B. Larsen, Noemi Rozlosnik, and Rafael Taboryski. Injection molded chips with integrated conducting polymer electrodes for electroporation of cells. *Journal of Micromechanics and Microengineering*, 20(5):055010, MAY 2010 2010.

[ALP+08] Guillaume Assie, Thomas LaFramboise, Petra Platzer, Jérôme Bertherat, Constantine A. Stratakis, and Charis Eng. Snp arrays in heterogeneous tissue: Highly accurate collection of both germline and somatic genetic information from unpaired single tumor samples. *The American Journal of Human Genetics*, 82:903–915, 2008.

[AP03] Donna G. Albertson and Daniel Pinkel. Genomic microarrays in human genetic disease and cancer. *Human molecular genetics*, 12:r145–r152, 2003.

[AvdB03] Helene Andersson and Albert van den Berg. Microfluidic devices for cellomics: a review. *Sensors and Actuators B*, 92:315–325, 2003.

[BD77] F. Brochard and PG Degennes. Dynamics of confined polymer-chains. *Journal of Chemical Physics*, 67(1):52–56, 1977. PT: J; NR: 13; TC: 144; J9: J CHEM PHYS; PG: 5; GA: DN635; UT: WOS:A1977DN63500007.

[BDNS08] Denis Bartolo, Guillaume Degré, Philippe Nghe, and Vincent Studer. Microfluidic stickers. *lab chip*, 8(2):274–278, 2008.

[Bec] Morten Bech. en.cipoc.dk. `http://en.cipoc.dk/the-project/the-objectives-for-cipoc/`. Accessed: 31-01-2014.

[Bec09a] Holger Becker. Chips, money, industry, education and the "killer application". *Lab on a Chip*, 9(12):1659–1660, 2009.

[Bec09b] Holger Becker. It's the economy ... *Lab on a Chip*, 9(19):2759–2762, 2009. PT: J; NR: 6; TC: 15; J9: LAB CHIP; PG: 4; GA: 494GM; UT: WOS:000269799800001.

[BEM82] E.W. Becker, W. Ehrfeld, and D. Münchmeyer. Production of separation-nozzle systems for uranium enrichment by a combination of x-ray lithography and galvanoplastics. *Naturwissenschaften*, 69(11):520–523, 1982.

[BF02] Michael T. Bjorndal and D. Kuchnir Fygenson. Dna melting in the presence of fluorescent intercalating oxazole yellow dyes measured wit a gel-based assay. *biopolymers*, 65:40–44, 2002.

[BFBM86] Kenneth J. Breslauer, Ronald Frank, Helmut Blöcker, and Luis A. Marky. Predicting dna duplex stability from the base sequence. *PNAS*, 83(11):3746–3750, 1986.

[BG08] Holger Becker and Claudia Gärtner. Polymer microfabrication technologies for microfluidic systems. *Analytical and bioanalytical chemistry*, 390:89–111, 2008.

[Bioa] UCSC Genome Bioinformatics. Ncbi build 36.1, mar. 2006 assembly (hg18). `http://genome-euro.ucsc.edu/goldenPath/stats.html#hg18`. Accessed: 13-03-2014.

[Biob] Sophion Biosciences. Qplates. `http://sophion.dk/media/30318/produktspecification_qplate%20measurement%20plate_a4%20171212.pdf`. Accessed: 20-03-2014.

[BL02] Holger Becker and Laurie E. Locascio. Polymer microfluidic devices. *talanta*, 56:267–287, 2002.

[BSBB97] Christoph G. Baumann, Steven B. Smith, Victor A. Bloomfield, and Carlos Bustamante. Ionic effects on the elasticity of single dna molecules. *PNAS*, 94(12):6185–6190, 1997.

[BSC+94] A. Bensimon, A. Simon, A. Chiffaudel, V. Croquette, F. Heslot, and D. Bensimon. Aligment and sensitive detection of dna by a moving interface. *science*, 265(5181):2096–2098, 1994.

[BTS+11] Michael Bache, Rafael Taboryski, Silvan Schmid, Jens Aamand, and Mogens Havsteen Jakobsen. Investigations on antibody binding to a micro-cantilever coated with a bam besticide residue. *Nanoscale Research Letters*, 6:386, 2011.

[CAS+03] Woo-Jin Chang, Demir Akin, Miroslav Sedlak, Michael R. Ladisch, and Rashid Bashir. Poly(dimethylsiloxane) (pdms) and silicon hybrid biochip for bacterial culture. *Biomedical Microdevices*, 5(4):281–290, 2003.

[cDWX13] chuanhua Duan, Wei Wang, and Quan Xie. Review article: Fabrication of nanofluidic devices. *Biomicrofluidics*, 7:026501, 2013.

[CEC+13] Andrew J. Capel, Steve Edmondson, Steven D. R. Christie, Ruth D. Goodridge, Richard J. Bibb, and Matthew Thurstans. Design and additive manufacture for flow chemistry. *Lab on a Chip*, 13:4583–4590, 2013.

[CGH+04] EY Chan, NM Goncalves, RA Haeusler, AJ Hatch, JW Larson, AM Maletta, GR Yantz, ED Carstea, M. Fuchs, GG Wong, SR Gullans, and R. Gilmanshin. Dna mapping using microfluidic stretching and single-molecule detection of fluorescent site-specific tags. *Genome research*, 14(6):1137–1146, JUN 2004.

[CHP+10] Rattikan Chantiwas, Mateusz L. Hupert, Swathi R. Pullagurla, Subramanian Balamurugan, Jesus Tamarit-Lopez, Sunggook Park, Proyag Datta, Jost Goettert, Yoon-Kyoung Choe, and Steven A. Soper. Simple replication methods for producing nanoslits in thermoplatics and the transport dunamics of double-stranded dna through these slits. *Lab Chip*, 10:3255–3264, 2010.

[CKR96] Stephen Y. Chou, Peter R. Krauss, and Preston J. Renstrom. Imprint lithography with 25-nanometer resolution. *science*, 272:85–87, 1996.

[CKZ+97] Stephen Y. Chou, Peter R. Krauss, Wei Zhang, Lingjie Guo, and Lei Zhuang. sub-10 nm imprint lithography and applications. *journal of vacuum science and technology B*, 15(6):2897–2904, 1997.

[Col09] R. Collier. Drug development cost estimates hard to swallow. *Canadian Medical Association Journal*, 180(3):279–280, 2009.

[Con01] International Human Genome Sequencing Consortium. Initial sequencing and analysis of the human genome. *Nature*, 409(6822):860–921, 2001.

[CTAC02] Han Cao, Jonas O. Tegenfeldt, Robert H. Austin, and Stephen Y. Chou. Gradient nanostructures for interfacing microfluidics and nanofluidics. *Applied Physics Letters*, 81(16):3058–3060, 2002.

[CTLB+08] Jenifer Clausell-Tormos, Diana Lieber, Jean-Christophe Baret, Abdeslam El-Harrak, Oliver J. Miller, Lucas Frenz, Joshua Blouwolff, Katherine J. Humphry, Sarah Köster, Honey Duan, Christian Holtze, David A. Weitz, Andrew D. Griffiths, and Christoph A. Merten. Droplet-based microfluidic platforms for the encapsulation and screening of mammalian cells and multicellular organisms. *Chemistry and Biology*, 15:427–437, 2008.

[DAA+10] Somes K. Das, Michael D. Austin, Matthew C. Akana, Paru Deshpande, Han Cao, and Ming Xiao. Single molecule linear analysis of dna in nano-channel labeled with sequence specific fluorescent probes. *Nucleic Acids Research*, 38(18):e177, 2010.

[Dana] DTU Danchip. Prisbog/pricebook. `http://www.portalen.dtu.dk/institutter/dtu_danchip/~/media/DANCHIP/Mette__Media%20folder/Pricebook%20for%20DTU%20Danchip%202013_v1.ashx`. Accessed: 20-03-2014.

[Danb] DTU Danchip. Specific process knowledge/lithography/ebeamlithography. http://labadviser.danchip.dtu.dk/index.php/Specific_Process_Knowledge/Lithography/EBeamLithography#Performance_of_the_e-beam_writer. Accessed: 20-03-2014.

[DHlH10] Michel Delseny, Bin Han, and Yue le Hsing. High throughput dna sequencing: The new sequencing revolution. *Plant Science*, 179:407–422, 2010.

[DMSW98] David C. Duffy, J. Cooper McDonald, Olivier J. A. Schueller, and George M. Whitesides. Rapid prototyping of microfluidic systems in poly(dimethylsiloxane). *analytical chemistry*, 70(23):4974–4984, 1998.

[DSTJJ+10] Rebecca Dylla-Spears, Jacqueline E. Townsend, Linda Jen-Jacobson, Lydia L. Sohn, and Susan J. Muller. Single-molecule sequence detection via microfluidic planar extensional flow at a stagnation point. *Lab Chip*, 10:1543–1549, 2010.

[EHL07] Christopher J. Easley, Joseph A. C. Humphrey, and James P. Landers. Thermal isolation of microchip reaction chambers for rapid non-contact dna amplification. *Journal of micromechanics and microengineering*, 17:1758–1766, 2007.

[EJE95] J. Elders, H.V. Jansen, and M. Elwenspoek. Deemo: A new technology for the fabrication of microstructures. *MEMS '95, Proceedings*, 69(11):238–243, 1995.

[EMMV+12] Shane M. Eaton, Carmela De Marco, Rebeca Martinez-Vazquez, Roberta Ramponi, Stefano Turri, Giulio Cerullo, and Roberto Osellame. Femtosecond laser microstructuring for polymeric lab-on-chips. *Journal of Biophotonics*, 55(8-9):687–702, 2012.

[EV08] Greg Elgar and Tanya Vavouri. tuning in to the signals: noncoding sequence conservation in vertebrate genomes. *Trends in Genetics*, 24(7):344–352, 2008.

[FFB+10] J. Fuchs, J.-B. Fiche, A. Buhot, R. Calemczuk, and T. Livache. Salt concentration effects on equilibrium melting curves from dna microarrays. *Biophysical Journal*, 99:1886–1895, 2010.

[flu] fluidigm. Nanoflex valves. http://www.fluidigm.com/technology.html. Accessed: 20-03-2014.

[FY10] James Friend and Leslie Yeo. Fabrication of microfluidic devices using polydimethylsiloxane. *biomicrofluidics*, 4:026502, 2010.

[Gal05] Robert C. Gallo. The discovery of the first human retrovirus: Htlv-1 and htlv-2. *Retrovirology*, 2:17, 2005.

[GBK+03] Oliver Gross, Bogdan Beirowski, Marie-Louise Koepke, Jeannine Kuck, Michael Reiner, Klaus Addicks, Neil Smyth, Eckhard Schulze-Lohoff, and Manfred Weber. Preemptive ramipril therapy

delays renal failure and reduces renal fibrosis in copl4a3-knockout mice with alport syndrome. *Kidney International*, 63:438–446, 2003.

[Gen] BioNano Genomics. Iryschips. `products/iryschip/`. Accessed: 20-03-2014.

[GFGL02] Lourdes Gude, María-José Fernández, Kathryn B. Grant, and Antonio Lorente. Dna interaction and photonicking properties of dna targeted acridine (2,2'-bipyridine)platinum(ii) complexes. *Bioorganic and medicinal chemistry letters*, 12:3135–3139, 2002.

[Gmba] Topas Advanced Polymers GmbH. Topas coc 5013l-10 data sheet. `http://www.topas.com/sites/default/files/tds_5013l-10_e-2.pdf`. Accessed: 24-03-2014.

[Gmbb] Topas Advanced Polymers GmbH. Topas coc polymers brochure. `http://topas.com/sites/default/files/files/topas_product-brochure_english.pdf`. Accessed: 24-03-2014.

[Gmbc] Topas Advanced Polymers GmbH. Topas optical data sheet. `http://topas.com/sites/default/files/files/optical_e.pdf`. Accessed: 24-03-2014.

[GMS10] Katrin Günther, Michael Mertig, and Ralf Seidel. Mechanical and structural properties of yoyo-1 complexed dna. *Nucleic Acids Research*, 38(19):6526–6532, 2010.

[GPC+13] Joshua W. Griffis, Ekaterina Protozanova, Douglas B. Cameron, Robert, and H. Meltzer. High-throughput genome scanning in constant tension fluidic funnels. *lab chip*, 13:240–251, 2013.

[GR92] Alexander N. Glazer and Hays S. Rye. Stable dye-dna intercalation complexes as reagents for high-sensitivity fluorescence detection. *Nature*, 359:859–861, 1992.

[GTH12] R. D. Goodridge, C. J. Tuck, and R. J. M. Hague. Laser sintering of polyamides and other polymers. *Progress in materials science*, 57:229–267, 2012.

[Guo04] L Jay Guo. Recent progress in nanoimprint technology and its applications. *Journal of Physics D: Applied physics*, 37:r123–r141, 2004.

[Ha01] Taekjip Ha. Single-molecule fluorescence resonance energy transfer. *Methods*, 25:78–85, 2001.

[Hag88] Paul J. Hagerman. Flexibility of dna. *ANNUAL REVIEW OF BIOPHYSICS AND BIOPHYSICAL CHEMISTRY*, 17:265–286, 1988.

[HC52] AD. Hershey and M. Chase. Independent functions of viral protein and nucleic acid in growth of bacteriophage. *journal of general physiology*, 36(1):39–56, 1952.

[HFS+93] D. Ted Harrison, Karl Fluri, Kurt Seiler, Shonghui Fan, Carlo S. Effenhauser, and Andreas Manz. micromachining a miniaturized capillary electrophoresis-based chemical analysis system on a chip. *Science*, 261(5123):895–897, 1993.

[HS03] M. Heckele and W. K. Schomburg. Review on micro molding of thermoplastic polymers. *J. Micromech. Microeng*, 14:r1–r14, 2003.

[HWL09] Xin Hu, Shengnian Wang, and L. James Lee. Single-molecule dna dynamics in tapered contraction-expansion microchannels under electrophoresis. *PHYSICAL REVIEW E*, 79:041911, 2009.

[HY03] K. R. Hawkins and Pal Yager. Nonlinear decrease in background fluorescence in polymer thin-films - a survey of materials and how they can complicate fluorescence detection in µtas. *Lab on a Chip*, 3:248–252, 2003.

[Ing] IDA Ingeniørforeningen. 2013 ida lønstatistik. `https://ida.dk/content/loenstatistik`. Accessed: 18-02-2014.

[JSL+11] Am Jang, Zhiwei Sou, Kang Kug Lee, Chong H Ahn, and Paul L Bishop. State-of-the-art lab chip sensors for environmental water monitoring. *Meas. Sci. Technol.*, 22:032001, 2011.

[KAD+08] Sarah Köster, Francesco E. Angilè, Honey Duan, Jeremy J. Agresti, Anton Wintner, Christian Schmitz, Amy C. Rowat, Christoph A. Merten, Dario Pisignano, Andrew D. Griffiths, and David A. Weitz. Drop-based microfluidic devices for encapsulation of single cells. *Lab Chip*, 8:1110–1115, 2008.

[KaR12] Alexander R. Klotz, Hugo B. Brand ao, and Walter W. Reisner. Diffusion resonance of nanoconfined polymers. *Macromolecules*, 45:2122–2127, 2012.

[KAT01] Claire Kanony, Björn Åkerman, and Aimer Tuite. Photobleaching of asymmetric cyanines used for fluorescence imaging of single dna molecules. *J. Am. Chem. Soc.*, 123:7985–7995, 2001.

[KKG02] Henning Klank, Jörg P. Kutter, and Oliver Geschke. Co_2-laser micromachining and back-end processing for rapid production of pmma-based microfluidic systems. *Lab on a Chip*, 2:242–246, 2002.

[KKK+11] Yoori Kim, Ki Seok Kim, Kristy L. Kounovsky, Rakwoo Chang, Gun Young Jung, Juan J. de Pablo, Kyubong Jo, and David C. Schwartz. Nanochannel confinement: Dna stretch approaching full contour length. *Lab on a Chip*, 11:1721–1729, 2011.

[KLC+13] Bong Suk Kim, Kyoung G. Lee, Ho Woon Choi, Tae Jae Lee, Kyun-Joo Park, Jung Youn Park, and Seok Jae Lee. Facile fabrication of plastic template for three-dimensional micromixer-embedded microfluidic device. *biochip journal*, 76(2):104–111, 2013.

[KLKC07] J.-P. Kruth, G. Levy, F. Klocke, and T.H.C. Childs. Consolidation phenomena in laser and powder-bed based layered manufacturing. *Annals of the CIRP*, 56:730–759, 2007.

[KP05] Ryan T. Koehler and Nicolas Peyret. Thermodynamic properties of dna sequences: characteristic values for the human genome. *Bioinformatics*, 21(16):3333–3339, 2005.

[Kri] Anders Kristensen. Polynano.org. `www.polynano.org/Technologies-applications`. Accessed: 31-01-2014.

[KRS+12] Philip J. Kitson, Mali H. Rosnes, Victor Sans, Vincenza Dragone, and Leroy Cronin. Configurable 3d-printed millifluidic and microfluidic 'lab on a chip' reactionware devices. *Lab Chip*, 12:3267–3271, 2012.

[LHL+12] ET Lam, A Hastie, C. Lin, D. Ehrlich, SK Das, MD Austin, P. Deshpande, H. Cao, N. Nagarajan, M. Xiao, and P-Y Kwok. Genome mapping on nanochannel arrays for structural variation analysis and sequence assembly. *Nature Biotechnology*, 30(9):771–776, 2012.

[LJmC+10] Hu Luo, Ran Jing, Yi min Cui, Hai long Wang, and Rong ming Wang. Improvement of fabrication precision of focused ion beam by introducing simultaneous electron beam. *Progress in Natural Science: Materials international*, 20:111–115, 2010.

[LJS+13] Junshan Liu, Xingxing Jin, Tuo Sun, Zheng Xu, Chong Liu, Jian Wang, Li Chen, and Liding Wang. Hot embossing of polymer nanochannels using pmma moulds. *Microsystem Technologies*, 19:629–634, 2013.

[LJY10] Lei Li, Stuart A. Collins Jr., and Allen Y. Yi. Optical effects of surface finish by ultraprecision single point diamond machining. *Journal of Manufacturing Science and Engineering*, 132:021002, 2010.

[LKB+13] Shuang Fang Lim, Alena Karpusenko, Ansel L. Blumers, Diana E. Streng, and Robert Riehn. Chromatin modification mapping in nanochannels. *biomicrofluidics*, 7:064105, 2013.

[LNG+07] Phil Latreille, Stacie Norton, Barry S. Goldman, John Henkhaus, Nancy Miller, Brad Barbazuk, Helge B. Bode, Creg Darby, Zijin Du, Steve Forst, Sophie Gaudriault, Brad Goodner, Heidi Goodrich-Blair, and Steven Slater. Optical mapping as a routine tool for bacterial genome sequence finishing. *BMC Genomics*, 8:321, 2007.

[LYZ+06] Jonathan W. Larson, Gregory R. Yantz, Qun Zhong, Rebecca Charnas, Christina M. D'Antoni, Michael V. Gallo, Kimberly A. Gillis, Lori A. Neely, Kevin M. Phillips, Gordon G. Wong, Steven R. Gullans, and Rudolf Gilmanshin. Single dna molecule stretching in sudden mixed shear and elongational microflows. *lab chip*, 6:1187–1199, 2006.

[LZZ+14] Xiaokang Li, Xinyong Zhang, Shan Zhao, Jingyu Wang, Gang Liu, and Yanan Du. Micro-scaffold array chip for upgrading cell-based high-throughput drug testing to 3d using benchtop equipment. *Lab Chip*, 14:471–481, 2014.

[Mal06a] Chantal G. Khan Malek. Laser processing for bio-microfluidics applications (part i). *Anal Bioanal Chem*, 385:1351–1361, 2006.

[Mal06b] Chantal G. Khan Malek. Laser processing for bio-microfluidics applications (part ii). *Anal Bioanal Chem*, 385:1362–1369, 2006.

[Mar11] Elaine R. Mardis. A decade's perspective on dna sequencing technology. *nature*, 470:198–203, 2011.

[MCSB08] Jeffrey R. Moffitt, Yann R. Chemla, Steven B. Smith, and Carlos Bustamante. Recent advances in optical tweezers. *Annual review of biochemistry*, 77:205–228, 2008.

[MD13] M. I. Mohammed and M. P. Y. Desmulliez. The manufacturing of packaged capillary action microfluidic systems by means of co_2 laser processing. *Microsyst Technol*, 19:809–818, 2013.

[MDA+00] J. Cooper McDonald, David C. Duffy, Janelle R. Anderson, Daniel T. Chiu, Honkai Wu, Olivier J. A. Schueller, and George M. Whitesides. Fabrication of systems in poly(dimethylsiloxane). *electrophoresis*, 21(1):27–40, 2000.

[MEF+97] Xavier Michalet, Rosemary Ekong, Françoise Fougerousse, Sophie Rousseaux, Catherine Schurra, Nick Hornigold, Marjon van Slegtenhorst, Jonathan Wolfe, Sue Povey, Jacques S. Beckmann, and Aaron Bensimon. Dynamic molecular combing: Stretching the whole human genome for high-resolution studies. *Science*, 277:1518–1523, 1997.

[Met10] Michael L. Metzker. Applications of next-generation sequencing; sequencing technologies -the next generation. *NATURE REVIEWS GENETICS*, 11:31–46, 2010.

[MGP+06] Dieudonne A. Mair, Emil Geiger, Albert P. Pisano, Jean M. J. Fréchet, and Frantisek Svec. Injection molded microfluidic chips featuring integrated interconnects. *Lab Chip*, 6:1346–1354, 2006.

[MNM+97] Randy M. McCormick, Robert J. Nelson, Goretty Alonso-Amigo M, Dominic J. Benvegny, and Herbert H. Hooper. Microchannel electrophoretic separations of dna in injection-molded plastic substrates. *Analytical Chemistry*, 69:2626–2630, 1997.

[MPB+13] Rodolphe Marie, Jonas N. Pedersen, David L. V. Bauer, Kristian H. Rasmussen, Mohammed Yusuf, Emanuela Volpi, Henrik Flyvbjerg, Anders Kristensen, and Kalim U. Mir. Integrated view of genome structure and sequence of a single dna molecule in a nanofluidic device. *PNAS*, 110(13):4893–4898, 2013.

[MPC+08] Andres W. Martinez, Scott T. Phillips, Emanuel Carrilho, Samuel W. Thomas III, Hayat Sindi, and George M. Whitesides. Simple telemedicine for developign regions: Camera phones and paper-based microfluidic devices for real-time, off-site diagnosis. *Anal. Chem.*, 80:3699–3707, 2008.

[MPW10] Andres W. Martinez, Scott T. Phillips, and George M. Whitesides. Diagnostics for the developing world: Microfluidic paper-based analytical devices. *Anal. Chem.*, 82:3–10, 2010.

[Nan] Nanoscribe. 3d laser lithography / direct laser writing. `http://www.nanoscribe.de/en/technology/direct-laser-writing`. Accessed: 19-03-2014.

[NDH11] Robert K. Neely, Jochem Deen, and Johan Hofkens. Optical mapping of dna: Single-molecule-based methods for mapping genomes. *Biopolymers*, 95(5):298–311, MAY 2011.

[NEW98] M. Niggemann, W. Ehrfeld, and L. Weber. Fabrication of miniaturized biotechnical devices. In *PROCEEDINGS OF THE SOCIETY OF PHOTO-OPTICAL INSTRUMENTATION ENGINEERS (SPIE)*, volume 3511, pages 204–213, 1998.

[NNB+03] T. Nielsen, D. Nilsson, F. Bundgaard, P. Shi, P. Szabo, O. Geschke, and A. Kristensen. Nanoimprint lithography in the cyclic olefin copolymer, topas, a highly ultraviolet-transparent and chemically resistant thermoplast. *Journal of Vacuum Science and Technology B*, 22:1770–1775, 2003.

[NNF+13] Charleston Noble, Adam N. Nilsson, Camilla Freitag, Jason P. Beech, Jonas O. Tegenfeldt, and Tobias Ambjörnsson. A fast and scalable algorithm for alignment of optical dna mappings. `http://arxiv.org/abs/1311.6379v1`, 11 2013. version 1.

[NPB+12] Lena K. Nyberg, Fredrik Persson, Johan Berg, Johanna Bergstrom, Emelie Fransson, Linnea Olsson, Moa Persson, Antti Stalnacke, Jens Wigenius, Jonas O. Tegenfeldt, and Fredrik Westerlund. A single-step competitive binding assay for mapping of single dna molecules. *Biochemical and biophysical research communications*, 417(1):404–408, JAN 6 2012 2012.

[NY07] Yuta Nakashima and Takashi Yasuda. Cell differentiation guidance using chemical stimulation controlled by a microfluidic device. *Sensors and actuators A-physical*, 139:252–258, 2007.

[Odi77] Theo Odijk. Polyelectrolytes near the rod limit. *Journal of Polymer Science*, 15:477–483, 1977.

[PDF10] Nancie Petrucelli, Mary B. Daly, and Gerald L. Feldman. Hereditary breast and ovarian cancer due to mutations in brca1 and brca2. *Genetics in Medicine*, 12(5):245–259, 2010.

[PNL+05] A. Piruska, Irena Nikcevic, Se Hwan Lee, Chong Ahn, William R. Heineman, Patrick A. Limbach, and Carl J. Seliskar. The autofluorescence of plastic materials and chips measured under laser irradiation. *Lab on a Chip*, 5:1348–1354, 2005.

[PSOH04] William K. Purves, David Sadava, Gordon H. Orians, and H. Craig Heller. *Life The Science of Biology*, volume 1. Sinauer Associates, 7 edition, 2004.

[RD10] Marcel Reuter and David T. F. Dryden. The kinetics of yoyo-1 intercalation into single molecules of double-stranded dna. *Biochemical and Biophysical Research Communications*, 403:225–229, 2010.

[RDK+09] Keil J. Regehr, Maribella Domenech, Justin T. Koepsel, Kristopher C. Carver, Stephanie J. Ellison-Zelski, William L. Murphy, Linda A. Schuler, Elaine T. Alarid, and David J. Beebe. Biological implications of polydimethylsiloxane-based microfluidic cell culture. *Lab Chip*, 9:2132–2139, 2009.

[Reh13] Heidi L. Rehm. Disease-targeted sequencing: a cornerstone in the clinic. *Nature reviews genetics*, 14:295–300, 2013.

[RLS+10] Walter Reisner, Niels B. Larsen, Asli Silahtaroglu, Anders Kristensen, Niels Tommerup, Jonas O. Tegenfeldt, and Henrik Flyvbjerg. Single-molecule denaturation mapping of dna in nanofluidic channels. *Proceedings of the National Academy of Sciences of the United States of America*, 107(30):13294–13299, JUL 27 2010 2010.

[RLW+05] R. Riehn, M. C. Lu, Y. M. Wang, S. F. Lim, E. C. Cox, and R. H. Austin. Restriction mapping in nanofluidic devices. *Proceedings of the National Academy of Sciences of the United States of America*, 102(29):10012–10016, 2005.

[RPA12] Walter Reisner, Jonas N. Pedersen, and Robert H. Austin. Dna confinement in nanochannels: physics and biological applications. *Reports on Progress in Physics*, 75:106601, 2012.

[RSD06] Greg C. Randall, Kelly M. Schultz, and Patrick S. Doyle. Methods to electrophoretically stretch dna: microcontractions, gels, and hybrid gel-microcontraction devices. *Lab Chip*, 6:516–525, 2006.

[RSSH03] Andrea Rainelli, Richard Stratz, Karin Schweizer, and Peter C. Hauser. Miniature flow-injectino analysis manifold created by micromilling. *talanta*, 61:689–665, 2003.

[SC75] F. Sanger and A. R. Coulson. Rapid method for determining sequences in dna by primed synthesis with dna-polymerase. *Journal of Molecular Biology*, 94(3):441–448, 1975.

[SDK+10] Feng Shen, Wenbin Du, Jason E. Kreutz, Alice Fok, and Rustem F. Ismagilov. Digital pcr on a slipchip. *Lab Chip*, 10:2666–2672, 2010.

[sHM96] syed H. Masood. Intelligent rapid prototyping with fused deposition modelling. *rapid prototyping journal*, 2(1):24–33, 1996.

[SJ08] Jay Shendure and Hanlee Ji. Next-generation dna sequencing. *Nature biotechnology*, 26(10):1135–1145, OCT 2008.

[SJB+88] EV Scott, RL Jones, DL Banville, G. Zon, LG Marzilli, and WD Wilson. H-1 and p-31 nmr investigations of actinomycin-d-binding selectivity with oligodeoxyribonucleotides containing multiple adjacent d(gc) sites. *Biochemistry*, 27(3):915–923, FEB 9 1988.

[SNC77] F. Sanger, S. Nicklen, and A. R. Coulson. Dna sequencing with chain-terminating inhibitors. *PNAS*, 74(12):5463–5467, 1977.

[SPC02] V. Studer, A. Pépin, and Y. Chen. Nanoembossing of thermoplastic polymers for microfluidic applications. *Applied physics letters*, 80(19):3614–3616, 2002.

[SSC+14] Aliaa I. Shallan, Petr Smejkal, Monika Corban, Rosanne M. Guijt, , and Michael C. Breadmore. Cost-effective three-dimensional printing of visibly transparent microchips within minutes. *analytical chemistry*, 86:3124–3230, 2014.

[Sta12] S. M. Stavis. A glowing future for lab on a chip testing standards. *Lab on a Chip*, 12:3008–3011, 2012.

[SvWY13] Mehdi Shahini, Frans van Wijngaarden, and John T. W. Yeow. Fabrication of electro-microfluidic channel for single cell electroporation. *Biomed Microdevices*, 15:759–766, 2013.

[TB06] Michael W. Toepke and David J. Beebe. Pdms absorption of small molecules and consequences in microfluidic applications. *Lab Chip*, 6:1484–1486, 2006.

[TBBB94] Paulos Tekola, Jan P.A. Baak, Jeroen A.M. Beliën, and Jane Brugghe. Highly sensitive, specific, and stable new fluorescent dna stains for confocal laser microscopy and image processing of normal paraffin sections. *Cytometry*, 17:191–195, 1994.

[TJA79] Stephen C. Terry, Jphn H. Jerman, and James B. Angell. Gas-chromatographic air analyzer fabricated on a silicon-wafer. *IEEE TRANSACTIONS ON ELECTRON DEVICES*, 26(12):1880–1886, 1979.

[TLJH03] E. Tøstesen, F. Liu, T-K. Jenssen, and E. Hovig. Speed-up of dna melting algorithm with complete nearest neighbor properties. *Biopolymers*, 70:364–376, 2003.

[TLK10] Lasse H. Thamdrup, Niels B. Larsen, and Anders Kristensen. Light-induced local heating for thermophoretic manipulation of dna in polymer micro- and nanochannels. *Nano Letters*, 10:826–832, 2010.

[TMC+13] Simone Tanzi, Marco Matteucci, Thomas L. Christiansen, Søren Friis, Mette T. Christensen, Jørgen Garnæs, Sandra Wilson, Jonatan Kutchinsky, and Rafael Taboryski. Ion channel recordings on an injection-molded polymer chip. *Lab on a Chip*, 13:4784–4793, 2013.

[TOM+12] Simone Tanzi, Peter Friis Østergaard, Marco Matteucci, Thomas Lehrmann Christiansen, Jiri Cech, Rodolphe Marie, and Rafael Taboryski. Fabrication of combined-scale nano and microfluidic polymer systems using a multilevel dry etching, electroplating and molding process. *J. Micromech. Microeng.*, 22:115008, 2012.

[TPC+04] Jonas O. Tegenfeldt, Christelle Prinz, Han Cao, Steven Chou, Walter W. Reisner, Robert Riehn, Yan Mei Wang, Edward C. Cox, James C. Sturm, Pascal Silberzan, , and Robert H. Austin. The dynamics of genomic-length dna molecules in 100-nm channels. *PNAS*, 101(30):10979–10983, 2004.

[TS12] Todd J. Treangen and Steven L. Salzberg. Applications of next-generation sequencing; repetitive dna and next-generation sequencing: computational challenges and solutions. *Nature reviews genetics*, 13:36–46, 2012.

[TvMB+05] R.M. Tiggelaar, P. van Male, J.W. Berenschot, J.G.E. Gardeniers, R.E. Oosterbroek, M.H.J.M. de Croon, J.C. Schouten, A. van den Berg, and M.C. Elwenspoek. Fabrication of a high-temperature microreator with integrated heater and sensor patterns on an ultrathin silicon membrane. *Sensors and Actuaters A-physical*, 119:196–205, 2005.

[TWG+10] Brian Teague, Micheal S. Waterman, Steven Goldstein, Konstantinos Potamousis, Shiguo Zhou, Susan Reslewic, Deepayan Sarkar, Anton Valouev, Christopher Churas, Jeffrey M. Kidd, Scott Kohn, Rodney Runnheim, Casey Lamers, Dan Forrest, Michael A. Newton, Evan E. Eichler, Marijo Kent-First, Urvashi Surti, Miron Livny, and David C. Schwartz. High-resolution human genome structure by single-molecule analysis. *PNAS*, 107(24):10848–10853, 2010.

[TWL03] Daniel Therriault, Scott R. White, and Jennifer A. Lewis. Chaotic mixing in three-dimensional microvascular networks fabricated by direct-write assembly. *Nature Materials*, 2:265–271, 2003.

[TZS+03] C.M. Sotomayor Torres, S. Zankovych, J. Seekamp, A. P. Kam, C. Clavijo Cede no, T. Hoffmann, J. Ahopelto, F. Reuther, K. Pfeiffer, G. Bleidiessel, G. Gruetzner, M. V. Maximov, and B. Heidari. Nanoimprint lithography: an alternative nanofabrication approach. *Materials science and engineering C*, 23:23–31, 2003.

[UCT+00] Marc A. Unger, Hou-Pu Chou, Todd Thorsen, Axel Scherer, and Stephen R. Quake. Monolithic microfabricated valves and pumps by multilayer soft lithography. *science*, 288:113–116, 2000.

[UPKL11] Pawel Utko, Fredrik Persson, Anders Kristensen, and Niels B. Larsen. Injection molded nanofluidic chips: Fabrication method and functional tests using single-molecule dna experiments. *Lab on a Chip*, 11(2):303–308, 2011.

[WC53] JD Watson and FHC Crick. Molecular structure of nucleic acids -a structure for deoxyribose nucleic acid. *Nature*, 171(4356):737–738, 1953.

[WE98] L. Weber and W. Ehrfeld. Molding of microstructures for high-tech applications. In *CONFERENCE PROCEEDINGS AT ANTEC '98: PLASTICS ON MY MIND, VOLS I-3: VOL I; PROCESSING, VOL II; SPECIAL AREAS, VOL III; MATERIALS*, volume 44, pages 3088–3093, 1998.

[Wet] KA Wetterstrand. Dna sequencing costs: Data from the nhgri genome sequencing program (gsp). `www.genome.gov/sequencingcosts`. Accessed: 15-01-2014.

[WJZ+88] WD Wilson, RL Jones, G. Zon, EV Scott, and LG Marzilli. Nmr analysis of the interaction of actinomycin-d with oligodeoxyribonucleotides containing multiple gc binding-sites. *Biophysical journal*, 53(2):A4–A4, FEB 1988.

[WKK+11] Mary E. Wilson, Nithyanand Kota, YongTae Kim, Yadong Wang, Donna B. Stolz, Philip R. LeDuc, and O. Burak Ozdoganlar. Fabrication of circular microfluidic channels by combining mechanical micromilling and soft lithography. *Lab on a Chip*, 11:1550–1555, 2011.

[WLW74] RM Wartell, JE Larson, and RD Wells. Netropsin - specific probe for a-t regions of duplex deoxyribonucleic-acid. *Journal of Biological Chemistry*, 249(21):6719–6731, 1974.

[WRT12] Y Wang, W. F. Reinhart, and D. R. Tree. Resolution limit for dna barcodes in the odijk regime. *Biomicrofluidics*, 6:014101–1, 2012.

[WRTD12] Yanwei Wang, Wes F. Reinhart, Douglas R. Tree, and Kevin D. Dorfman. Resolution limit for dna barcodes in the odijk regime. *Biomicrofluidics*, 6(1):014101, MAR 2012.

[WSDR12] R. L. Welch, R. Sladek, K. Dewar, and W.W. Reisner. Denaturation mapping of saccharomyces cerevisiae. *Lab-on-a-Chip*, Advance article, 2012.

[WTD11] Yanwei Wang, Douglas R. Tree, and Kevin D. Dorfman. Simulation of dna extension in nanochannels. *Macromolecules*, 44:6594–6604, 2011.

[XLT+06] J. H. Xu, S. W. Li, J. Tan, Y. J. Wang, and G. S. Luo. preparation of highly monodisperse droplet in a t-junction microfluidic device. *AICHE journal*, 52(9):3005–3010, 2006.

[XPH+07] Ming Xiao, Angie Phong, Connie Ha, Ting-Fung Chan, Dongmei Cai, Lucinda Leung, Eunice Wan, Amy L. Kistler, Joseph L. DeRisi, Paul R. Selvin, and Pui-Yan Kwok. Rapid dna mapping by fluorescent single molecule detection. *Nucleic Acids Research*, 35(3):e16, 2007.

[XXQ+12] Youchun Xu, Fengbo Xie, Tian Qiu, Lan Xie, Wanli Xing, and Jing Cheng. Rapid fabrication of a microdevice with concave microwells and its application in embryoid body formation. *biomicrofluidics*, 6:016504, 2012.

[YEF+06] Paul Yager, Thayne Edwards, Elain Fu, Kristen Helton, Kjell Nelson, Milton R. Tam, and Berhard H. Weigl. Microfluidic diagnostic technologies for global public health. *Nature*, 442:412–418, 2006.

[YYC13] Can Yang, Xiao-Hong Yin, and Guang-Ming Cheng. Microinjection molding of microsystem components: new aspects in improving performance. *J. Micromech. Microeng*, 23:093001, 2013.

[ZBP+07] Shiguo Zhou, Michael C. Bechner, Michael Place, Chris P. Churas, Louise Pape, Sally A. Leong, Rod Runnheim, Dan K. Forrest, Steve Goldstein, Miron Livny, and David C. Schwarts. Validation of rice genome sequence by optical mapping. *BMC Genomics*, 8:278, 2007.

List of publications

Paper 1: *Fabrication of combined-scale nano- and microfluidic polymer systems using a multilevel dry etching, electroplating, and molding process.* Simone Tanzi, Peter Friis Østergaard, Thomas Lehrmann Christiansen, Jiri Cech, Rodolphe Marie, and Rafael Taboryski. J. Micromech. Microeng 2012 **22** 115008

Paper 2: *DNA barcoding via counterstaining with AT/GC sensitive ligands in injection-molded all-polymer nanochannel devices.* Peter Friis Østergaard, Marco Matteucci, Walter Reisner, and Rafael Taboryski. Analyst, 2013 **138** 1249-1255

Paper 3: *All Polymer, Injection Molded Nanoslits, Fabricated Through Two-Level UV-LIGA Processes.* Peter Friis Østergaard, Marco Matteucci, Rodolphe Marie, Anders Kristensen, and Rafael Taboryski. Nanotech 2012 Vol. 2 Nanotechnology 2012: Electronics, Devices, Fabrication, MEMS, Fluidics and Computational, 2012 **2** 482-485

Paper 4: *Optical mapping of single molecule human DNA in disposable, mass produced all polymer devices.* Peter Friis Østergaard, Joanna Lopacinska-Jørgensen, Jonas Nyvold Pedersen, Asli Silahtaroglu, Niels Tommerup, Anders Kristensen, Henrik Flyvbjerg, Rodolphe Marie, and Rafael Taboryski. Manuscript in preparation

Paper 5: *Fabrication and characterization of injection molded multi level nano and microfluidic systems.* Marco Matteucci, Thomas Lehrmann Christiansen, Simone Tanzi, Peter Friis Østergaard, Simon Tylsgaard Larsen, and Rafael Taboryski. Microelectronic Engineering 2013 **111** 294-298

Paper 6: *Injection Moulded All-Polymer Capillary Microvalves for Passive Microfluidic Control: Performance Versus Prediction.* Kasper Kistrup, Carl Esben Poulsen, Peter Friis Østergaard, Kenneth Brian Haugshøj, Rafael Taboryski, Anders Wolff, and Mikkel Fougt Hansen. Submitted for publication at Microfluidics and Nanofluidics

Paper 1

Fabrication of combined-scale nano- and microfluidic polymer systems using a multilevel dry etching, electroplating, and molding process

Simone Tanzi, Peter Friis Østergaard, Thomas Lehrmann Christiansen, Jiri Cech, Rodolphe Marie, and Rafael Taboryski

J. Micromech. Microeng 2012 **22** 115008

Fabrication of combined-scale nano- and microfluidic polymer systems using a multilevel dry etching, electroplating and molding process

2012 J. Micromech. Microeng. 22 115008

(http://iopscience.iop.org/0960-1317/22/11/115008)

IOP Publishing Journal of Micromechanics and Microengineering

J. Micromech. Microeng. **22** (2012) 115008 (11pp) doi:10.1088/0960-1317/22/11/115008

Fabrication of combined-scale nano- and microfluidic polymer systems using a multilevel dry etching, electroplating and molding process

Simone Tanzi[1], Peter Friis Østergaard[1], Marco Matteucci, Thomas Lehrmann Christiansen, Jiri Cech, Rodolphe Marie and Rafael Taboryski[2]

Department of Micro- and Nanotechnology, Technical University of Denmark, DTU Nanotech, Building 345E, DK-2800 Kongens Lyngby, Denmark

E-mail: rata@nanotech.dtu.dk

Received 29 May 2012, in final form 23 July 2012
Published 25 September 2012
Online at stacks.iop.org/JMM/22/115008

Abstract

Microfabricated single-cell capture and DNA stretching devices have been produced by injection molding. The fabrication scheme employed deep reactive ion etching in a silicon substrate, electroplating in nickel and molding in cyclic olefin polymer. This work proposes technical solutions to fabrication challenges associated with chip sealing and demolding of polymer high-volume replication methods. UV-assisted thermal bonding was found to ensure a strong seal of the microstructures in the molded part without altering the geometry of the channels. In the DNA stretching device, a low aspect ratio nanoslit (1/200) connecting two larger micro-channels was used to stretch a 168.5 kbp DNA molecule, while in the other device single-HeLa cells were captured against a micro-aperture connecting two larger microfluidic channels. Different dry etching processes have been investigated for the master origination of the cell-capture device. The combination of a modified Bosch process and an isotropic polysilicon etch was found to ensure the ease of demolding by resulting in slightly positively tapered sidewalls with negligible undercut at the mask interface.

(Some figures may appear in colour only in the online journal)

Introduction

In recent years, polymeric materials [1–4] have gradually replaced glass and silicon [5, 6] as the preferred production platform for the production of microfluidic devices. Polymers exhibit a broad range of appealing chemical, mechanical, electrical and optical properties [7]. Moreover, the multitude of different methods to manufacture microstructures in polymers make polymeric materials suitable for almost any given application, ranging from fast prototyping methods such as polydimethylsiloxane (PDMS) casting, laser milling or micromachining [8–10] to high volume mass production. In terms of physical parameters and thus technological pathways to fabrication, polymers can be classified into thermosets, thermoplastics and elastomers [7]. While PDMS have become a primary choice for fast prototyping and low-volume manufacturing in the academic environment [11], technical thermoplastic polymers are employed by commercial replication methods like injection molding [12, 13] and hot embossing [14]. However, polymer mass replication methods are poorly compatible with the requirements for flexibility and fast turnaround times in the research environment. Traditional injection-molding tools are expensive and very time-consuming to fabricate. We propose a technology that aims to narrow the gap between methods and materials used

[1] These two authors contributed equally to this article.
[2] Author to whom any correspondence should be addressed.

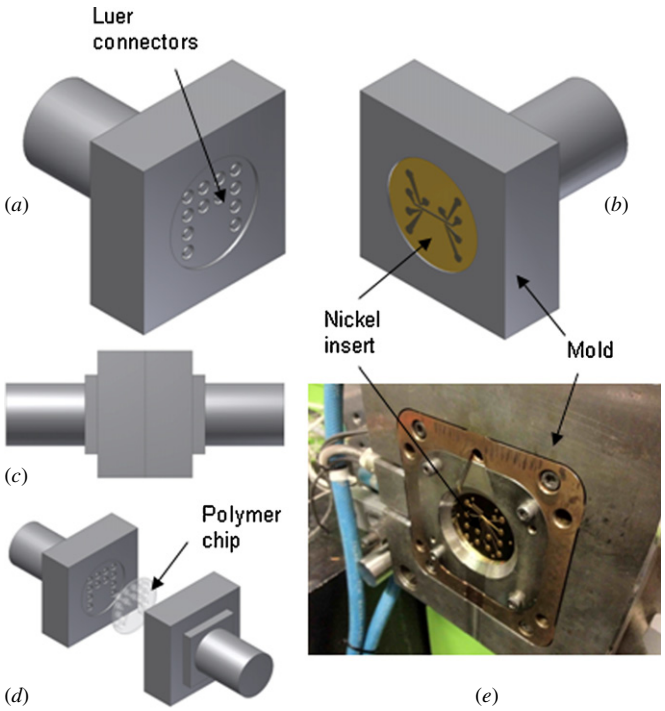

Figure 1. The figures illustrate the principle of the injection molding process. (*a*) Mold shaped with the Luer connectors. (*b*) Mold containing the microstructured nickel shim. (*c*) Mold is closed in order to form the cavity where polymer is injected. (*d*) Mold is pulled apart and the polymer chip can be removed. (*e*) Pictures of the mold with the nickel insert.

in the academic and industrial environments. This consists of a versatile prototyping technology directly applicable to mass production. A nickel electroform is produced from a microfabricated silicon master to transfer micrometer features to a substrate suitable for injection molding, as shown in figure 1. Origination of a master having the inverse structures of the final part is the underlying principle of any replication technology [7]. The relatively expensive step requiring microfabrication is only performed once on a single master and identical polymer substrates can be produced in high quantity [7]. Various techniques have been used in the past for mold insert origination such as micromachining methods and electroplating methods [15]. Among those methods, the most commonly used are LIGA[3] [16], and LIGA-like techniques, depending on the source of radiation employed [17, 18]. Although LIGA remains the best choice for high aspect ratio microstructures [19], it suffers from serious drawbacks when required facilities and the associated costs are considered. LIGA-like processes, in particular, the well-established UV-LIGA, then becomes the low-cost alternatives. Despite the fact that SU-8 is a versatile material, it suffers from technological limitations when multilevel structuring in the microrange and a silicon single-crystal polished master surface flatness are needed. Therefore, an alternative fabrication process has to be evaluated. A method where micro-channels are not made in thick photoresist but directly in silicon using wet etching was first described by McCormick *et al* [20].

[3] German acronym for lithographie (lithography), galvanoformung (electroplating), abformung (molding).

Elwenspoek *et al* [21] proposed a process in which the x-ray lithography step of the LIGA process is substituted by dry etching. The process was called DEEMO, which is the acronym for dry etching, electroplating and molding [21, 22]. The state of the art in dry etching techniques makes it possible to design advanced microfluidic systems, where the intersection between channels with heights in broad ranges from nanometers or micrometers to tens of micrometers are required [23]. Moreover, this method exploits the advantages of dry etching in terms of directional freedom—the serious drawback when wet etching is used—low roughness and high selectivity with respect to the mask material [24–26]. We describe a procedure to fabricate combined microfluidic and nanofluidic systems in a thermoplastic polymer platform. Networks of microfluidic channels down to 100 nm in height are demonstrated. The performance of microfluidic systems, originated by using a multilevel DEEMO process, has been evaluated by fabricating two different devices addressing specific biological applications such as single-cell trapping and stretching of DNA molecules. A multilevel fabrication scheme has been adopted where a silicon oxide mask is employed to define the small features on the Si master. Reactive ion etching (RIE) and deep reactive ion etching (DRIE) techniques are used for etching. The parts are injection molded in cyclic olefin copolymers (COCs) [27, 28]. As reviewed by Nunes *et al* [29] COCs are increasingly popular as substrates for microfluidic applications. They have promising properties such as high chemical resistance, low water absorption, good optical transparency and ease of fabrication by injection molding [15]. Devices in COCs have already been implemented for a multitude of applications, including capillary electrophoresis [30], electrochromatography [31] and mass spectroscopy [32].

The novel feature of this work is the demonstration of DEEMO processes to fabricate combined scale microfluidic chips for cell capture and for DNA stretching. The key feature of the cell trapping chip is a few micrometer-sized side channels that connect two 50 μm deep channels, while the key feature of the DNA chip is the combined scale of a 100 nm slit connecting two micrometer-sized main channels. Both devices were fabricated by injection molding of COC Topas and sealed by UV-assisted thermal bonding to a thin polymer foil. The complete device resulted from only two parts bonded together. Figure 2 shows a 3D model of the polymer device and the molded part before bonding. The use of the thin polymer foil addresses the requirements of the short working distance for microscopy in both applications. Integrated inlet/outlet ports designed according to the Luer-fitting standard [33] for practical fluidic interconnects are defined by the traditional machined part of the injection-molding tool, figure 1(*a*). In addition, we also propose technical solutions to the fabrication challenges of any injection-molded microfluidic device such as chip sealing and part demolding.

Chip design and motivation

Two different chip designs have been studied. The first design addresses the capture of single cells, while the second one is concerned with stretching of DNA macromolecules.

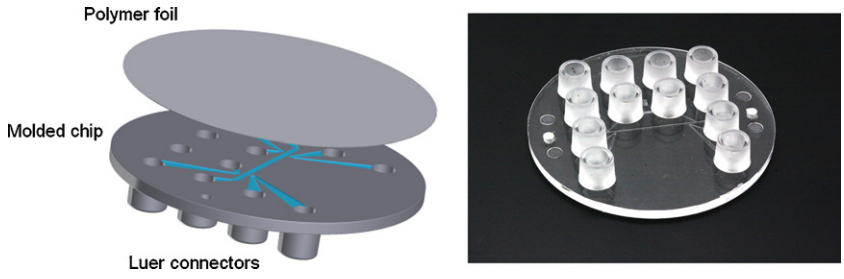

(*a*) (*b*)

Figure 2. (*a*) 3D representation of the polymer device concept. Both the final devices result from UV-assisted thermal bonding between an injection-molded polymer part and a 100 μm thick lid. The blue color shows the microfluidics open system for the cell-capture device. (*b*) Molded part for the cell-capture device.

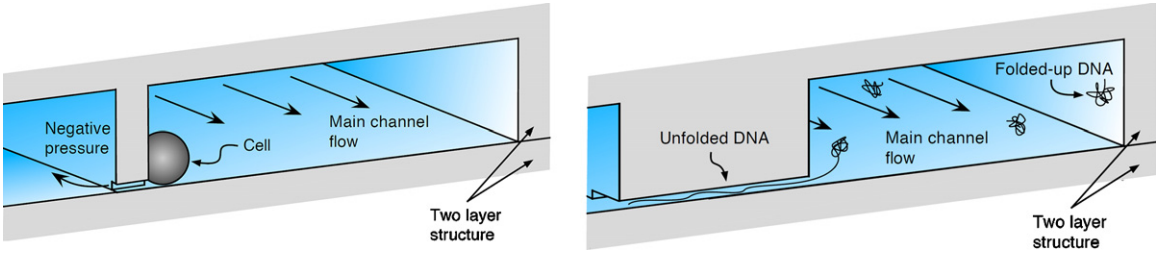

(*a*) (*b*)

Figure 3. (*a*) Concept design of the cell-capture device with 'cornered' apertures based on microfluidic junctions between a large chamber for cell delivery and a lateral capillary for cell trapping. (*b*) Concept design of DNA stretching device with intersection between a nanoslit and a large inlet channel.

Figure 3 shows the concept design for both devices. Precise manipulation of cells and DNA molecules at micro- and nanoscale are both becoming widely used techniques with a broad range of biological applications. Here we utilize these devices as examples to present solutions to specific fabrication challenges related to polymer microfluidic systems such as demolding of the polymer parts and sealing of structures with a very low aspect ratio (height over width).

Single-cell capture

Manipulation of single cells is basic for cell-related studies, such as drug screening and cell impedance analysis. The most commonly used technologies for cell trapping in microfluidic systems comprise both non-contact and contact mode trapping techniques [34–36]. Either hydrodynamic effects are used to retain cells or externally applied field gradients that induce forces on cells such as electrical [37], optical [38], magnetic [39] or acoustic [40] fields are used to enable cell trapping conditions. Among hydrodynamic cell trapping methods, the most common way consists of creating side channels in a main transport channel, where the side channel dimensions are sufficiently small to trap cells to it by suction. Seo *et al* [41] reported on lateral apertures in the PDMS microfluidic device for electrophysiology recordings. Lee *et al* [42] reported on the device for monitoring direct cell–cell communication via gap junctions between individual cell pairs. Our device enables us to capture a cell flowing in a carrier channel close to a small microhole by the application of suction. The chip comprises a 'cornered' (non-planar) aperture based on a microfluidic junction between a large chamber for cell delivery and a lateral capillary for cell trapping. Similar apertures have been reported by Zanetti *et al* [43], but for an elastomeric platform. The silicon master contains both suction channels (5 μm wide, 4 μm deep) and carrier channels (200 μm wide, 50 μm deep). The critical dimensions of the suction channels are comparable with defects associated with demolding, as will be discussed later.

DNA stretching

Stretching of DNA macromolecules through nanofluidic networks is becoming a powerful tool for direct sizing and mapping of DNA [44, 45]. Utko *et al* [46] have demonstrated DNA stretching experiments performed on individual double-stranded molecules in nanochannels on an injection-molded substrate. Rough sequencing of the genetic code of DNA can be performed by melting mapping experiments of elongated DNA, as explained by Reisner *et al* [47, 48]. Polymer systems intended for such purposes have been fabricated by the use of injection molding [46], but for long strands of DNA, narrow channels are not preferable, as the DNA can get in the way of itself, blocking the channel. Instead, nanoslits, that have a height in the nanometer regime, but a width in the micrometer regime, can be used [49, 50]. For fabricating the slit devices, the use of very expensive e-beam pattering is thus not required as the nanometer-sized dimension is defined by the oxide thickness [46]. The chip comprises nanoconducts (100 nm deep, 20 μm wide) intersecting a micro-scale channel. In this case the main challenge is the sealing of the fluidic system using UV-assisted bonding, when the extremely low aspect ratio may cause a collapse of the nanostructures.

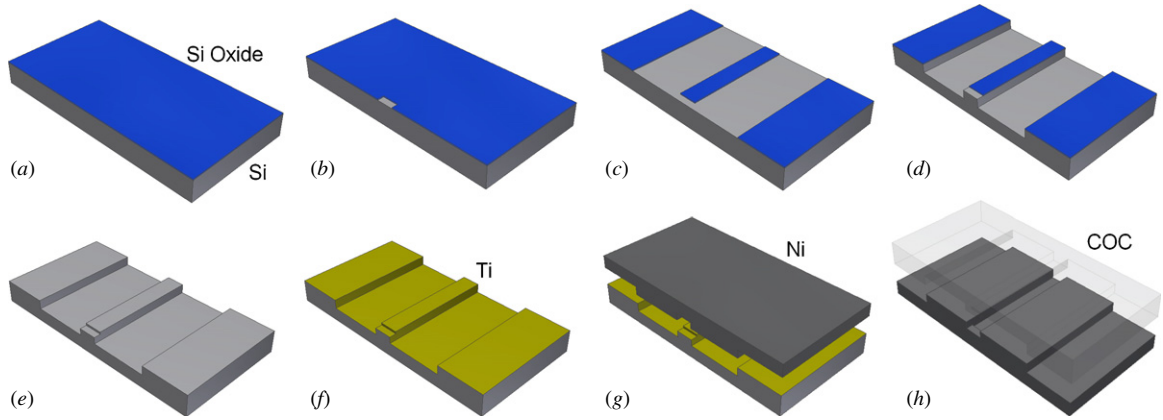

Figure 4. Schematics of the fabrication process for the cell-capture device after main steps: (*a*) oxidation with 100 nm thick silicon oxide; (*b*) oxide etching of the shallow microchannels; (*c*) oxide etching of the main chambers; (*d*) DRIE of the main chambers; (*e*) RIE of the shallow channels and oxide removal; (*f*) sputtering of 100 μm titanium seed layer; (*g*) electroplating of 340 μm nickel shim; (*h*) injection molding of COC Topas chips.

Table 1. The table shows the process parameters for the silicon master origination for both devices. For the etching of the inlet channels (called deep in the table) two different processes have been used: DRIE for the cell-capture device and RIE for the DNA stretching device.

Process	Parameters cell-capture device	Parameters DNA stretching device
Oxide deposition	1050 °C dry oxidation; $t = 90$ min + 20 min annealing	
Spin coating	HMDS vapor deposition 2.2 μm AZ5214E pre-bake: 90 °C for 90 s	HMDS vapor deposition 1.5 μm AZ5214E pre-bake: 90 °C for 90 s
Photolithography	hard contact mode, front side alignment W/A = 7 mW cm^{-2}; $t = 9$ s AZ351 developer; $t = 90$ s	hard contact mode, front side alignment W/A = 7 mW cm^{-2}; $t = 7$ s AZ351 developer; $t = 70$ s
Oxide etch (shallow channels)	$CF_4/CHF_3 = 14/26$ sccm; $t = 210$ s; $W_{RF} = 60$ W; P = 100 mTorr	
Spin coating	HMDS vapor deposition 6.2 μm AZ5214E pre-bake: 100 °C for 100 s	HMDS vapor deposition 1.5 μm AZ5214E pre-bake: 90 °C for 90 s
Photolithography	hard contact mode, front side alignment W/A = 7 mW cm^{-2}; $t = 30$ s AZ351 developer; t = 300 s	hard contact mode, front side alignment W/A = 7 mW cm^{-2}; $t = 7$ s AZ351 developer; t = 70 s
Oxide etch (deep channels)	$CF_4/CHF_3 = 14/26$ sccm; $t = 210$ s; $W_{RF} = 60$ W; P = 100 mTorr	
Si DRIE/RIE (deep channels)	$SF_6/O_2/Ar = 180/160/100$; P = 246≫91mT, coil 2.8kW, platen (HF) 170≫215W, $t =$ 2:40 min	$SF_6/O_2 = 32/8$ sccm; $W_{RF} = 30$ W; $t = 13.5$ min; P = 80 mTorr
Si RIE (shallow channels)	$SF_6/O_2 = 32/8$ sccm; $W_{RF} = 30$ W; $t = 4$ min; P = 80 mTorr	Not required
Oxide removal	BHF bath; $t = 3$ min	Not required

Experimental details

Fabrication

The fabrication scheme for the two systems is similar, as can be seen in table1. Hence, the description will be made in parallel and only substantial differences between the processes will be marked and explained. A two-step lithography process is needed to fabricate the Si master, figure 4. We start from 100 mm, ⟨1 0 0⟩, single side polished, 525 μm thick silicon wafers. Wafers are oxidized for 90 min in a Tempress horizontal furnace at 1050 °C with an oxygen flow of 5 slm[4] and 20 min annealing at the same temperature, with a nitrogen flow of 3 slm. During heating and cooling, a nitrogen flow of 3 slm is used.

While for the cell-capture device the oxide layer is used only to mask the Si along the process, for the DNA chip the 100 nm thick oxide defines the height of the nanoslits. A chemical treatment with hexamethyldisilazane (HMDS) before any spin coatings is used to promote the adhesion of the resist. The treatment is performed in a STAR2000 HMDS/vapor prime oven from IMTEC. A μm range thick layer of AZ5214E photoresist from MicroChemicals is applied to the substrates, using a SSE Maximus 804 cluster system. The desired layouts are then transferred to the wafer, using a

[4] Standard liters per minute.

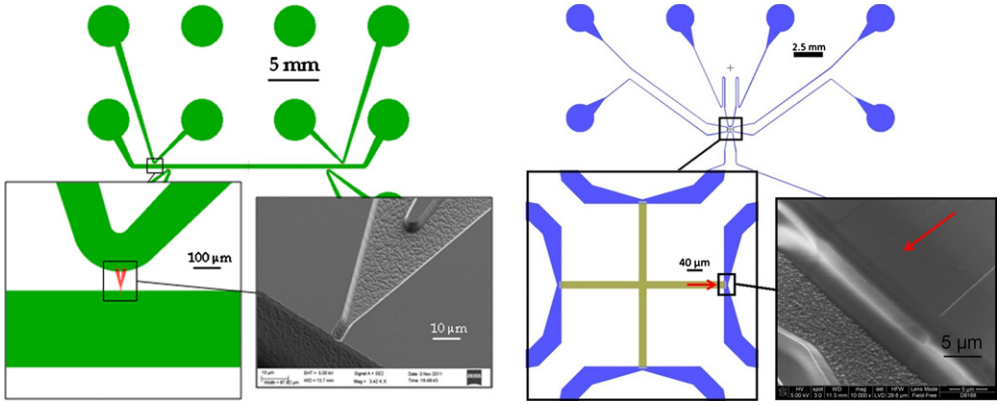

(*a*) (*b*)

Figure 5. Layout of the two devices. (*a*) Design of the cell-capture chip, with an enlargement of the suction channel and a SEM micrograph of it. (*b*) Design of the DNA stretching chip, with an enlargement of the crossing nanoslits and a SEM micrograph of the intersection.

Karl Süss Mask Aligner MA6 (exposure wavelength 365 nm) in hard contact mode and front side alignment. To obtain the nanoslits and the shallow channels, the wafers are then developed in AZ351 and exposed to a CF_4/CHF_3 plasma reactive ion etch in an STS (surface technology systems) cluster system C004. The high SiO_2/Si selectivity of this etching process ensures that the final height corresponds to the height of the oxide layer. The remaining photoresist is then removed in oxygen plasma. A second lithography step is performed for the fabrication of the carrier channels in Si, and to access the Si the oxide is etched as described above. The process for producing the carrier channels differs between the two chips; for the DNA chip an anisotropic RIE etching of Si is performed, while for the cell-capture chip a DRIE is required. A continuous process is performed with a Pegasus STS system. The $SF_6/O_2/Ar$ plasma was optimized to obtain tapered sidewalls and smooth surfaces. For the fabrication of the shallow channels in the cell-capture system, a final RIE etching into silicon is performed using the oxide left as mask. The final result gives shallow channels of 4 μm deep and 5 μm wide. The proposed scheme, in which the fabrication of the small channels is postponed, allows the use of the RIE step to eliminate the small undercut that the carrier channels exhibit after the continuous DRIE process. The removal of the oxide mask in a buffered HF completes the process. To prepare the samples for electroplating, a conductive seed layer is sputtered by a sputtering system from Lesker. For the DNA chip, a 90 nm nickel/vanadium thick layer is used, while a 100 nm thick layer of Ti is deposited for the cell-capture chip. Different seed materials are needed due to the fact that it was not possible readily to separate the Ni shim from the Si wafer for the cell-capture device, so the Si was etched away in KOH, and long etching time in KOH was found to damage the NiV. Electroplating is performed in a Technotrans Microform 200 electroplater. In this process, the current is increased linearly from 0 to 0.5 A during the first 15 min, and from 0.5 to 1.5 A for the next 15 min. Then the current is constantly raised up to 17 A. This gives a nickel shim with a thickness of about 300 μm. The silicon wafer is removed. If the wafer is loosely attached to the Ni shim, then this can be carried out by lifting it off by hand, and with stronger adhesion, the Si wafer is dissolved in KOH (figures 2 and 5). The resulting nickel-electroplated sample is punched into an 85 mm diameter shim by using a hydraulic press fitted with a customized punching tool. The shims have two flats to ensure rotational direction definition when mounted in the injection-molding tool. Standard epoxy high-temperature resistant glue is used to fill up the resultant cavities on the backside of the shim, and then manually polished with fine grade sand paper to even the backside.

Replicas of the original structures are injection molded in an ENGEL Victory 80/45 Tech injection molder, with the Ni-shim installed into the mold. The custom designed mold produces 50 mm in diameter and 2 mm in thickness polymer chips that contain 12 Luer-fittings [15] used to connect the microfluidic channels on the chip to external flow or air-pressure controls, figure 2(*b*).

Parts are molded from COC TOPAS grade 5013 from TOPAS Advanced Polymers GmbH. Topas grade 5013 has a glass transition temperature (T_g) of 135 °C and is molded using a variotherm process with a nozzle temperature of 280 °C, a mold temperature of 110 °C and a demolding temperature of 65 °C. A high holding pressure of 1300 bar was used to prevent the polymer from backflowing during the cool down period.

The molded chip is sealed against an extruded 100 μm thick TOPAS foil of the same grade, by UV-assisted thermal bonding. A 3D model of the final device is shown in figure 2.

UV-assisted thermal bonding

Both the chip and thelid were exposed to a UV radiation for 30 s. The exposure was performed using a DIMAX mercury UV bulb F/5000 lamp emitting over the full unfiltered Hg line spectrum and the bonding by using a P/O/Weber press with decoupled internal temperature control of both plates. In order to ensure uniform pressure all over the chip surface, an aluminum holder was built in which the Luer-fitting protrusions could be inserted. In addition, the top lid was covered with a combination of a 300 μm thick nickel disc and a thin PDMS layer with the purpose of compensating possible non-uniformities in flatness. Sealing of the cell-capture device employed a piston force of 10 kN applied for

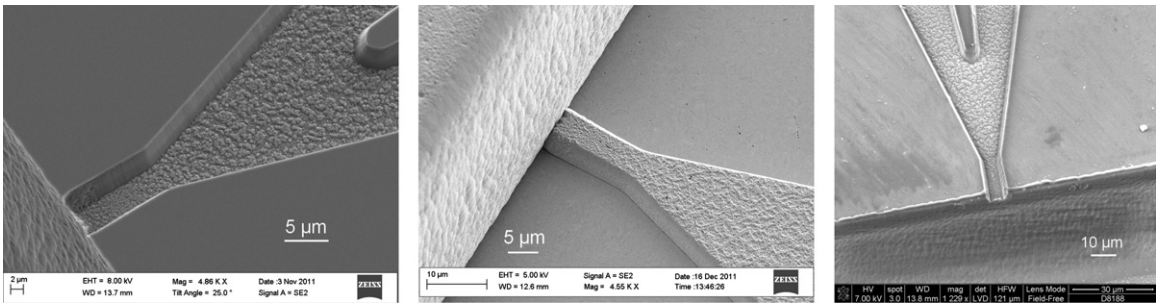

(*a*) (*b*) (*c*)

Figure 6. SEM micrographs of the capturing channel after the main steps of the DEEMO process; shaping of the silicon master (*a*), electroplating of the nickel insert (*b*) and molding of the final part (*c*).

Table 2. Sample surfaces have been evaluated using tapping mode AFM. We used DME DualScope C-21 with BS-TAP300AL probes. Probe force constant was 40 N m^{-1}. We collected topology data from three regions (10.5 μm $\times$ 10.5 μm) on each of investigated samples, selected regions have been cca 75 μm apart. Each region was scanned with resolution of 512 $\times$ 512 points.

	Silicon master			Nickel tool			TOPAS polymer		
	A	B	C	A	B	C	A	B	C
S_A(nm)	0.780	0.773	0.801	0.877	1.000	1.090	0.636	1.060	0.941
S_{RMS}(nm)	1.180	1.010	1.100	1.200	2.640	2.540	0.837	1.400	1.250
S_{SK}	6.020	1.030	2.240	1.240	19.700	18.900	0.600	−0.830	−1.460

5 min, while maintaining a temperature of 120 °C.[5] For the DNA stretching device, the force was applied for 10 min at 110 °C as the standard procedure. The timing and choice of pressure are fairly critical as the polymer begins to deform plastically as it approaches the glass transition temperature.

Validation of the cell-capture chip

HeLa cells were cultured on collagen (type 1, Sigma Aldrich) coated Nunclon T25 flasks (Nunc A/S). Cells were detached using trypsin, triturated to loosen cell clumps, centrifuged at 1200 rpm for 3 min and resuspended in phosphate-buffered saline (PBS, Lonza). The cell solution was vortexed on a vortex mixer to distribute the cells evenly. Microscope images and videos were obtained using an AxioObserver A1 microscope with Axiovision software (Carl Zeiss, GmbH). Prior to experiments, the fluidic channel system of the cell-capture chip was filled with PBS. Cells were introduced into the inlet port by using a 1 ml syringe and they slowly flowed along the carrier channel. When a targeted cell approached within 100 μm from the lateral aperture, a slight suction (<20 mbar) was applied to the side channel using a custom-made pressure controller build from a piezo-valve terminal from Festo controlled with Labview software (National Instruments).

Validation of the nanoslit chip

To ensure that the low aspect ratio nanoslit is open after the bonding, the channels are filled with ethanol. Since the COC polymer is hydrophilic toward ethanol, the filling happens by capillary forces, and no external pumps are required to do the testing. In order to verify that the slit is not collapsed, the chip was observed under a reflective microscope (Zeiss Axioskop 40), and the difference of refractive indexes between ethanol and air makes it easy to see when the nanoslit is filled. See figure 9. To further verify the functionality of the chip, preliminary experiments[6] were performed with YOYO-1 (Invitrogen) stained T4GT7-DNA, with a length of 168.5 kbp suspended in TBE buffer. The DNA was driven into the nanoslit by the application of hydrostatic pressure to relevant Luer ports of the chip and observed by fluorescence microscopy. See the bottom panel of figure 9.

Results and discussions

An overview of the two layouts of the channel patterns is shown in figure 5. In the cell-capture device, a shallow microfluidic channel works as a hydraulic connection between two of the deep inlet channels. The suction channel has a depth and a width shallower than the size of the cells at the opening for the cell capture. It has a wider opening at the other end for the reduction of the total hydraulic resistance of the suction channel for the ease of cell capture by the application of a negative pressure difference across it. A support structure has been introduced for the prevention of collapse of the channel during the bonding process. The second design shows a cross of two nanoslits connected to inlet channels. In both devices the inlet channels connect to buffer reservoirs consisting of female Luer connectors, which provide direct access to the described fluidic systems.

The intersections between inlet channels and either suction capillary or nanoslit are the key features in both the designs. The replication accuracy of those structures at the intersection gives a vital indication about the device performance after bonding. The replication quality of the injection-molded microstructures is investigated by scanning electron microscopy (SEM) and atomic force microscopy

[5] Further details on the bonding process will be reported elsewhere.

[6] Further results on the usage of the DNA devices will be reported elsewhere.

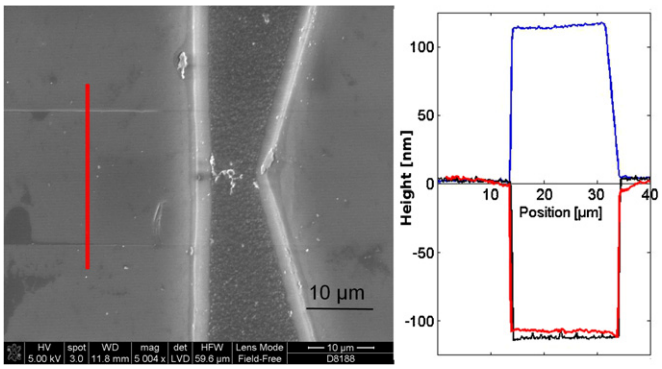

(*a*) (*b*)

Figure 7. Detail of the intersection between nanoslits and carrier channels in the DNA-stretching chip (*a*) together with atomic force microscope (AFM) measurements of the nanoslit section (red line). (*b*) Profile across the slit measured on the silicon wafer (black line), the nickel shim (blue line) and the polymer part (red line).

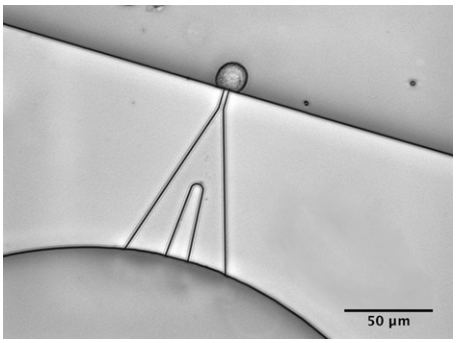

Figure 8. Optical microscope image of a single HeLa cell captured at the cornered aperture at one end of the capturing channel. This chip is a replica of a silicon master fabricated with the modified Bosch process.

(AFM). Figure 6 shows SEM micrographs of the capturing channel after the main steps of the DEEMO process. All details are faithfully replicated from the silicon to the thermoplastic chip. Moreover, the surface roughness of the three samples, respectively, silicon wafer, nickel shim and COC part was investigated by AFM. The polymer part exhibited a very low surface roughness (Sa <1 nm) comparable with the initial roughness of the silicon wafer demonstrating an optimal replication through the whole process. Topology data from the bonding surfaces are shown in table 2. The surface roughness in the channels was somewhat higher, but this was not critical for the functionality of the devices. In the DNA chip, the replication of the nanoslits was verified by the characterization of the silicon, nickel and polymer samples by AFM, results shown in figure 7.

A strong motivation for employing a DEEMO process instead of UV-LIGA is the possibility of exploiting the enormous potential of the MEMS tool box. Multilevel microfluidic systems have been realized by SU-8 [51, 52], and two level SU-8 structures have been used to fabricate high aspect ratio gear structures in plastic by the UV-LIGA process [53]. However, the very low surface flatness across the silicon wafer is easily compromised in the double-layer LIGA process making it very challenging to seal the resulting parts afterward.

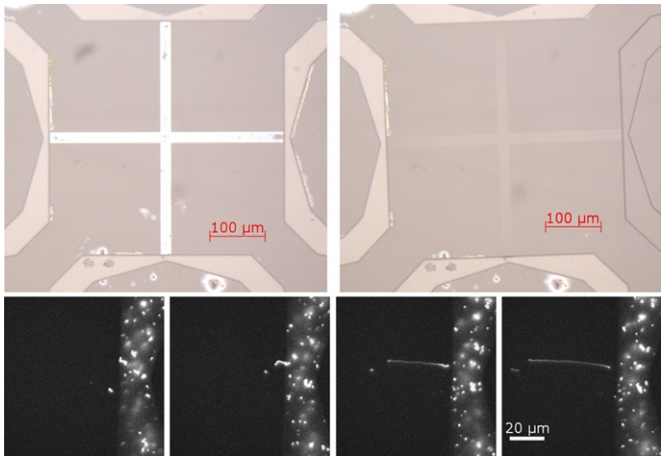

Figure 9. Bonded nanoslit. On the top image to the left, the slit is empty, on the image to the right, the slit has been filled with ethanol. In the bottom pictures, the fluorescence micrographs show a strand of T4GT7-DNA being pushed into the nanoslit. In the picture to the left, the DNA is at the inlet of the nanoslit. For each picture further to the right, it has been pushed further into the slit, until all of it has entered the slit in the picture to the far right.

In addition, the possibility of originating the positive geometry in the silicon master allows a single electroforming, where a nickel 'mother' electroform is not needed [20]. This results in a more robust process avoiding possible challenges when it comes to the mechanical separation of the nickel electroform 'daughter' from the 'mother'.

Injection molding of micron and sub-micron scale structures is achieved through a molding process known as varioterm [7, 54], where the cavity is heated to a temperature close to the glass transition temperature of the polymer to facilitate the polymer to flow into the microfeatures of the mold insert. The part is ejected when the mold is cooled down below a suitable release temperature (in our case 60 °C) to release the molded part well after freeze of the polymer. This process substantially increases the cycle time, which was 220 s long in our case, of which the mold cool down time was 130 s. However, we believe that this time can be significantly reduced in an industrial framework by redesigning the mold for lower thermal mass, and a local cooling and heating system that does not require the whole mold to be heated and cooled. In addition, a parallelization of the molding and bonding process, using a multicavity mold for molding, and a bonding process that allows for bonding of more than one chip at a time would dramatically increase the throughput.

The efficiency of the thermal bonding on both devices was verified by filling the fluidic structures with liquid, as shown in figure 9. The DNA nanoslits with aspect ratios down to 1/200 could be successfully sealed only if great care was taken, using a special rig that allowed avoiding the direct contact between the piston and the foil in the critical slit areas of the devices. Failure modes resulting in collapse were caused by misalignment in the rig, leading to low but finite yield between 5% and 10% for the nanoslit devices. We do not see this issue as prohibitive for commercialization of the devices though, as automated precision alignment is possible on industrial scale. If the aspect ratio was increased to 1/20, the bonding occurred

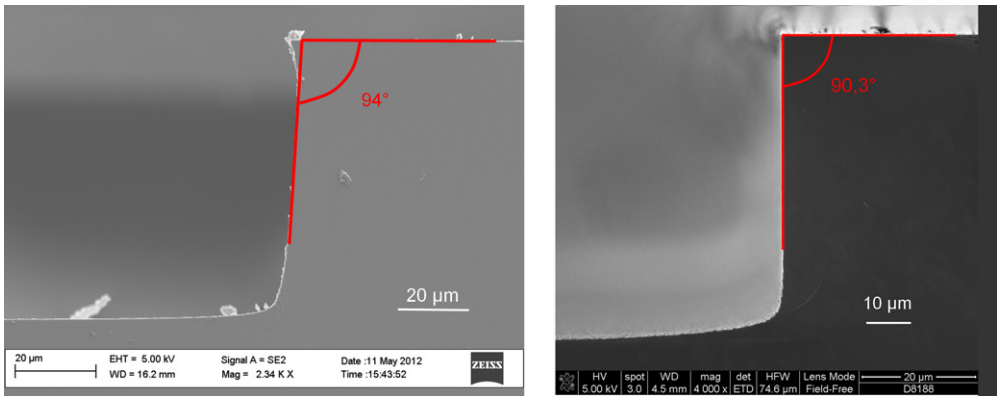

(*a*) (*b*)

Figure 10. (*a*) SEM micrograph of the cross-sectional profile of the deep channel from a cleaved wafer processed with continuous SF6/O2/Ar plasma isotropic etch process. The sidewall is positively tapered with an angle of 94°, while the underetching is about 4 μm. (*b*) SEM micrograph of the cross-sectional profile of the deep channel from a cleaved wafer processed with modified Bosch etching process. The sidewall slope is 90.3° and the underetching at the surface of the wafer is almost non-existing.

without collapse of the structures at almost all times using our standard procedure described above. Moreover, the bonding of chips for cell capture was not prone to channel collapse. When performed properly, the bonding process did not change the channel geometry significantly. This was verified by recording the electrical resistance of the channels, when those were filled with the electrolytic buffer solution. This measurement was then compared with the theoretical value calculated using the specific resistivity of the electrolyte and the detailed channel geometry. This method is very sensitive, since the electrical resistance of microfluidic channels is always dominated by the narrowest channel dimensions. Typically, correspondence within 10% was found between measured and calculated resistance. X-ray photoelectron spectroscopy (XPS) indicated that the UV treatment did not alter the surface chemistry of the parts, as opposed to plasma treatment, which is known to create O–C radicals on the surface. Rather the UV treatment seemed to have an annealing effect on the surface.

HeLa cells were used to demonstrate the functionality of the cell-capture device. Cells were introduced through the Luer ports into the inlet channel and then successfully attracted and trapped to the microopening by applying suction to the end of it. Figure 8 shows an optical micrograph of the capture of an HeLa cell at a cornered aperture. The functionality of the nanoslit system was also demonstrated by preliminary DNA stretching experiments with T4GT7 DNA molecules, as shown in figure 9.

Several dry etching processes for the silicon master origination for the cell-capture design were investigated, as this appeared to be a crucial step in the DEEMO process. Some applications can require channel depths of more than 100 μm, and the deeper the inlet channels, the larger are the challenges associated with demolding of the polymer parts in the injection-molding process. These issues occurred mainly due to undercuts at the interface with the mask in the DRIE process and caused scratching of the inlet channel sidewalls during demolding. In the worst scenario, the scratching can seal off the capture opening and make the device useless. The requirements for a proper mold are smooth and slightly positively tapered sidewalls and negligible undercut.

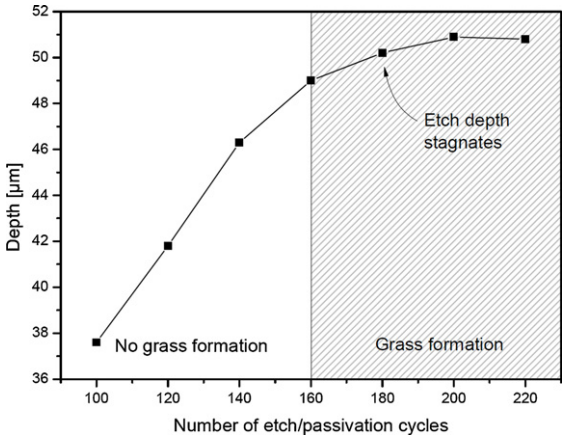

Figure 11. A plot of the etched depth as a function of the number of cycles in the modified DRIE Bosch process for the deep channel etches. It is seen that for high numbers of cycles, the etched depth stagnates, which is consistent with the observation of grass formation in the bottom of the etched channels.

Roxhed *et al* [55] reported on a method for etching tapered sidewalls in silicon using DRIE based on consecutive switching between anisotropic etching using the Bosch process and isotropic dry etching. Li *et al* [56] reported on a continuous DRIE of tapered via holes for three-dimensional integration. Jo *et al* [57] reported on a modified Bosch-type process applied to silicon mold fabrication used for structuring a microarray.

Two fabrication iterations have shown good results and they will be discussed. A continuous SF6/O2/Ar plasma isotropic etch process, as previously described in table 1, resulted in smooth tapered sidewalls (94°) with a mask undercut of about 4 μm, figure 10. The taper deviation at the interface between the oxide mask and the etched substrate is mainly caused by the difficulty of the etch gas to reach regions close below the mask [55]. This curvature generated challenges in terms of demolding when structures shallower than 4 μm have been structured. For smaller and in particular shallower (2 μm) lateral apertures, we used a modified Bosch etching process as a powerful alternative. Smaller capture holes are

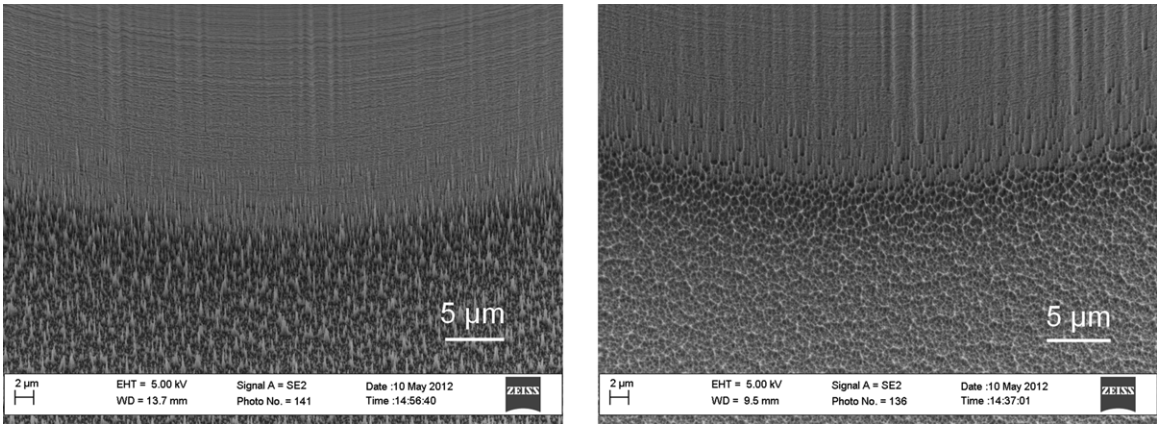

(*a*) (*b*)

Figure 12. (*a*) SEM micrograph of the grass developed in the bottom of the channel due to the high passivation to etch cycle time in the end of the etch process. (*b*) SEM micrograph of the same detail after the polysilicon (mixture of HNO_3, BHF and H_2O) wet etching process.

crucial when the device is intended for electrophysiological recordings [43]. A standard DRIE Bosch process is based on many repetitions of alternating etch and passivation cycles [58]. The etch depth is controlled by adjusting the number of cycles. This results in a scalloped sidewall with a slightly negative slope for deep etching, since ions are experiencing increased deflection from the bottom and sidewalls of the channel, thereby degrading the passivation layer and allowing slight lateral etching [59]. In order to correct this effect, the etch/passivation cycle time over the duration of the process was ramped. The slope of the ramping of the passivation cycle was set to be lower than the slope of the etch cycle time, hence resulting in an increase in the passivation to etch ratio. This was found to counteract the lateral etching and improve the sidewalls slope (90.3°) compared with a standard Bosch etching, see figure 10(*b*). The process showed almost no taper deviation (<0.2 μm). However, the passivation layer was not sufficiently removed, due to the high passivation to etch cycle time at the end of the etch creating substantial grass formation at the bottom of the channel, figure 12(*a*). As can be seen from figure 11, showing the etched depth for varying numbers of etch/passivation cycles, the etch depth starts to stagnate around 160–180 cycles, indicating that the grass formation is dominating for higher cycle numbers. This might potentially be a problem during molding, as the polymer will fill up many small cavities in the nickel shim created by the grass, hence impeding the de-molding process. To this end, a polysilicon etch mixture of HNO_3, BHF and H_2O in the ratio 20:1:20 was found to remove the grass. Wet etching agents were previously used to smoothen rough silicon surfaces [60]. Well-known etchants such as KOH and TMAH can be used to smoothen surfaces, but both KOH and TMAH are anisotropic silicon etching agents, while polysilicon etch is a completely isotropic etch [61]. Figure 12 shows how the wet isotropic etching successfully reduced the grass and smoothened the scallops. The polymer parts injection molded from a silicon master originated with this second method showed excellent replication of the microstructures down to 2 μm in depth. The chip shown in figure 8 was fabricated with the modified Bosch process.

Conclusion

In this work, we presented a replication method for thermoplastic materials that we believe is suitable for prototyping, but also directly applicable to large-scale production. We used a standard injection-molding machine to demonstrate it. We have developed a fabrication scheme to produce multilevel all-polymer devices for biological applications. We employed the DEEMO method, which enables the direct etching of the silicon substrate, and exploits the large MEMS tool box for Si microfabrication. Using dry etching techniques, multilevel microfluidic systems can be structured in silicon and then replicated in thermoplastic polymers. This work also proposes technical solutions to typical challenges for molding of any polymer microfluidic devices such as chip sealing and chip demolding. UV-assisted thermal bonding was found to ensure strong seals of both micro- and nanostructured fluidic channels in the molded parts without altering their geometry. Two different etching processes have been demonstrated for master origination.

Acknowledgments

This work is supported by the Danish Advanced Technology Foundation through the Advanced Technology Project PILOC (grant no 061-2010-1) and by Sophion Bioscience for the part regarding the cell capture and by the Danish Council for Strategic Research through the Strategic Research Center PolyNano (grant no 10-092322/DSF) for the DNA stretching.

References

[1] Becker H and Gaertner C 2008 Polymer microfabrication technologies for microfluidic systems *Anal. Bioanal. Chem.* **390** 89–111
[2] de Mello A 2002 Plastic fantastic? *Lab Chip* **2** 31N–6N
[3] Figeys D and Pinto D 2000 Lab-on-a-chip: a revolution in biological and medical sciences *Anal. Chem.* **72** 330A–5A
[4] Curtis A and Wilkinson C 2001 Nantotechniques and approaches in biotechnology *Trends Biotechnol.* **19** 97–101

[5] Andersson H and van den Berg A 2003 Microfluidic devices for cellomics: a review *Sensors Actuator* B **92** 315–25

[6] Harrison D, Fluri K, Seiler K, Fan Z, Effenhauser C and Manz A 1993 Micromachining a miniaturized capillary electrophoresis-based chemical-analysis system on a chip *Science* **261** 895–7

[7] Becker H and Gartner C 2000 Polymer microfabrication methods for microfluidic analytical applications *Electrophoresis* **21** 12–26

[8] Becker H and Locascio L 2002 Polymer microfluidic devices *Talanta* **56** 267–87

[9] Duffy D, McDonald J, Schueller O and Whitesides G 1998 Rapid prototyping of microfluidic systems in poly(dimethylsiloxane) *Anal. Chem.* **70** 4974–84

[10] Klank H, Kutter J and Geschke O 2002 CO_2-laser micromachining and back-end processing for rapid production of PMMA-based microfluidic systems *Lab Chip* **2** 242–6

[11] McDonald J and Whitesides G 2002 Poly(dimethylsiloxane) as a material for fabricating microfluidic devices *Acc. Chem. Res.* **35** 491–9

[12] Heckele M and Schomburg W 2004 Review on micro molding of thermoplastic polymers *J. Micromech. Microeng.* **14** R1–14

[13] Giboz J, Copponnex T and Mele P 2007 Microinjection molding of thermoplastic polymers: a review *J. Micromech. Microeng.* **17** R96–109

[14] Heckele M, Bacher W and Muller K 1998 Hot embossing—The molding technique for plastic microstructures *Microsyst. Technol.* **4** 122–4

[15] Andresen K O *et al* 2010 Injection molded chips with integrated conducting polymer electrodes for electroporation of cells *J. Micromech. Microeng.* **20** 055010

[16] Becker E *et al* 1982 Production of separation-nozzle systems for uranium enrichment by a combination of x-ray-lithography and galvanoplastics *Naturwissenschaften* **69** 520–3

[17] Kupka R, Bouamrane F, Cremers C and Megtert S 2000 Microfabrication: LIGA-X and applications *Appl. Surf. Sci.* **164** 97–110

[18] Piotter V, Hanemann T, Ruprecht R and Hausselt J 1997 Injection molding and related techniques for fabrication of microstructures *Microsyst. Technol.* **3** 129–33

[19] Malek C and Saile V 2004 Applications of LIGA technology to precision manufacturing of high-aspect-ratio micro-components and -systems: a review *Microelectron. J.* **35** 131–43

[20] McCormick R, Nelson R, AlonsoAmigo M, Benvegnu J and Hooper H 1997 Microchannel electrophoretic separations of DNA in injection-molded plastic substrates *Anal. Chem.* **69** 2626–30

[21] Elders J, Jansen H, Elwenspoek M and Ehrfeld W 1995 DEEMO: A new technology for the fabrication of microstructures *IEEE Proc. Micro Electro Mechanical Systems (New York, NY)* pp 238–43

[22] Fintschenko Y and van den Berg A 1998 Silicon microtechnology and microstructures in separation science *J. Chromatogr.* A **819** 3–12

[23] Judy J 2001 Microelectromechanical systems (MEMS): fabrication, design and applications *Smart Mater. Struct.* **10** 1115–34

[24] Kastenmeier B, Matsuo P, Beulens J and Oehrlein G 1996 Chemical dry etching of silicon nitride and silicon dioxide using CF4/O-2/N-2 gas mixtures *J. Vac. Sci. Technol.* A **14** 2802–13

[25] Bondur J 1976 Dry process technology (reactive ion etching) *J. Vac. Sci. Technol.* **13** 1023–9

[26] Yih P, Saxena V and Steckl A 1997 A review of SiC reactive ion etching in fluorinated plasmas *Phys. Status Solidi* b **202** 605–42

[27] Lamonte R and McNally D 2000 Uses and processing of cyclic olefin copolymers *Plast. Eng.* **56** 51–5

[28] Shin J, Park J, Liu C, He J and Kim S 2005 Chemical structure and physical properties of cyclic olefin copolymers—(IUPAC technical report) *Pure Appl. Chem.* **77** 801–14

[29] Nunes P S, Ohlsson P D, Ordeig O and Kutter J P 2010 Cyclic olefin polymers: emerging materials for lab-on-a-chip applications RID A-7838–2012 RID E-3256–2010 *Microfluid. Nanofluid.* **9** 145–61

[30] Castano-Alvarez M, Fernandez-Abedul M and Costa-Garcia A 2005 Poly(methylmethacrylate) and topas capillary electrophoresis microchip performance with electrochemical detection *Electrophoresis* **26** 3160–8

[31] Faure K *et al* 2008 Development of an acrylate monolith in a cyclo-olefin copolymer microfluidic device for chip electrochromatography separation *Electrophoresis* **29** 4948–55

[32] Liu J, Ro K, Nayak R and Knapp D R 2007 Monolithic column plastic microfluidic device for peptide analysis using electrospray from a channel opening on the edge of the device *Int. J. Mass Spectrom.* **259** 65–72

[33] International Standard ISO 1986 1st edn 5941

[34] Di Carlo D and Lee L P 2006 Dynamic single-cell analysis for quantitative biology *Anal. Chem.* **78** 7918–25

[35] Jang L and Wang M 2007 Microfluidic device for cell capture and impedance measurement *Biomed. Microdevices* **9** 737–43

[36] Nilsson J, Evander M, Hammarstrom B and Laurell T 2009 Review of cell and particle trapping in microfluidic systems *Anal. Chem. Acta* **649** 141–57

[37] Taff B and Voldman J 2005 A scalable addressable positive-dielectrophoretic cell-sorting array *Anal. Chem.* **77** 7976–83

[38] Grier D 2003 A revolution in optical manipulation *Nature* **424** 810–6

[39] Lee H, Purdon A and Westervelt R 2004 Manipulation of biological cells using a microelectromagnet matrix *Appl. Phys. Lett.* **85** 1063–5

[40] Evander M *et al* 2007 Noninvasive acoustic cell trapping in a microfluidic perfusion system for online bioassays *Anal. Chem.* **79** 2984–91

[41] Seo J, Ionescu-Zanetti C, Diamond J, Lal R and Lee L 2004 Integrated multiple patch-clamp array chip via lateral cell trapping junctions *Appl. Phys. Lett.* **84** 1973–5

[42] Lee P, Hung P, Shaw R, Jan L and Lee L 2005 Microfluidic application-specific integrated device for monitoring direct cell-cell communication via gap junctions between individual cell pairs *Appl. Phys. Lett.* **86** 223902

[43] Ionescu-Zanetti C, Shaw R, Seo J, Jan Y, Jan L and Lee L 2005 Mammalian electrophysiology on a microfluidic platform *Proc. Natl Acad. Sci. USA* **102** 9112–7

[44] Tegenfeldt J *et al* 2004 The dynamics of genomic-length DNA molecules in 100-nm channels *Proc. Natl Acad. Sci. USA* **101** 10979–83

[45] Riehn R, Lu M, Wang Y, Lim S, Cox E and Austin R 2005 Restriction mapping in nanofluidic devices *Proc. Natl Acad. Sci. USA* **102** 10012–6

[46] Utko P, Persson F, Kristensen A and Larsen N B 2011 Injection molded nanofluidic chips: Fabrication method and functional tests using single-molecule DNA experiments RID F-3057–2011 RID C-4746-2008 *Lab Chip* **11** 303–8

[47] Reisner W *et al* 2005 Statics and dynamics of single DNA molecules confined in nanochannels *Phys. Rev. Lett.* **94** 196101

[48] Reisner W *et al* 2010 Single-molecule denaturation mapping of DNA in nanofluidic channels *Proc. Natl Acad. Sci. USA* **107** 13294–9
[49] Chantiwas R *et al* 2010 Simple replication methods for producing nanoslits in thermoplastics and the transport dynamics of double-stranded DNA through these slits *Lab Chip* **10** 3255–64
[50] Lee J, Yun Y, Kim Y and Jo K 2009 PDMS nanoslits without roof collapse *Bull. Korean Chem. Soc.* **30** 1793–7
[51] Huang S, Tan W, Tseng F and Takeuchi S 2006 A monolithically three-dimensional flow-focusing device for formation of single/double emulsions in closed/open microfluidic systems *J. Micromech. Microeng.* **16** 2336–44
[52] Steigert J *et al* 2008 A versatile and flexible low-temperature full-wafer bonding process of monolithic 3D microfluidic structures in SU-8 *J. Micromech. Microeng.* **18** 095013
[53] Lorenz H, Despont M, Fahrni N, Brugger J, Vettiger P and Renaud P 1998 High-aspect-ratio, ultrathick, negative-tone near-UV photoresist and its applications for MEMS *Sensors Actuator* A **64** 33–39
[54] Fu G, Loh N, Tor S, Tay B, Murakoshi Y and Maeda R 2005 A variotherm mold for micro metal injection molding *Microsyst. Technol.* **11** 1267–71
[55] Roxhed N, Griss P and Stemme G 2007 A method for tapered deep reactive ion etching using a modified bosch process *J. Micromech. Microeng.* **17** 1087–92
[56] Li R, Lamy Y, Besling W F A, Roozeboom F and Sarro P M 2008 Continuous deep reactive ion etching of tapered via holes for three-dimensional integration *J. Micromech. Microeng.* **18** 125023
[57] Jo S, Lee M, Lee S, Lee E, Park S and O B 2005 Characterization of a modified Bosch-type process for silicon mold fabrication *J. Vac. Sci. Technol.* A **23** 905–10
[58] Ayon A A, Braff R, Lin C C, Sawin H H and Schmidt M A 1999 Characterization of a time multiplexed inductively coupled plasma etcher *J. Electrochem. Soc.* **146** 339–49
[59] Dixit P and Miao J 2006 Effect of SF(6) flow rate on the etched surface profile and bottom grass formation in deep reactive ion etching process *J. Phys.: Conf. Ser.* **34** 577–82
[60] Tezcan D S *et al* 2006 Development of vertical and tapered via etch for 3D through wafer interconnect technology *Proc. Conf. Electron. Packaging Technol. (New York, NY)* pp 22–8
[61] Kovacs G, Maluf N and Petersen K 1998 Bulk micromachining of silicon *Proc. IEEE* **86** 1536–51

Paper 2

DNA barcoding via counterstaining with AT/GC sensitive ligands in injection-molded all-polymer nanochannel devices

Peter Friis Østergaard, Marco Matteucci, Walter Reisner, and Rafael Taboryski

Analyst, 2013 **138** 1249-1255

Analyst

RSC Publishing

PAPER

View Article Online
View Journal | View Issue

Cite this: *Analyst*, 2013, **138**, 1249

DNA barcoding *via* counterstaining with AT/GC sensitive ligands in injection-molded all-polymer nanochannel devices

Peter Friis Østergaard,[a] Marco Matteucci,[a] Walter Reisner†[b] and Rafael Taboryski†*[a]

Received 19th October 2012
Accepted 11th December 2012

DOI: 10.1039/c2an36522g

www.rsc.org/analyst

Nanochannel technology, coupled with a suitable DNA labeling chemistry, is a powerful approach for performing high-throughput single-molecule mapping of genomes. Yet so far nanochannel technology has remained inaccessible to the broader research community due to high fabrication cost and/or requirement of specialized facilities/skill-sets. In this article we show that nanochannel-based mapping can be performed in all polymer chips fabricated *via* injection molding: a fabrication process so inexpensive that the devices can be considered disposable. Fluorescent intensity variations can be obtained from molecules extended in the polymer nanochannels *via* chemical counterstaining against YOYO-1. In particular, we demonstrate that the counterstaining induced fluorescent intensity variations to a large degree appear to be proportional to the theoretically computed sequence-maps of both local AT and GC variation along DNA sequences.

1 Introduction

Genomics technology today has two serious drawbacks: (1) extensive fragmentation of the genome is necessitated by sample preparation steps required for currently available sequencing platforms and (2) some form of molecular or clonal amplification is required to produce sufficient sample for analysis. These difficulties tend to increase the complexity of existing platforms, lowering throughput and ultimately increasing cost. For example, the low read lengths of currently available sequencing platforms[1] ensure that the genome assembly and validation, not actual sequencing, is the rate limiting step for de novo analysis of genomes. Moreover, a large portion of the variability in human genomes arises from structural variation[2] (*e.g.* balanced/unbalanced translocations, insertions/deletions, inversions), a large-scale (10 kbp to 1 Mbp) reshuffling of genetic content that can be more difficult to assess from short reads. Critical contextual information, arising from linkage of multiple markers over Mbp-scale genomic regions, is also lost during genomic fragmentation. Amplification steps introduce additional complexity and uncertainty, in particular drop-out of alleles[3] and misrepresentation of certain genomic regions. Finally, there is growing interest in technology platforms with the capability to perform direct genomic analysis at the level of single-cells. Such a capability would preclude the need for cell culture (still relatively time-consuming and laborious) and avoid ensemble averaging over large heterogeneous cellular populations (*e.g.* in a diagnostic situation where sequence information at the single-cell level might be important for optimizing treatment strategies, such as cells obtained from a tumor biopsy).

Nanofluidic devices have the capability of performing analysis at the level of single-molecules, potentially eliminating the need for amplification steps and enabling direct assessment of a biological material in its native state. Nanochannels, constructed with dimensions below the coil-size of typical DNA analytes have the property that they can unscroll individual DNA molecules for linear analysis.[4,5] Parallel nanochannel arrays can be used to isolate and extend many molecules at one time. Continuous throughput is assured by simply driving the molecules through the array *via* either electrophoresis or pressure actuated hydrodynamics, leading to potential throughput ~Gbp per hour. Sequence information is obtained from optical interrogation of the parallel extended molecules *via* a sensitive electron multiplying CCD (EMCCD). Nanochannel technology, despite its advantages, has had limited dissemination into the broader community due to the significant specialized expertise and expense required to produce conventional glass/silicon nanochannel devices. In addition, the cost of the devices tends to limit experimental development of the technique and requires chips to be reused, resulting in nonspecific binding of various compounds to the surface of the chip[6] and cross-contamination issues between experiments.

Specialized labeling strategies are required to read-out sequence maps from the nanochannel extended molecules. One early approach was to perform a restriction digest of a single

[a]*Department of Micro- and Nanotechnology, Technical University of Denmark, DK-2800 Kongens Lyngby, Denmark. E-mail: rata@nanotech.dtu.dk; Tel: +45 4525 8155*

[b]*Department of Physics, McGill University, Montreal, QC, Canada*

† These two authors have shared last authorship.

molecule in a nanochannel.[7] This approach necessarily has the disadvantage that it fragments the analyte during analysis. An alternative enzymatic-based mapping scheme, that does not require DNA fragmentation, is to use a single-stranded nicking enzyme to create a break in one strand (at a particular recognition motif) that is subsequently filled in by DNA polymerase with fluorescent nucleotides.[8–10] These approaches are powerful,[11] but they have the disadvantage of requiring fairly complex and expensive labeling probes or chemistries, and are difficult to implement on-chip, particularly in the context of single-cell analysis. Consequently, there is interest in developing barcoding strategies that are both inexpensive and simple to apply. One recently developed 'non-enzymatic' barcoding strategy is based on a fluorescent analog of denaturation mapping.[12] The principle of this technique is to stain nanochannel extended DNA with a fluorophore (YOYO-1) that unbinds from single-stranded regions. When the molecule is melted *via* a combination of heating and added chemical denaturants, a characteristic pattern of bright and dark bands develops along the molecule containing information on local melting probability (a pattern that can be ultimately related to sequence *via* algorithms that model local chain statistical mechanics). While denaturation mapping has been scaled to enable analysis of intermediate size genomes (such as yeast, ~11 Mbp (ref. 13)), it has a number of drawbacks, in particular the requirement of external heating and the use of toxic reagents such as formamide to ensure denaturation conditions remain in place during an experiment. Such conditions add complexity for any potential commercial realization of the denaturation mapping technique. Moreover, denaturation mapping is naturally limited by fundamental physics to produce banding-patterns that are a function of local melting conditions, with dark-regions of the barcode tending to be AT rich and bright regions GC rich. Recently, Nyberg *et al.*[14] proposed a new type of barcoding technique based on counterstaining the double stranded DNA molecule with netropsin. Netropsin is a minor groove binder with a preference for AT rich regions.[15] The binding of netropsin blocks the binding of uniform DNA stains such as YOYO-1, creating a variation intensity profile that tracks local AT concentration. Since this method does not require partial melting of the DNA, it is not sensitive to the temperature at which the experiment is conducted, eliminating the need for thermal control in the experimental setup and the addition of denaturants to the running buffer.

Here we present a low-cost nanochannel mapping platform based on injection-molded polymer devices.[16,17] Injection-molding is one of the most inexpensive production technologies available (used for example to produce small plastic items used in our everyday life such as tooth-brushes, lego bricks, bottle-caps, *etc.*). Consequently, our injection molded devices have a production cost and time that is significantly lower than that for conventionally nanofabricated silicon and glass devices, so low that these devices can be considered truly disposable. While injection-molded devices have been previously used for extending individual DNA molecules,[18] this publication demonstrates that all-polymer injection-molded devices can be fabricated with a sufficiently low autofluorescence to perform actual DNA sequence mapping. In particular, inspired by chemistries used for counterstaining in classic chromosomal scale karyotyping applications,[19] we demonstrate that the counterstaining approach developed by Nyberg *et al.* can be generalized to include compounds with high GC affinity as well as AT affinity. This generalization of the counter-staining technique allows us to reverse the barcode pattern obtained and enhance the flexibility of the technique to probe sequences with different AT/GC content, a critically important feature due to the large variation of AT/GC content between genomes.

2 Methods and materials

2.1 Chip fabrication

The fluidic chips used for the experiments were fabricated in the cyclic olefin co-polymer TOPAS 5013L-10 (TOPAS Advanced Polymers) *via* injection molding.

To fabricate the chips, a silicon wafer is processed in clean room facilities, using UV-lithography, e-beam-lithography, and reactive ion etching. This gives a silicon wafer with the same topology as the final polymer chips. A 100 nm thick seed layer of nickel vanadium (93% Ni, 7% V) is sputtered on top of the silicon wafer, and a 300 μm thick shim is electroformed on top of the wafer. After separation from the Si wafer, the shim is cut out to fit into a commercial injection molder, enabling mass-production of polymer devices. The reproduced nanochannels at the microchannel inlet are seen in Fig. 1.

After injection molding, the polymer part is bonded with a polymer foil in an UV assisted thermal bonding process,[20] where both foil and chip are exposed for a short time under a UV lamp. The foil and chip are then bonded for 10 min at 115 °C with a pressure of 5 bar. A finished polymer chip is seen in Fig. 2. The dimensions of the nanochannels in these chips are 440 nm wide and 120 nm high. This dimension turned out to ensure the best

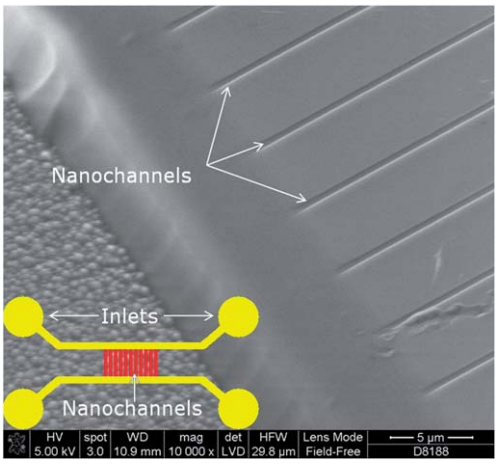

Fig. 1 Scanning electron micrograph of the nanochannels on the injection molded portion of the device. The nanochannels are shown interfaced to the microchannel used for loading polymer solution. The nanochannels have a width of 440 nm and a depth of 120 nm. The sketch at the lower left corner shows the layout of the system.

Fig. 2 Injection molded polymer chip. The chip includes ISO-standard Luer fittings for easy access and application of pneumatic pressure. Since a single nanochannel device requires only four inlets, and the chip contains twelve inlets, the design can be iterated three times increasing the multiplexing capability of each chip.

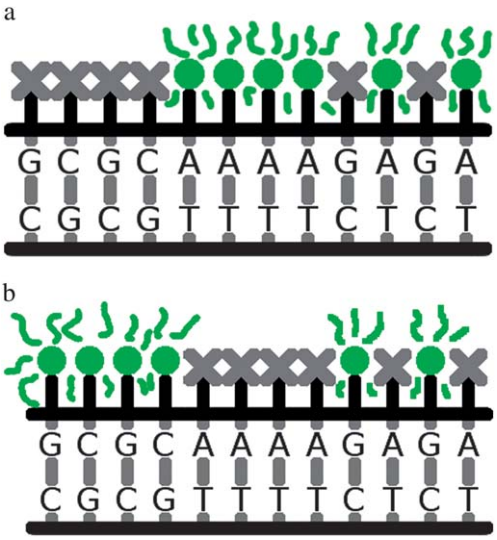

Fig. 3 Principle of the counterstaining approach. The figure on the left corresponds to counterstaining, using actinomycin D, that binds to GC rich regions of the DNA, lowering the degree of binding of YOYO-1 at GC rich regions. The figure on the right corresponds to counterstaining, using netropsin, that binds to AT rich regions of the DNA, lowering the binding of the YOYO-1 at AT rich regions.

trade off between fabrication yield and functionality. The carrier channels leading to the nanochannels are 50 μm wide and 5 μm deep. The fabrication process for producing polymer chips of this kind has been described thoroughly by Tanzi *et al.*[17] These dimensions indicate that we should expect a de Gennes confinement regime[5] rather than the Odijk regime.[21] However, as will be shown, this is sufficient for the experiments performed in this work.

2.2 DNA preparation

Linear λ-DNA (48.5 kbp) and the linear but circularly permuted sequence T4GT7-DNA (168.5 kbp) are used as test constructs to assess the counterstaining technique in injection-molded devices. DNA used in the barcoding experiment is stained with YOYO-1 (Invitrogen), using either netropsin (Sigma-Aldrich) or actinomycin D (Invitrogen) as the counterstaining agent. Netropsin is known to bind to the AT-rich regions of the DNA molecule,[15] limiting the binding of YOYO-1 at this position, while the actinomycin D binds to the GC-rich regions.[22,23] Counterstaining with netropsin will thus result in an inverted fluorescent intensity profile to the one obtained by counterstaining with actinomycin D. The principle behind the counterstaining is presented graphically in Fig. 3.

For 100 μL of stained DNA, counterstained with actinomycin D, 1 μg of DNA is mixed with actinomycin D and YOYO-1. The ratio of base pairs to YOYO-1 molecules is 10 : 1 and the ratio of actinomycin D molecules to YOYO-1 molecules is 250 : 1. The suspension is incubated for 2 h at 50 °C, and stored at −20 °C until use. The best results are obtained if experiments are performed shortly after staining of the DNA. Counterstaining with netropsin is performed exactly as described above, only exchanging the actinomycin D with netropsin in a concentration that is 4000 times higher than the concentration of YOYO-1.

2.3 Experimental setup

The polymer chips are initially pre-wetted with a 7% ethanol solution which is exchanged with 0.5× Tris/Borate/EDTA (TBE) prior to introduction of DNA. The counterstained and YOYO-1 labelled DNA solution is then diluted 1 : 10 in degassed 0.5× TBE. Triton X-100 (Sigma-Aldrich) is added at 0.5% (v/v) to the loading buffer to prevent sticking of the DNA to the polymer surface. In addition, 0.5× TBE containing 3% (v/v) β-mercaptoethanol (Sigma-Aldrich) is added to avoid photonicking. The DNA solution is then introduced into one of the luer ports on the device and the ports are connected to an air-pump for applying positive pressure. DNA molecules are brought from the luer reservoir to the nanochannel inlet by applying the pressure drop across the microchannel. Subsequently, the flow can be redirected to drive DNA into the nanochannel array by applying pressure across the nanochannels. As the DNA enters the nanochannel, the channel confinement forces the DNA to stretch out to around 25% of its contour length, in good agreement with previously published simulated data.[21] The dimensions of the channels correspond to the DNA being in the de Gennes regime, as described by Reisner *et al.*[5] and Brochard and de Gennes,[24] and while a more profound stretching would be beneficial for the resolution of the data,[25,26] it was still possible to get a high confidence of the results obtained during the experiments. The fluorescence profile across the nanochannel DNA contains sequence information with a resolution limited by optical diffraction and the degree of stretching to around 2 kbp. Raw images of λ-DNA inside the nanochannels are shown in Fig. 4. Data acquisition is performed using an inverted Nikon microscope (Nikon Eclipse Ti) with a 100× oil immersion objective (NA = 1.4) and an EMCCD (Andor). Molecules are imaged for 50 consecutive images with a frame rate of 10 fps.

During the time used for an experiment, neither significant photonicking nor photobleaching was experienced.

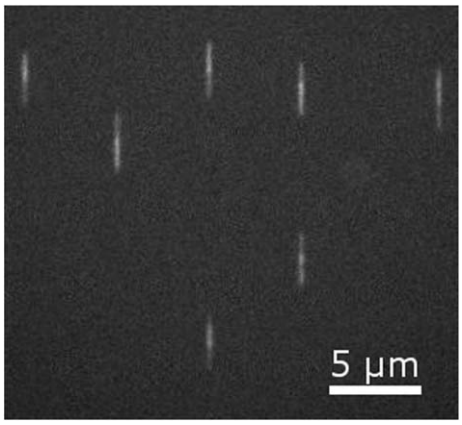

Fig. 4 λ-DNA inside the nanochannels. The physical confinement of the nanochannels forces the DNA molecules to stretch out.

3 Results and discussion

3.1 Barcoding

The goal of our analysis procedure is to extract a high-signal to noise barcode from the raw single-molecule data. To obtain this goal, it is important, that the autofluorescence of the polymer chip is as low as possible. The TOPAS COC is known for having a small change in autofluorescence over time,[27,28] along with an initially low autofluorescence value. In our setup, the average measured background signal measured over the entire field of view, was only 1.6 ± 0.3 times higher than that of a similar chip, fabricated in fused silica, excited with light having a wavelength of 480 nm and data recorded at 535 nm (a method proposed by S. Stavis[29]). Four measurements were performed on both polymer and glass chips to obtain the quoted standard deviation.

The intensity profile transverse to the axis of stretching contains information only about the optical resolution. Consequently, for a given molecule, we sum the intensity transverse to the nanochannel axis and plot this intensity along the nanochannel, converting the image stack to a gray scale plot of intensity *vs.* the position along the channel on one axis and time on the other axis. In order to average intensity profiles captured at different times we must take into account thermal (Brownian) fluctuations of the molecule that induce distortions of the barcode between frames. Brownian dynamics create displacements of the center-of-mass position *via* diffusion and fluctuations in local molecule concentration (arising as a superposition of spatial Fourier modes along the extended molecule). Thermal fluctuations are taken into account *via* the approach described by Reisner *et al.*[12] Center-of-mass motion of DNA is removed *via* direct calculation of molecule spatial translation (obtained from correlation of intensity profiles between frames). Concentration fluctuations are removed by computing the series of local dilations that minimize the least squared difference between a reference frame (taken as the initial frame) and a given frame in the image series. If this procedure is applied to all frames acquired, the intensity profile between frames will be normalized and can be averaged together, yielding a single-molecule barcode with the highest signal-to-noise possible for the given dataset. For each set of parameters used, at least 30 molecules are measured, so that it is possible to obtain average barcodes that represent the consensus of a number of single-molecule measurements.

We expect intensity variation arising from counterstaining to be a function of the local AT/GC concentration. In particular, we expect the local intensity $I(s)$ as a function of sequence position s along the nanochannel extended molecule to be proportional to the local GC concentration (for netropsin) and AT concentration (actinomycin D) with a proportionality factor that depends on the level of YOYO-1 staining. The local AT/GC concentration is obtained convolving a binary version of the genetic code, where ATs and GCs are converted into either ones or zeros, depending on whether netropsin or actinomycin is used, with a Gaussian profile having a standard deviation of 1.5 pixels/200 nm to simulate broadening due to finite optical resolution.

The experimentally obtained barcode is normalized using the algorithm

$$P_{\mathrm{exp}} = \frac{I_{\mathrm{exp}} - \langle I_{\mathrm{exp}} \rangle}{\sqrt{\left\langle \left(I_{\mathrm{exp}} - \langle I_{\mathrm{exp}} \rangle \right)^2 \right\rangle}}$$

where I_{exp} is the EMCCD camera pixel value reading.

The normalized barcodes were aligned to the theoretical profile, after normalization of the theoretical barcode, the same way as for the experimental one.

$$P_{\mathrm{theory}} = \frac{I_{\mathrm{theory}} - \langle I_{\mathrm{theory}} \rangle}{\sqrt{\left\langle \left(I_{\mathrm{theory}} - \langle I_{\mathrm{theory}} \rangle \right)^2 \right\rangle}}$$

Inter-profile shift that yields a minimum of the squared intensity difference between the profiles (summed across all pixels), was then found, *i.e.* we find the least squares estimator for barcode no. i as

$$\delta_i = \min \sum_{n=s}^{m+s} \frac{\left(P_{\mathrm{exp},i}(n) - P_{\mathrm{theory}}(n) \right)^2}{m}$$

where s is the starting point along the theoretical barcode that is used as an optimizing parameter, and m is the pixel length of the barcode.

During this alignment process we also dilated or contracted the theoretical barcode by up to 15% to yield the best fit (this procedure takes into account the fact that the measured barcode may not exactly represent the true equilibrium profile). In addition, for the linear λ-DNA sequence we must find the reading direction of the molecule that yields the best alignment, while alignment of the circularly permuted T4GT7-DNA sequence also requires determination of the sequence-starting point. The average of the fitted barcodes, $P_{\mathrm{consensus}} = \langle \delta_i \rangle$, from the DNA used in the experiments is shown in Fig. 5. The expected inversion of the barcodes, occurring as an effect of changing the counterstaining agent from actinomycin D to netropsin, is easily seen, when comparing the figures to the left of Fig. 5 to the figure to the right.

Although it is shown, that there is a clear correspondence between the measured intensity and the level of AT/GC content in the molecule, the difference in exposure over the field of view of the microscope makes it challenging to directly translate a measured intensity profile to an AT/GC content of a molecule. However, we can always normalize to the intensity variation caused by non-uniform illumination by analysis of how the background levels vary. This normalization was not necessary for the relatively short molecules used in these experiments as the region of interest was small enough for the background to be constant within the region. Hence if part of the molecule is known and can be used as reference, the AT/GC level of the rest of the molecule can also be measured.

3.2 Validity of fit

To ensure that the fit to the theoretical barcode is not just a fit based on random noise in the system, but a fit to the underlying DNA sequence, the experimental profile is also aligned to 500 randomly generated barcodes, giving 500 consensus barcodes, using the same procedure as the alignments to the true theoretical barcode. In order to measure the goodness of fit, we will define an estimator that is the standard deviation between the average experimental barcode and the theoretical barcode.

$$\sigma_j = \sqrt{\left\langle \left(\Delta P_j - \langle \Delta P_j \rangle\right)^2 \right\rangle}$$

ΔP being the difference between the consensus barcode, and its corresponding, randomly generated, theoretical barcode.

In the case of T4GT7 DNA stained with actinomycin D, estimator values for all 500 random barcodes are histogramed and are seen to follow a near perfect Gaussian distribution with a mean of 0.742 and standard deviation of 0.086 as seen in Fig. 6. We observe that the estimator value found when aligning the experimental barcodes to the real theoretical barcode is far away from the centre of this distribution, so that it has a very low probability of happening by chance (we find the probability that an alignment of this quality would happen by chance is 1.9×10^{-7}). However, even though there is a clear correspondence between the data and the theory in Fig. 5, some deviations are observed, *e.g.* peaks between 30 and 50 kbp are not present in the data at the top right graph. We believe these deviations most probably should be explained by shortcomings of the simple theoretical model applied here. As previously described by Nyberg *et al.*,[14] the large peaks in the intensity map are easily seen when comparing the experimental data with the theoretical curve, but the small features are blurred out due to thermal fluctuation and diffusion.

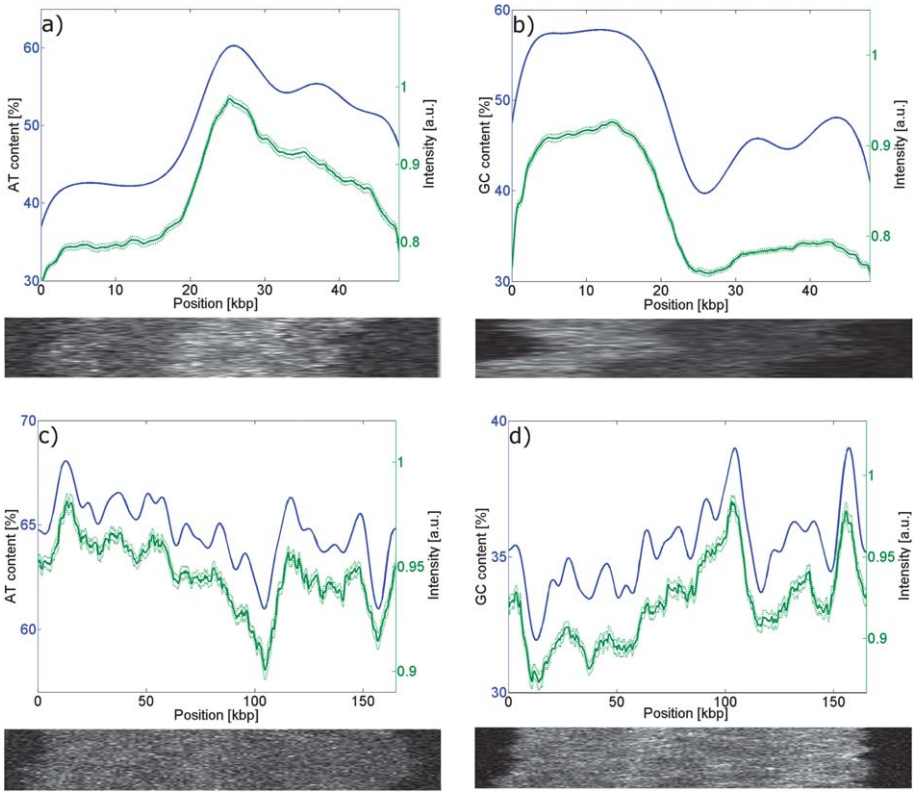

Fig. 5 Theoretical and experimental barcodes for the DNA sequences used in the experiments. (a) is λ-DNA counter stained with actinomycin D, (b) is λ-DNA counterstained with netropsin, (c) is T4GT7-DNA counter stained with actinomycin D, and (d) is T4GT7-DNA counter stained with netropsin. In all cases, the blue line uses the *y*-axis on the left, and corresponds to the theoretical barcode, while the green line uses the *y*-axis on the right, and corresponds to the average experimental barcode. The dotted green lines indicate the standard deviation of the average barcode. Below each barcode is seen a recording of a single molecule, measured for that specific experiment. At least 30 molecules were used in order to get the average experimental barcode and the corresponding confidence limits.

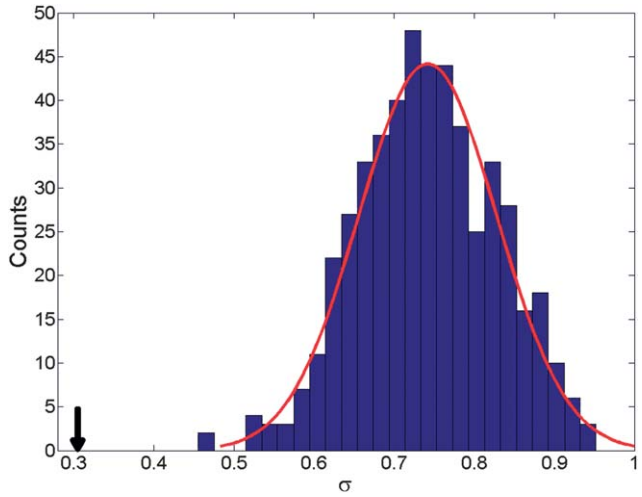

Fig. 6 Distribution of estimator values σ obtained by comparing experimental barcode for T4GT7 counter stained with actinomycin D against random barcodes. The dark arrow indicates the estimator value obtained from the fit against a theoretical barcode determined from the known sequence. This estimator value is sufficiently low that we would not expect it to occur by chance.

4 Conclusion

In conclusion we have demonstrated a proof of concept that direct barcoding using counterstaining against YOYO-1 with either GC or AT selective ligands can facilitate fast identification of specific DNA samples. We have also demonstrated that this barcoding can be performed *via* disposable injection molded devices, a feature which may facilitate future adoption of this technology. We emphasize that the possibility of mapping chemistries that can probe either GC or AT content is highly advantageous, as it allows selection of the mapping chemistry that gives the highest signal contrast possible for a given sequence region. For example, if a sequence loci under investigation is known to have a large GC concentration, it would be beneficial to use netropsin, since this will still leave the GC sites mostly free and YOYO-1 will bind to the residual regions of high AT concentration. The same is true for sequences having a large AT content, where it would be beneficial to use actinomycin D. Along with the use of cheap, disposable polymer chips, this counterstaining technique has potential of reducing the cost of performing genetic barcoding, as – with the single exception of YOYO-1 – it does not require any expensive fluorescent probes or reagents.

Acknowledgements

The authors gratefully acknowledge funding from the Danish Council for Strategic Research, DSF, under the grant agreement no. 10-092322 (PolyNano). The authors would like to thank Henrik Flyvbjerg, Rodolph Marie, and Rob Welch for fruitful discussions, and the staff of DTU DANCHIP for practical help with the device fabrication.

References

1 J. Shendure and H. Ji, *Nat. Biotechnol.*, 2008, **26**, 1135–1145.
2 J. M. Kidd, G. M. Cooper, W. Donahue, H. Hayden, N. Sampas, T. Graves, N. Hansen, B. Teague, C. Alkan, F. Antonacci, E. Haugen, T. Zerr, N. Yamada, P. Tsang, T. Newman, E. Tuzun, Z. Cheng, H. Ebling, N. Tusneem, R. David, W. Gillett, K. Phelps, M. Weaver, D. Saranga, A. Brand, W. Tao, E. Gustafson, K. McKernan, L. Chen, M. Malig, J. Smith, J. Korn, S. McCarroll, D. Altshuler, D. Peiffer, M. Dorschner, J. Stamatoyannopoulos, D. Schwartz, D. Nickerson, J. Mullikin, R. Wilson, L. Bruhn, M. Olson, R. Kaul, D. Smith and E. Eichler, *Nature*, 2008, **453**, 56–64.
3 W. Piyamongkol, M. G. Bermudez, J. C. Harper and D. Wells, *Hum. Mol. Genet.*, 2003, **9**, 411–420.
4 J. Tegenfeldt, C. Prinz, H. Cao, S. Chou, W. Reisner, R. Riehn, Y. Wang, E. Cox, J. Sturm, P. Silberzan and R. Austin, *Proc. Natl. Acad. Sci. U. S. A.*, 2004, **101**, 10979–10983.
5 W. Reisner, K. Morton, R. Riehn, Y. Wang, Z. Yu, M. Rosen, J. Sturm, S. Chou, E. Frey and R. Austin, *Phys. Rev. Lett.*, 2005, **94**, 196101.
6 D. Huber, R. Manginell, M. Samara, B. Kim and B. Bunker, *Science*, 2003, **301**, 352–354.
7 R. Riehn, M. C. Lu, Y. M. Wang, S. F. Lim, E. C. Cox and R. H. Austin, *Proc. Natl. Acad. Sci. U. S. A.*, 2005, **102**, 10012–10016.
8 K. Jo, D. M. Dhingra, T. Odijk, J. J. de Pablo, M. D. Graham, R. Runnheim, D. Forrest and D. C. Schwartz, *Proc. Natl. Acad. Sci. U. S. A.*, 2007, **104**, 2673–2678.
9 M. Xiao, A. Phong, C. Ha, T.-F. Chan, D. Cai, L. Leung, E. Wan, A. L. Kistler, J. L. DeRisi, P. R. Selvin and P.-Y. Kwok, *Nucleic Acids Res.*, 2007, **35**, e16.
10 S. K. Das, M. D. Austin, M. C. Akana, P. Deshpande, H. Cao and M. Xiao, *Nucleic Acids Res.*, 2010, **38**, e177.
11 E. Lam, A. Hastie, C. Lin, D. Ehrlich, S. Das, M. Austin, P. Deshpande, H. Cao, N. Nagarajan, M. Xiao and P.-Y. Kwok, *Nat. Biotechnol.*, 2012, **30**, 771–776.
12 W. Reisner, N. B. Larsen, A. Silahtaroglu, A. Kristensen, N. Tommerup, J. O. Tegenfeldt and H. Flyvbjerg, *Proc. Natl. Acad. Sci. U. S. A.*, 2010, **107**, 13294–13299.
13 R. L. Welch, R. Sladek, K. Dewar and W. Reisner, *Lab Chip*, 2012, **12**, 3314–3321.
14 L. K. Nyberg, F. Persson, J. Berg, J. Bergstrom, E. Fransson, L. Olsson, M. Persson, A. Stalnacke, J. Wigenius, J. O. Tegenfeldt and F. Westerlund, *Biochem. Biophys. Res. Commun.*, 2012, **417**, 404–408.
15 R. Wartell, J. Larson and R. Wells, *J. Biol. Chem.*, 1974, **249**, 6719–6731.
16 K. O. Andresen, M. Hansen, M. Matschuk, S. T. Jepsen, H. S. Sorensen, P. Utko, D. Selmeczi, T. S. Hansen, N. B. Larsen, N. Rozlosnik and R. Taboryski, *J. Micromech. Microeng.*, 2010, **20**, 055010.
17 S. Tanzi, P. F. Østergaard, M. Matteucci, T. L. Christiansen, J. Cech, R. Marie and R. Taboryski, *J. Micromech. Microeng.*, 2012, **22**, 115008 (11pp.).
18 P. Utko, F. Persson, A. Kristensen and N. B. Larsen, *Lab Chip*, 2011, **11**, 303–308.
19 D. Schweizer, *Hum. Genet.*, 1981, **57**, 1–14.
20 M. Matteucci, T. L. Christiansen, S. Tanzi, P. F. Østergaard and R. Taboryski, Presented at the 38th International

Conference on Micro and Nano Engineering, September 16–20, 2012, Toulouse, France, 2012, submitted.
21 Y. Wang, D. R. Tree and K. D. Dorfman, *Macromolecules*, 2011, **44**, 6594–6604.
22 E. Scott, R. Jones, D. Banville, G. Zon, L. Marzilli and W. Wilson, *Biochemistry*, 1988, **27**, 915–923.
23 W. Wilson, R. Jones, G. Zon, E. Scott and L. Marzilli, *Biophys. J.*, 1988, **53**, A4.
24 F. Brochard and P. de Gennes, *J. Chem. Phys.*, 1977, **67**, 52–56.
25 Y. Wang, W. F. Reinhart and D. R. Tree, *Biomicrofluidics*, 2012, **6**, 014101.
26 Y. Kim, K. S. Kim, K. L. Kounovsky, R. Chang, G. Y. Jung, J. J. de Pablo, K. Jo and D. C. Schwartz, *Lab Chip*, 2011, **11**, 1721–1729.
27 K. R. Hawkins and P. Yager, *Lab Chip*, 2003, **3**, 248–252.
28 A. Piruska, I. Nikcevic, S. H. Lee, C. Ahn, W. R. Heineman, P. A. Limbach and C. J. Seliskar, *Lab Chip*, 2005, **5**, 1348–1354.
29 S. M. Stavis, *Lab Chip*, 2012, **12**, 3008–3011.

Paper 3

All Polymer, Injection Molded Nanoslits, Fabricated Through Two-Level UV-LIGA Processes

Peter Friis Østergaard, Marco Matteucci, Rodolphe Marie, Anders Kristensen, and Rafael Taboryski

Nanotech 2012 Vol. 2 Nanotechnology 2012: Electronics, Devices, Fabrication, MEMS, Fluidics and Computational, 2012 **2** 482-485

All Polymer, Injection Molded Nanoslits, Fabricated Through Two-Level UV-LIGA Processes

P. F. Østergaard*, M. Matteucci*, R. Marie*, A. Kristensen*, R. Taboryski*†

* DTU Nanotech, Ørsted Plads, Building 345 east,
Technical University of Denmark, DK-2800 Kongens Lyngby, Denmark
† e-mail: rata@nanotech.dtu.dk, phone: +45 4525 2155, fax: +45 4588 7762

ABSTRACT

Introducing double stranded DNA (dsDNA) into confined channels with height and/or width smaller than the radius of gyration of the molecule, forces it to elongate in the channel, as described by the de Gennes theory [1].
Such systems have typically been fabricated in silicon and glass, with the use of electron beam lithography to define the nanofluidic channels.
This article describes, how nano- and microchannels can be transfered from silicon masters to a mass production polymer platform, greatly reducing the price of the system, along with the time used on the individual chip.
Since the systems described in this article are intended to be used with long strand DNA, nanoslits are required, making it necessary to bond low aspect structures in polymer materials. Aspect ratios of 1:200 have been achieved.

Keywords: UV-lithography, injection molding, polymer fabrication, nanoslits

1 MOTIVATION

Rough sequencing of DNA can be performed by melting mapping experiments of elongated DNA, as explained by Reisner et al. [2].
Polymer-based systems intended for such purposes have been fabricated by the use of injection molding [3], but for long strands of DNA, low-aspect ratio nanoslits are preferable to narrow nanochannels, where the DNA can block the channel [4].
Where nanochannels have dimensions in the nanometer scale in both width and height, nanoslits have widths in the micrometer scale, while the height is still in the nanometer scale.
These systems are mostly fabricated in silicon and glass, mostly because of the excelent optical properties of glass, but also because of the rigidity of the materials, assuring that the nanoslit is not occluded due to torsial or strain forces distorting the structure, [5]. In addition, silicon fabrication process knowledge obtained over the last decades has made fabrication of such structures routine on this substrate.
However, even though silicon processing is highly developed, the cost and time used for processing a silicon wafer is still prohibitive in many applications, calling for cheaper and faster alternative fabrication methods.
This can be obtained by moving production over to a polymer-based platform, based on injection molding. Such a transfer requires the processing of a single silicon master wafer, that can be replicated in hundreds to thousands of identical chips by injection molding.

2 FABRICATION

Production of polymer chips in the injection molder requires several preparatory steps, starting with the design and routing of the microfluidic channels, followed by processing of a silicon master wafer in the cleanroom and electroplating of the silicon wafer. Actual fabrication begins with injection molding, and finally bonding of the molded chip with a foil in order to create a sealed system.

2.1 Design

In order to avoid costly electron beam lithography, as used by Utko et. al [3], and instead employ the cheaper, UV lithography, all length scales are chosen to be larger than 1 µm
The proposed design is a two layer design, with one layer defining the nanoslits, and the other layer defining the microchannels leading to the slits, as seen in Fig. 1.
Dark field chromium masks were used for the UV-lithography.

2.2 Cleanroom Work

The initial silicon master is fabricated using standard UV-lithography, and Reactive Ion Etching (RIE). First, an oxide layer is grown on top of the wafer, Fig. 2(a). This has a thickness of 100 nm, which will define the height of the nanoslit. UV-lithography is performed, followed by an oxide specific RIE, Fig. 2(b)+(c). The width of the structures in this step is 20 µm, giving an aspect ratio of 1:200 of the structures. A second UV-lithography step is performed, defining 50 µm wide microchannels, followed by a RIE that goes through the oxide layer and 5 µm into silicon layer, Fig. 2(d)+(e). This ends the process for the silicon master wafer.

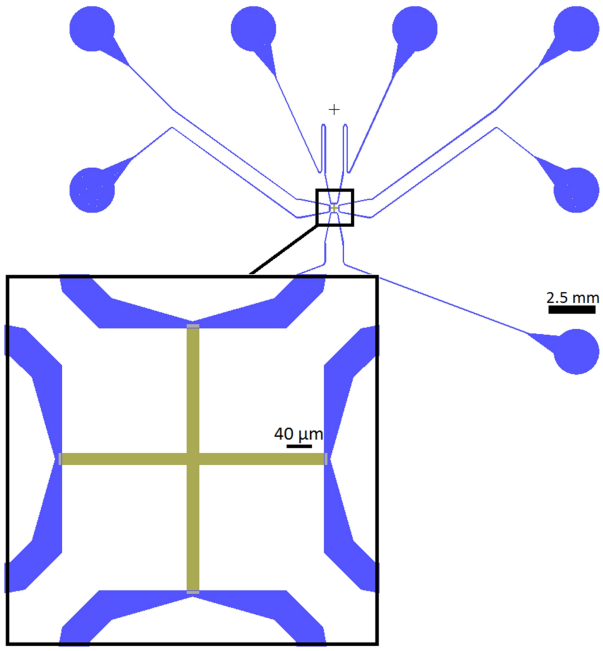

Figure 1: CAD drawing of the proposed design. Microchannels, drawn in blue, lead to the nanoslit, drawn in green. No dimensions on the design are smaller than 20 µm.

2.3 Electroplating

The nickel shim to be used as an insert in the IM, is made by electroplating the silicon wafer. To accomplish this, a 100 nm layer of Ni/V is sputtered on top of the wafer in order to obtain an electrically conductive layer on top of the silicon surface, Fig. 2f). Electroplating is performed until a 300 µm thick nickel layer is obtained, Fig. 2(g). The wafer is removed, either by being lifted off or by being dissolved in KOH, Fig. 2(h).
Finally, the finished nickel-shim is punched out in a dedicated tool, to fit into the injection molder.

2.4 Injection Molding

Injection molding is performed in an ENGEL injection molder, (see Fig. 3(a)) using the COC co-polymer TOPAS 5013L-10 [6]. Molding is performed in a variotherm process, where the polymer is injected into the mold cavity while the mold is maintained at the glass transition temperature (T_g) of the polymer [7]. The mold is then cooled down to 70 °C, the chip is demolded, and transfered to a conveyor belt, see Fig. 3(b).
The mold containing the shim in the injection molder includes standard LUER-fittings that are integrated into all molded parts. This makes it easy to use the finished chips in experimental setups, as no custom fittings are needed between potentiostats, pumps, etc. and the polymer chip, [8].

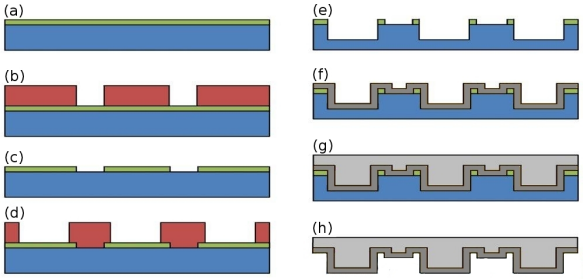

Figure 2: Process flow for the silicon wafer: (a) An oxide layer is grown on top of the silicon wafer. (b) Photoresist is spun on, and UV lithography is performed in order to define the nanoslits. (c) Oxide specific RIE etch is performed. (d) Second level of UV-lithography to define microchannels. (e) RIE etch, etching through first the oxide layer, then into the silicon. (f) Ni/V is sputtered onto the sample. (g) The wafer is electroplated, creating a Ni-shim. (h) The silicon wafer is removed.

2.5 Bonding

To finish the chip, a COC polymer foil of same grade as the polymer used in the injection process, is bonded onto the chip.
To facilitate the bonding, foil and chip are exposed to UV-light for 30 sec prior to bonding. This decreases the glass transition temperature, T_g at the surface, making it possible to bond at lower temperatures, avoiding deformations of the structures in the chip, [9].
The chip is placed in a dedicated holder with the foil on top, with UV-treated surfaces toward each other. A nickel plate with mirror-like finish is placed on top of the foil, and a piece of PDMS is placed on top of this. The entire stack is placed inside a press, and bonded for 10 min at 115 °C with a pressure of 50 bar, [10].
If 100 chips are made, based on the above mentioned steps, the individual chip has a unit price of $100 USD, roughly 1/10 of the price for a silicon chip produced in a cleanroom.

3 TESTING

To verify that the nanoslits have not collapsed during bonding, the chip is placed under a reflective microscope. All the parts of the chip that are not bonded with the foil, i.e. the microchannels and the nanoslits, appear, as shown in Fig. 4(a) because of the difference in refractive index between air and polymer.
In order to confirm that the transition between microchannel and nanoslit is not blocked, the nanoslit can be filled with ethanol, purely by capillary forces. This is seen in Fig. 4(b).

(a) The injection molder.

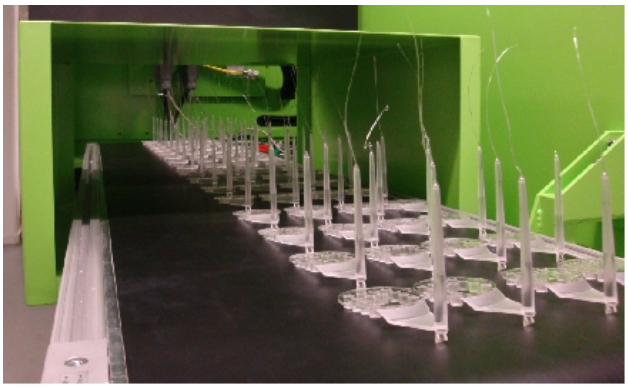

(b) Molded chips are transported to a conveyor belt for temporary storage.

Figure 3: Injection molding equipment used for fabrication of the fluidic chips.

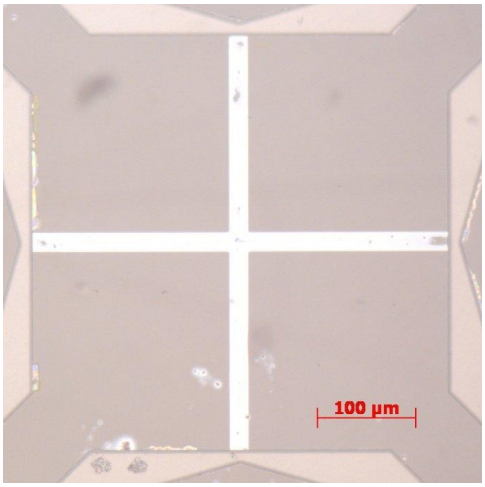

(a) Empty nanoslit.

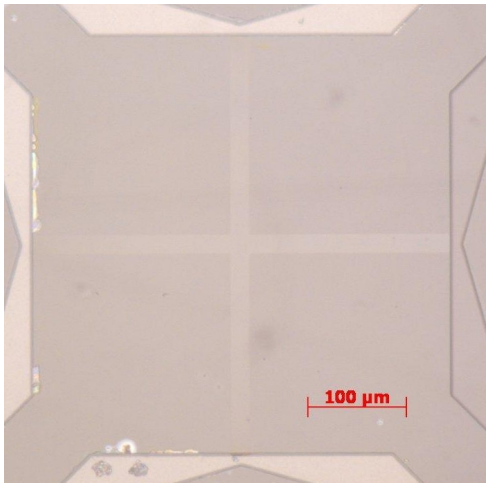

(b) Filled nanoslit

Figure 4: When microchannels and nanoslits are filled with ethanol, it is easy to see, that they are not collapsed.

4 RESULTS AND DISCUSSION

We have shown, how structures can be transfered from silicon, where many well-known techniques exist for surface processing, to a cheap polymer platform.
During this work, we were able to fabricate extremely low aspect ratio structures (1:200) in soft materials.
The prospect of making large quantities of microfluidic systems in polymers, in almost the same time it takes to make a single system in silicon, will leave scientists with more time for doing actual experiments, as less time is consumed by cleanroom work.
A reduction by a factor of 10 or more in the cost of the individual system also allows for chips to be considered as disposables. This greatly reduces the chance of cross-contamination between experiments, ultimately increasing experimental validity.

5 ACKNOWLEDGEMENTS

This work is supported by the Danish Council for Strategic Research through the Strategic Research Center PolyNano (grant no. 10-092322/DSF)

REFERENCES

[1] M. Rubinstein, R. H. Colby, “Polymer Physics”, Oxford University Press, Oxford, 2003.
[2] W. Reisner et. al, “Single-molecule denaturation mapping of DNA in nanofluidic channels” PNAS, 107 (30), 13294-13299, 2010.
[3] P. Utko et. al, “Injection molded nanofluidic chips: Fabrication method and functional tests using single-molecule DNA experiments”, Lab on a Chip, 2, 303-308, 2010.

[4] J. Tang et. al, "Revisiting the Conformation and Dynamics of DNA in Slitlike Confinement", Macromolecules, 43(17), 7368-7377, 2010

[5] K. Rasmussen et. al, "A device for extraction, manipulation and stretching of DNA from single human chromosomes", Lab on a Chip, 11(8), 1431-1433, 2011.

[6] T. Nielsen et. al, "Nanoimprint lithography in the cyclic olen copolymer, Topas® , a highly ultraviolet-transparent and chemically resistant thermoplast", American Vacuum Society, 22(4), 1770-1775, 2004

[7] L. Xie and G. Ziegmann, "A visual mold with variotherm system for weld line study in micro injection molding", Microsystem Technologies, 14 (6), 809-814, 2008

[8] K. Ø Andresen et. al, "Injection molded chips with integrated conducting polymer electrodes for electroporation of cells", Journal of Micromechanics and Microengineering, 20 (5), 055010, 2010.

[9] C.-W. Tsao and D. L. DeVoe, "Low temperature bonding of PMMA and COC microfluidic substrates using UV/ozone surface treatment", Lab on a Chip, 7, 499-505, 2007

[10] M. Matteucci et. al, "A simple model for estimating the delamination pressure in allpolymer microchannels and optimization of bonding strength with a razor blade test", submitted for publication.

Paper 4

Optical mapping of single molecule human DNA in disposable, mass produced all polymer devices

Peter Friis Østergaard, Joanna Lopacinska-Jørgensen, Jonas Nyvold Pedersen, Asli Silahtaroglu, Niels Tommerup, Anders Kristensen, Henrik Flyvbjerg, Rodolphe Marie, and Rafael Taboryski

Manuscript in preparation

Optical mapping of single molecule human DNA in disposable, mass produced all polymer devices†

Peter Friis Østergaard,[a‡] Joanna Lopacinska-Jørgensen,[b‡] Jonas Nyvold Pedersen,[a] Asli Silahtaroglu,[b] Niels Tommerup,[b], Anders Kristensen,[a] Henrik Flyvbjerg,[a] Rodolphe Marie,[a*] and Rafael Taboryski[a*].

Received Xth XXXXXXXXXX 20XX, Accepted Xth XXXXXXXXX 20XX

First published on the web Xth XXXXXXXXXX 200X

DOI: 10.1039/b000000x

We demonstrate an all polymer device with ultra low aspect ratio of 1:200 used for optical mapping of single molecule DNA from the human genome. Optimizing the production of the devices allows for a significant decrease in the background signal, and a massive economics of scale, leading to device costs as low as $3.13 USD. Single DNA molecules are successfully mapped to the human reference genome, something that has previously only been seen on expensive, silica devices.

1 Introduction

Current day sequencing techniques, known as next generation sequencing [1] (NGS) have been able to reduce the cost of performing such work by orders of magnitude. This is due to a fundamental change in the concept by which sequencing is performed [2]. Despite the advancements of NGS, it does have certain drawbacks caused by the procedures used for data acquisition.

All NGS techniques rely on upscaling and massive fragmentation of the sample. Upscaling of DNA sample can lead to repetitive allele drop-out [3], and the massive fragmentation result in read lengths in the order of 1000 bp or lower [4]. Such short read lengths can lead to 6 billion reads having to be assembled after each sequencing procedure [5], causing assembling of the fragments, not the actual sequencing, to be the rate limiting step in NGS techniques.

Optical mapping has been shown to work as a support for NGS in the assembly of genomes of rice [6] and certain bacteria. [7] Optical mapping has also been used for larger genomes, where the entire yeast genome [8] and single strands of human DNA [9] have been successfully mapped to reference genomes.

State of the art devices, as the one used by Marie *et al* [9] allows for a stretching of the molecule of 98% of the contour length, and a resolution of ~ 1 Mbp.

The working principle behind the nanoslit design has been described in detail by Marie *et al* [9] in silica chips. DNA is stained with the intercalating dye YOYO-1, followed by a partial denaturation of the molecule, leading to the release of the fluorophore in the denatured areas. These AT rich areas can be identified by cooling the sample down, thereby causing a renaturation of it. This is followed by stretching out the DNA in the nanoslit by use of a shear flow, and utilizing fluorescent microscopy for obtaining the local concentration of YOYO-1 which is mapped against a reference genome.

In order to cause as little damage to the DNA as possible, the entire protocol of denaturation, renaturation, and stretching of the DNA is performed on-chip. This greatly reduces the risk of fragmenting the long-strand DNA due to the shear flow induced by pipetting the sample between sample tubes and chip.

Since optical mapping works on a single molecule level, differences between individual cells in a population can be investigated using this technique, as no ensemble averaging is required. [10,11]

So far, the main problem regarding optical mapping is that the devices used during experiments are silica chips, fabricated in low numbers, intended solely for a small community of highly specialized researchers and bearing a price tag of several hundred dollars. With an aim at sequencing an entire human genome for $1.000 USD, [12,13] any supporting technique used for sequencing has to be cheap and widely accessible in order to be successful and have a high impact. [14,15] If not, the added cost is too high compared to the extra information obtained.

If high performance chips can be fabricated as cheap plastic devices using industrial production methods rather than being

† Electronic Supplementary Information (ESI) available: [details of any supplementary information available should be included here]. See DOI: 10.1039/b000000x/

[a] *Department of Micro- and Nanotechnology, Technical University of Denmark, DK-2800 Kongens Lyngby, Denmark. Tel: +45 4525 8155; E-mail: Rodolphe.Marie@nanotech.dtu.dk and Rafael.Taboryski@nanotech.dtu.dk*

[b] *Faculty of Health and Medical Sciences, University of Copenhagen, Copenhagen, Denmark.*

‡ These two authors contributed equally to this article

∗ Corresponding authors.

produced one by one in costly silica wafers using expensive cleanroom facilities, more researchers can gain access to the platform. This will help in the development of the technique, thereby releasing the full potential found in optical mapping regarding aiding, and validating current day, state of the art NGS systems. Disposable systems will furthermore have the advantage of removing the chance of cross contamination between experiments, which is essential when performing analysis of human DNA.

Injection molding is an industry standard for production of plastic parts, such as bottle caps, LEGO bricks, and tooth brushes, but has also been shown to be a good tool for replicating structures fabricated in silicon wafers.[16,17]

Such injection molded polymer Lab-on-a-Chip systems have previously been used for experiments with DNA, but these experiments have either been aimed at investigating the physical properties of homogeneously stained DNA,[18] or mapping of consensus barcodes of smaller λ-DNA and T4GT7-DNA found by averaging data from many molecules.[19]

Devices similar to the ones used by Marie *et al*[9] have also been fabricated before in polymer, but with a limited yield, reported to be as low as 5-10%[20]. We demonstrate, that an all polymer device with ultra low aspect ratio structures of 1:200, similar to the devices seen in Tanzi *et al*[20], can be injection molded and bonded with a final yield as high as 95%, considerably higher than what has been reported previously. By the addition of a masterbatch to the polymer substrate, the background signal of the device is reduced to nearly half the original value, leading to optimized signal properties, comparable to silica. The data found when performing experiments on single strands of human DNA are found to be of a quality high enough for mapping against a reference genome, in a fashion similar to what is seen in state of the art silica devices, but here done in polymer chips having a cost as low as $3.13 USD.

The reason for using a nanoslit design rather than nanochannels is that nanoslits only confines the DNA molecule in one dimension, making it easier to introduce the molecule into the confinement compared to if the DNA was introduced into a nanochannel where the molecule is confined in two dimensions.

2 Methods and Materials

2.1 Chip fabrication

A microfluidic system with a layout as seen in Figure 1a) is fabricated using dry etching, electroplating and molding (DEEMO)[16] in a fashion similar to the one described by Tanzi *et al*.[20]

Functional devices used for patch clamping of cells have previously been fabricated using this method,[21] however in this work, the dimensions of the structures fabricated are significantly smaller.

In short, a master silicon wafer is produced using thermal oxide growth, standard UV lithography and RIE etch. This silicon master is electroplated in a nickel bath and the resulting nickel insert is used for injection molding of the polymer chips.

This entire process is sketched in Figure 1b).

Injection molding of the devices is performed in an Engel Victory 80/45 Tech injection molder, using COC TOPAS grade 5013L-10 granulate from TOPAS Advanced Polymers GmbH. For black polymer devices, 2% (w/w) of black UNS 949 227 masterbatch from Gabriel Chemie GmbH is added to the polymer granulate.

This technique gives a cycle time of 60 sec per device, everything included.

Standard LUER ports are integrated into the injection molding tool, making it easy to connect the final device with equipment such as Fluigent pressure controllers.[22]

The change in the protocol that gives a yield of 95% in this work, compared to 5-10% in previous recordings[20], is the bonding protocol. The devices are bonded in a UV assisted thermal bonding process[23]. The polymer device and a piece of 150 µm thick TOPAS COC 5013L-10 foil is exposed to UV light for 30 sec. The two pieces are placed with the irradiated surfaces against each other, and a specially designed PDMS slab is placed on top of it. The PDMS slab contains cavities with a diameter of 3 mm over the low aspect ratio structures in order to avoid collapse of these during the bonding.

5 polymer devices are positioned in a custom made holder and bonded in two sequences. First the devices are bonded for 5 min at 125 °C and 0.6 bar. The PDMS devices is changed into one containing cavities with a diameter of 1 cm over the nanoslit, and the devices are bonded for an additional 5 min at 125 °C and 1.3 bar bar. This procedure allows for a throughput of 25 chips per hour, with a yield of 95%.

The final devices, transparent and black, are seen in Figure 1c).

2.2 DNA preparation

Human chromosomal DNA in nuclei from the fibroblast cell line was supplied in 100 µl, 0.6% agarose gel.

The agarose gel is melted by heating the gel to a temperature of 67 °C for 10 min. The solution is cooled down to 42 °C over a period of 2 min and 2 µl of β-agarase (1000 U/ml) (New England Biolabs, MA, USA) is added. The sample is incubated at 42 °C for 3 h.

500 µl 0.5× Tris/Borate/EDTA (TBE) (Sigma-Aldrich, MO, USA) is added to the solution and the DNA stock incubates for an additional 16 h at 42 °C.

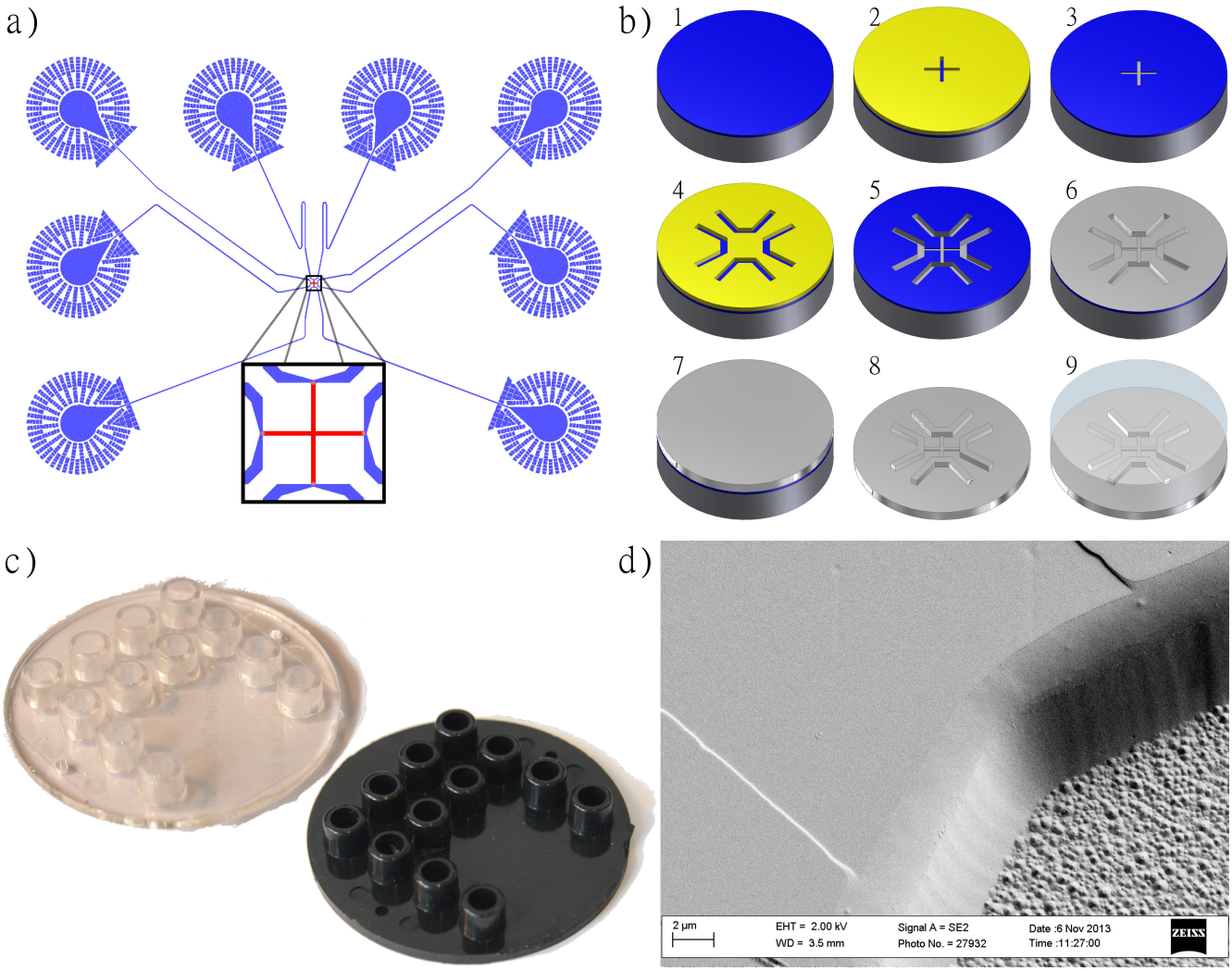

Fig. 1 a) The design used for the microfluidic system. The blue structures defines the carrier channels, and the red cross (enlarged) defines the nanoslit. Support structures have been implemented around the inlets to avoid channel squeeze by pins defining the LUER ports during injection molding. b) Production scheme for the polymer chips: 1: An oxide layer is thermally grown on a silicon wafer. 2: UV lithography is used to define the 20 µm wide, 450 µm long nanoslit. 3: An oxide specific reactive ion etch is performed, using the silicon substrate as an etch stop. 4: A second UV lithography step is used for defining the carrier channels. 5: The channels are etched using a second reactive ion etch. 6: A Ni/V seed layer is sputtered on top of the wafer. 7: The wafer is electroplated in a Ni bath. 8: Removal of the Si wafer leaves the Ni insert ready for 9: injection molding, creating large quantities of identical polymer chips. c) Polymer chips can be fabricated in clear polymer (left) or, with the addition of 2% (w/w) masterbatch, in black (right). The polymer chip contains integrated standard LUER fittings to facilitate access of a pressure controller. d) SEM image showing the interface between the nanoslit (110 nm deep and 20 µm wide) and the carrier channel in the injection molded chip.

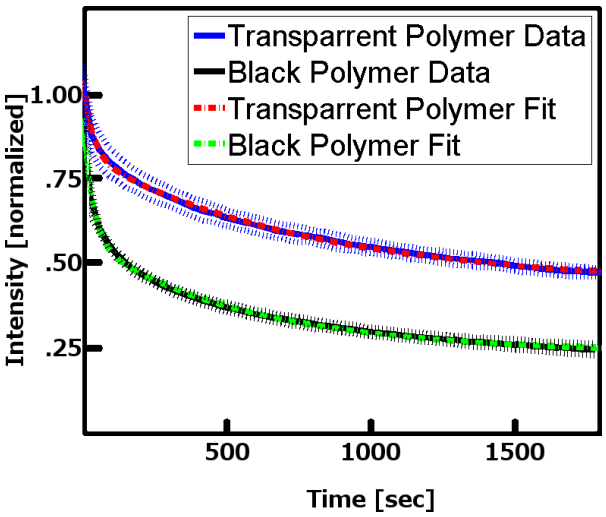

Fig. 2 Autofluorescence of a black and a transparent TOPAS chip as a function of time, when photo-bleached. The figure shows both the measured background signal with standard deviations, along with a fitted model.

The DNA is stained in a 0.1 μM YOYO-1(Invitrogen, CA, USA) solution. The solution incubates 1 h at room temperature, followed by 1 h at 50 °C.

2.3 Chip preparation

TOPAS has previously been reported to have a low autofluorescence[24,25], but to decrease the background signal from the chip even further, the chip is illuminated with high intensity light having a wavelength of 480 nm prior to the experiment. This reduces the autofluorescence, measured at 535 nm significantly as seen in Figure 2. Here, the autofluorescence is compared between the transparent chips fabricated in 100% COC TOPAS and chips fabricated in COC TOPAS containing 2% black masterbatch. After quenching of the autofluorescence, the final background level of the transparent chip reaches a level of 0.419 ± 0.004 of the starting value, while the black chip reaches 0.226 ± 0.001, almost half the value of the transparent chip. The two wavelengths used here correspond to the wavelengths used during experiments, as proposed by S. Stavis[26]. The model used for fitting the data in Figure 2is of the form

$$I(t) = c_0 + c_1 \exp -t/t_1 + c_2 \exp -t/t_2 \qquad (1)$$

showing that the autofluorescence has several origins in the polymer substrate. Models containing even more terms have previously been proposed for polymer substrate,[25] but in this case, an exponential decay containing two exponential terms is capable of explaining the behaviour of the system.

2.4 Experimental setup

To ease the filling of the microchannels and reduce the degree of photo-nicking, 0.5× TBE is degassed in an ultrasonic bath for 1 h. For the experiment, three buffers are prepared.

Buffer 1: 0.5× (v/v) trition X-100 (Sigma-Aldrich), 3% (v/v) β-mercaptoethanol (BME) and 1% (v/v) 10 mg/ml Bovine Serum Albumin (BSA)(New England Biolabs) in 0.5× TBE.

Buffer 2: 2.5% (v/v) trition X-100 in Buffer 1.

Buffer 3: 2% (v/v) proteinase K (Invitrogen) (20 mg/ml) in Buffer 1

The chip is wetted in a solution consisting of 7% (v/v) ethanol in the degassed 0.5× TBE. This solution is exchanged with Buffer 2, and the chip is left for incubation at room temperature for 10 min in order for the triton X-100 and the BSA to inhibit the surface of the microchannels, thereby avoiding the sticking of the DNA to the walls.

After incubation, Buffer 2 is flushed out using Buffer 1. 3 μl DNA solution is placed in one of the inlets along with 30 μl of Buffer 3. The remaining inlets are filled with 30 μl of Buffer 1.

Thermal expansion of the polymer chip during heating made it impossible to heat up the chip from above, since this would create to much stress in the polymer foil, causing it to break. Instead the denaturation-renaturation temperature is controlled by a flatbed PCR-machine.

The chip is positioned in the flatbed PCR-machine, and a custom made aluminum piece, working as a heat conductor, is fitted on top of the LUER ports. The system is sealed using a PCR-foil (Microseal 'A' Film, Bio Rad). To ensure a tight sealing of the LUER ports, a PMMA plate is position on top of the PCR-foil. The lid is closed, and a heat cycle is performed consisting of 55 °C for 1 hour, allowing the proteinase K to digest the histones. This is followed by a ramping of the temperature by 1 °C/sec to a final temperature of 86 °C where the denaturation takes place and the YOYO-1 fluorophore can diffuse away from these locations. This temperature is held for 10 min, after which the chip is cooled down to 70 °C for 1 min allowing controlled renaturation. Finally, the chip is set on ice to avoid diffusion of YOYO-1 along the backbone of the molecule. This process is sketched in Figure 3a).

After the denaturation-renaturation, data is recorded from the chip. This follows the same protocol as used by Marie *et al*. For the acquisition of data, a Nikon Eclipse microscope equipped with a 60× NA=1.4 objective and an additional internal 1.5× magnification in the microscope is used. A Fluigent pressure controller, connected through 8 of the integrated LUER connectors in the chip is used to manipulate the flow, introducing DNA into the nanoslit. Once a sufficiently long strand of DNA is positioned in the nanoslit, the flow is redirected in order to induce a shear flow force on the DNA as seen in Figure 3b), stretching it out to between 95%

and 100% of its contour length. Data from the stretched out DNA is acquired using a highly sensitive electron multiplying CCD camera.

With the DNA stretched out in the nanoslit, a script is run in the acquisition software MetaMorph (Molecular Devices), acquiring 50 images with a shutter speed of 50 ms in each of 9 different field of views. From the acquired images, the DNA is located and an average intensity along the DNA is found.

A strand of DNA stretched out from one end of the nanoslit to the other is seen in Figure 3c), where the intensity profile for part of the molecule is also shown.

3 Results and Discussion

The production method used for the devices fabricated for this project has an enormous economics of scale. If as few as 10 devices are fabricated, the price per device is $514.60 USD, but if 10,000 devices are fabricated, each device has a total price, including down-payment of equipment, cleanroom access time, engineering fees and cost of materials, of only $3.13 USD (For elaborate calculations of the cost, see SI).

The bonding process used increased the yield of usable nanoslit devices from a reported 5-10%[20] to 95%.

During production 2% black masterbatch was added to the polymer, and it was observed to drastically reduce the background signal, thereby increasing the quality of the signal.

The low cost of the devices has allowed an extensive use of chips for characterizing the optical properties, along with optimizing the protocol used during experiments. In total, almost 1,000 chips were fabricated and used either for characterization, optimizing of protocols, or for research partners in other projects.

During experiments, DNA was only pipetted once while still being coiled up around the histones. All processes following this pipetting step were performed on chip, greatly decreasing the risk of fragmenting the sample during the experimental procedure. This is essential, since the length of the nanoslit is 450 μm long and therefore requires DNA molecules longer than 1.4 Mbp in order to work as intended. Molecules shorter than this will not stretch through the entire nanoslit, and as an effect of this, they will be exposed to unequal shear flow forces towards the two ends of the nanoslit, causing the molecule to drift during data acquisition.

In two days of performing experiments with the black polymer devices, 24 molecules were chosen for potential mapping against the human reference genome. These molecules were mapped against a theoretically obtained barcode found using Bubblyhelix[27] and the reference genome hg18,[28] with the algorithm described by Marie *et al*[9]. Acquired data, mapped against chromosome 16 is seen in Figure 3d).

20 of the 24 molecules were successfully mapped, while an identification of the rest was not possible. That 4 molecules could not be mapped can be a consequence of several factors. In the reference genome used, 7% of the genome is unknown,[28] and there is a chance that the unidentified molecules originates from some of these areas. The probability that these black regions are the only reason why some of the molecules could not be identified is higher than 9%, making it statistically plausible. Other factors can also be causing the missing mapping of the molecules. It is possible that there can be large structural variations in the molecules compared to the reference genome, making it impossible to map it, and finally, there is a chance that the data is not good enough for these few molecules due to drifting and other experimental effects.

4 Conclusion

We have demonstrated single molecule DNA mapping of human chromosomal DNA on a cheap, disposable polymer device. This has been done on chips with a price per device as low as $3.13 and the potential of producing several thousands of them within a short timescale and a high yield.

The background signal of the polymer devices was reduced significantly by the addition of black masterbatch in the polymer substrate along with quenching of the autofluorescence with the use of strong light similar to what is used during experiments.

Denaturation, renaturation, and stretching of the DNA was all performed on-chip, thereby reducing the risk of fragmenting the DNA during the experiment.

DNA was positioned in nanoslits with a length of 450 μm, and stretched out to more than 95% of the contour length of the molecule. This leads to more than 1.4 Mbp being imaged in a single data acquisition.

Out of 24 molecules considered for mapping in this particular validation study, 20 were identified on the reference genome, and the missing mapping of the remaining 4 molecules can statistically be caused by black holes in the reference genome, although other reasons have also been considered.

With 20 identified molecules it is seen that cheap polymer devices, fabricated in large numbers with a short production cycle of each device, has the capability of performing equally well as low yield, high cost, long production time silica devices.

5 Acknowledgements

We gratefully acknowledge financial support from the Danish Council for Strategic Research through the Strategic Research Center PolyNano(grant no. 10-092322/DSF) and from the Danish Agency for Science, Technology and Innovation

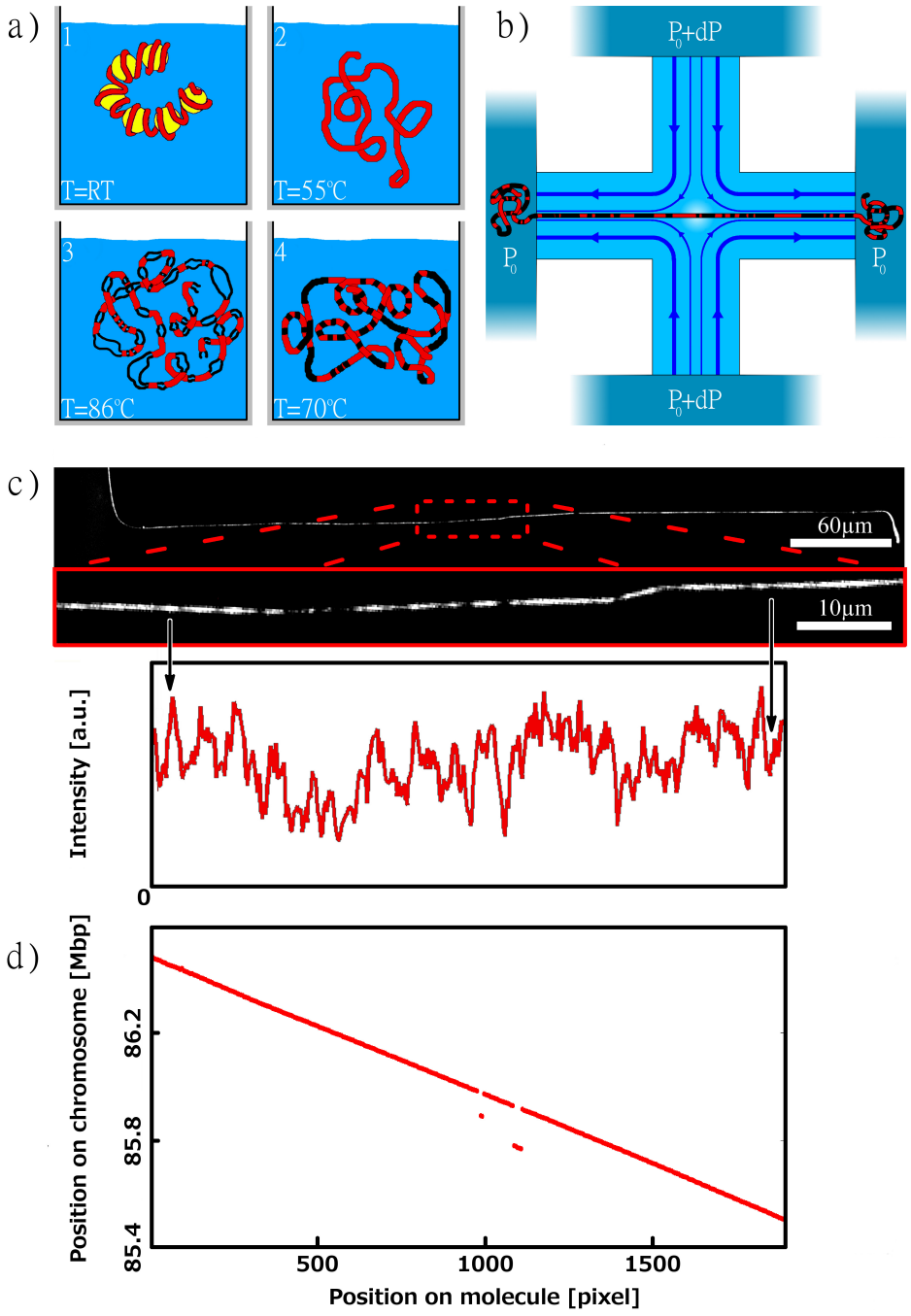

Fig. 3 a) Fluorescent barcodes are created by heating DNA through a series of steps on chip. 1: At room temperature, the DNA is coiled up around the histones. 2: Adding the enzyme proteinase K and heating the sample up to 55 °C for 1 h digests the histones, releasing the DNA. 3: Heating the DNA up to 86 °C for 10 min creates a partial denaturation of the molecule, allowing the fluorescent molecule YOYO-1 to diffuse away at these locations. 4: cooling the sample down to 70 °C for 10 min allows for a controlled renaturation, ensuring constant mechanical properties along the backbone. b) The denaturated-renaturated DNA is stretched out in the nanoslit. Applying pressure from top and bottom creates a flow that stretches out the DNA to almost 100%. c) The fluorescent barcode can be acquired using an optical microscope, and the profile along the molecule can be extracted. d) The acquired data is successfully mapped to chromosome 16

through DELTA's performance contract, CiPOC (grant no. 10-076609).

References

1 J. Shendure and H. Ji, *Nature biotechnology*, 2008, **26**, 1135–1145.
2 I. H. G. S. Consortium, *Nature*, 2001, **409**, 860–921.
3 W. Piyamongkol, M. G. Bermudez, J. C. Harper and D. Wells, *Human Molecular Genetics*, 2003, **9**, 411–420.
4 M. L. Metzker, *NATURE REVIEWS GENETICS*, 2010, **11**, 31–46.
5 T. J. Treangen and S. L. Salzberg, *Nature reviews genetics*, 2012, **13**, 36–46.
6 S. Zhou, M. C. Bechner, M. Place, C. P. Churas, L. Pape, S. A. Leong, R. Runnheim, D. K. Forrest, S. Goldstein, M. Livny and D. C. Schwarts, *BMC Genomics*, 2007, **8**, 278.
7 P. Latreille, S. Norton, B. S. Goldman, J. Henkhaus, N. Miller, B. Barbazuk, H. B. Bode, C. Darby, Z. Du, S. Forst, S. Gaudriault, B. Goodner, H. Goodrich-Blair and S. Slater, *BMC Genomics*, 2007, **8**, 321.
8 R. L. Welch, R. Sladek, K. Dewar and W. Reisner, *Lab-on-a-Chip*, 2012, **12**, 3314–3321.
9 R. Marie, J. N. Pedersen, D. L. V. Bauer, K. H. Rasmussen, M. Yusuf, E. Volpi, H. Flyvbjerg, A. Kristensen and K. U. Mir, *PNAS*, 2013, **110**, 4893–4898.
10 M. Levy-Sakin and Y. Ebenstein, *Current opinion in biotechnology*, 2013, **24**, 690–698.
11 M. Levy-Sakin, A. Grunwald, S. Kim, N. R. Gassman, A. Gottfried, J. Antelman, Y. Kim, S. O. Ho, R. Samuel, X. Michalet, R. R. Lin, T. Dertinger, A. S. Kim, S. Chung, R. A. Colyer, E. Weinhold, S. Weiss and Y. Ebenstein, *ACS nano*, 2014, **8**, 14–26.
12 R. F. Service, *Science*, 2006, **311**, 1544–1546.
13 E. R. Mardis, *Genome Biology*, 2006, **7**, 112.
14 H. Becker, *Lab on a Chip*, 2009, **9**, 2759–2762.
15 H. Becker, *Lab on a Chip*, 2009, **9**, 1659–1660.
16 J. Elders, H. Jansen and M. Elwenspoek, *MEMS '95, Proceedings*, 1995, **69**, 238–243.
17 R. M. McCormick, R. J. Nelson, G. A.-A. M, D. J. Benvegny and H. H. Hooper, *Analytical Chemistry*, 1997, **69**, 2626–2630.
18 P. Utko, F. Persson, A. Kristensen and N. B. Larsen, *Lab on a Chip*, 2011, **11**, 303–308.
19 P. F. Østergaard, M. Matteucci, W. Reisner and R. Taboryski, *Analyst*, 2013, **138**, 1249–1255.
20 S. Tanzi, P. F. Østergaard, M. Matteucci, T. L. Christiansen, J. Cech, R. Marie and R. Taboryski, *J. Micromech. Microeng.*, 2012, **22**, 115008.
21 S. Tanzi, M. Matteucci, T. L. Christiansen, S. Friis, M. T. Christensen, J. Garnæs, S. Wilson, J. Kutchinsky and R. Taboryski, *Lab on a Chip*, 2013, **13**, 4784–4793.
22 K. O. Andresen, M. Hansen, M. Matschuk, S. T. Jepsen, H. S. Sorensen, P. Utko, D. Selmeczi, T. S. Hansen, N. B. Larsen, N. Rozlosnik and R. Taboryski, *Journal of Micromechanics and Microengineering*, 2010, **20**, 055010.
23 M. Matteucci, T. L. Christiansen, S. Tanzi, P. F. O. S. T. Larsen and R. Taboryski, *Microelectronic engineering*, 2013, **111**, 294–298.
24 K. R. Hawkins and P. Yager, *Lab on a Chip*, 2003, **3**, 248–252.
25 A. Piruska, I. Nikcevic, S. H. Lee, C. Ahn, W. R. Heineman, P. A. Limbach and C. J. Seliskar, *Lab on a Chip*, 2005, **5**, 1348–1354.
26 S. M. Stavis, *Lab on a Chip*, 2012, **12**, 3008–3011.
27 E. Tøstesen, F. Liu, T.-K. Jenssen and E. Hovig, *Biopolymers*, 2003, **70**, 364–376.
28 U. G. Bioinformatics, *NCBI Build 36.1, Mar. 2006 Assembly (hg18)*, `http://genome-euro.ucsc.edu/goldenPath/stats.html#hg18`, Accessed: 13-03-2014.

Paper 5

Fabrication and characterization of injection molded multi level nano and microfluidic systems

Marco Matteucci, Thomas Lehrmann Christiansen, Simone Tanzi, Peter Friis Østergaard, Simon Tylsgaard Larsen, and Rafael Taboryski

Microelectronic Engineering 2013 **111** 294-298

Microelectronic Engineering 111 (2013) 294–298

Contents lists available at SciVerse ScienceDirect

Microelectronic Engineering

journal homepage: www.elsevier.com/locate/mee

Fabrication and characterization of injection molded multi level nano and microfluidic systems

Marco Matteucci *,[1], Thomas Lehrmann Christiansen [1], Simone Tanzi, Peter Friis Østergaard, Simon Tylsgaard Larsen, Rafael Taboryski

Department of Micro- and Nanotechnology, Technical University of Denmark, DTU Nanotech, Building 345E, DK-2800 Kongens Lyngby, Denmark

ARTICLE INFO

Article history:
Available online 14 February 2013

Keywords:
Dry etching
Electroplating
Injection molding
Thermal bonding
Lab-on-chip
Microfluidics

ABSTRACT

We here present a method for fabrication of multi-level all-polymer chips by means of silicon dry etching, electroplating and injection molding. This method was used for successful fabrication of microfluidic chips for applications in the fields of electrochemistry, cell trapping and DNA elongation. These chips incorporate channel depths in the range between 100 nm and 100 μm and depth to width aspect ratios between 1/200 and 2. Optimization of the sealing process of all-polymer COC microfluidic chips by means of thermal bonding is also presented. The latter includes comparing the bonding strength of UV-treated foils and presentation of a simple model for estimating the delamination pressure. With UV surface treatments, foils of 100 μm thickness were found to withstand pressures up to 9 atm in Ø4 mm cylindrical inlets when thermally bonded to micropatterned substrates of 2 mm thickness.

1. Introduction

For the fabrication of micro- and nano-machined systems for as Lab-on-chip (LoC) applications polymers are gaining at present more and more consideration over materials used for standard IC fabrication like Silicon and glass [1,2].

Polymer manufacturing is performed mostly by means of rapid prototyping methods such as polydimethylsiloxane (PDMS) casting, laser milling, or micromachining [3–5].

Although such fabrication methods are quite mature, they suffer from serious drawbacks when it comes to industrial production and cost efficiency. While the feasibility of more and more applications has been successfully demonstrated, only a few of the presented prototypes have reached the market. For large scale fabrication of polymer chips for Lab-on-Chip (LoC) applications, the most common methods for micro- and nanopatterning are LiGA (German acronym for Lithography, Electroplating and Molding) [6] or LiGA-like processes that involve, for example, the use of UV lithography [7]. In order to avoid the use of expensive synchrotron sources necessary for LiGA, obtain extremely flat and smooth sample surfaces and at the same time avoid the double inversion of stamp polarity [8], it is possible to carve the structures into the Si wafers in a so-called DEEMO (acronym for Dry Etching, Electroplating and Molding) process as first proposed by Elders et al. [9].

The procedure we here present is a variation of the DEEMO process performed using multiple and overlapped Si dry etching steps described in detail elsewhere [10]. This process enables high spatial resolution both in the width and the depth of the channels. The patterned Si wafers are then used to make nickel multi-level stamps (hereby referred to as shims) that are used for the fabrication of all-polymer chips by means of injection molding of Cyclic Olefin Copolymer (COC) 5013L10 from Topas™. Although a large number of polymers can be used for injection molding purposes, Topas is optimal when a material with low autofluorescence (for optical detection) and high chemical and thermal resistance are required.

Sealing of the devices was performed by thermal bonding with Topas foils of the same grade with thickness ranging from 100 μm to 2 mm. We focused on two methods based on previous works [11–14]: Plasma assisted and UV assisted thermal bonding. Of these, the UV bonding was superior and less time-consuming and is presented here. Data on the plasma method is given in Supplementary material S1.

The bonding procedure should be optimized for maximum bonding strength while still preserving the integrity of the channel geometry. We here report on such an optimization by applying the so-called razor blade test to measure the bonding strength [15], as this method can be applied while still maintaining the functionality of the device. In addition, we have deduced and experimentally verified that the crack length measured in the razor blade test can

* Corresponding author.
E-mail address: mamat@nanotech.dtu.dk (M. Matteucci).
[1] These two authors contributed equally to this research.

0167-9317/$ - see front matter © 2013 Elsevier B.V. All rights reserved.
http://dx.doi.org/10.1016/j.mee.2013.01.060

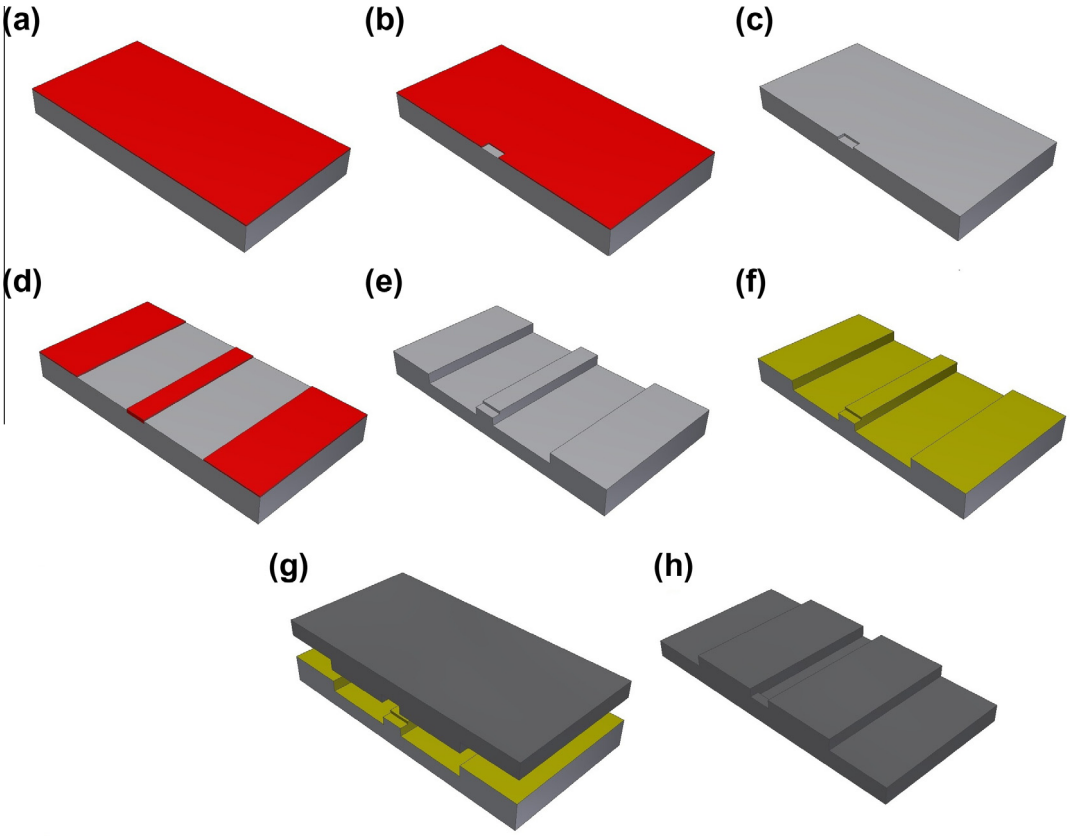

Fig. 1. Fabrication procedure for Ni shims: Spin coating (a), UV lithography (b), RIE etching of shallow channels and resist removal (c), spin coating and UV lithography (d), DRIE of Si for deep channels and resist removal (e), sputtering (f), Ni electroplating (g) and KOH etching of Si (h).

be directly related to the critical delamination pressure in a microfluidic channel by means of a simple model, see Supplementary material S2 for details. In this model, the delamination pressure in a circular inlet is given by:

$$P_{\max} = \frac{2E'\delta\tau^3}{a^2L^2} \tag{1}$$

where a is the inlet radius, τ the lid thickness, $E' = E/(1-\nu^2)$ E being Young's modulus and ν the Poisson ratio of the lid material, δ the blade thickness, and L the measured crack length.

Regarding the shim fabrication, we here describe a simplified version of a multi-level etching process presented in detail elsewhere [10].

The modified process is sketched in Fig. 1.

In respect to the one previously used, we here simplify the procedure by substituting an oxide etch mask with a spin coated resist layer of 2.2 μm thickness during both RIE and DRIE processing. The use of a resist mask was made possible by using only the modified BOSCH process described in [10]. As in previous work [10], the shim thickess was tuned to be around 300 μm. Using this process, chips equipped with luer fittings were injection molded with an ENGEL Victory 80/45 with a maximum clamping force of 450 Tons. Mold temperatures between 110 and 130 °C as well as an injection pressure of 1700 Bars were used for sample molding. Samples having features ranging in width from 5 to 50 μm and in depth between 100 nm and 50 μm and with aspect ratios as low as 1/200 without channel collapse. The cycle times of the injection molding were noticeably reduced compared to the process described in [10] to about 1 min by inserting a system for localized heating and cooling of the sample area.

For the bonding, commercially available TOPAS 5013L10 foils (T_g = 134 °C) of thickness between 100 and 500 μm purchased from TOPAS Advanced Polymers GmbH were used as sealing lids. The foils are obtained by extrusion of the same material provided for injection molding. All bonding experiments here described were performed with 100 μm thick foils. Such thickness was chosen because a large number of bio-applications use thin lids in order to have small working distances and allow on-chip optical detection. To test also the bonding of thicker substrates, 2 mm thick flat disks, similar to the patterned ones were injection molded to be used as sealing lids. An example of a bonded chip is shown in Fig. 2. Before thermal bonding, the surfaces of both the foil and the 2 mm thick sample were exposed to a UV lamp (DYMAX mercury UV-bulb F/5000) emitting over the full unfiltered Hg line spectrum with a power of 44.5 W/cm^2 measured at the wavelength 365 nm. All samples were kept under the UV light for 30 s.

After bonding samples at temperatures between 110 and 125 °C, we concluded that at higher temperatures the main issue is the partial filling of the channels with lower aspect ratios. In particular, at T = 125 °C it was not possible to separate the thin 100 μm thick folis from the 2 mm thick substrates. For this reason we kept a maximum bonding temperature of 120 °C.

Bonding (further details in Supplementary material S3) was therefore performed applying forces between 2 and 15 kN at temperatures of 115 and 120 °C. In order to assess the influence of bonding time, samples were bonded at 115 °C for both 5 min and 10 min. The razor blade test was then performed as shown in Fig. 3. To obtain the crack length L the horizontal projection of the blade slope L' was added to the distance L_0 between the blade tip and the last fringe. The blades used (Millarco) were of rectangular shape 39.5 × 20 mm. After the measurement of the crack length, a measurement of the delamination pressure was performed on the same samples by inserting a liquid dye into the microchannels and then applying pressure until delamination

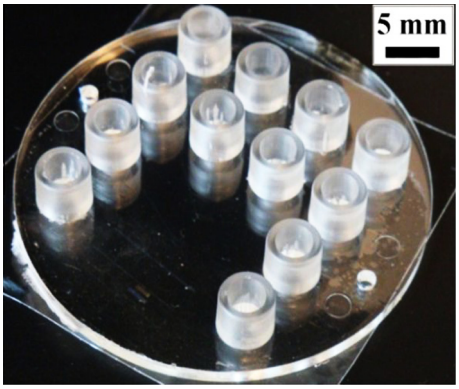

Fig. 2. An injection molded TOPAS 5013 microchip with Luer fittings bonded to a 100 μm thick TOPAS 5013 foil.

occured, acting as a reference for validating the delamination model. The critical pressure was considered to be the one at which the area near the Luer fittings started to delaminate.

During optimization, we observed that, as can be seen in Fig. 4, the samples bonded at 120 °C showed a much better bonding strength than the ones bonded at 115 °C for the same time. The data in Fig. 4 also show how bonding time plays a major role: Samples bonded for 10 min at 115 °C exhibit crack lengths comparable with the ones obtained at 120 °C and more than a factor of three shorter than the samples bonded at the same temperature for 5 min. This suggests that samples with critical dimensions could be bonded at lower temperatures for a longer time with the drawback of a more time consuming process.

Tuning of temperature and pressure is also fundamental to avoid microchannel deformation. Although no evident effects were found on micron-sized structures after optimization of bonding parameters (see SEM micrographs on Fig. 6) and functionality was assured in nanochannels, optical methods are at study at the

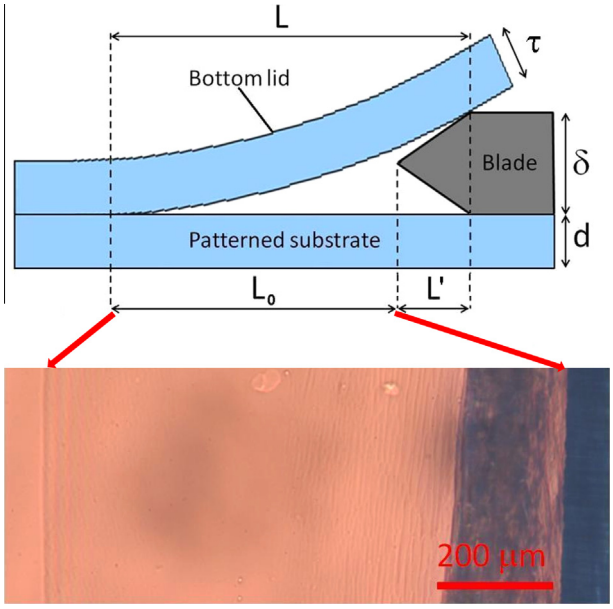

Fig. 3. Illustration of the razor blade test between two polymer sheets of thickness τ and d (top) together with the optical measurement of the distance L_0 between the blade tip and the fringes that indicate the detachment of the polymer sheet (bottom). The crack length L is obtained by adding the horizontal projection of the blade slope L' to L_0. The area near the blade tip is darker because of the high stress released by the stiffer plate during blade insertion.

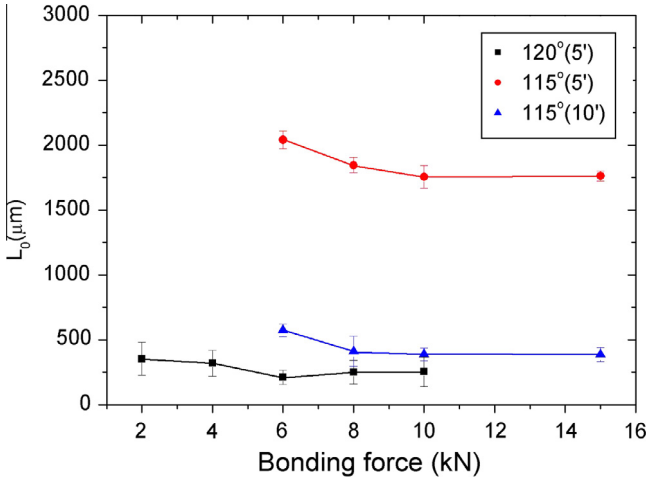

Fig. 4. L_0 values for UV-treated samples as a function of bonding force at both 115 and 120 °C.

moment to verify micro and nanochannel dimensions without having to cleave the samples.

In order to study the surface modifications that cause the bonding strength enhancement after UV treatment, XPS measurements of treated and untreated surfaces were performed. Since no surface modifications were recorded, the bonding enhancement was believed to be caused by thermal reordering of surface molecules (further details in Supplementary material S4).

The comparison between the delamination pressures calculated with Eq. (1) and the measured values is shown in Fig. 5. The theory shows very good correspondence with the experimental data for both longer and shorter crack lengths. SEM micrographs illustrating the quality of the bonding are also inserted in Fig. 5, showing un-collapsed polymer microchannels after bonding.

For values of L around 250 microns, the maximum reachable pressure was 9 atmospheres, equivalent to a binding energy of 61 μJ/m^2, and a mode I fracture toughness of $K_I = 425$ Pam$^{1/2}$. Such values are up to two orders of magnitude higher than the ones

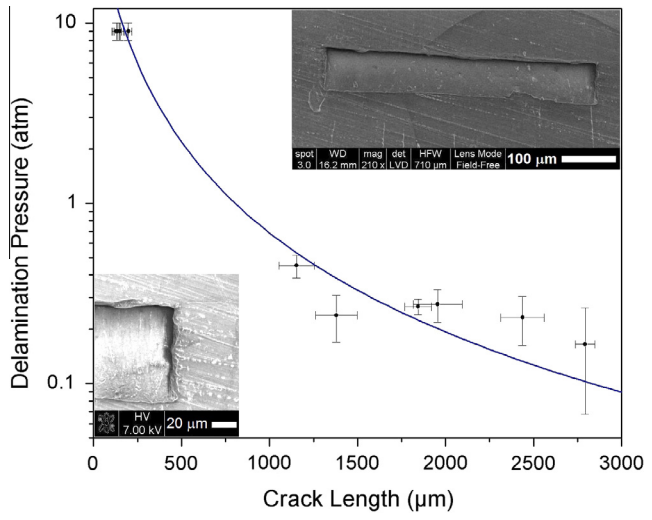

Fig. 5. Delamination pressure as a function of crack length. The pressure curve is calculated with the measured values $a = 2$ mm, $\delta = 60.3$ μm, $L' = 134$ μm. For Topas 5013 a Young's modulus of 2550 MPa and a Poisson's ratio of 0.37 were used. The small panels show SEM details of a microchannel cross-section obtained by cleaving a sample after UV-enhanced bonding.

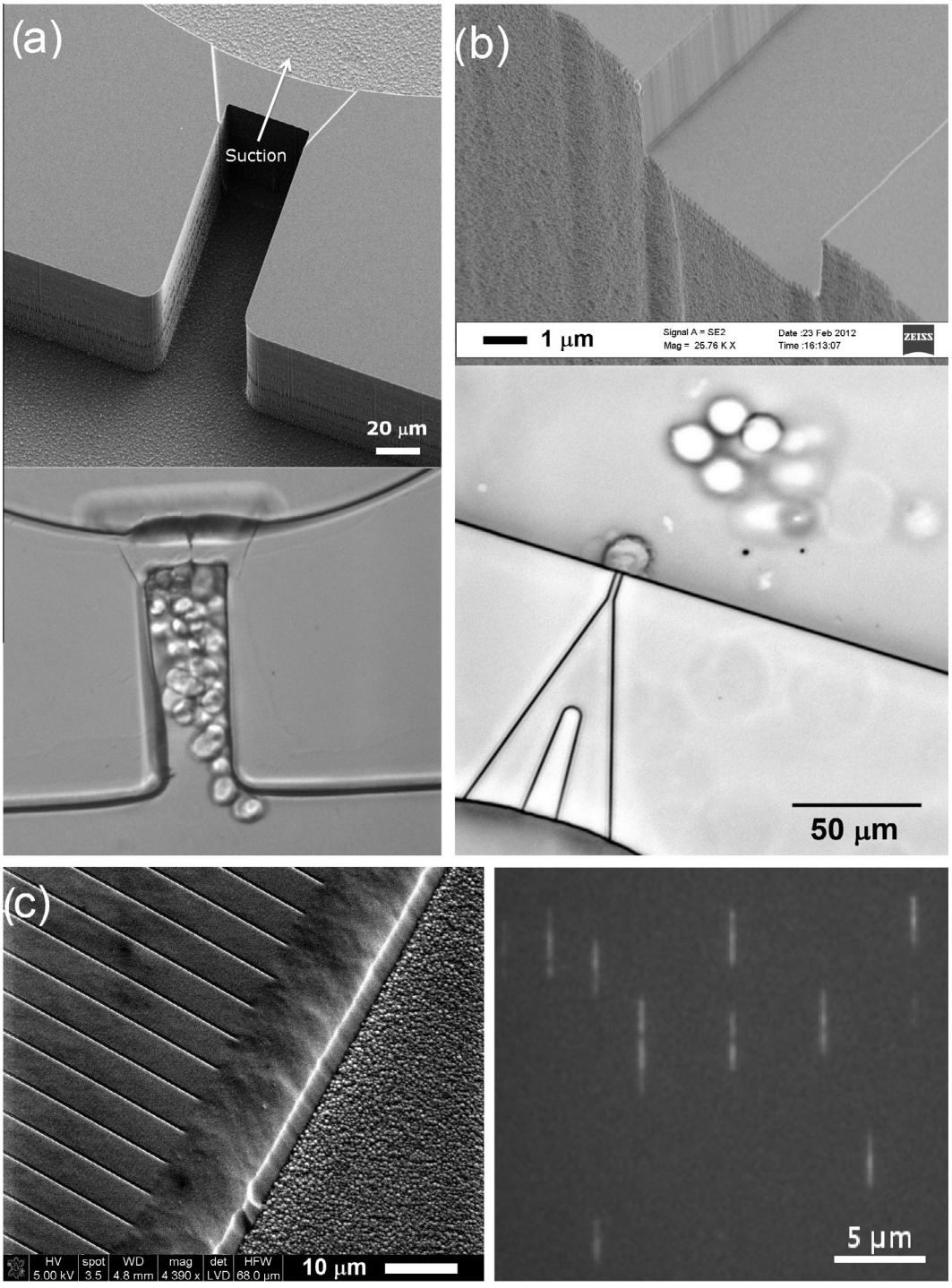

Fig. 6. Silicon master and final polymer chips for capture of PC 12 cells (a), and single HeLa cells (b). Detail of the polymer chip with nanochannels for λ-DNA elongation and fluorescence microscopy measurements (c).

obtained with UV/O_3 treated COC and PMMA substrates [8]. After such value, the polymer foil in most cases exceeded its yield strength and fractured at the Luer edges without delaminating, emphasizing the fact that after optimization, the bonding was no longer the limiting factor in high-pressure applications such as nanochannels with high hydraulic resistance.

In order to demonstrate the capabilities of the presented fabrication process, LoC chips with different functionalities have been successfully tested as can be seen in Fig. 6.

Neurotransmitter detection with microfabricated Pedot:Tosylate electrodes was previously demonstrated in [16,17], and as an extension to this, LoCs for multi (6a) and single (6b) cell capture have been fabricated and tested for cell capture. Both these chips will be combined with electrodes to perform "on chip" neurotransmitter detection.

Devices for single (6b) and multi (6a) cells capture has been successfully tested with respectively PC12 and HeLa cells [10]. Manipulation of single cells is basic for many cell-related studies

such as drug screening and impedance analysis, while capture of large groups of cells is relevant when studying detection of neurotransmitter release.

Stretching of DNA macromolecules through nanofluidic networks is also considered a powerful tool for direct sizing and mapping of DNA [18,19].

Fig. 6c shows a device with nanochannels enables to perform barcoding of DNA macromolecules by means of fluorescence microscopy measurements [20]. Fluorescent intensity variations from extended macromolecules have been demonstrated via chemical counterstaining against a cell-impermeant stain.

In conclusion, a platform for fabrication of all-polymer LoCs by means of silicon dry etching, electroplating and injection molding was here described. Moreover, the thermal bonding of injection molded TOPAS 5013 chips to commercially available TOPAS foils of 100 μm thickness and the same grade was optimized. The characterization of bonding strength was performed by measuring the bonding strength with the razor blade test. UV-treatment of surfaces was performed in order to enhance surface bonding. A simple method that is able to predict the delamination pressure of microchannels as a function of crack length was also verified: in optimized bonding conditions, the reached pressures was as high as 9 atm, equivalent to a binding energy of 53 $\mu J/m^2$, and a mode I fracture toughness of $K_I = 375\ Pam^{1/2}$. Finally, examples of applications were given in the fields of single/multi cell capture and DNA elongation.

Acknowledgements

This work is supported by the Danish Council for Strategic Research through the Strategic Research Center PolyNano (Grant No. 10-092322/DSF).

Appendix A. Supplementary data

Supplementary data associated with this article can be found, in the online version, at http://dx.doi.org/10.1016/j.mee.2013.01.060.

References

[1] A. de Mello, Lab Chip 2 (2002) 31N–36N.
[2] H. Andersson, A. van den Berg, Sens. Actuators B 92 (2003) 315–325.
[3] T. Hanemann, W. Bauer, R. Knitter, P. Woias (Eds.), MEMS/NEMS Handbook, Springer, 2006. pp. 801–869.
[4] J. Zhou, A.V. Ellis, N.H. Voelcker, Electrophoresis 31 (2010) 2–16.
[5] P.S. Nunes, P.D. Ohlsson, O. Ordeig, J.P. Kutter, Microfluid. Nanofluid. 9 (2010) 145–161.
[6] E. Becker, W. Ehrfeld, D. Munchmeyer, H. Betz, A. Heuberger, S. Pongratz, et al., Naturwissenschaften 69 (11) (1982) 520–523.
[7] R. Kupka, F. Bouamrane, C. Cremers, S. Megtert, Appl. Surf. Sci. 164 (2000) 97–110.
[8] K.Ø. Andersen, M. Hansen, M. Matschuk, S.T. Jepsen, H.S. Sørensen, P. Utko, D. Selmeczi, T.S. Hansen, N.B. Larsen, N. Rozlosnik, R. Taboryski, J. Micromech. Microeng. 20 (2010) 055010 (9pp.).
[9] J. Elders, H. Jansen, M. Elwenspoek, W. Ehrfeld, DEEMO: A New Technology for the Fabrication of Microstructures, IEEE, 345 E 47th St., NY 10017, New York, 1995.
[10] Simone Tanzi, Peter Østergaard, Marco Matteucci, Thomas Christiansen, Jiri Cech, Rodolphe Marie, J. Micromech. Microeng. 22 (2012) 115008.
[11] K. Cho, Y. Setsuhara, K. Takenaka, M. Shiratani, M. Sekine, M. Hori, Thin Solid Films 519 (2011) 6810–6814.
[12] R. Truckenmüller, P. Henzi, D. Herrmann, V. Saile, Microsyst. Technol. 10 (2004) 372–374.
[13] C.W. Tsao, L. Hromada, J. Liu, P. Kumar, D.L. DeVoe, Lab Chip 7 (2007) 499–505.
[14] A. Bhattacharyya, C.M. Klapperich, Lab Chip 7 (2007) 876–882.
[15] H. Taylor, D. Boning, C. Iliescu, J. Micromech. Microeng. 21 (2011) 067002.
[16] S.T. Larsen, R. Taboryski, Analyst 137 (2012) 5057–5061.
[17] S.T. Larsen, R.F. Vreeland, M.L. Heien, R. Taboryski, Analyst 137 (2012) 1831–1836.
[18] J. Tegenfeldt et al., Proc. Natl Acad. Sci. USA 101 (2004) 10979–10983.
[19] R. Riehn, M. Lu, Y. Wang, S. Lim, E. Cox, R. Austin, Proc. Natl. Acad. Sci. USA 102 (2005) 10012–10016.
[20] Peter Friis Østergaard, Macro Matteucci, Walter Reisner, Rafael Taboryski, Analyst 138 (2013) 1249.

Paper 6

Injection Moulded All-Polymer Capillary Microvalves for Passive Microfluidic Control: Performance Versus Prediction

Kasper Kistrup, Carl Esben Poulsen, Peter Friis Østergaard, Kenneth Brian Haugshøj, Rafael Taboryski, Anders Wolff, and Mikkel Fougt Hansen

Submitted for publication at Microfluidics and Nanofluidics

Authors

Kasper Kistrup[1*], Carl Esben Poulsen[1*], Peter Friis Østergaard[1], Kenneth Brian Haugshøj[2], Rafael Taboryski[1], Anders Wolff[1], Mikkel Fougt Hansen[1]

[1] Department of Micro- and Nanotechnology, Technical University of Denmark, DTU Nanotech, Building 345 East, DK-2800 Kongens Lyngby, Denmark.

[2] Centre for Microtechnology and Surface analysis, Danish Technological Institute, Gregersensvej, DK-2630 Taastrup, Denmark.

E-mail: mikkel.hansen@nanotech.dtu.dk, Phone: +45 4525 6338

Title

Injection Moulded All-Polymer Capillary Microvalves for Passive Microfluidic Control: Performance Versus Prediction.

Abstract

All-polymer, passive flow controlled lab-on-a-chip systems are preferential when developing chips for point-of-care, since they can be inexpensive to manufacture. Additional, rapid prototyping is desired when developing products. In this paper we present a chip system with geometric capillary microvalve test structures as an example of a prototype that can be simply manufactured using injection moulding and ultrasonic welding. A numerical model was constructed to investigate if simulations using a level-set method could be used to predict the burst pressures of rectangular capillary microvalves, effectively reducing the iterations required to craft a functional prototype. In addition, a systematic comparison between experimentally measured, numerically estimated and analytically calculated burst pressures is presented. It was found that injection moulding and ultrasonic welding was effective for prototype production and that there was a good correlation between the measured, numerical and analytical data.

Keywords

Injection moulding, capillary stop, polymer microfluidics, microvalve, ultrasonic bonding, numerical

*) These two authors contributed equally to this article.

1 Introduction

Ever since Manz *et al.* (Manz et al. 1990) coined the term 'miniaturized total analysis system' (μTAS), that laid out the fundamental requirements for lab-on-a-chip systems, it has been recognized that microfluidics plays a central role as the mediator linking all the components of a μTA. It is clear that precise control of fluids on-chip is critical for the success of such a microfluidic device.

In general, on-chip fluid management can be divided into two types: active and passive. Examples of active flow control include a variety of, *e.g.*, electrostatic and piezoelectric pumps (Abhari et al. 2012) and magnetic, electric and pneumatic valves (Oh and Ahn 2006). A more simplistic approach to flow control is to utilise the capillarity available due to the large surface-to-volume ratio of microsystems. This approach is known as passive or autonomous flow control. Two examples include capillary pumps and capillary microvalves (Zimmermann et al. 2008). Both types of flow control have their benefits and disadvantages. A major drawback of active control is that it adds complexity to the system, which is non-beneficial as most lab-on-a-chip devices aim to be low-cost and easy-to-fabricate. While passive components are inexpensive to incorporate, they are single-use and may be unidirectional. Furthermore, these systems may be sensitive to surfactants altering the surface and wetting properties. Depending on the desired application one should carefully choose the appropriate components to include in a given μTAS.

Two strategies for creating capillary microvalves exist (Fig. 1): (1) an abrupt geometry change, and (2) patterns of altered wetting properties. A geometric capillary microvalve consists of an abrupt expansion of a micro channel, with expansion angle, α, see Fig. 1a. From geometric considerations, it is evident that when the interface reaches the edge of the expanded region, the interfacial contact angle to the expanded region, ϕ, is smaller than the advancing contact angle, θ, and the interface is thus pinned as long as $\phi \leq \theta + \alpha$ (Cho et al. 2007). A similar pinning effect may be achieved in a hydrophobic capillary microvalve. Here, pinning is achieved by an abrupt change in the wetting properties, increasing the contact angle, see Fig. 1b. In several studies, this pinning effect have been exploited to create "virtual walls", guiding the liquid phase (Bouaidat et al. 2005; Zhao et al. 2002).

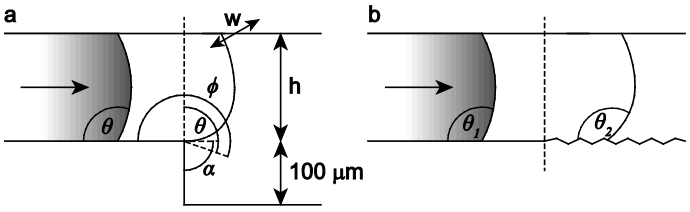

Fig. 1 Capillary microvalve types (cross section): **a** Geometric capillary microvalve, where pinning is achieved through a sudden change in geometry. $\boldsymbol{\theta}$, $\boldsymbol{\alpha}$ and $\boldsymbol{\phi}$ denote the channel contact angle, expansion angle and effective contact angle, respectively. *w* and *h* denote width and height of the channel. **b** Hydrophobic capillary microvalve, where pinning is achieved by abrupt changes in the wetting properties of one or more channel walls. $\boldsymbol{\theta_1}$ and $\boldsymbol{\theta_2}$ denote the contact angles of the smooth and rough channel, respectively.

Since passive flow control is promising for many applications, it is interesting to investigate the relations between analytical expressions and numerical evaluations that predict the rheology of microfluidics, and the performance of on-chip passive flow control components. Previously, controlled filling of micro channels using capillary microvalves has been under some investigation both experimentally, analytically and numerically:

Chibbaro *et al.* compared three computational methods (volume of fluid (VOF), lattice Boltzmann equations, and molecular dynamics) for modelling capillary filling in a nano channel containing a geometrical capillary stop (Chibbaro et al. 2009). Though deviation from the Lucas-Washburn equation was observed for the

diffuse-interface methods, the finite interface thickness was not observed to influence the pinning of the interface until the interface width was comparable to the size of the obstacle, suggesting that this approach may be applicable for estimating the pressure drop on pinned interfaces (Chibbaro et al. 2009). Likewise, the VOF method has been utilised to predict capillary flows of surface-patterned channels (Huang et al. 2006), filling of micro reservoirs (Tseng et al. 2002) and droplet formation in a squeeze mode inkjet device (Wu et al. 2005).

Though the VOF method has been applied to many models of incompressible two phase flows and is good for tracking the interface and ensuring mass conservation, one major disadvantage is the difficulty to calculate local surface curvatures (Sussman and Puckett 2000) and hence surface tension effects (Gerlach et al. 2006). Opposed to that, using the level-set (LS) method the calculation of the surface curvature is simple, but good conservation of mass is lacking (Sussman and Puckett 2000). Therefore, methods combining VOF and LS have been created (Olsson and Kreiss 2005; Sussman and Puckett 2000) and implemented in commercial software (COMSOL 2012).

Bouaidat *et al.* derived an analytical expression for the meniscus position during capillary flow. They confirmed their predictions using a parallel-glass-plate setup with channels defined by selective chemical modification of the glass surface. The channel height was varied by adding layers of tin foil. They recorded the temporal position of the meniscus and compared it to theoretical predictions (Bouaidat et al. 2005). Jokinen and Franssila examined the spontaneous filling of straight micro channels fabricated by SU-8 etching with varying contact angles on the walls of the channels realised by plasma treatment (Jokinen and Franssila 2008). Zimmermann *et al.* reported a range of passive valve systems, where capillary delay and stop valves were combined with capillary pump systems. These systems were created in silicon using photolithography and sealed with a cured piece of Polydimethylsiloxane (PDMS) (Zimmermann et al. 2008).

Duffy *et al.* presented a lab-on-a-disc system for enzymatic assays cast in PDMS using a mould prepared via photolithography. As a part of their study, they measured the angular velocity required to burst geometrical capillary microvalves of various cross-sections using water or PCR buffer (with 0.1% Triton-X) (Duffy et al. 1999). Cho *et al.* reported the theoretical background on capillary microvalves and compared analytical results to experimental (angular rotation) values obtained from a PolyCarbonate (PC)-PDMS chip created using soft lithography, featuring geometrical capillary microvalves (Cho et al. 2007). Thio *et al.* conducted a rigorous analysis of the equations governing capillary microvalves in lab-on-a-disc systems including a comparative study of experimental vs. analytically calculated burst pressures of geometrical capillary microvalves. Their system was a chip fabricated from two layers of machined Polymethyl methylacrylate (PMMA) bonded with a layer of pressure-sensitive adhesive foil. They measured the angular rotation required for bursting vs. various geometries (Thio et al. 2013).

An important aspect of lab-on-a-chip systems is the fabrication process itself. When developing a disposable chip for commercial use, it is highly desirable to apply rapid prototyping technologies that are directly compatible with mass production. Lab-on-a-chip systems presented in the scientific literature often consist of different materials that need to be carefully aligned prior to assembly (Begolo et al. 2011). While this is no hindrance for prototyping, a redesign is necessary for implementation into an assembly line or to reduce fabrication costs. Furthermore, the fabrication of a single chip is laborious for silicon chips, glass etched chips and to some extent PDMS chips leading to long production times for each chip.

Injection moulding of thermoplastics is well established as a commercial production technique and serves well to reliably replicate structures down to nanometer size at turn-around times of < 1 min per chip (Matteucci et al. 2013; Tanzi et al. 2012).

Ultrasonic welding is also widely used in production around the world, though its usage for lab-on-a-chip-systems is limited. Ultrasonic welding functions without the need of additional adhesives or substrates and only applies a localised friction heating where the bonding takes place. This is advantageous when working with lab-on-a-chip systems where interactions of chip reagents or sample with the bonding material might dissolve the chip or contaminate the sample. Since the heating only occurs at the welding seam, structures of large width/height ratios that would collapse during a thermal bonding process can be bonded with ultrasonic welding. Additionally, as the bulk of the chip is not heated, pre-loading of dried or jellified reagents is possible, which is of high relevance to Point-of-Care devices (Sun et al. 2013). The local heating is applied with high power (50-250 W for ~0.1 s) leading to turn-over times of < 5s per welding, which is considerably shorter than other common bonding processes such as thermal bonding and plasma assisted bonding (Bu et al. 2013). This makes ultrasonic welding very desirable for mass production. Since ultrasonic welding does not have the same cross material compatibility as, *e.g.*, adhesive bonding, the most common practise is to weld together like materials, however, it does allow for bonding through thin-film layers or thin sheets of other polymer types (Bu et al. 2011; Truckenmüller et al. 2006).

In this paper, we address the feasibility of using the level set method to numerically predict fluid behaviour in a surface tension controlled all-polymer system. We present a systematic comparison between experimentally measured, numerically estimated and analytically calculated burst pressures of a selection of geometrical capillary microvalves as sketched in Fig. 1a with the nominal dimensions width [μm]/height [μm]: 100/100, 200/100, 300/150, 500/150 and 500/250, respectively. Our experimental model system is an example of rapid prototyping of an all-polymer injection moulded chip. It consists of two pieces of polymer, which have been thin film coated to increase the hydrophobicity. The chip parts are bonded using ultrasonic welding. Apart from the shim fabrication, all parts of the chip fabrication are directly applicable to mass production and require no careful alignment during assembly.

2 Theory

The theoretical pressure drop required for forcing a liquid through an expanding microfluidic structure such as a capillary microvalve may be found analytically for simple geometries. Cho *et al.* assumed that the liquid interface will pin to the corner of the expansion forming an angle α (Fig. 1a) if the interface angle to the expanded wall, ϕ, is smaller than the advancing contact angle, θ, leading to the pinning condition (Cho et al. 2007)

$$\theta \leq \phi \leq \theta + \alpha \qquad \textbf{(2.1)}$$

also known as Gibbs' inequality condition (Dyson 1988; Gibbs 1906).

By geometric considerations, the curvature of the pinned surface can be described and used for calculating the Young-Laplace pressure of the interface (Equation (2.2)) of the capillary microvalve illustrated in Fig. 1a (Cho et al. 2007; Delamarche et al. 1998; Huang et al. 2006)

$$\Delta p = -\gamma\left(\frac{2\cos\theta}{w} + \frac{\cos\phi}{h} + \frac{\cos\theta}{h}\right) \qquad \textbf{(2.2)}$$

where γ is the surface tension of the gas-liquid interface, and w and h are the dimensions of the microvalve geometry, see Fig. 1a. Maximising the pressure drop with regards to ϕ expressed in terms of Equation (2.1) yields the theoretical burst pressure,

$$p_{burst} = -\gamma\left(\frac{2\cos\theta}{w} + \frac{\cos(\min\{\theta+\alpha; 180°\})}{h} + \frac{\cos\theta}{h}\right). \quad \textbf{(2.3)}$$

This expression may also be obtained by considering the change in total interfacial energy of the system as a result of the change in volume (Andersson et al. 2001; Huang et al. 2006).

3 Experimental

3.1 Chip fabrication and characterisation

The polymer chip consists of two parts: an injection moulded main part of Cyclic Olefin-Copolymer (COC) polymer (TOPAS grade 5013L-10) and a 0.254 mm extruded COC sheet (TOPAS grade 5013S-04) both from TOPAS Advanced Polymers GmbH, Frankfurt-Höchst, Germany. The main part features capillary stops laid out in parallel, each with its own luer-fitted inlet, see Fig. 2a. Injection moulding was conducted on Engel Victory 80/45 Tech injection moulder (ENGEL, Schwertberg, Austria) fitted with a custom milled aluminium master featuring the negative counter-part of the channel layout on one side of the injection moulding tool and a luer-layout counter-part with through-holes (Andresen et al. 2010) on the other. To complete the chip, the injection moulded part was bonded to the COC sheet using a Telsonic USP4700 ultrasonic welder (Telsonic, Erlangen, Germany).

The channel layout features eight sets of channels with capillary microvalves connecting separate luer fittings to a collective outlet, see Fig. 2a. Each channel has a unique width and height (see Table 1) and a capillary microvalve constructed by a 90° expansion towards the floor of the channel, see Fig. 1a for a schematic drawing. Energy directors used for the ultrasonic welding were 130 μm wide triangular prism shaped protrusions (apex angle=60°) centred 500 μm from the channel sidewalls.

Prior to bonding, both the injection moulded part and the COC sheet were coated with a hydrophobic 1H,1H,2H,2H-perfluorodecyltrichlorosilane (FDTS, CAS No 78560-44-8) layer using a gas phase multi-step deposition process. While FDTS and analogous perfluoroalkylsilanes alone provide a hydrophobic coating on silicon (Ashurst et al. 2004; Ashurst et al. 2003; Mayer et al. 2000), polymers require a metal oxide adhesion layer prior to deposition of FDTS (Kobrin et al. 2007; Kobrin et al. 2005). Otherwise, the contact angle with water may be rather low, depending on the substrate. For the present work, silicon dioxide was used as the adhesion layer. The deposition was performed at 35°C in a MVD100 system from Applied Microstructures (San Jose, California). In brief, the system consists of a deposition chamber, vaporization chambers for the precursors and cylinders housing the different precursors, where the connections between precursor cylinders, vaporization chambers and deposition chamber are controlled by valves. The system is connected to a pump via the deposition chamber. Precursor is vaporized from the cylinders into the vaporization chambers. Once a set pressure in the vaporization chamber is reached, the precursor vapour is introduced into the deposition chamber by means of the pressure difference between vaporization chamber and deposition chamber. During the precursor introduction step and the subsequent reaction, no pumping on the chamber is performed. After the reaction is finished, the reaction chamber is pumped down and purged several times with nitrogen. Prior to the deposition, the sample surface is activated using a remote oxygen plasma generated from a plasma source in the MVD100 system. Subsequently, silicon dioxide and FDTS is deposited at 35°C in two consecutive process steps. Silicon tetrachloride and water were used as precursors for silicon dioxide. The two precursors are introduced simultaneously and allowed to react for a given time. The simultaneous presence of the two precursors means that the layer thickness obtained in one reaction

cycle depends on the partial pressures of the two precursors and the reaction time (Kobrin et al. 2005). For formation of the FDTS-layer, FDTS and water are introduced simultaneously. The simultaneous action of FDTS and water allows for the deposition of a self-assembled monolayer (SAM) of the perfluoroalkylsilane (Mayer et al. 2000). The contact angle of water to FDTS coated COC has previously been measured to 120±2° (data not shown).

The chip topography characterization was carried out using a Nova 600 NanoSEM (FEI, Eindhoven, Netherlands) for images and a PLu Neox 3D Optical Profiler (Sensofar-Tech, S.L, Terrassa, Spain) for topographic data.

Ultrasonic welding causes an increase in channel height, which was estimated by deriving the height of the welding seam based on the average measured seam width (from microscope images) and the calculated energy director area (based on topographical data).

3.2 Burst pressure measurements

Hydrostatic burst pressures were measured by slowly raising a water column (50 mL syringe without piston) above chip level using a Thorlabs LTS150 motorized stage (Thorlabs, Newton, NJ, USA). The water column was connected to the chip via tubing with luer fittings, resulting in a stable hydrostatic pressure. Before initiating a measurement, the chip was positioned so the surface vertical position matched that of the water surface. The syringe was then raised at 1 mm/s while the capillary stop under investigation was carefully monitored. Once the water advanced into the channel leading to the capillary stop, the stage was paused and the fluid allowed to pin at the capillary stop after which the stage was re-engaged. When the water burst through the capillary stop, the stage was stopped immediately and the height recorded. The syringe vertical position was then reset and after the meniscus had retracted past the capillary stop, the process was repeated for a total of three measurements per capillary stop. The chips were then rinsed and dried before another set of measurements were conducted. The burst pressures were calculated using $p = \rho g H$, where p is the calculated pressure, $\rho = 998\ \mathrm{kg/m^3}$, $g = 9.82\ \mathrm{m/s^2}$ and H is the measured height.

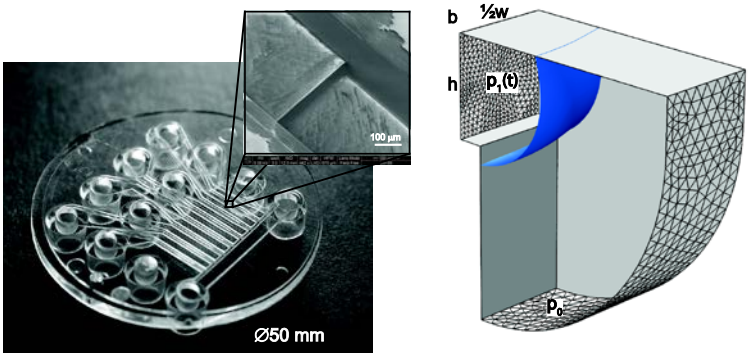

Fig. 2 a Photograph of a chip (pre-welding) showing the overall lay-out of the channels containing the capillary stops. The location of a single capillary stop has been marked (box) along with an inset with a SEM image of the same capillary stop. **b** Geometry used in the COMSOL Multiphysics finite element calculations. The symmetry plane is the transparent face of the figure and an advancing meniscus is illustrated as a blue isosurface representing 50% water content. ½w, h, $\boldsymbol{p_1(t)}$ and $\boldsymbol{p_0}$ indicate half width, height, inlet pressure and outlet pressure, respectively.

3.3 Numerical simulations

A numerical analysis of the capillary microvalves was conducted using the “Laminar Two-Phase Flow, Level Set” package in COMSOL Multiphysics 4.3a (COMSOL A/S, Kgs. Lyngby, Denmark). The

governing equations were the Navier Stokes equation and the reinitialized level set function, $\phi_{\text{ls}}(\boldsymbol{r})$, to track the interface and interpolate the material properties(COMSOL 2012; Olsson and Kreiss 2005). $\phi_{\text{ls}}(\boldsymbol{r}) = 1$ for 0% water and $\phi_{\text{ls}}(\boldsymbol{r}) = 0$ for 100% water. Properties, such as the density, are determined by $\rho = \phi_{\text{ls}}(\boldsymbol{r})\rho_{air} + \left(1 - \phi_{\text{ls}}(\boldsymbol{r})\right)\rho_{water}$. (COMSOL 2012).

Models were constructed on the basis of the geometry of the microfluidic chip with the selected channel dimensions. The inlet channel length was chosen to accommodate the relaxation of the initial (flat) interface. Likewise, the outlet chamber was made sufficiently large for the meniscus to burst without interacting with the outlet boundary, see Fig. 2b. To reduce computational demands and to reduce convergence problems when relaxing the initial interface, both phases were assumed to be incompressible. The central symmetry plane (cf. Fig. 2b) was exploited to minimise computational demands. The simulation was run as a time-dependent model with the pressure drop $\Delta p(t) = p_1(t) - p_0$ across the geometry (cf. Fig. 2b) gradually increasing as time progressed. p_0 was set to 0. To ensure that bursting would not occur due to dynamic effects in the fluid from the constantly increasing pressure, and to elucidate the minimum pressure required for bursting, a model coupled damping term was included in the expression for the pressure drop,

$$\Delta p(t) = p_{\text{start}} + \alpha t - \beta\overline{\phi_{\text{ls}}}(t). \qquad \textbf{(3.1)}$$

P_{start} was set larger than the capillary pressure of the models inlet channel, pressure ramping rate (α) was set to 50.000 Pa/s and the damping range (β) was set to 200 Pa. Effectively, $\overline{\phi_{ls}}(t) = \frac{Volume_{water}(t)}{Volume_{geometry}} = \frac{\int_V \phi_{\text{ls}}(\boldsymbol{r},t)d\boldsymbol{r}}{\int_V d\boldsymbol{r}}$. The pressure drop is thus reduced as more volume is occupied by water, resulting in a damping of the interface advance.

The rationale of this model coupling is that the pressure drop increases more slowly when the interface expands. Additionally, as the burst pressure is reached and the valve starts bursting, the pressure drop is reduced as a result of the increasing volume fraction occupied by water, but the interface will continue to grow due to the smaller Laplace pressure of the larger (and less curved) interface.

To achieve faster convergence, 'transformer oil' ($\rho = 0.879\ \text{g/cm}^3, \eta = 20.8\ \text{mPa s}$) with surface tension equal to that of an air-water interface ($\gamma_{water/air} = 72.89\ \text{mN/m}$) was used as a substitute for air. As stated above, this does not take into account the compressibility of air, however, due to the nature of the simulation it is not expected to affect the results. Additionally, the increased density and viscosity of oil will affect the inertial component, however, since the model is already damped by equation (3.1) this is not expected to influence the burst pressure.

4 Results and discussion

We first present a validation of the numerical model including the modus operandi of determining the burst pressure. We then comment on the fabrication process and finally the experimental burst pressures are presented.

4.1 Numerical model analysis

To confirm that the model coupled damping term, Equation (3.1), used to control the pressure drop in the simulation functioned as intended, the pressure drop developing over time is plotted in Fig. 3a. As evident, the two opposing terms in Equation (3.1) results in three stages: interface settling (Fig. 3a(I)), linear pressure

rise (Fig. 3a(II)) and bursting (Fig. 3a(IV)). To study the behaviour of the virtual meniscus during the simulation and its interaction with the model geometry, contour plots of fraction-of-water on the symmetry plane (see Fig. 2b) are plotted for the selected times in Fig. 3b. The readily recognisable peak in Fig. 3a and the on-going bursting illustrated Fig. 3b(V) confirms that the constructed model coupling works as intended and does not prevent continued bursting of the valve.

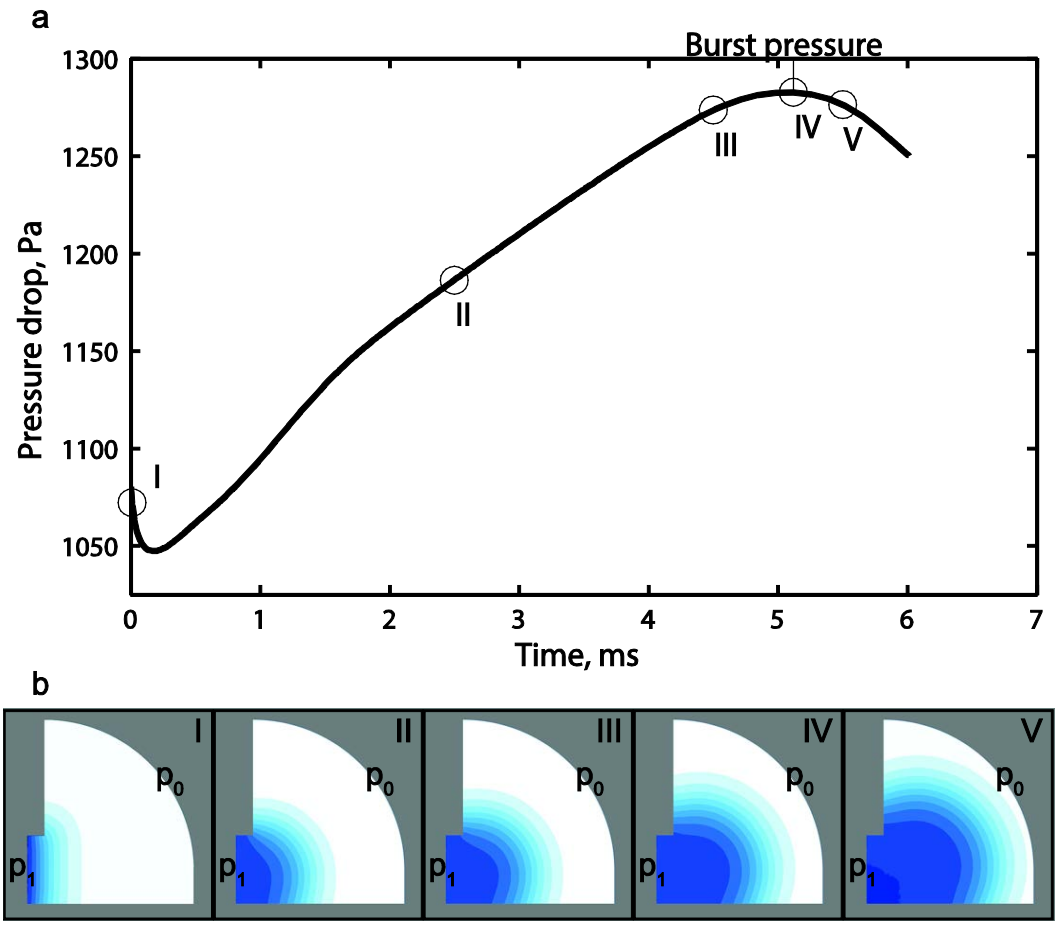

Fig. 3 a Pressure drop developing over time, controlled by the model coupling Equation (3.1). **b(I-V)** Contour plots of fraction of water (ϕ_{ls}) spanning 0:0.1:1, dark blue being 100% water. **b(I)** Initial flat interface with forced contact angle = 90°. **b(II)** Stabilised and linearly growing interface. **b(III)** Interface immediately prior to bursting. **b(IV)** Bursting meniscus. Note the concentration of water at the pinning corner is >90%. **b(V)** Rapidly expanding meniscus, where the damping term reduces the pressure drop.

The fact that the meniscus has a finite width that spans to both sides of the pinning corner at all times may seem counter intuitive from an experimentalists point of view, but this is intrinsic for the level-set method. As mentioned in the introduction, the level-set function operates on an interface of finite thickness with intermediate properties of the two phases. This makes the level-set method ideal for calculating curvatures, but weak at conserving mass and tracking the meniscus position. When conducting experiments, the temporal meniscus position defines the burst pressure, whereas in simulations using the level-set method, the exact meniscus position is not available (Fig. 3b). Therefore a different approach for determining the burst pressure has to be taken. In this study, the maximum pressure drop that can be applied without causing a rapid expansion of the meniscus defines the burst pressure (peak in Fig. 3a).

When investigating sources of deviation, the model was generally found to be robust in terms of the parameters α and β (data not shown), meaning that the results were not sensitive to doubling or halving of

these parameters. However, the simulation time could be significantly prolonged if the α/β ratio was decreased, see Equation (3.1). On the other hand, a too high ratio would complicate the determination of the burst pressure.

To validate the numerical model, a set of axial symmetrical geometries was analysed. Contrary to the rectangular geometries, the burst pressures of the cylindrical geometries have a closed-form analytical solution, see supplementary information. From supplementary Fig. S2 it is evident that the simulations consistently underestimate the analytically calculated burst pressures by 6.7%. As discussed by Olsson and Kreiss, the diffusive representation of the interface results in an attraction between the interface and the walls when the distance is close to the interface thickness (Olsson and Kreiss 2005). This effect may be the cause of the consistent burst pressure undershooting of the level-set based model. Obviously, this effect depends in part on the geometry and the impact on the numerical burst pressure varies accordingly. In light of the intrinsic limitations of the level-set method such as the diffuse interface definition and the poor conservation of mass, which may destabilise the pinned interface, the consistent underestimation of the burst pressure by 6.7% is acceptable for most applications.

Fig. 4 shows numerical simulations as well as analytical calculations (Equation (2.3)) of the burst pressure in structures that is illustrated in Fig. 1a for 50 μm ≤ w ≤ 500 μm and 25 μm ≤ h ≤ 281 μm (details given in supplementary information). We again observe a consistent underestimation of the numerical burst pressure compared to the analytical result, except the difference is larger (11.2%). This behaviour can be explained by the more complex geometry, which is more taxing for the numerical simulations and also causes the analytical predictions to be less accurate, since a complete solution does not exist. As stated above, we believe that this is an acceptable error for most applications, such as using our model to check burst pressures of complex microfluidic systems prior to fabrication.

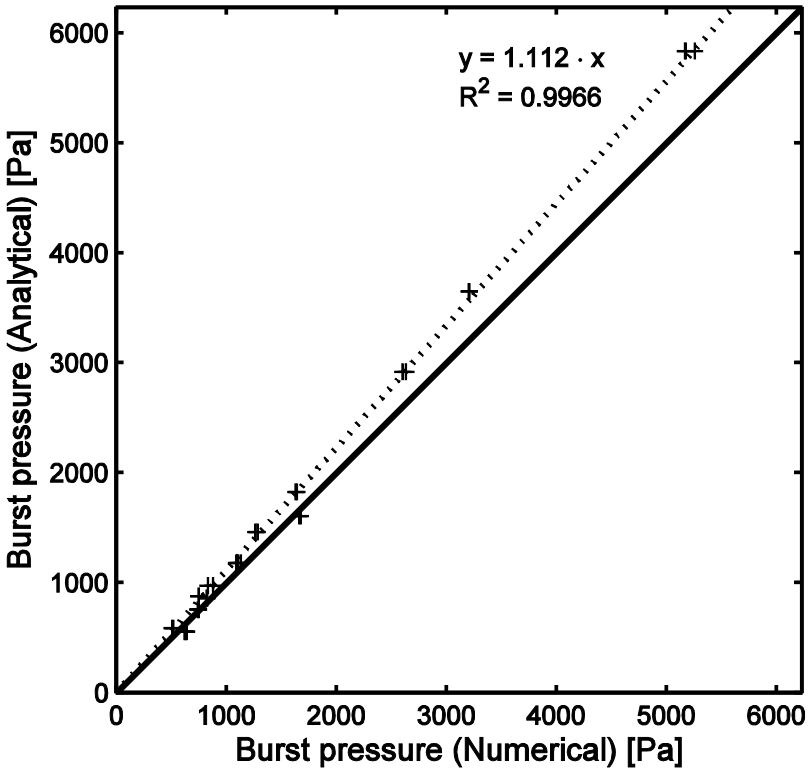

Fig. 4 Analytically calculated burst pressures of all nominal and measured geometries plotted versus numerically determined burst pressures (+) of the same geometries (See supplementary information, for a complete list of geometries and results). The solid line represents $\boldsymbol{x = y}$ and the dashed line is a linear fit of the data points.

The R-squared values (>0.995) for the linear fits of the correlations between the numerically modelled and analytically calculated burst pressures (*cf.* Fig. 4 and Fig. S2) suggests that the model is robust and precise for a wide range of geometries. Furthermore, the similarity in underestimating between the cylindrical and rectangular geometries shows that the model performs equally well with simple and complex problems.

4.2 Geometrical characterisation of chips

A total of eight capillary microvalve geometries (nominal width/nominal height in μm) were chosen for investigation; 50/25, 50/50, 100/50, 100/100, 200/100, 300/150, 500/150 and 500/250, see Fig. 2a inset for a SEM photograph and Fig. 1a for the schematic layout of a single capillary microvalve. It was not possible to conduct experiments on the smallest geometries (50/25, 50/50 and 100/50) due to polymer blocking the channels after ultrasonic welding.

The micro milling and injection moulding added some error to the nominal geometries chosen, but for clarity the labels for the different capillary stops have been kept in the “nominal width/nominal height” format. The actual widths and heights deviate 1.2-10.7% from their nominal values as determined by the chip characterisation (see Table 1 for geometries). It is estimated that the majority of the error comes from the milling process whilst the polymer filling/shrinkage associated with injection moulding of 5013L-10 is negligible (Tanzi et al. 2012). The average arithmetic mean roughness (Sa) of the chip bottom part surface was measured to 0.6 μm.

Table 1 Nominal geometries compared to the post fabrication geometries as determined by chip characterisation. Note that the heights contain the added height from the welding process.

	***w* [μm]**		***h* [μm]**	
Valve #	**Nominal**	**Actual**	**Nominal**	**Actual**
100/100	100	92	100	135
200/100	200	202	100	134
300/150	300	286	150	182
500/150	500	486	150	181
500/250	500	447	250	281

Ultrasonic welding is performed by applying vibrations through a transducer to an energy director that melts and welds two layers together, as illustrated in Fig. 5. Depending on the success of the welding there are two main outcomes; if too much energy is applied, polymer may flow into cavities, known as flash (Fig. 5 bottom left). Conversely if too little energy is deposited, the energy directors will not completely melt, leaving small gaps (Fig. 5 bottom right). In either case, there will be an increase in height due to the presence of the polymer welding seam which in the present study was 23.9 ± 1.7 μm. Ultrasonic welding was chosen over thermal bonding in part because thermal bonding is not applicable with the hydrophobic coating.

The actual widths and heights have been used as input in the analytical expressions as well as the numerical simulations.

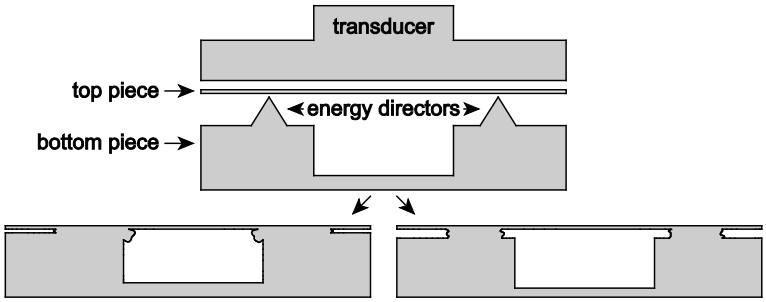

Fig. 5 Cross sectional schematic of a channel before (top) and after ultrasonic welding (bottom left and right). The top part of the chip is pressed onto the bottom part with an ultrasonic transducer, which then vibrates to melt the energy directors. Depending on the amount of energy that is deposited via the transducer different outcomes will arise: Too much energy causes flash to form (bottom left) while too little energy causes a gap in the upper part of the channel (bottom right). In both cases, an added height results from the welding process.

In this study the estimated turn-around time for the total fabrication and assembly of a single chip was <2 minutes not taking into account transport of parts between equipment and hydrophobic coating. It is concluded that the rapid prototyping used in this study is promising for mass production.

4.3 Experimental burst pressures

Two sets of measurements were conducted per chip on a total of two to three chips. Each set consisted of three measurements, where the meniscus was pulled back in-between each measurement by re-aligning the

water column with the chip surface. This resulted in a total of 12-18 measurements per capillary stop geometry. An example of a single measurement can be seen in supplementary Video 1.

Fig. 6 shows the average measured hydrostatic burst pressures for each microvalve geometry compared to the analytically calculated and numerically simulated values. In general, the measured burst pressures are lower than the analytical results with larger relative deviations for larger burst pressures, ranging from 2.2% to 18%. There is good reproducibility of the experimental data with regards to repetitions on the same chip and repetitions in-between chips, with a mean coefficient of variation of 2.2%. The large deviation from the analytical and numerical values for the 100/100 capillary microvalve can be explained by incomplete polymer melting during ultrasonic welding: The small gaps left by ultrasonic welding (*cf*. Fig. 5 bottom right) were observed to have lower capillary pressure than the actual capillary microvalve. This led to a premature bursting of the microvalve and hence a lower than expected capillary burst pressure (*cf*. Fig. 6). Disregarding the 100/100 microvalve, a good correlation between the experimental and analytical burst pressures is observed with an average deviation of 4.3%.

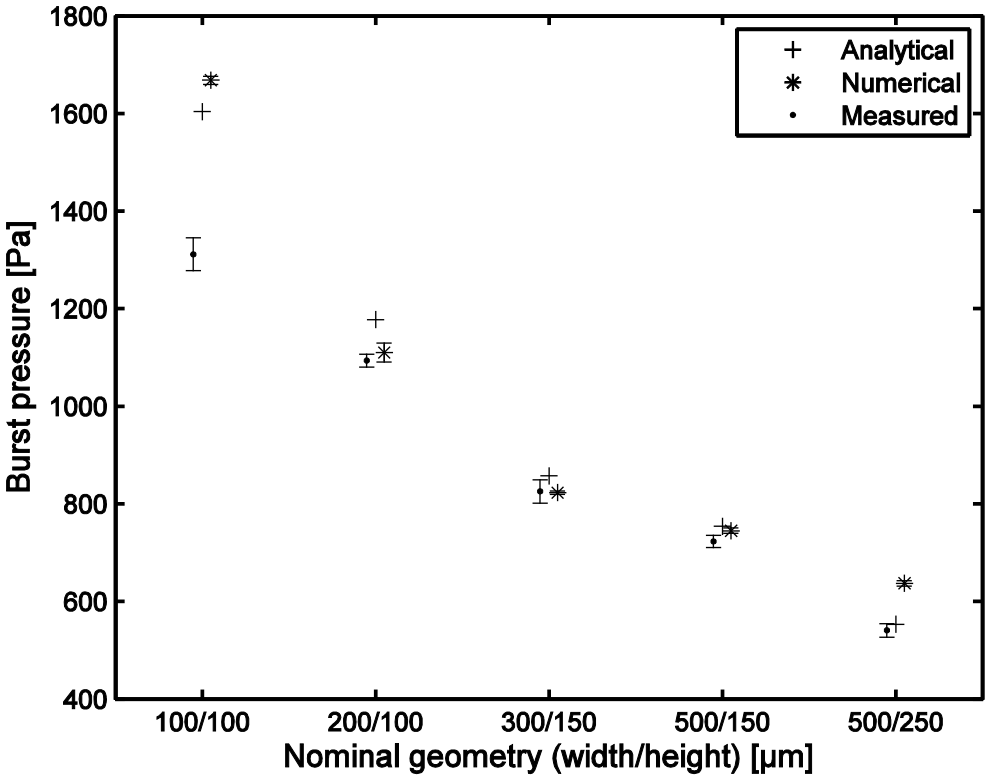

Fig. 6 Analytical, numerical and experimental burst pressures of the selected capillary microvalve geometries. + denotes the burst pressures calculated from the analytical expression (Equation (2.3)). ∗ denotes the numerically simulated burst pressures, n = 2, 3, 2, 3 and 3 for 100/100, 200/100, 300/150, 500/150 and 500/250, respectively. • denotes the experimentally measured hydrostatic burst pressures, n=18 for 100/100 and 500/250 and n=12 for 200/100, 300/150 and 500/150. Error bars represent the sample standard deviation.

Although the analytical results deviate slightly from the measured burst pressures, they do show that over the investigated aspect ratios and dimensions, Equation (2.3) can predict the burst pressures within 20 %. The small standard deviations on the experimental results demonstrate that injection moulded and ultrasonically welded chips provide excellent reproducibility and stable results. For the smallest geometries it was not possible to produce functional channels, due to polymer blocking the channels after bonding by ultrasonic

welding (Fig. 5 bottom left). However, it is expected that this can be avoided by optimising the chip design, shim quality, the energy director geometry and bonding parameters. The chip design used in this study had a high local density of energy directors, which complicates the ultrasonic welding. Micromilling is also not ideal for producing small (~50 μm) structures, because it is difficult to maintain precise alignment upon tool switching with the machines used in the present work.

4.4 Numerically simulated burst pressures

As previously described, the numerical simulations were carried out for both nominal- and actual (measured) chip dimensions using starting pressures (p_{start}) lying in-between the analytical capillary pressure of the inlet channel and the analytical capillary burst pressure, see Equation (3.1). For each geometry, two additional control simulations were conducted by using starting pressures of approximately 90% and 70% of the predicted burst pressure of the preceding simulation.

As can be observed in Fig. 6, the numerical estimates fit well with the experimental values, except for the 100/100 geometry. The numerical model does, however, show good agreement with the analytical estimate for this geometry. When comparing Fig. 6 and Fig. 4, there is a general trend of the numerical predictions to deviate more from the analytical results for large burst pressures, while for small burst pressures there is a better correlation. From the linear fit it can be seen that the numerical model is a good alternative to the analytical expression. It is also evident that the width/height aspect ratio does not influence the results for the investigated range of geometries.

As can be seen in Fig. 6 there is good agreement between the numerical predictions and the measured burst pressures. Together with the demonstrated robustness of our numerical model, this indicates that the level-set method is promising for burst pressure predictions of more complicated geometries that are not readily described by analytical expressions. The results presented here indicate that numerical calculations may be applicable as a tool to predict burst pressures of complex geometries, however, further studies need to be undertaken to confirm this.

5 Concluding remarks

We have presented an all-polymer chip system fabricated using injection moulding and ultrasonic welding, which can be directly implemented in mass production, going hand-in-hand with concepts such as rapid prototyping.

The chip features geometrical capillary burst valves of several dimensions and aspect ratios. The measured burst pressures were found to be reproducible and have been systematically compared to numerical and analytical approximations of like geometries. In both cases the burst pressures were found to be similar. The numerical model was validated, by modelling a more simple geometry for which a complete analytical expression exists. The numerical model was found to be precise and robust with regards to geometry and model parameters. Using the level-set approach to calculate burst pressures is untraditional, since it lacks good mass conservation and meniscus tracking, however, a consistent method of determining burst pressures was found by introducing a dampening term to the model. Thus, using this approach might be beneficial to others when simulating unstable systems.

The data presented in this study supports the idea of using numerical simulations as a tool in rapid prototyping to predict burst pressures of complex geometries before physically crafting the prototypes, ideally reducing the number of iterations needed from idea to functioning prototype to final product.

The ability to tailor and mass-produce capillary microvalves with a quantitatively predictable behaviour in all-polymer microfluidic systems is important and beneficial for many medical, biological and chemical applications.

Acknowledgements This work is supported by the Danish Council for Strategic Research through the Strategic Research Center PolyNano (Grant No. 10-092322/DSF).

We would like to acknowledge Minqiang Bu, Department of Photonics Engineering, Technical University of Denmark, and Ivan R. Perch-Nielsen, DELTA, Hørsholm, Denmark, for sharing experience in micro-fabrication and ultrasonic welding, and Fridolin Okkels, Department of Micro- and Nanotechnology for discussions on COMSOL related topics.

References

Abhari F, Jaafar H, Yunus NA (2012) A Comprehensive Study of Micropumps Technologies. Int J Electrochem Sci 7:9765–9780.

Andersson H, van der Wijngaart W, Griss P, et al. (2001) Hydrophobic valves of plasma deposited octafluorocyclobutane in DRIE channels. Sensors Actuators B Chem 75:136–141. doi: 10.1016/S0925-4005(00)00675-4

Andresen KØ, Hansen M, Matschuk M, et al. (2010) Injection molded chips with integrated conducting polymer electrodes for electroporation of cells. J Micromechanics Microengineering 20:055010. doi: 10.1088/0960-1317/20/5/055010

Ashurst RW, Carraro C, Chinn JD, et al. (2004) Improved Vapor-phase Deposition Technique for Anti-stiction Monolayers. In: Maher MA, Jakubczak JF (eds) Proc. SPIE Vol. 5342. pp 204–211

Ashurst WR, Carraro C, Maboudian R (2003) Vapor phase anti-stiction coatings for MEMS. IEEE Trans Device Mater Reliab 3:173–178. doi: 10.1109/TDMR.2003.821540

Begolo S, Colas G, Viovy J-L, Malaquin L (2011) New family of fluorinated polymer chips for droplet and organic solvent microfluidics. Lab Chip 11:508–12. doi: 10.1039/c0lc00356e

Bouaidat S, Hansen O, Bruus H, et al. (2005) Surface-directed capillary system; theory, experiments and applications. Lab Chip 5:827–36. doi: 10.1039/b502207j

Bu M, Perch-Nielsen IR, Sun Y, Wolff A (2011) A microfluidic control system with re-usable micropump/valve actuator and injection moulded disposable polymer lab-on-a-slide. 2011 16th Int. Solid-State Sensors, Actuators Microsystems Conf. IEEE, pp 1244–1247

Bu M, Perch-Nielsen IR, Sørensen KS, et al. (2013) A temperature control method for shortening thermal cycling time to achieve rapid polymerase chain reaction (PCR) in a disposable polymer microfluidic device. J Micromechanics Microengineering 23:074002. doi: 10.1088/0960-1317/23/7/074002

Chibbaro S, Costa E, Dimitrov DI, et al. (2009) Capillary filling in microchannels with wall corrugations: a comparative study of the Concus-Finn criterion by continuum, kinetic, and atomistic approaches. Langmuir 25:12653–60. doi: 10.1021/la901993r

Cho H, Kim H-Y, Kang JY, Kim TS (2007) How the capillary burst microvalve works. J Colloid Interface Sci 306:379–85. doi: 10.1016/j.jcis.2006.10.077

COMSOL (2012) COMSOL Multiphysics 4.3 Microfluidics Module User's Guide.

Delamarche E, Bernard A, Schmid H, et al. (1998) Microfluidic Networks for Chemical Patterning of Substrates: Design and Application to Bioassays. J Am Chem Soc 120:500–508. doi: 10.1021/ja973071f

Duffy DC, Gillis HL, Lin J, et al. (1999) Microfabricated Centrifugal Microfluidic Systems: Characterization and Multiple Enzymatic Assays. Anal Chem 71:4669–4678. doi: 10.1021/ac990682c

Dyson DC (1988) Contact line stability at edges: Comments on Gibbs's inequalities. Phys Fluids 31:229. doi: 10.1063/1.866851

Gerlach D, Tomar G, Biswas G, Durst F (2006) Comparison of volume-of-fluid methods for surface tension-dominant two-phase flows. Int J Heat Mass Transf 49:740–754. doi: 10.1016/j.ijheatmasstransfer.2005.07.045

Gibbs JW (1906) Scientific Papers of J. Willard Gibbs...: Thermodynamics. Longmans, Green and Company

Huang W, Liu Q, Li Y (2006) Capillary Filling Flows inside Patterned-Surface Microchannels. Chem Eng Technol 29:716–723. doi: 10.1002/ceat.200500332

Jokinen V, Franssila S (2008) Capillarity in microfluidic channels with hydrophilic and hydrophobic walls. Microfluid Nanofluidics 5:443–448. doi: 10.1007/s10404-008-0263-y

Kobrin B, Dangaria N, Chinn J (2007) Low Temperature Nanolayers Of Metal Oxides By MVD TM. Tech. Proc. 22007 NSTI Nanotechnol. Conf. Trade Show Vol. 4. pp 575–577

Kobrin B, Nowak R, Yi RC, Chinn J (2005) Controlled deposition of silicon-containing coatings adhered by an oxide layer. WO Pat. WO 2005121396 A2

Manz a., Graber N, Widmer HM (1990) Miniaturized total chemical analysis systems: A novel concept for chemical sensing. Sensors Actuators B Chem 1:244–248. doi: 10.1016/0925-4005(90)80209-I

Matteucci M, Christiansen TL, Tanzi S, et al. (2013) Fabrication and characterization of injection molded multi level nano and microfluidic systems. Microelectron Eng In press. doi: 10.1016/j.mee.2013.01.060

Mayer TM, de Boer MP, Shinn ND, et al. (2000) Chemical vapor deposition of fluoroalkylsilane monolayer films for adhesion control in microelectromechanical systems. J Vac Sci Technol B Microelectron Nanom Struct 18:2433. doi: 10.1116/1.1288200

Oh KW, Ahn CH (2006) A review of microvalves. J Micromechanics Microengineering 16:R13–R39. doi: 10.1088/0960-1317/16/5/R01

Olsson E, Kreiss G (2005) A conservative level set method for two phase flow. J Comput Phys 210:225–246. doi: 10.1016/j.jcp.2005.04.007

Sun Y, Høgberg J, Christine T, et al. (2013) Pre-storage of gelified reagents in a lab-on-a-foil system for rapid nucleic acid analysis. Lab Chip. doi: 10.1039/c2lc41386h

Sussman M, Puckett EG (2000) A Coupled Level Set and Volume-of-Fluid Method for Computing 3D and Axisymmetric Incompressible Two-Phase Flows. J Comput Phys 162:301–337. doi: 10.1006/jcph.2000.6537

Tanzi S, Østergaard PF, Matteucci M, et al. (2012) Fabrication of combined-scale nano- and microfluidic polymer systems using a multilevel dry etching, electroplating and molding process. J Micromechanics Microengineering 22:115008. doi: 10.1088/0960-1317/22/11/115008

Thio THG, Soroori S, Ibrahim F, et al. (2013) Theoretical development and critical analysis of burst frequency equations for passive valves on centrifugal microfluidic platforms. Med Biol Eng Comput 51:525–35. doi: 10.1007/s11517-012-1020-7

Truckenmüller R, Ahrens R, Cheng Y, et al. (2006) An ultrasonic welding based process for building up a new class of inert fluidic microsensors and -actuators from polymers. Sensors Actuators A Phys 132:385–392. doi: 10.1016/j.sna.2006.04.040

Tseng F, Yang I, Lin K, Ma K (2002) Fluid filling into micro-fabricated reservoirs. Sensors Actuators A 97-98:131–138. doi: 10.1016/S0924-4247(01)00826-3

Wu H-C, Lin H-J, Hwang W-S (2005) A numerical study of the effect of operating parameters on drop formation in a squeeze mode inkjet device. Model Simul Mater Sci Eng 13:17–34. doi: 10.1088/0965-0393/13/1/002

Zhao B, Moore JS, Beebe DJ (2002) Principles of surface-directed liquid flow in microfluidic channels. Anal Chem 74:4259–68.

Zimmermann M, Hunziker P, Delamarche E (2008) Valves for autonomous capillary systems. Microfluid Nanofluidics 5:395–402. doi: 10.1007/s10404-007-0256-2